Identifying mineral dust emission sources in the Middle East using remote sensing techniques

PhD

School of Archaeology, Geography and Environmental Science (SAGES)

Mark Hennen

September 2017

Declaration of original authorship

Declaration: I confirm that this is my own work and the use of material from other sources has been properly and fully acknowledged.

Mark Hennen

Acknowledgments

I would like to dedicate this thesis to my wife Catherine Hennen, who has supported me throughout my PhD and has always been there to make me smile through the tough times - this thesis is as much yours as it is mine.

I would also like to thank my supervisors, Dr Maria Shahgedanova and Dr Kevin White for the support and excellent advice – thank you for giving me this opportunity and enabling me to achieve my ambitions. I consider you both to be true friends.

I extend my gratitude to the SAGES academic team at the University of Reading, several of whom I have known for many years, and who have always been more than generous in offering their help and advice. Special thanks goes to Dr Steve Musson, Dr Geoff Griffiths, Dr Steve Robinson, Dr Hilary Geoghegan, Dr Steve Gurney and Mrs Sue Hawthorne.

I must thank my friends and colleagues in the PhD office, you have all been a huge support and a fantastic group of people that I feel privileged to have known. We have had some great times, whether it be discussing the values of instant coffee during a break, trying to figure out a statistical test in the office or crying over our collective woes in SCR, your support and laughter have helped me no end. I wish you all, the best of luck in your future endeavours and hope to remain your friend for many years to come.

I would like to thank the University of Reading for giving me this opportunity and for being my home for the past eight years. I have experienced much here and am leaving the better for it – this will always be my second home.

Finally, I thank my friends and family back home, who have patiently stood by me as I have strived to reach my goals.

Abstract

This investigation presents a new high-resolution mineral dust climatology for the Middle East, describing the dust emission source of over 27,000 dust emission events during the period 2006 – 2013. The inventory was derived from the dust RGB product of the Spinning Enhanced Visual and InfraRed Imager (SEVIRI) on-board Meteosat's second-generation satellite (MSG). Mineral dust emissions were derived from visual inspection of the SEVIRI scenes, which have 4-5 km^2 spatial and 15-minute temporal resolution. The location of every emission event was recorded in a database, along with time and trajectory of dust movement. This is an improvement on previous studies, which derive dust source areas from the daily observations of Aerosol Optical Depth whose maxima do not necessarily coincide with sources of emissions, producing more accurate information on the location of the important dust sources in the region.

Results showed that dust sources are constrained to relatively small areas, with 23% of dust emissions generated from areas covering just 1% of the total land surface of the Middle East. Important sources include the Tigris-Euphrates flood plains of Iraq and Syria, Western and Northern Saudi Arabia and the Sistan Basin in Eastern Iran. The Tigris-Euphrates flood plain was the most active dust region, producing 37% of all dust events. Here, agricultural surfaces, especially those producing rain-fed wheat and barley appear to be particularly sensitive to drought conditions, with greatest dust emission frequency at the peak of the 2007 – 2009 drought – the most severe drought in instrumental history. Normalised Difference Vegetation Index (NDVI) data was acquired from the Moderate Resolution Imaging Spectrodiometer (MODIS) (MOD13A2) 1km database and correlated with dust emission frequency data in the region of greatest dust activity. These dust emission 'hotspots' showed a significant correlation between vegetation cover and dust emission frequency, with increased vegetation cover during non-drought years producing a marked decrease in dust emission frequency.

The southern areas of the Arabian Peninsula recorded very few dust emission observations, contrasting directly to many previous studies, which do not use such high temporal resolution data. The activation and frequency of dust emissions are characterised by strong seasonality developing in response to specific synoptic conditions. ERA Interim reanalysis data were used

to characterise synoptic conditions on identified dusty days, demonstrating a concurrent increase in dust emission frequency with intensifying summer (JJA) Shamal (northerly) winds over the Arabian Peninsula.

Table of Contents

List of Figures

List of Tables

List of abbreviations

IPCC	International Panel on Climate Change
SEVIRI	Spinning Enhanced Visible and Infrared Imager
MSG	Meteosat Second Generation (Satellite)
RGB	Red Green Blue image
AOD	Aerosol optical depth
DOD	Dust optical depth
TOMS	Total Ozone Monitoring Satellite
AI	Aerosol index
MODIS	Moderate Resolution Imaging Spectrodiameter
DEP	Dust enhancement product
OMI	Ozone Monitoring Instrument
DSF	Dust source frequency
NDVI	Normalised Difference Vegetation Index
AEW	African easterly waves
ABL	Atmospheric boundary layer
ECMWF	European Centre for Medium range Weather Forecasting
BoDEx	Bodélé Dust experiment
AERONET	Aerosol Robotic Network
QUEST	Quantifying and Understanding the Earth System
DEM	Digital elevation models
GIN12	(Ginoux *et al.,*2012) Anthropogenic dust classification
TEG04	(Tegen et al., 2004) Anthropogenic dust classification
TOA	Top of atmosphere
CBL	Convective boundary layer
SABL	Saharan atmospheric boundary layer

SCBL	Saharan convective boundary layer
SRL	Saharan Residual Layer
SAL	Saharan Air Layer
PBL	Planetary boundary layer
CALIOP	Cloud-Aerosol Lidar with Orthogonal Polarization
ITD	Intertropical discontinuity
GERBILS	Geostationary Earth Radiation Budget Inter-comparison of Long-wave and Short-wave radiation
ENSO	El Nino Southern Oscillation
NAO	North Atlantic Oscillation
LLJ	Low level jets
MSLP	Mean Sea Level Presure
UTC	Co-ordinated Universal Time
MASL	Meters above sea level
HYSPLIT	Hybrid Single-Particle Lagrangian Integrated Trajectory
TIR	Thermal infrared
SWIR	Short wave infrared
UV	Ultra-violet
BT	Brightness temperature
BTD	Brightness temperature differences
NASA	National Aeronautics and Space Administration
EOS	Earth Observing System
CWV	Column water vapour
COAMPS	Coupled Ocean/Atmospheric Mesoscale Prediction System
USGS	United States Geological Survey
DSAF	Dust Source Activation Frequency
SDF	SEVIRI Dust Flag
ΔT_{BG}	BT 10.8 μm – BT 8.7 μm

ΔT$_{BR}$	BT 12.0μm − BT 10.8μm
IDL	Interactive Data Language
DOC	Degree of Confidence
USDA	U.S. Department of Agriculture
PBDB	Polygonal drainage basin database
SRTM	Shuttle Radar Topography Mission
TM	Thematic Mapper
CV	Coefficient of variation
TEB	Tigris Euphrates Basin
LEB	Lake Eyre Basin
CD	Chihuahua Desert
NCDC	National Climatic Data Centre
UMES	Upper Mesopotamia
LMES	Lower Mesopotamia
CMIP5	Coupled Model Intercompariosn Project phase 5
GCM	General circulation model

Chapter 1: Introduction and justification

1.1 The Importance of atmospheric dust

Airborne mineral dust can have many important effects on the climate systems at both regional and global scale (Shao *et al.*, 2011). Each year, around 2000 Mt of dust is emitted into the atmosphere, with desert mineral dust the major type of aerosol by mass, accounting for, on average, ~40% of the global aerosol burden (Banks and Brindley, 2013). Measuring the total effect of airborne mineral dust is challenging because of the large number of differing impacts, both direct and indirect on the radiation budget and nutrient cycles. Recent simulations presented in the IPCC 5th assessment report (2013) estimate mean radiative forcing of dust as –0.10 (+/- 0.20 W m^{-2}) (Myhre *et al.*, 2013) (Fig 1.1). Estimates suggest that mineral dust emissions are responsible for approximately 30% of the instantaneous radiative impact of aerosols on the global energy balance - referred to as direct radiative effect (DRE) (Heald *et al.*, 2014). Importantly, the net radiative forcing of mineral dust is still debated, due to the fact that the non-spherical dust particles of different chemistry and composition limit the ability of models to accurately simulate scattering and absorption of solar and terrestrial radiation (Ginoux *et al.*, 2010). These estimates are further complicated by the indirect effect of airborne dust, which acts as cloud condensing nuclei, altering cloud formation, optical properties and precipitation activity (Tegen, 2003). Consequently, it is unclear whether dust creates a positive or negative overall radiative forcing (Shao *et al.*, 2011; Hsu *et al.*, 2004 see Fig. 1.1). Furthermore, these radiative impacts play an important role in numerical weather prediction (NWP) models, with the use of dust-specific radiation parametrisation schemes shown to improve the accuracy over dust prone areas (Haywood *et al.*, 2005).

Mineral dust plays an important role in many of the world's ecosystems, with long-range transport from the Sahara Desert linked to the nutrient cycle of both the Atlantic Ocean and maintaining the fertility of the Amazon Rainforest (Koren *et al.*, 2006; Thieuleux *et al.*, 2005; Husar *et al.*, 2001). Here, deposition of important mineral nutrients such as iron, are vital in maintaining the fertility of ocean and land surfaces alike, consequently effecting CO_2 sequestration through vegetation coverage (Ginoux *et al.*, 2010).

During its atmospheric lifetime, dust particles present multiple hazards to dryland communities at each stage; from nutrient loss in agricultural soils during entrainment, to sand blasting of crops and poor air quality during the transport phase, and contamination of drinking water and burial of structures in deposition downwind (Middleton, 2017). Dust storm conditions reduce visibility, closing airports and affecting driving conditions (Criado and Dorta, 2003). Fine particles, including salts and chemical pollutants are carried by these dust storms, causing physical irritation, respiratory complaints and a host of illnesses (Goudie, 2009; Middleton and Sternberg, 2013). A single dust storm caused the delay of Operation Iraqi Freedom by 5 days in 2003, as visibility prevented the military capabilities in that region of the Middle East (Walker *et al.*, 2009).
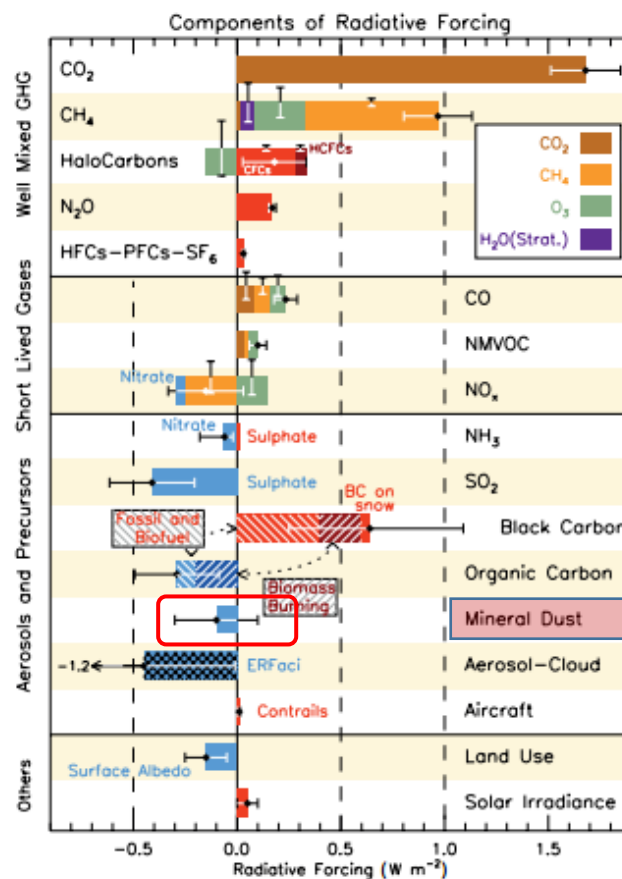
Figure 1.1: Radiative forcing by emitted compounds (gases, aerosols), land use and solar irradiance changes for the period 1750-2011. Highlighted is the radiative forcing of mineral dust. (Source: Myhre *et al.* 2013 - IPCC, 2013)

The variety and magnitude of the effects of dust depend on the physical, chemical, biological and optical characteristics of the particles (Ackerman, 1997). It is, therefore, important to gain precise knowledge of dust sources, their location, emission frequency and how they respond to climate variability (Schepanski *et al.*, 2012). These data will help to better constrain both global climate-aerosol models (Gherboudj *et al.*, 2017) and dust-radiation parametrisation schemes in NWP models (Pérez *et al.*, 2006). These are essential assets for dryland communities, which rely on accurate dust emission predictions to introduce effective mitigation and adaptation techniques, which are required to cope with all hazards posed by atmospheric dust (Middleton, 2017).

Globally, a high proportion of dust emissions (by mass) are generated by large synoptic-scale dust plumes or dust storms, originating from regional sources such as the Sahara Desert and the Sahel, the Arabian Peninsula and the deserts of China and central Asia (Prospero *et al.*, 2002). Observing dust events in these regions is complicated, as dust sources are often found in inhospitable areas and emission is unpredictable (Tegen, 2003; Ashpole and Washington, 2012). Without remote sensing data, monitoring on a regional scale would rely on lengthy and inefficient field based research or serendipitous observations (Husar *et al.*, 2001). Remote sensing in the ultra violet (UV), visible and thermal infrared (TIR) by earth orbiting missions provides the most comprehensive and reliable data for these regions (Schepanski *et al.*, 2009).

1.2   Dust source environments

Remote sensing analyses have routinely observed high levels of atmospheric dust in the vicinity of large inland topographic depressions, typically of endorheic drainage (e.g. Bodélé Depression, Chad); accordingly these dryland areas are recognised as important features in global dust emission scenarios (Ginoux *et al.*, 2012; Prospero *et al.*, 2002). Importantly, these large areas are comprised of a mosaic of multiple land surface types, formed by various geomorphological processes, characterised by different densities of vegetation and sedimentary environments (Bullard *et al.*, 2008). These heterogeneous land surfaces create preferential emission surfaces, typically in areas of abundant fine alluvial material and sparse vegetation (e.g. dry lakebed, ephemeral channel, alluvial plains) (Baddock *et al.*, 2011). The dust emission potential of these surfaces vary both spatially and temporally in response to

changing environmental conditions (Bullard *et al.*, 2011; Wang *et al.*, 2014; Zender *et al.*, 2003). Estimations of dust emission flux have been poorly constrained where the emission potential of specific surface types have not been taken into consideration (Johnson *et al.*, 2011), creating variability across models by a factor of up to 30 in certain situations (Todd *et al.*, 2008). The lack of dust emission observations, of a spatial and temporal resolution sufficient to resolve the emission characteristics at a sub-basin scale, creates the largest barrier to accurately representing this dynamism in climate-aerosol simulations (Shao *et al.*, 2011; Walker *et al.*, 2009).

Currently, the majority of dust emission data are produced by polar-orbiting satellites that, due to low sampling frequency (typically one image per day) are rarely able to detect discreet dust emissions at time of emission (Ashpole and Washington, 2013). Instead, these systems capture larger evolved dust plumes, typically several hours after emission and spatially offset from their source areas (Schepanski *et al.*, 2012).

Utilising the sub-hourly resolution of the Spinning Enhanced Visible and Infrared Imager (SEVIRI), dust emission sources in the Middle East during the period 2006 – 2013 will be located with greater accuracy than has previously been achieved.   These data will fulfil the current demand for a high-resolution dust emission inventory, enabling greater insights into the dust emitting processes in one of the world's most important regions of atmospheric dust production.

1.3   Dust emission in the Middle East

The Middle East is widely recognised as an important dust-producing region, second only to North Africa, with its global dust emission contribution estimated to be around 20% (Hamidi *et al.*, 2017). Multiple model simulations (Ridley et al., 2016; Fig. 1.2) and dust emission observations indicate persistent dusty conditions over the Arabian Peninsula, peaking during the hot and dry summer months (JJA) (Ginoux et al., 2012; see Fig. 2.1). Previous work has identified dust emission from multiple areas, including the alluvial plains of the Tigris Euphrates Basin (Middleton, 1986; Notaro *et al.*, 2015), the Ad Dahna sand sea of Saudi Arabia and the upland areas of the Al-Hajar Mounatins in Oman (Prospero *et al.*, 2002; Washington *et al.*, 2003). In Iran, frequent dust emission has been linked to the large internal salt flats

(Dasht-e-Kavir and Dasht-e-Lut) (Abdi Vishkaee *et al.*, 2011) and ephemeral lakes within the Sistan Basin (Kaskaoutis *et al.*, 2015a). Dust emission sources in the Middle East have received comparatively less attention to those in North Africa. The Middle East requires specific attention, as dust emission here has a significant effect on local communities, which unlike North Africa, are more densely populated in areas of significant dust activity (Notaro *et al.*, 2015). Furthermore, the land surface here is heavily disturbed by human activity, resulting from intensive agriculture in known dust emitting areas such as the Tigris Euphrates Basin (Kelley *et al.*, 2015). Investigating the dust emission frequency across these surfaces will provide information for comparison with anthropogenic surfaces in other drylands. These findings will have particular significance for future climate scenarios, as the recent periods of extreme drought in the region are likely to become more frequent throughout the 21st Century (Trigo *et al.*, 2010; Notaro *et al.*, 2015). How dust emission frequency reacts to these environmental conditions will have a large effect on local communities (Middleton, 2017) and on future global climate change (Shao et al., 2011). Currently, insufficient knowledge exists on discrete dust emission sources globally - especially those outside North Africa; precluding an accurate representation of dust emission frequency and subsequent net radiative effect in future climate change scenarios (Ridley *et al.*, 2016; Benedetti *et al.*, 2011; Mahowald *et al.*, 2010). This investigation will therefore help to fulfil the current requirement for high-resolution dust emission data in the Middle East - an important dust-emitting region.
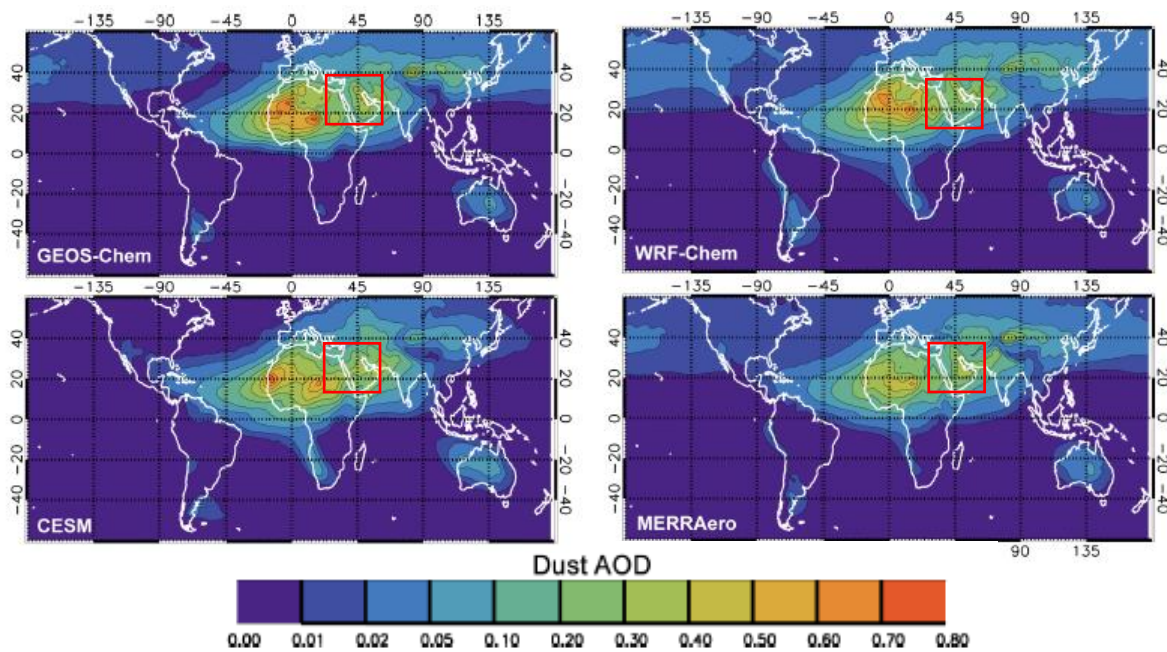
Figure 1.2: Annual dust-aerosol optical depth simulations from four widely used aerosol-climate models (GEOS-Chem[1]; CESM[2]; WRF-Chem[3]; MERRAero[4]), averaged over 2004 – 2008. Red outline depicts study area in this thesis. Source Ridley et al., (2016).

[1]**GEOS-Chem - Goddard Earth Observing System Chemical transport model (CTM)**

[2]**CESM – Community Earth System Model**

[3]**WRF-Chem – Weather Research and Forecasting model Chemical transport model (CTM)**

[4]**MERRAero – Modern Era Retrospective analysis for Research and Applications Aerosol Reanalysis**

1.4   Aims and Objectives

The main aims of this PhD are:

- Observe and record mineral dust emission events in the Middle East during the period 2006 - 2013, using remote sensing techniques, to create a high-resolution inventory of dust emission surfaces and their respective emission frequency.

- Use this information to gain a greater knowledge of dust source emitting processes, in a region not previously studied with this methodology and to this spatial resolution.

These aims will be met by achieving the following objectives.

(i)   Utilise imagery from the Spinning Enhanced Visible and Infra-Red Imager (SEVIRI) aboard the Meteosat Second Generation (MSG) Satellite to monitor the Middle East at a sub-hourly temporal and 4-5 km^2 spatial resolution. Detect all observable dust storms using the thermal infrared Dust RGB product. Manually identifying the source area of each dust storm by back-tracking through consecutive images. Compiling all locations into a dust source inventory, describing the dust climatology of the Middle East for the period 2006 - 2013.

(ii)   Spatially attribute dust emission sources with land surface characteristics. Study the relative emission frequency of different land surface types, with a focus on vegetation cover, soil properties and landforms.

(iii)   Identify and describe areas of frequent dust emission, and investigate the processes, which increase their surface deflation potential.

(iv)   Compare the relative emission frequency of dust emission surfaces at a sub-basin scale; use the high-resolution dust emission inventory to explore the respective responses of each surface type to environmental conditions such as drought and synoptic climate patterns.

(v)   Compare the performance of the manually derived SEVIRI dust emission inventory with datasets currently used to describe dust emission sources in the Middle East. Determine the advantages of this approach, describing how these data can be beneficial for future research opportunities.

1.5   Thesis structure

A summary of each chapters included in this thesis:

Chapter 2 – Literature Review: A comprehensive account of relevant literature, structured around the objectives set out in Chapter 1. Firstly, the geographical distribution of dust sources are discussed at a global scale. Following this, processes of dust emission are discussed, looking at both the land surface and atmospheric conditions required for dust emission, presenting current understanding and providing a background for *Objectives 2, 3 and 4*. Finally, dust emission in the Middle East is explored, relating known dust source areas to emission processes discussed in the previous section. This review highlights the gaps in current understanding, which motivate the research presented in this thesis.

Chapter 3 – Data and Methods: A review of current data, remote sensing platforms and methods used to describe global dust sources. The first section describes the three types of analysis currently used to determine dust emission sources (i.e. statistical analysis of atmospheric dust loadings, emission observations and coupled aerosol-climate models), the limitations of each and the important benefits of using SEVIRI imagery in the Middle East. Secondly, the SEVIRI Dust RGB product is analysed in detail, identifying the limitations, current applications and defining the methodology used to create the dust source inventory. Finally, a description of the secondary data used to characterise dust source locations identified in the inventory, which are necessary to complete *Objectives 2, 3* and *4*.

Chapter 4 – SEVIRI Dust Source Inventory of the Middle East (2006 – 2013): Results of the SEVIRI Dust RGB analysis described in Chapter 3, describing the spatial and temporal patterns of dust emission across the Middle East while also providing information on the duration, trajectory and sub-regional variability of dust emission frequency. This chapter produces a high-resolution inventory of dust emission sources in the Middle East their respective dust climatology, fulfilling *Objective 1* and thus the primary aim of this thesis.

Chapter 5 – Land surface environments and dust emission process in the Middle East: Analysis of land surface conditions of dust emission surfaces in the Middle East, as determined by the SEVIRI dust emission inventory (Chapter 4). This chapter fulfils Objectives 2 and 3 by analysing the relative dust emission potential of various land surface types commonly found in drylands, focussing on vegetation cover, soil texture, fluvial regime and geomorphological

process. This analysis includes identification of areas of frequent dust emission, referred to as 'hotspots' and determining the causes for increased emission in these areas.

Chapter 6 – Discussion, Dust emission in the Tigris Euphrates Basin (2006 – 2013): This chapter discusses the dust emission patterns observed at a sub-basin scale across the Tigris Euphrates Basin – an important dust source area due to the high population density and abundance of disturbed agricultural soils in what is commonly referred to as the 'Fertile Crescent'. This area has suffered from a prolonged period of drought (2007 – 2013), and thus provides a unique opportunity to observe how these extreme environmental conditions influence changes in dust emission frequency, thereby fulfilling *Objective 4*. This chapter begins by discussing the performance of the SEVIRI dust emission inventory with existing products and databases previously used to determine dust emission sources across the Middle East, completing *Objective 5*.

Chapter 7 – Conclusion: A summary of the findings generated by the research presented in this thesis, discussing limitations encountered and possible applications of the SEVIRI dust source inventory and future research goals.

Chapter 2: Literature Review

2.1   Introduction

Through increased use of satellite derived remote sensing, daily maps of global atmospheric aerosol concentrations have allowed us to locate sources of dust emission with increasing accuracy (Walker *et al.*, 2009). Recently, higher resolution platforms have enabled observation of entire regions at a sub hourly frequency (Schepanski *et al.*, 2012). This has opened up an area of research, which allows us to observe dust emissions as they happen, giving a far more accurate interpretation of the precise dust source area, their landform characteristics and individual dust emission behaviour.

This chapter will review published literature, exploring current understanding of land surface and atmospheric processes involved with dust emission within dryland environments around the world. The chapter begins by exploring the broad geography of dust emission, discussing the global positioning of high levels of dust in the atmosphere, how this relates to dust sources and the seasonality of dust emission (Section 2.2). The following section discusses processes of entrainment; how changes in soil moisture, sediment texture and surface roughness control the wind speed thresholds required for dust emission (Section 2.3). Section 2.4 explores the production and availability of fine sediments, specifically, their relationship to certain geomorphology and how they are spatially distributed at a sub-basin scale. Section 2.5 examines meteorological conditions that are conducive to the development of dust storms including individual variables such as soil moisture, surface wind speed and vertical velocities and synoptic and mesoscale conditions.

The chapter concludes with a discussion of studies of dust emissions and dust load in the Middle East (Section 2.6). Conclusions and research goals to be addressed by the thesis are outlined in the final section (Section 2.7).

2.2   Geographical distribution of mineral dust sources.

Aridity plays an important role in defining areas of possible dust emission (Goudie, 2009). Global measurements of dust in the atmosphere, through average levels of aerosol optical depth (AOD), have shown a spatial link to the arid or hyper-arid regions of the world (Fig. 2.1). These dryland areas cover over 41% of the Earth's surface, encompassing deserts, grassland and savannah (Feng and Fu, 2013). Arid and hyper-arid areas account for 10% and 16% of global land surfaces respectively, covering 36.2 million km^2 (Thomas, 2011). The ecosystems of these areas are especially fragile and sensitive to climate change, existing at the edge of sustainability as water resources remain stressed throughout the year (Seidel *et al.*, 2008). With 38% of the population living in dryland regions globally (Reynolds *et al.*, 2007), the monitoring and conservation of these areas is important.

Satellite data have shown that dust emissions do not emit homogeneously across all dryland areas, nor do these source areas emit continuously in all seasons (Fig. 2.1), in fact, they appear in concentrated dust source areas. Dust sources are routinely inferred using data from sun-synchronous orbiting satellites, producing global data sets of high atmospheric aerosol load and correlating them with areas at the surface (Prospero *et al.*, 2002; Washington *et al.*, 2003; Engelstaedter *et al.*, 2006; Ginoux *et al.*, 2012). There are problems in inferring precise volumes of dust in the atmosphere from satellites, related to the assumptions made concerning particle size, refractive index and particle shape (Harrison *et al.*, 2001). Nevertheless, these data have provided an essential tool in reconstructing spatial and seasonal patterns of dust emission around the globe. Data from the Total Ozone Monitoring Satellite (TOMS) aerosol index (AI) show dust emissions are overwhelmingly more abundant in the Northern Hemisphere, with the largest concentrations extending from Northern Africa, through the Middle East and into central Asia in an intercontinental 'dust belt' (Prospero *et al.*, 2002).

North Africa is widely accepted as the largest global source of atmospheric dust with emission estimates ranging from 170 to 1600 Tg yr^{-1} (Prospero *et al.*, 2002; Washington, Todd, *et al.*, 2006; Ginoux *et al.*, 2012), accounting for over half (40-70%) of the global atmospheric dust burden (Engelstaedter *et al.*, 2006). Africa carries the largest percentage of arid areas of all the continents around the globe (Table 2.1), with a large area of hyper aridity (<200 mm/yr^{-1}) extending from 18˚N to the Atlas Mountains and the Mediterranean coast in the north (Fig.

2.1). Prospero *et al.* (2002) observed persistent high concentrations of atmospheric dust over topographic depressions, such as the Bodélé Depression in Chad, where large quantities of fine diatomite alluvium had built up from intermittent flooding since the early Quaternary (Washington *et al.*, 2003). Observations from the Moderate Resolution Imaging Spectrodiameter (MODIS), describe distinctly seasonal distributions of atmospheric dust (Fig. 2.1), especially over the Sahel region during spring (Ginoux *et al.* 2012). Here specific areas including parts of Maurintania, Niger and the aforementioned Bodélé Depression exceeded their dust detection threshold more than 75% of the time (Fig. 2.1). Extending east, Ginoux *et al.* (2012) observed seasonal increases in dust emission over large parts of the Middle East, including Mesopotamia and the Arabian Peninsula during summer (JJA). In Central Asia, summertime dust emissions remain high over eastern Uzbekistan and Turkmenistan and into the Indo-Gangetic basin, especially during the pre-monsoon months in spring (MAM) (Ginoux *et al.*, 2012).

Table 2.1: Percentage of global drylands by continent. Source: Thomas, (2011)

Continent	% total global arid area
Africa	31.9
Asia – including the Middle East	31.7
Australasia	10.8
North America	12.0
South America	8.8
Europe	4.9

These data have helped to highlight the key mineral dust emitting regions around the world, and have been widely applied to subsequent studies in key dust source regions, especially North Africa. Importantly, the global areas highlighted in these studies are extensive, with a multitude of different surface characteristics including differences in sedimentary types and vegetation cover (Bullard *et al.*, 2008). A gap therefore exists in our understanding of key dust emitting processes at a local scale, especially in the Middle East, largely due to the coarse temporal resolution of the data sets. With daily observations of dust in the atmosphere, source areas are attributed by a statistical interpretation of persistently high AOD and nearby

topographic formations such as large-scale drainage basins (Schepanski *et al.*, 2012). This not only denies the ability to infer high resolution information of precise dust source locations, their associated surface properties or individual dust event characteristics, it also assumes that instantaneous snapshots of high AOD relate to dust source area. In North Africa, Schepanksi *et al.* (2012) have shown that this assumption is misplaced, with observations of surface emission occurring several hours before these fixed daily snapshots, and a significant distance upwind of areas of high AOD. This distorts regional and global aerosol estimates used as inputs in atmospheric models and results in inaccurate assessment of the dust emitting potential of certain land surfaces and landforms.

The research presented in this thesis will fill this gap in understanding, providing a uniformly applied method across the Middle East. Through observing dust emission at source, this research provides a high-resolution inventory of dust emission in a region not previously studied with such data, allowing the in-depth study of local dust emission processes.
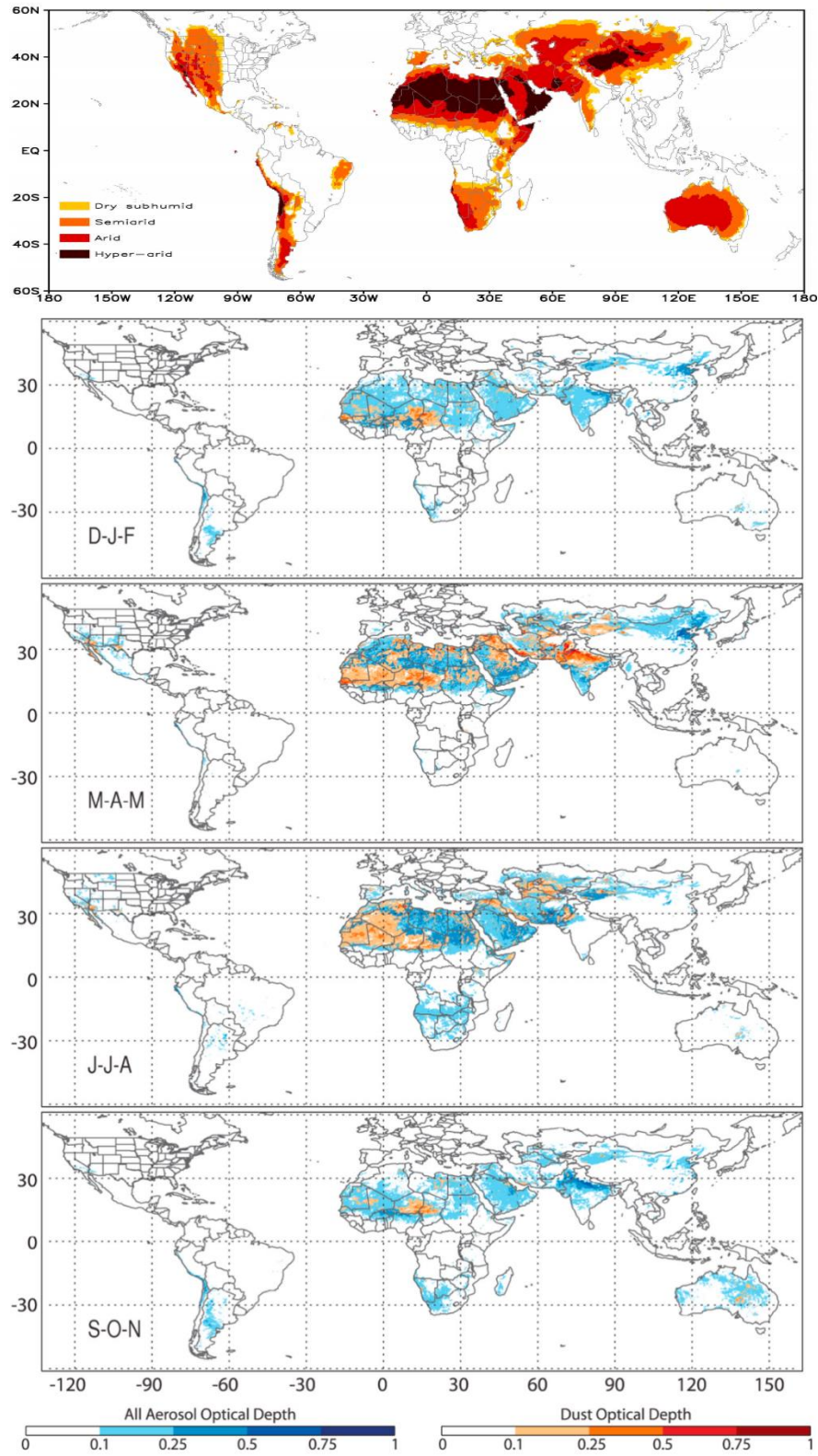
Figure 2.1: Comparison between global dryland areas and prevalent atmospheric dust distribution. (a) Distribution of global drylands for 1961-1990 based on *P/PET* ratio (Source: Feng and Fu, 2013). (b) MODIS seasonal average aerosol and dust optical depth (AOD / DOD) (Source: Ginoux *et al.*, 2012).

2.3   Dust entrainment: sediment characteristics and meteorological thresholds.

The entrainment of dust requires both the supply of fine sediments (erodibility) and sufficient surface winds (erosivity) (Washington and Todd, 2005). This section will discuss the complex dynamic thresholds that are dictated by many surface characteristics including: sediment textures (2.3.1), surface roughness (including vegetation cover) (2.3.2) and soil moisture (2.3.3) (Harrison *et al.*, 2001; Gherboudj *et al.*, 2017).

2.3.1   Sediment texture

The existence and availability of fine sediments is critical for the development of sources of dust (Engelstaedter *et al.*, 2006). Typically, deflation surfaces contain a combination of minerals, including e.g. quartz, clays, calcite, gypsum and iron oxides (Sokolik and Toon, 1999). These fine grained sediment particles are normally grouped into 3 size classes (clay, silt and sand) depending on their respective diameter (Table 2.2). The finest are clay = < 2 µm, with silt particles = between 2 and 62.5 µm and sand = between 62.5 and 2000 µm (Tegen and Fung, 1994). Soils are rarely made up of only one of these sediment size classes and are often a combination of all three with the addition of coarser gravel. Typically, atmospheric dust particles contain sediments smaller than 62.5 µm, at the boundary between silt and sand (Goudie and Middleton, 2001). Preferential deposition quickly removes particles larger than 65 µm, resulting in the omission of regions consisting of coarse particles from dust emission models (Tegen and Fung, 1994). However, the cohesive nature of smaller particles effectively prevents deflation of these particles by aerodynamic forces alone (Chomette *et al.*, 1999). The availability of coarser particles (greater than 70 µm) is necessary to initiate deflation by impacting and breaking up the adjacent finer sediment surfaces (Bullard and White, 2005). Dependent on surface particle size distribution, surface deflation occurs from three main mechanisms (Fig. 2.2), these include saltation (70 – 500 µm), creep (greater than 500 µm) and suspension (less than 20 µm) (Shao and Lu, 2000) (Shao and Lu, 2000).
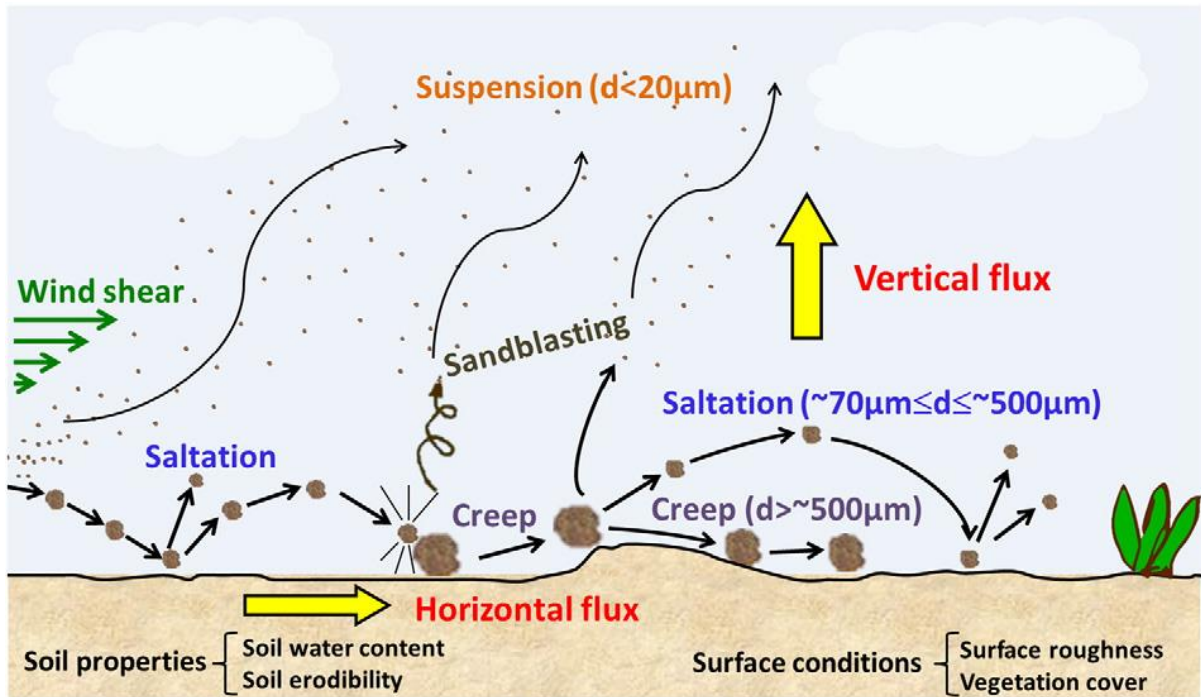
Figure 2.2: A depiction of the key physical processes related to dust emission and horizontal transport. Source Gherboudj *et al.*, (2017)

As the most effective mechanism, saltation accounts for 50-90% of sediment transportation (Gherboudj *et al.*, 2017). Surface winds allow medium sized particles (85 – 500 μm) to be bounced along the surface in a series of short jumps, continuously disintegrating the particle or the impacted surface into smaller particles until they become small enough to be suspended by the prevailing wind (Zender *et al.*, 2013). Soils that contain a range of particle sizes (less than aggregates and gravels), tend to have the highest erodibility function and dust generation potential (Table 2.2). Creep accounts for 5-25% of surface transportation (Gherboudj *et al.*, 2017), occurring as saltation impacts upon larger sediments. Each impact causes the larger sediment to roll across the surface; these large particles are unlikely to be lofted due to gravitation forces unless wind speeds increase or particle size is sufficiently reduced by saltation. Suspension accounts for a small proportion of surface movement (1%), where very small particles (less than 20 μm) are uplifted by local winds. This process can transport these fine mineral or pollutant particles many thousands of meters up into the atmosphere, and over 100 – 1000s of km from the deflating regions (Haywood and Boucher, 2000). The impact of dust over such a large range is one of the reasons why it has become a global issue and an important consideration in climate models (Goudie, 2009; IPCC, 2013).

Indeed, dust from the Sahara has been found in the Gulf of Guinea, the Mediterranean Sea, and the UK, and is recognised an important nutrient input to the Amazon Rain Forest (Koren *et al.*, 2006; Goudie, 2009;). Dust from the Middle East has been discovered within the snow pack atop Mount Elbrus in the Caucasus (Kutuzov *et al.*, 2013; Shahgedanova *et al.*, 2012) and dust from the Lake Eyre Basin in Australia is known to accumulate over Eastern Antarctica (Bullard et., 2008). Analysis of dust particle sizes deposited far from known dust sources show a particle size distribution between 5 and 30 µm (Goudie and Middleton, 2001).

Table 2.2: Sediment texture described by combinations of different sediment particle sizes and examples of their associated landforms. Deflation characteristics are described by qualitative indicators of wind erodibility and the dust emission potential. Source: Bullard *et al.* (2011).

Sediment Texture	Wind Erodibility	Dust Generation Potential	Example of Sedimentary Environments
Mixed sand / gravel	Low	Low	Alluvial fans
Mixed clay / silt + gravel	Low	Moderate	Stoney surfaces, Distal alluvial fans
Sand	Moderate	Moderate	Sandy aeolian deposits, sand sheets, sand dunes
Mixed sand / silt	High	High	Source-proximal loess
Silt / clay	High	Low	Ephemeral and dry unconsolidated lakes
Sand / clay	High	High	Fluvial-coupled ephemeral lakes, margins of ephemeral and dry lakes

2.3.2   Surface roughness and vegetation

Dust emission is strongly constrained by the presence of non-erodible elements on the surface, inhibiting deflation by absorbing a portion of the wind energy at the surface through frictional forces (Harrison *et al.*, 2002). These roughness elements can be formed of soils of non-erodible particle size (greater than 85 µm) known as aggregate, or by the presence of vegetation (Raupach et al, 1993). Semi-arid areas show strong seasonal suppression in dust emission during the annual growth of grasses and shrubs, even when shrubs are not in leaf (Tegen *et al.*, 2002). The amount of energy absorbed by vegetation (how much it inhibits deflation) is defined by the height, the leaf area and the connectivity between individual plants. Studies have shown that dust emission in extensively vegetated areas is still considerable where large gaps appear in the vegetation coverage (Okin *et al.*, 2011).

Simulations of dust emission that do not consider the presence and type of vegetation will usually require empirical adjustments to match observations (Engelstaedter *et al.*, 2003). By extension, ignoring the role played by vegetation affects our ability to simulate future climate change correctly; such is its influence on aerosol models (Tegen *et al.*, 2002). Through analysis of dust storm frequency (DSF) data from more than 2400 meteorological stations, Engelstaedter *et al.* (2003) show areas defined as bare ground experience a much higher dust storm frequency (DSF) (79.4 d/yr) compared to either forest (DSF 1.5 d/yr) or tundra (DSF 1.1 d/yr). When only considering vegetation, these data show reduced leaf area index has the greatest impact on dust emission potential, while differences in vegetation type, including structure and density have a smaller impact.

Kim *et al.* (2016) studied 27 years of observed and modelled dust emission, wind speed and Normalised Difference Vegetation Index (NDVI) data over North Africa, demonstrating the impact of vegetation on dust emission. North Africa can be separated into two distinct regions by the differences in vegetation cover, with the permanently arid region (Sahara) to the north and a semi-arid region (Sahel) at lower latitudes (Kim *et al.*, 2016). In the persistently arid Sahara, NDVI remained relatively stable, and changes in wind speed correlated well with changes in dust emission (R=0.92). In contrast, the more humid Sahel region was negatively correlated (R= -0.65) with NDVI, with dust emission reducing as NDVI increased by 0.8% per year from 1982 to 2001.

When using low vegetation cover as an indicator of potential dust sources, 33% of the planet's land surfaces and 9% of all surfaces are potential source areas (Tegen and Fung, 1994). However, as shown here, the lack of vegetation is not the sole characteristic required for an effective dust source.

2.3.3   *Soil moisture and surface crusts*

The cohesive nature of the deflating surface is vital in determining the flux of dust emission (Fécan *et al.*, 1999). Cohesion of surface soils is determined by the particle size distribution and moisture content. During the deflation of finer particles, aerodynamic forces are countered by the inter-particle cohesion and gravity, causing particles to aggregate together, especially in mixed soils where dust sized particles will adhere to larger sand particles

(Ishizuka *et al.*, 2008). The ensuing formation of a surface crust limits the deflation potential of the surface unless broken up by saltation bombardment (Zender *et al.*, 2013), rain droplet impact (Ishizuka *et al.*, 2008) and weathering by surface flow (Fecan *et al.*, 1999). Soil moisture affects deflation potential by two main processes (i) increases the growth of seasonal vegetation, reducing wind energy by friction, and (ii) increases soil cohesion through capillary force, causing the aggregation of smaller particles and shifting the soil to a larger particle size distribution (Gherboudj *et al.*, 2017). Importantly, the soil moisture effect on deflation is dependent on the absorptive characteristic of the soil. The amount of water required to prevent surface deflation increases with surface area, meaning soils with high clay content require more precipitation or surface flow before capillary force prevents emission, as these soils have a high storage and infiltration capacity (Fécan *et al.*, 1999). Specifically, surface deflation models stipulate that soil deflation only takes place when the soil moisture content of sandy, silty and clayey soils remain 20%, 25% and 50% below field capacity respectively (Tegen and Fung, 2005).

2.3.4   Surface winds and emission thresholds.

The uplift of dust requires (i) strong surface winds, (ii) strong vertical velocities; (iii) and low soil moisture. While low soil moisture is a typical feature of the arid environments and is controlled largely by seasonal cycles in precipitation (e.g. Cooke *et al.*, 2009), a range of synoptic and mesoscale meteorological conditions ensure the occurrence of strong surface wind and vertical velocities in the boundary layer. This section provides a brief description of the meteorological conditions involved with strong surface wind speeds in the Middle East and other dust emitting regions around the world; before discussing the wind speed thresholds associated with surface deflation in Section 2.3.4.2. A more in depth account of these meteorological conditions is given in Section 2.5.

2.3.4.1 Meteorological conditions on different scales

Many seasonal dust events are driven by continental scale circulations, particularly monsoon circulations with associated acceleration towards seasonal heat lows over Pakistan, the Western Sahara and the Arabian Peninsula (Knippertz *et al.*, 2014; Bou Karam *et al.*, 2017). Synoptic scale systems are associated with the episodic nature of large dust emission events

and are key drivers of dust emission throughout tropical and sub-tropical latitudes (Knippertz and Todd, 2012). These systems include extratropical cyclonic disturbances, associated with high winds within a trailing cold front. Such patterns are commonly found in the lee of the Atlas Mountains in the Northern Sahara (Schepanski and Knippertz, 2011), before travelling on an eastward storm track across the Middle East (Middleton, 1986). Further examples include the African easterly waves (AEWs) over the Sahel / southern Sahara (Knippertz and Todd 2010) and the longer lasting anticyclonic systems formed by deep penetration of cold air into lower latitudes (Cavazos *et al.*, 2009). In each of these systems, the establishment of a large surface pressure gradient is key, providing the required surface winds to entrain dust emission and transport it over long distances (Knippertz and Todd, 2012). Mesoscale dust events such as Haboobs (Arabic word for strong wind) are common among many deserts worldwide, particularly in pre monsoon seasons in West Africa and India/Pakistan (Knippertz and Todd, 2012). Similarly, these events occur near orographic features such as the Al Hajar mountain range in the United Arab Emirates / Oman (Miller *et al.*, 2008) or the Atlas Mountains in Morocco (Knippertz *et al.*, 2007). These mesoscale features are formed by cold, evaporation driven near surface downdrafts, close to areas of moist convection (Knippertz and Todd, 2012; Miller *et al.*, 2008). Following a diurnal cycle of moist convection, Haboobs appear in the late afternoon as a cluster of mesoscale features that occasionally converge into one larger event (Miller *et al.*, 2008). Turbulent circulations in the dry convective atmospheric boundary layer (ABL) are known to cause dust events on a microscale (up to several hundred meters) (Knippertz and Todd, 2012). Taking the form of either small rotating dust devils or larger, non-rotating dust plumes, these short-term events (typically under an hour) can lift large quantities of dust up to 3 km into the atmosphere (Ansmann *et al.*, 2009).

2.3.4.2 Wind speed thresholds of dust emission

The emission flux of dust in relation to wind speed is not linear; instead, a complex process whereby the kinetic energy of the wind must exceed the velocity threshold of the deflating surface before emission can take place (Chomette *et al.*, 1999). Emission flux is calculated as a function of the difference between the surface wind speed and local threshold (Knippertz and Todd, 2012). The local surface threshold is often determined by characteristics of surface roughness (including vegetation), soil texture and soil moisture (Marticorena and Bergametti,

1995) (see Sections 2.3.1 to 2.3.3). Incorporation of simple surface velocity thresholds have helped improve simulations of dust emission activity and potential surface erodibility (Tegen and Fung, 1994; Marticorena and Bergametti, 1995). However, there exist numerous dust emission models, utilising a range of schemes of varying complexity. Global models tend to be more simplistic, producing coarse resolution (1°x 1°) grids of surface erodibility based on 10 m surface wind speed and soil roughness coefficients. Chomette *et al.* (1999) calculated wind speed thresholds between 6 and 9 m/s^{-1} across seven locations throughout the Sahara by combining 10 m surface wind speed reanalysis data from ECMWF (European Centre for Medium range Weather Forecasting) and satellite observed dust storms in North Africa. Models of this spatial resolution may be too simplistic to account for the surface heterogeneity and emission variability of dust emitting regions. Regional models tend to have a much higher spatial resolution and utilise a larger range of physical characteristics in parameterising wind speed thresholds. These include calculations of size-resolved saltation flux, a key element in the effective breakup and emission of fine particles (see Section 2.3.2), which is dependent on particle size distribution, moisture content and surface roughness (Shao, 2004). Laurent *et al.* (2006) emphasise that the vertical emission flux is not only dependent on the erodibility of the parent soil, but also on the flux of fine transportable sediment, a process strongly influenced by the saltation flux. Furthermore, they stipulate that the emission flux is dependent on the size of the area not protected by roughness elements (vegetation, aggregates) i.e. the grid cell erodible fraction.

Due to their large variability in parameters and spatial resolutions, dust emission models rarely agree. Todd *et al.* (2008) observed an order of magnitude range of emission estimates from a suite of emission models during the Bodélé Dust experiment (BoDEx 2005). This is perhaps unsurprising, given that dust emission is borne out of highly dynamic meteorological and land surface characterisitics, which can vary at spatial and temporal scales that even the highest resolution regional models do not match (Knippertz and Todd, 2012). Consequently, many regional models have attempted to tune their emission thresholds to empirically derived dust emission observations (i.e. MODIS / TOMS) (Ginoux *et al.*, 2001). Given the low temporal resolution of polar orbiting satellites, it is believed that the high frequency data provided from this investigation will provide a far more accurate picture of local dust emission behaviour, proving invaluable for future tuning of dust emission thresholds in the Middle East.

2.4   Deflation surfaces and emission processes.

Daily maps of AOD have shown a clear link between dust emissions and large-scale topographical depression of internal drainage (Prospero et al, 2002; Ginoux *et al.*, 2012; see Section 2.2). Examples of these features can be found in many of the arid and semi-arid areas of the world, including the Bodélé and Taoudenni basins in Northern Africa, the Tarim basin in China, the Sistan basin in eastern Iran, the Lake Eyre basin in Australia and the Etosha basin in Northern Namibia (Ginoux *et al.*, 2012). However, field observations show that actual sources of dust can be highly localised within the broad dust source areas (Middleton, 1986). In this section, deflation activity on a sub basin scale will be discussed, looking specifically at the different landforms, which create the heterogeneous mosaic of land surfaces in arid drainage basins. Firstly, Section 2.4.1 uses the example of the Bodélé Depression, recognised as the greatest source area of dust in the world, to explain the need to understand the sub-basin dynamics of dust emission. Section 2.4.2 introduces Bullard *et al.* (2011) classification of geomorphological land types, with examples where this classification scheme has already been applied to basins around the world. Section 2.4.3 discusses the individual land types set out in Bullard *et al.* (2011), and the controls over seasonal production and availability of fine sediments. Finally, Section 2.4.4 discusses anthropogenic land surfaces, including land surfaces disturbed by agriculture and river channel management. These land surfaces are not considered in Bullard et al (2011) classification, but are of high significance in the Middle East, where population density is high compared to other arid environments (e.g. Sahara).

2.4.1   Dust emission within a drainage basin - Bodélé Depression

Surface measurements of horizontal visibility from meteorological stations and data from the Aerosol Robotic Network (AERONET) have noted a distinct heterogeneity of dust emission across broad arid regions (Engelstaedter *et al.*, 2006). These data indicate that dust emission occurs from distinct source areas (Goudie and Middleton, 1992), far smaller than the regional scale determinations derived from AOD concentrations. Described as dust 'hot spots' by (Gillette, 1999), these areas have been linked to geomorphological features with specific sediment characteristics, typically sub basin scale, surface depressions of internal drainage (Ginoux *et al.*, 2001) and their associated catchment areas, where fine alluvial sediment preferentially accumulates (Zender *et al.*, 2003).

This is evident in the Bodélé Depression, reported by many studies to be the largest dust sources in the world (Middleton and Goudie, 2001; Prospero *et al.*, 2002; Washington *et al.*, 2003; Washington, M. C. Todd, *et al.*, 2006; Koren *et al.*, 2006; Ginoux *et al.*, 2012). This can be attributed to both its size (~133,532 km2) (Ben-Ami *et al.*, 2010) and the geomorphological characteristics of the region. Sitting between Lake Chad to the southeast and the Tibesti Mountains to the northwest, this area is made up of a collection of large ephemerally flooding salt playas (Koren and Kaufman, 2004), which previously represented the lakebed under the northern extent of Lake Mega-Chad (Ginoux *et al.* 2010). Due to its fluvial past, the surface sediments are largely made up of very fine diatomite and lacustrine sediments several hundred metres thick in places (Washington and Todd, 2006). At the outer extremities of the basin, contemporary hydrology is dominated by streams draining from the Tibesti Massif (Goudie and Middleton, 2001), supplying silty alluvium via ephemeral wadis (Arabic for mountain valley) and alluvial fans, where the weathered sediments are deposited as channel velocity decreases (Ginoux *et al.*, 2012).

This combination of geomorphological features is typical of many dryland surface depressions. However, the potential for, and frequency of, dust emission is strongly controlled by the specific characteristics of each individual drainage basin. When attempting to pinpoint the most important geomorphological feature within an endorheic system, (Herman *et al.*, 1997) noted that all previous studies appeared to disagree on this point, inferring that accurate source mapping was, therefore, very important.

This example highlights the gap in understanding dust emission processes at the sub-basin scale, due in part, to the historical lack of sub daily satellite observations, in addition to the scale and inhospitable conditions preventing continuous surface observations in these environments (Bullard *et al.*, 2008). This information is important for a number of reasons, one of which is increasing our ability to simulate the dust cycle accurately on a regional scale. With recent modelling approaches, dust emissions are simulated from a combination of land surface parameters including: land use, soil texture and soil roughness; and the positioning of high AOD (Shao *et al.*, 2002; Tegen *et al.*, 2002; Uno *et al.*, 2006). Without the use of empirically derived emission source data, these approaches failed to correctly capture the spatial and temporal variability of dust emissions at a sub basin scale. Furthermore, recently recognised dust-emitting landforms, such as alluvial fans (Schepanski *et al.*, 2009), were

excluded from the model. A demand therefore exists for high-resolution dust emission observations, to allow a greater understanding of which surface characteristics and geomorphological landforms are most susceptible to surface deflation. With these data, the implementation of a global modelling framework, which extends beyond the initial area of observation and covers a variety of past and future climate scenarios, could be possible (Bullard *et al.*, 2011).

2.4.2 Sub Basin dust source classification

As dust production is heterogeneous across basins (Wang *et al.*, 2006; Bullard *et al.*, 2008; Baddock *et al.*, 2011), many studies have characterised the geomorphological features within dryland basins and attempted to relate each to a respective emission frequency (Wang *et al.*, 2006; Mahowald *et al.*, 2003). To aid comparison of different dust hotspots around the world, the Quantifying and Understanding the Earth System (QUEST) dust working group attempted to create a common, geomorphology-based classification of sub basin land forms (Baddock *et al.*, 2011). Based on a combination of remote sensing data, including satellite imagery, aerial photographs and digital elevation models (DEM), Bullard *et al.* (2009) formulated a classification using a limited number of easily identifiable geomorphological types prevalent within these basins (Table 1). Due to the availability of fine sediments in these environments, they have all been linked with emitting dust, with the relative importance of each obtained from dust emission observations.

No sub-basin assessments of this type have been carried out in the Middle East due to the lack of dust emission observations. The Tigris-Euphrates Basin is already known to be a source of atmospheric mineral dust (Middleton, 1986; Ginoux *et al.*, 2012; Karma Francis *et al.*, 2017), and provides a good setting to test the application of this form of analysis. In the following section, results of sub-basin analysis of preferential dust sources, from multiple basins around the world are discussed. It then proceeds to discuss our understanding of the dust emission processes from the different landforms described in Table 2.3.

Table 2.3: Classification of sub basin geomorphology and their associated importance to dust emission as described by Bullard *et al.* (2009).

Main geomorphological class	Geomorphology Sub-division	Importance for dust emission
Lakes	Wet	Low
	Ephemeral	High - Med
	Dry - consolidated	Low
	Dry - non consolidated	High - Med
High Relief alluvial systems	Armoured - incised	Low
	Armoured - unincised	Low
	Unarmoured - incised	Medium
	Unarmoured – unincised	Med - High
Low relief alluvial systems	Armoured - incised	Low
	Armoured - unincised	Medium
	Unarmoured - incised	Low
	Unarmoured – unincised	Medium
Stoney Surfaces		Low
Aeolian systems	Sand Sheet	Low - Med
	Aeolian sand dunes	Low - High
Loess		Low - Med
Low emission surfaces		Low

2.4.2.1 Case Study - Lake Eyre

Using a combination of meteorological station data and MODIS satellite data, Bullard *et al.* (2008) studied the dust emission frequency from the Lake Eyre Basin, in Australia (Fig. 2.3). From this, 529 individual dust plumes were identified from 2003 to 2006 and classified regarding different sub-basin scale landforms. The 1.17 million km^2 basin was classified into 5 main geomorphological units that predate but loosely match the QUEST classification scheme (Fig. 2.3b), including ephemeral lakes, alluvial channels, stone covered plains, aeolian sands and plains and low hills. The 529 point sources were included in Bullard *et al* (2011) where

they were used to determine the erosion potential of each landform (Fig. 2.3a). The results clearly demonstrate the importance of ephemeral lakes as a dust source, with 29% of dust emissions sourced from ephemeral lakes, despite only making up 2.26% of the land surface area. The same distribution is observed in the Chihuahuan Desert on the border of Mexico and the USA, where only 4% of the study area consists of ephemeral lakebeds yet still account for 48% of dust events (Baddock *et al.*, 2011). Importantly, the ability to determine the point source of dust plumes has given further insight into the sub-basin dust emission behaviour, demonstrating the additional importance of both alluvial (11.5% of land surface area) and aeolian (32.6% of land surface area) deposits, contributing 30% and 37% of dust emissions respectively. When analysing the results by number of events per unit area, ephemeral lakes are far more active dust emitters, with the bed of Lake Eyre produced 11 times more dust emission events per unit area than aeolian sediments and 6 times more than alluvium (Bullard *et al.*, 2008). Despite being less effective producers of dust, alluvial and aeolian sediments have been shown to contribute towards total aerosol burden and may bear a larger relative contribution during periods of decreased supply from ephemeral lakes.

With MODIS offering a maximum of two images a day (one each from Aqua and Terra spacecraft), dust emission observations were limited, i.e. when observations were not masked by meteorological clouds or upwind dust plumes. Of the 529 observations made, just over half of dust sources were observed as either a discrete point source, with a 'sharp' upwind edge (i.e. individually identifiable) of a scale less than 10 km wide, with the remainder observed as large scale (greater than 10 km wide) dust producing zones, with a less defined edge that may involve multiple sources. The type of observation varied across the dust emitting land surfaces, with more 70% of observations from ephemeral lakes described as discrete point sources. This is as expected, as most ephemeral lakes represent relatively small, concentrated zones of deflating material, creating a more clearly defined emitting surface than the larger expanses of alluvial and aeolian deposits.
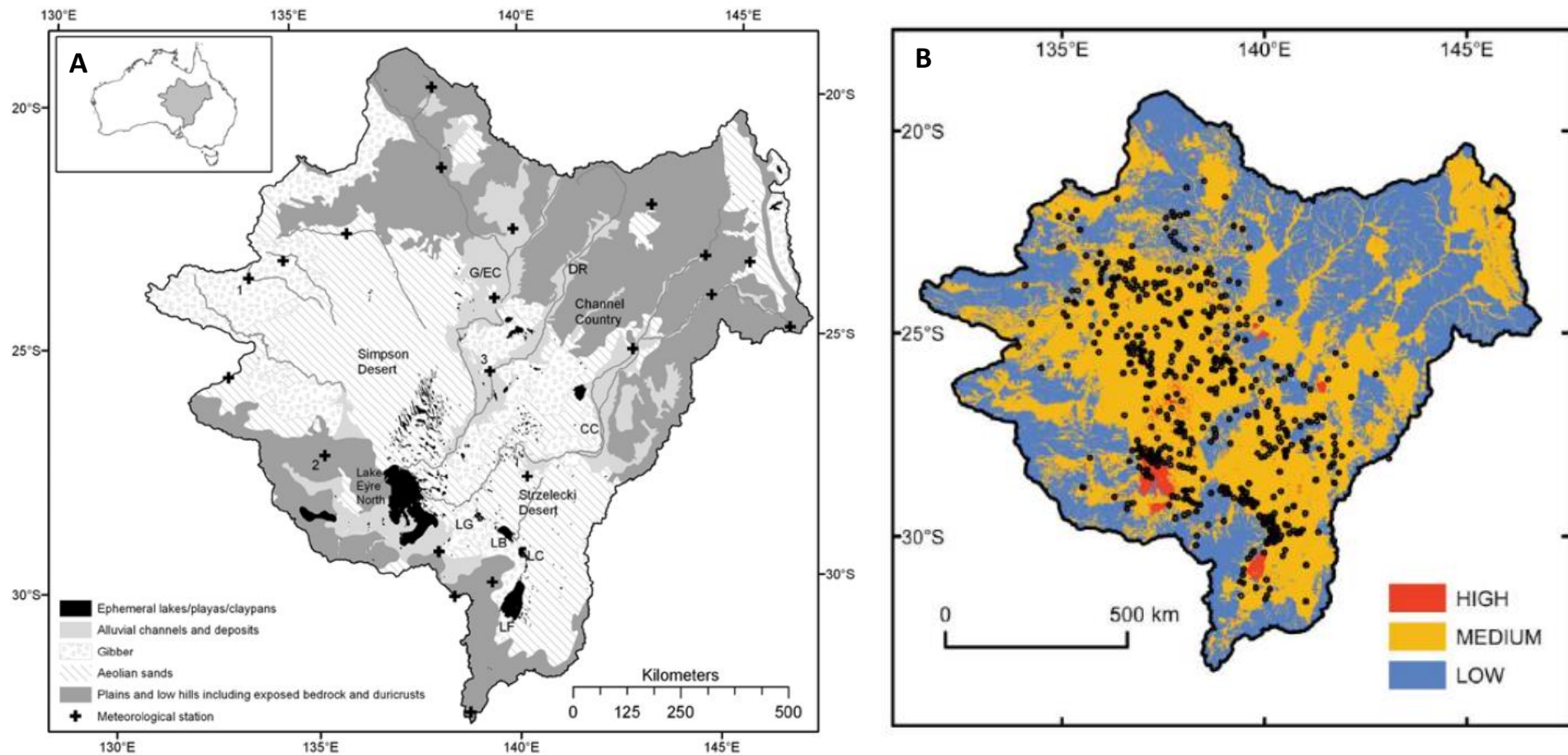
Figure 2.3: 2003 – 2006 classification of Lake Eyre Sub-basin geomorphology and observed dust sources. A) Lake Eyre Basin sub basin Geomorphology (Source: Bullard *et al.*, 2008).   B) 529 individually observed dust sources with geomorphic land surfaces dust emitting potential described as either high, medium or low (Source: Bullard *et al.*, 2011).

2.4.3 *Dust emission and geomorphology*

While each of the drainage basins, analysed in Bullard *et al.* (2011) are located firmly in the arid zone, a link between deflation and recent rainfall and runoff is clear, and has long been acknowledged as an important factor in dust source development (Prospero *et al.*, 2002). The link between fluvial activity and dust emission has been shown by the existence of a range of fluvial features including alluvial fans, flood plains and ephemeral lakes and rivers (Bryant, 2003; Mahowald *et al.*, 2003; Bullard *et al.*, 2011). As Bullard *et al.* (2011) have shown, ephemeral lakes are a very effective source of dust emission, and are regularly studied as a source of dust.

2.4.3.1 Supply and availability of fine sediments on deflating surfaces

Dust sources are usually described as either supply or availability limited. Supply refers the amount of sediment in the source area, whereas availability describes the ease at which the sediments are available for deflation. Bullard *et al.* (2011) adapted a conceptual model by (Kocurek, 1998) to describe how sediment production, supply and availability are affected by phases of humid and arid conditions (Fig. 2.4). Their model demonstrates the importance of humid (rainy) periods in producing fine sediments through the weathering of coarser sediments and their transport and accumulation by fluvial systems. Wetter phases reduce availability of sediment for deflation by increased vegetation and soil wetness, increasing the store of sediment at source as production exceeds transport. Upon the onset of an arid phase, dust emission is availability limited, as increased vegetation continues to bind together the surface, whilst the canopy reduces transport capacity by slowing surface winds by frictional forces. As the arid phase continues, dust emission increases progressively. At this stage, dust emission is only limited by the transport capacity of the wind until the reserves of sediment provided during the humid phase dissipate to the point of limited supply.

The transition from humid to arid phases occurs both temporally (i.e. between seasons) and spatially, where drainage basins extend across large distances and over many lines of latitude (Bullard and McTainsh, 2003). In such areas, the channel system may be the only source of sediment supply, with the floodplain providing the link between fluvial and aeolian systems. This is demonstrated by the global link between alluvial deposits and dust emission in arid

environments (Prospero *et al.*, 2002; Baddock *et al.*, 2011; Bullard *et al.*, 2011; Ginoux *et al.*, 2012). This could be said for the Tigris and Euphrates Rivers, as they extend across distinctly different climate zones from the more humid upland areas to the arid deserts to the south (Worldclim, 2011; see Section 2.6).
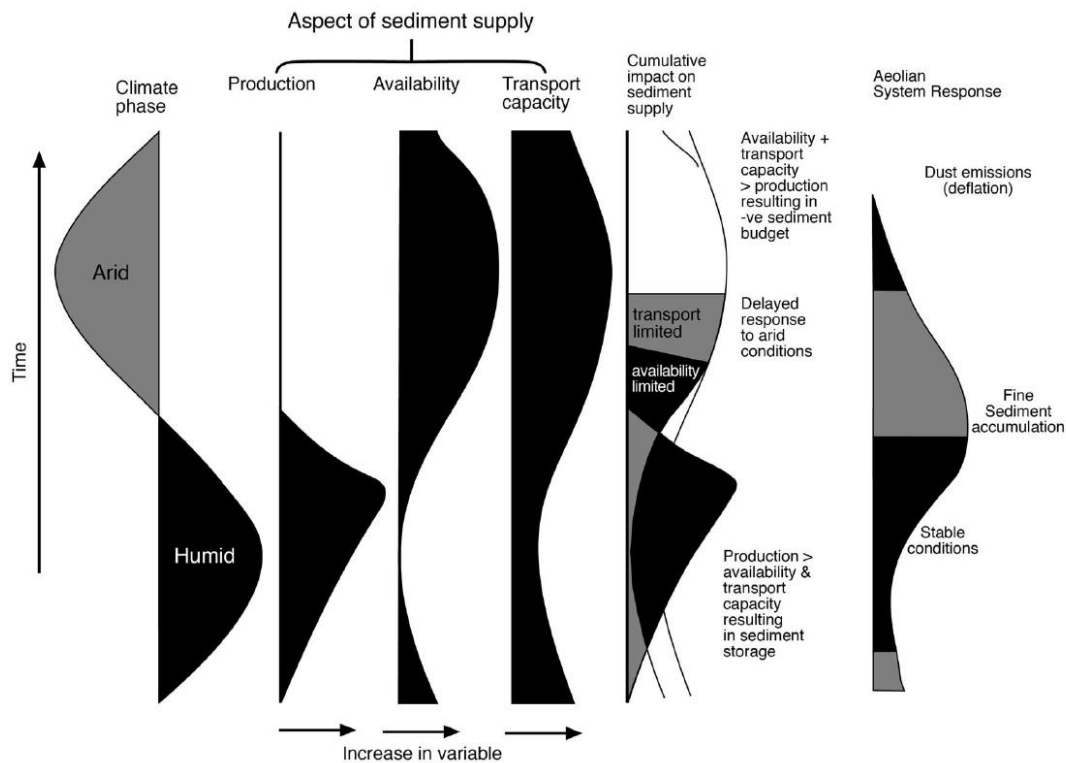
Figure 2.4: The production and deflation of fine sediments, modelled through both humid and arid phases within arid environments (Source: Bullard *et al.*, 2011).

2.4.3.2 Ephemeral Lakes and Playas

In drylands, where rainfall is characterised by short intense storms, the infiltration capacity of the surface is quickly overcome, creating a large amount of overland flow, commonly referred to as a flash flood. Due to large amounts of loose dry sediment on hillslopes and along the channel bed, these ephemeral floods are very effective at eroding and transporting large amounts of sediment (Thomas, 2011). At the lowest point of many arid or semi-arid depressions, ephemeral lakes exist as the result of these sudden inundation events (Cooke *et al.*, 1993). These landforms are believed to be very effective emitters of mineral dust

worldwide, Ginoux *et al.* (2012) attribute up to 30% of dust emissions to ephemeral landforms, although this figure varies considerably by region / continent. Ephemeral and seasonal lakes are commonly found throughout many parts of the Middle East (Prospero *et al.*, 2002). Near the capital city of Tehran, intermittent fluvial activity has created multiple ephemeral lakes and channels near the salt lake Daryachen-ye Namak (Abdi Vishkaee *et al.*, 2011). Further east, both the Sistan Basin and the Hamoon Jazmoorian basins contain many ephemeral lakes (Alizadeh Choobari *et al.*, 2013; Rashki *et al.*, 2017).

During dry seasons, ephemeral lakes will commonly dry up to form playas, whose characteristics are largely determined by their sedimentary and hydrological properties (Bryant, 1999). Through monitoring dust emission frequency of the chotts (an Arabic term applied to salt playas) of Tunisia and Algeria, Mahowald *et al.* (2003) related seasonal increases in dust activity to the seasonal hydrological regime. Using TOMS AI data, the atmospheric dust load in the vicinity were monitored and compared to periods of inundation between 1989 and 1991. The chott basins exist between the Atlas Mountains in Algeria to the lowlands of southern Tunisia. On average, this region receives 90-120mm annual rainfall, although inter-annual variability is high. With as little as 5-10% inundation, dust emission activity here increased significantly during the subsequent dry period, relative to previous years of little to zero inundation.

The 1990 inundation event of the Chott el Djerid (Tunisia) was monitored by Bryant *et al.* (1994), who identified 4 distinct stages between inundation and eventual desiccation of the ephemeral lake. The flooding stage took place after a week of heavy rainfall, up to 50 times the monthly mean, introducing 2200×10^6 m^3 of runoff across southern Tunisia. The subsequent surface runoff and rising water table inundated most of the saline mudflats. The surface runoff rapidly became saline as flood waters dissolved the salt crust on the chott surface, creating a brackish ephemeral lake. At this stage, flow deceleration causes rapid deposition of the coarser materials at the lake margin (Bullard *et al.*, 2011). The following stages took place over the following 9 months as the high evaporation rates (2500 to 3100 mm a^{-1}) desiccated the lake, precipitating halite and gypsum at the receding shoreline of the saline lake. The next phase is initiated by the water table dropping below the lakebed, limiting groundwater supply and leaving only small pools of concentrated brine. Finally, as the surface water disappears the surface begins to crust and crack into distinctive polygons. Evaporative

pumping of ground water continues through both final stages of lake desiccation, precipitating carnallitite, an evaporite mineral formed of mostly potassium and magnesium, where the water table is closest to the surface. The inundation creates areas of concentrated gypsum, halite and carnallitite at the surface, while the removal of the surface water by evaporation makes these minerals available to deflation by surface winds. Despite the availability of fine particles, high dust flux was only observed during higher than average surface winds, as measured from local meteorological stations (Mahowald *et al.*, 2003), highlighting the importance of local surface wind speed thresholds (see Section 2.3.4.2).

Basins that have only existed as seasonal or ephemeral lakes have much lower sediment storage than those that had previously existed as a perennial (non-seasonal) lakes. In the former, sediment supply is reliant on sporadic ephemeral floods (Mahowald *et al.*, 2003; Prospero *et al.*, 2002), with fine materials concentrated into small areas, relating to the later stages of lake desiccation. Once this fine material has been deflated, the lakebed will quickly shut down as a dust emission source (Bullard *et al.*, 2008). Furthermore, the probability of surface deflation decreases with extended dry periods, as continuous evaporation draws ground water into the surface sediments, increasing the surface salinity and consolidating the surface crust (Bullard *et al.*, 2011). Thus, to be a source of dust emission, salt playas are especially reliant on surface flow for both sediment supply and the breakdown of salt crust formation.

Not all ephemeral lakes are dependent on a constant supply of fine sediments; those that formed from perennial lakes during wetter phases will often retain a thick layer of sediments beneath the playa surface. Examples include the Bodélé Depression (Washington *et al.*, 2003) and Etosha Pan (Bryant, 2003). In the Middle East, Breeze *et al.* (2015) discovered 1338 possible paleolakes across the Arabian Peninsula, with a scale ranging from less than 1 km^2 to 387 km^2, with potential sediment depth of 1 - 99 m. Furthermore, the recent management of many river channels in the Middle East have resulted in a number of perennial lakes or marshes being desiccated over a short timescale (Richardson, 2005), mimicking what has been seen in known dust emitting areas such as the Aral Sea (Micklin, 2007).

The Mesopotamian Marshes have been extensively drained since the implementation of upstream drainage and agricultural irrigation programs since the mid-1980's (Richardson, 2005). The drainage of the marshes has caused mass loss of vegetation and destruction of

ecosystem, while the increased salinity of the soils prevents future restoration of vegetation, increasing the dust emission potential of the area.

2.4.3.3 Alluvial deposits

Alluvial deposits are categorised by Bullard *et al.* (2009) into two formations, dependent on the gradient on which they are found (Table 2.3). High relief deposits exist where the slope is greater than 3˚; slopes below this threshold are described as low relief. High relief alluvial formations exist in the piedmonts and they include alluvial fans, bajadas and pediment slopes.

Alluvial fans are commonly found where rivers discharge onto gentler and more open plains (Prospero *et al.*, 2002). As the stream widens and shallows, flow speeds dissipate causing the narrow mountain channel to divert into many smaller shifting and unstable channels (Cooke *et al.*, 1985). On sparsely vegetated mountain plains, stream channels remain unfixed allowing fine alluvium to be deposited in a broad cone, increasing in width downstream (Cooke *et al.*, 1993). When multiple fans appear from adjacent mountain outflow valleys, they can converge to form a bajada, an apron of sediment blanketing the piedmont. As they contain fine alluvial sediments, along with coarse gravels, cobbles and boulders, these landforms are known to produce atmospheric dust (Bullard *et al.*, 2011). While some fans remain annually or seasonally active, many are ephemeral, only receiving water and sediment during extreme rain events (Prospero, *et al.*, 2002). Using an inverse distance-weighted method, Wang *et al.* (2006) used data from over 300 meteorological stations in Northern China between 1999 to 2003 to shown how dust emissions over the Gobi Desert originated from the alluvial fans along the piedmont of the Kunlam, Qilan and Helan Mountains. This contradicted previous assumptions that the large sand seas, prevalent in the Taklamakan desert, were the key dust source. Results from the Tazhong weather station in the centre of the Taklamakan Desert recorded, on average, less than half the number of dust days per year than the Minfeng station on the margin of the desert (13 to 31 days/year). The Minfeng station lies on the piedmont slopes of the Kunlun Mountains, where glacial grinding and frost weathering have produced a large amount of fine sediment that is transported to the alluvial fans and plains below.

Pediment slopes are erosional piedmonts, areas of bedrock, usually thinly covered by a layer of alluvium, that commonly form at the foothills of mountain chains and escarpments (Cooke

et al., 1993). Pediment slopes can become incised by stream flow that is usually complex with many shallow rills.

The lower reaches of alluvial fans and pediment slopes form the boundary between high and low relief alluvial features, with low relief features consisting of gently sloping alluvial plains extending to the lowest parts of the basin (Prospero *et al.*, 2002). Alluvial plains have been regularly studied as paraglacial outwash plains, which have been known to emit dust in reaction to the seasonal influx of fine sediments provided by the melting and subsequent flooding of proglacial areas (Bullard *et al.*, 2016). In arid environments, they consist of braided and incised flood plains (Cooke *et al.*, 1993). An example of alluvial plains can be found at the lower parts of the Tigris – Euphrates basin in southern and central Iraq and eastern Syria (Parajuli *et al.*, 2014) or the flat areas flanking the Okavango in Botswana, where the seasonally flooded floodplains emit large quantities of dust during arid years (Krah *et al.*, 2004).

The sediment texture and consequent dust emitting ability of both high and low relief alluvial deposits are affected by two main variables: armouring and channel Incision (Bullard *et al.*, 2011). How these variables combine, defines their geomorphological type in the QUEST classification (Table 2.3).

Armouring. Stream flows and occasional debris flows deposit a large particle size range of sediment. Through preferential removal of finer sediments by surface deflation (winnowing), or a sudden influx of larger debris, the surface of these features can become dominated by coarse material. This effectively armours the surface, reducing the dust emission potential. This effect is more prominent on high relief surfaces, where the energy required to carry larger sediments is more readily available.

Channel incision. Commonly, both high and low relief surfaces will be incised by channels, with the depth of the incision affecting the frequency of supply. Deep and narrow incisions will limit the area to which fine sediments can be supplied, with wider, braided channels supplying sediments over a much larger area. The relative impact of channel incision is evident during particularly wet phases, when floods overtop the incised channels and surface flows extend further across the floodplain. McTainsh *et al.*, (1999) recorded significantly high dust emission from the floodplain of the Diamantina River (which flows into the Lake Eyre

Basin) during a particularly wet 1997. In previous years, the channelling of the higher plains constrained the fine sediments to the river channels, diminishing the deflation potential. With stream flow overtopping the narrow channels, sediment was deposited across the flat floodplain, being subsequently deflated during short dry periods. Unlike drier years, dust emission in 1997 exceeded that of the dune fields and ephemeral lakebeds downstream.

A combination of these alluvial landforms exist across the Middle East and while it is beyond the scope of this thesis to create a high resolution description - including all sub categories of alluvial landforms (Table 2.3) for the entire Middle East, analysis of persistent dust sources will provide vital information on the importance of alluvial sediments in the region.

2.4.3.4   Aeolian environments and Stone Pavements

Aeolian sand deposits cover approximately 5% of the global land surface and 20% of the world's dryland areas (Thomas, 2011). Bullard *et al.* (2011) classify aeolian deposits into either sand sheets or sand dunes. The main definition being the relative relief, sand sheets are relatively flat expanses of sand. They usually lie at the margins of dunefields, and are underlain by only a few metres of sand where conditions are unfavourable to dune formation (Cooke *et al.*, 1993). They range from the very large (100,000 km^2) Selima Sand Sheet in the Sahara to relatively small (a few square kilometres) marginal features (Thomas, 2011).

The sediment characteristics of sand sheets prevent these areas from being an effective dust emitter (Cooke *et al.*, 1993). In general, the surface material is too coarse, with mean particle size of around 1.5 mm. Vegetation, especially grass, can develop and bind the surface together, preventing the formation of dunes by reducing surface wind speeds. Sand sheets will often be positioned very close to the water table and are sometimes inundated; the high soil moisture content and potential for increased vegetation and crusting all limit dust emission.

Sand dunes are wind worked sand deposits with distinct relief that occupy over 60% of aeolian environments (Thomas, 2011). Formed by the movement of sand sized particles in relation to prevailing winds, sand dunes can take many different forms and can be up to 400 m in height and over 1 km wide (Cooke *et al.,* 1993). Sand dune research is extensive, but is not fully explored here because most research indicates that dunes do not contribute a large

percentage to net global dust emission. Instead, most researchers contend that dust originates in dune margin areas, where fluvial channels and dry lakebeds accumulate substantial amounts of fine-grained sediment (Prospero *et al.*, 2002; Tegen, 2003; Washington, Martin C. Todd, *et al.*, 2006). Due to the very effective sorting of fine sediments by aeolian processes, 90% of erg (Arabic for sand sea) particles are of sand size (between 50 - 2000 μm) (Thomas, 2011) and are too coarse to be suspended in the atmosphere. Nonetheless, their contribution to the production of fine sediments, especially around alluvial margins, can still be argued. Bullard and White, (2005) used laboratory experiments to determine the potential production of fine sediment dust from only aeolian abrasion of coarse sand particles. The study focussed on iron-rich (hermatite) dust that frequently traverses the Atlantic Ocean from the Sahara. The large Bodélé depression is commonly identified as the dominating dust source for such far-reaching dust emissions. However, the precise dust-emitting surface is less well known, with the common consensus identifying ephemeral lake basins (Ginoux *et al.*, 2012) and alluvial channels (Schepanski *et al.*, 2009). Bullard and White (2005) argue that each of these surfaces contain large quantities of evaporitic salts and not iron oxides. They hypothesise that the iron oxide clay coated quartz sand particles, found commonly on the sand dunes of North Africa were in fact a significant contributor for the iron oxide content commonly reported in atmospheric dust. Through laboratory simulations, they demonstrated that considerable amounts of iron rich clay particles <10 μm could be produced from just 120 hours of simulated aeolian abraision (i.e. saltation; see Section 2.3.1). The sand dunes of Erg du Djourab, adjacent to the Bodélé depression, could be producing the large amount of fine iron-rich dust by this method, contributing to the trans-Atlantic mineral dust transport routes previously noted.

Large areas of sand dunes (known as sand seas) fail to show as significant dust sources in satellite derived dust archives, however, in the marginal areas, where sand seas meet alluvial deposits, dust emission hot spots regularly appear (Prospero *et al.*, 2002; Schepanski *et al.*, 2009; Ginoux *et al.*, 2012). The dunes of Erg du Djourab and their active migration across the dry lakebed had been indirectly linked to emissions from the Bodélé depression (Prospero *et al.*, 2002). The lacustrine origin of these surfaces creates aerodynamically smooth plains, often consolidated by salt crusting, which together prevent surface winds from deflating the surface material. The saltation bombardment by coarse sand particles from these migrating

dunes break up the surface crusts and allow the prevailing wind to entrain the disaggregated sediments (Prospero *et al.*, 2002). This effective dust-source-activation process has been proposed in other marginal areas including around the Taklamakan sand sea (Wang *et al.*, 2014), the Erg Chech in Algeria and the sabkhas (Arabic for coastal salt playa) of the United Arab Emirates (Prospero *et al* 2002).

Stone Pavements

Known as *gibber* in Australia, *hammada* in North Africa and *gobi* in Asia, stone pavements are formed from one or two layers of closely packed stones and ventifacts (wind shaped stones) >2000 μm in diameter above a layer of much finer sediments of silt or clay (Bullard *et al.*, 2011). Not commonly recognised as a prime dust source, the size of the surface clasts prevent the deflation of the underlying fine sediments. However, where the surface mantle is disturbed or removed by land use practices, the fine sediments below will be exposed and free to deflate (Belnap, J and Warren, 2002). Stone pavements make up large portions of the Tigris Euphrates Basin and the Jordanian Desert (Parajuli *et al.*, 2014).

2.4.4 Anthropogenic sources

One element that is absent from the Bullard *et al.* (2011) classification, is the recognition of anthropogenic land cover, more specifically agricultural and urban settlements. The importance of these types of land cover will vary by region, however in the Middle East, many of the recognised dust source areas (e.g. Tigris Euphrates Basin, Sistan Basin) are significantly disturbed by anthropogenic activities (Ginoux *et al.*, 2012; Notaro *et al.*, 2015; Parajuli *et al.*, 2014).

It has been widely reported that human activity has a direct impact on surface characteristics, changing the deflation potential of the land surface and influencing net dust emission (Gill 1996). Recent remote sensing research has indicated a wide range of recorded anthropogenic dust contribution, from 10% (Tegen *et al.*, 2004) to as much as 50% (Mahowald and Luo, 2003). The range of uncertainty comes from the lack of a high-resolution map of dust sources and the difficulty of defining anthropogenic sources, due to the inconsistency of scale used in land surface / dust emission data and the complexity of human-dust interactions. When comparing anthropogenic dust emission investigations by Tegen *et al.* (2004) (TEG04) and

Ginoux *et al.* (2012) (GIN12), it is clear to see why a range of results is inevitable. In each case, anthropogenic source areas were designated from gridded land use data sets, with TEG04 and GIN12 using 0.5° and 0.1° grid cell classification respectively. To define a cell as anthropogenic or natural, each cell must exceed a chosen percentage threshold of land use. The 0.5° TEG04 cells are classified as anthropogenic, when more than 5% of the surface is disturbed. In comparison, 0.1° GIN12 cells have a threshold of 30% land use. Both simulations reduce the 50% anthropogenic contribution calculated by (Mahowald and Luo, 2003), however, their estimations of 10% (TEG04) and 25% (GIN12) are still significantly different. These studies conclude that while anthropogenic dust has a small significance to global emissions, local dust flux can be significantly influenced by disturbed soils (Tegen *et al.*, 2004). The regional disparity is shown by Ginoux *et al.* (2012), who attribute 30% of dust emissions from the Middle East to anthropogenic sources. In comparison, North Africa, where dust emission typically emanates from the sparsely populated Sahara, only 8% of emissions are from anthropogenic surfaces, while Australia records 75% anthropogenic dust. Importantly, these simulations are reliant on precise dust source locations and emission frequency; thus the addition of the high-resolution dust source inventory, such as the one presented in this study, will significantly improve the accuracy of any subsequent estimations.

Human activity effects the erodibility (see Section 2.3) of land surfaces in two main ways: (i) directly disturbing soils in source area through land use, and (ii) disruption of fluvial activity by irrigation and channel management.

2.4.4.1 Anthropogenic dust - Land Use

The consensus of scientific research attributes land use change, with emphasis on agriculture disturbance of soils, with increased probability of surface deflation and expansion of existing dust source areas (Gill, 1996; Tegen *et al.*, 2004; Ginoux *et al.*, 2012; Lee and Kim, 2012). Disturbed soils also include areas where significant vegetation change has taken place for cultivation or grazing or other type of land use change (Middleton, 2016). Overgrazing on Australian rangelands significantly reduces surface soil stability, increasing dust emission potential, particularly during periods of drought (Aubault *et al.*, 2015). Croplands are particularly vulnerable to surface deflation during the post-harvest and tilling periods. Through the removal of vegetation during harvest, the fine surface sediments are exposed to

wind erosion; the subsequent tilling process increases surface roughness and surface area of top soil, causing rapid loss of soil moisture through evaporation (Lee *et al.*, 1994). The dry soils, cleared of all remaining vegetation, have very little surface cohesion and remain vulnerable to surface winds until the onset of more humid weather and vegetation growth (Lee *et al.*, 2012), producing around 20% more dust than uncultivated soils (Gill, 1996). The loss of agricultural soils can have a significant impact on the productivity of the crop during the following growing season, as preferential entrainment, derives mostly from finer particles, clay, silt and organic matter, detrimentally effecting soil stability and water retention capabilities (Middleton, 2017).

A key element to anthropogenic dust is the conversion of dryland areas that were previously stable into potential deflation surfaces once cultivated. Indeed, 85% of desert surfaces worldwide are not actively emitting dust (Gill, 1996). However, through human induced land use change, areas such as aeolian sand sheets of the Southern High Plains in northwestern Texas and New Mexico (USA) are now key local sources of dust (Lee *et al.*, 2012). Previous studies (e.g. Bullard *et al.*, 2008) reported how these surface types were relatively stable compared to alluvial and ephemeral lake surfaces, however, observations from Lee *et al.* (2012) attribute 79% of dust emissions in the Southern High Plains to undisturbed and disturbed sand sheets. These cultivated sand sheets are largely cultivated to produce cotton, and account for 57% of the 625 dust sources observed. The change in land use of these sand sheets produce two orders of magnitude more dust sources per km^2 (0.01) than the same surface type in the Chihuahua Desert (USA – Mexico) (0.0007) (Baddock *et al.*, 2011) or Lake Eyre Basin (Australia) (0.0002) (Bullard *et al.*, 2011). This pattern is replicated in the Sahel, where the end of the dry season is brought about by the encroachment of the ITCZ and development of large convective thunderstorms. Maurer *et al.* (2009) observe how these aeolian croplands, left bare during the dry season, are particularly vulnerable to erosion from the strong winds associated with these intense rainstorms. During the growing season, cultivated land surfaces have a negative correlation with dust activity, with increased vegetation and high soil moisture content from irrigation stabilising the surface (Wang *et al.*, 2006). Key agricultural areas in the Middle East, such as the Tigris Euphrates basin, Sistan Basin and the Hamoun Jaz Mourain basin have come under increasing pressure from periods of severe drought since the beginning of the 21st Century (Kelley *et al.*, 2015; Moridnejad *et*

al., 2015; Notaro *et al.*, 2015; Rashki *et al.*, 2017). Heavily reliant on winter rains (Kelley *et al.*, 2015); these regions are increasingly recognised as dust sources, as prolonged dry seasons remove vast areas of vegetation (Moridnejad *et al.*, 2015; see Section 2.6).

Human influence on dust emission extends beyond direct disturbance of soils, with arguably the greatest impact coming from changes to the hydrological regime of arid environments. 85% of all anthropogenic sources are associated with the ephemeral water bodies whose frequency and extent may have been directly affected by land use activities further upstream (Ginoux *et al.*, 2012).

2.4.4.2 Anthropogenic dust – Hydrological regime

Extraction of fresh water for irrigation from either rivers or groundwater has been linked to the desertification of many terminal lakes and playas in semi-arid environments since the beginning of the 20th Century (Gill, 1996). Ginoux *et al.* (2012) link 85% of all anthropogenic dust emission to water bodies (ephemeral and receding), with these frequently or permanently dry lakebeds, commonly becoming a local source of dust emission. Examples such as the Owens and Mono Lakes (USA) (Gillette, 1999; Lancaster *et al.*, 2015) and the Aral Sea (Kazakhstan, Uzbekistan) (Micklin, 2007) illustrate the impact of upstream channel management, with each now recognised as a major source of local dust. In the Middle East, management of the Tigris Euphrates rivers has caused extensive land cover changes in the areas downstream of dams and constructed irrigation channels, including increased desertifaction in the north and west of Iraq (Moridnejad *et al.*, 2015) and the destruction of the Mesopotamian Marshes (Richardson, 2005) (see Section 2.4.3.2).

Both Mono and Owens Lakes were cut off from Sierra Nevada drainage channels by the Los Angeles Aqueduct in 1913. The subsequent draining of Owens Lake lowered its surface from 1,096 m (asl) in 1872, to a mostly dry playa at 1085 m (asl) (Lancaster *et al.*, 2015). The level of Mono Lake dropped by around 14 m, exposing 65 km^2 of highly erodible playa surface made up of a mixture of sulphate-rich evaporate salts, volcanoclastic materials and arsenic from hydrothermal activity (Gill, 1996). The increased availability of fine sediments on the desiccated Owens Lake has re-initiated dune activity to the North East of the Basin (Lancaster *et al.*, 2015). The increased dust emissions from both playas have had a negative effect on

local air quality, with 'dust days' producing six times the Californian standard for Total Suspended Particulates (100 µg m^{-3}), while the arsenic content potentially increased cancer risk in the immediate area (Gill, 1996).
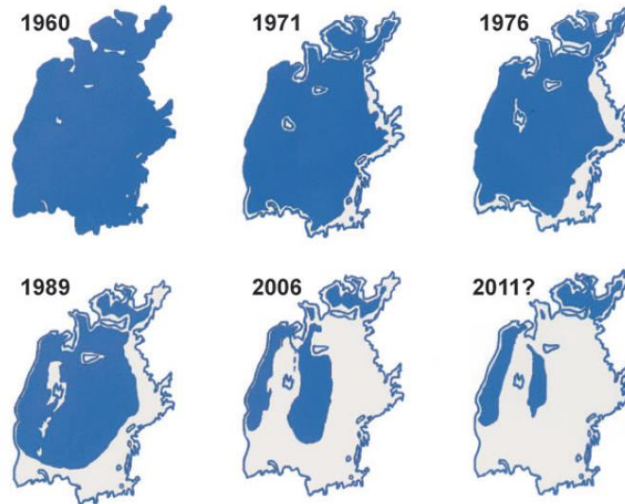
Figure 2.5: The changing profile of the Aral Sea 1960 – 2011. Blue area depicts lake extent. (Source: Micklin, 2007)

The desiccation of the Aral Sea has been cited as one of the greatest environmental disasters of the 20th Century (Wiggs *et al.*, 2003). Once the 4th largest lake in the world, the terminal lake covered 67,000 km^2 in 1960, before intensification of irrigated agriculture in the region (Ginoux *et al.*, 2012). The surface area of the lake has since reduced by 74% (Fig. 2.5), lake height has dropped by 23 m, total volume has reduced by 90% and the sea now exists as two separate lakes (North and South Aral Sea) (Micklin, 2007).

The lowering of the water table has extended the capillary zone beyond what is sustainable for vegetation, disconnecting from the surface and causing reduced surface moisture making the surface vulnerable to wind erosion (Gill, 1996). As a result, the dried lakebed has become a key dust source to the area since the 1970's (Prospero *et al.*, 2002; Ginoux *et al*, 2012). Dust plumes extend up to 500 km downwind, depositing around 40-150 million tonnes of dust per year on the surrounding area (Micklin, 2007).

2.5   Meteorology and Climate

For dust emission, local surface thresholds in wind speed or frictional force must be overcome; discussed in Section 2.3.4.2, these thresholds rely on a complex relationship between variables including surface roughness (including vegetation), soil texture and soil moisture. To overcome these thresholds, specific meteorological conditions are required to produce strong surface winds. In Section 2.3.4.1, it was shown that dust uplift was caused by a variety of specific weather patterns, from continental and synoptic scales down to local mesoscale and microscale conditions. These conditions tend to occur seasonally (Cuesta *et al.*, 2009; Knippertz and Todd, 2012; Miller *et al.*, 2008), with the strength of synoptic-scale conditions and therefore the dust emission flux heavily dependent on climate variability (Mahowald *et al.*, 2010). Through this section, meteorological processes will be discussed in more detail, exploring the variables involved in surface deflation including precipitation and soil moisture (2.5.1), boundary layer dynamics including vertical velocities (2.5.2), the range of scales of dust emission, with examples of synoptic (2.5.3) and mesoscale (2.5.4) conditions prevalent in dust emission. Finally, atmospheric conditions that define the diurnal regime of dust emission are discussed (2.5.5).

2.5.1   Soil Moisture

As has been shown throughout this chapter, soil moisture plays a crucial role in the dust emission potential of a given area. Soil moisture is derived from either direct precipitation or inflow from stream and groundwater from the surrounding catchment. The availability of water will directly characterise the proportion of fine sediments (sediment texture), the surface chemistry (salinity), surface cohesion and ability to grow vegetation (Gherboudj *et al.*, 2017). Each of these variables have been shown to influence the frequency of dust emission (see Section 2.4.3.1), relating dust emission directly to the precipitation frequency of a given catchment (Bryant, 2003; Mahowald *et al.*, 2003). These factors are clearly demonstrated in ephemeral lakes such as the Etosha Pan, where the intensity of intermittent humid phases strongly dictate the emission flux from this known dust-emitting feature.

The pan was created from the desiccation of a once perennial lake (Mahowald *et al.*, 2003) and unlike other ephemeral lakes such as the chotts in Tunisia and Algeria, the pan's sediment supply comes from a thick layer of saline sediments, formed during the Miocene period

(Bryant, 2003). Tectonic activity has since diverted the flow of the Okovango and Kunene Rivers away from the basin, meaning that this 6000 km^2 endorheic basin currently generates only ephemeral lakes, fed mostly by seasonal channels from the north (known locally as oshanas) (Mahowald *et al.*, 2003). With inter-annual rainfall varying considerably (between 300 mm below to 500 mm above long term mean), surface flow into the pan varies considerably. Like the chotts of Tunisia and Algeria, the desiccation of the ephemeral lake is expected to produce higher dust loads in the subsequent dry season (see Section 2.4.3.2); however, Bryant *et al.* (2003) demonstrate that this relationship is not always apparent. Figure 2.6 shows how TOMS AI records from the Etosha Pan area are affected differently by successive periods of inundation in April 1997 and 2000. For the latter, the AI response is as predicted, with an increasing AI during the following dry summer months (Oct – Jan). In contrast, the previous inundation reveals a lag in AI response, not peaking until the dry season in the following year, 12 months after lake desiccation. Variation in emission flux is a function of the extent of lake inundation and spatial distribution of precipitation. During the 1997 event, the inundation was more widespread, with a larger proportion of the precipitation falling directly on the pan, including non-inundated areas. Soil moisture is therefore increased across the entire pan, constraining emission from surfaces that would otherwise deflate during channel-only inundation events. Subsequent vegetation growth increases soil roughness, limiting surface deflation during the following dry season. In contrast, the 2000 inundation was triggered by surface flow via oshanas to the north of the pan, with very little precipitation falling directly on to the pan. Reduced vegetation growth enables dust emission directly after lake desiccation. In comparison, after the 1997 inundation, the equivalent peak in dust emission was not observed until the following year's dry season.

This study highlights the importance of physical factors within the pan itself, especially vegetation and soil moisture as controls on dust emission (see Section 2.3). In the Mesopotamian Marshes, thick vegetation existed as recently as the early 2000's, and recently (since Operation Iraqi Freedom, 2003) uncontrolled release of dam waters have caused intermittent inundation of the area, increasing the potential of vegetation restoration (Richardson, 2005) and reduced surface deflation. It will be interesting to see if, like the Etosha Pan, this area (a) appears as a dust source and (b) shows a similar inter annual variability due to the dynamics of inundation and vegetation growth.

Variability in precipitation is expected to play a key role in future climate change, with an increase in the frequency of extreme weather events, including intensified drought periods and extreme wind events more likely (IPCC, Fifth Assessment 2013). The combination of these climate variables will play an important role in future soil moisture and vegetation levels in arid environments, and the deflation and transport of mineral dust (Middleton, 2017). Indeed, the increased frequency of drought worldwide has already had a negative effect on agricultural production, especially in arid environments (Meladze and Meladze, 2017), causing social and political unrest in climate stressed regions such as the Middle East (Kelley *et al.*, 2015).
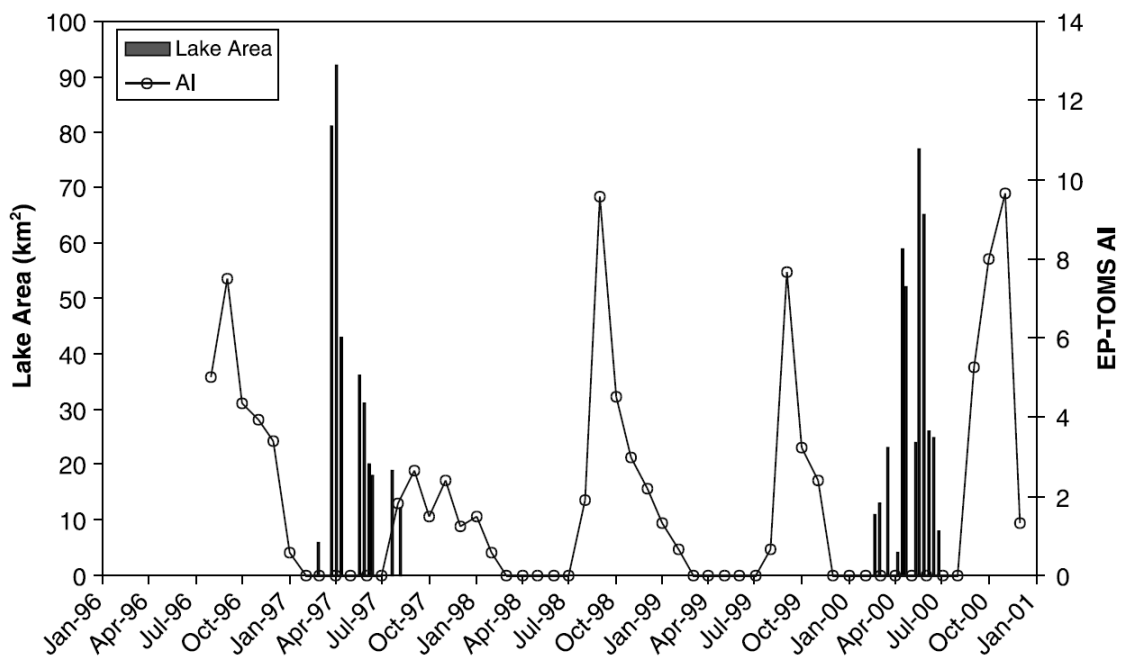
Figure 2.6: A comparison of inundation events and dust emission data of Etosha Pan from Earth Probe TOMS. (Source: Bryant, 2003)

The Dust Bowl event of the 1930's North America gives an insight into how reduced soil moisture, brought about by typical climate variability can be amplified by changes in land use and contribute to increased surface deflation. Analysis by Cooke *et al.* (2009) demonstrated how the typical La Nina derived drought across North America was shifted and intensified over the Great Plains of North America, bringing both a positive temperature anomaly and negative precipitation anomaly across the region.

Expansion of agriculture across the Great Plains during the 1920's saw drought resistant prairie replaced with drought sensitive wheat. From the outset of the drought, wheat crop failure and field abandonment were widespread, exposing barren surfaces to wind erosion. The subsequent dust storms were of unprecedented levels and through a complicated feedback cycle, caused an alteration of atmospheric temperature profile, enhancing the drought across the region. Top of the atmosphere (TOA) and surface net radiation were reduced by increased short wave reflectance by higher AOD, creating a negative geopotential height anomaly at 300 and 850 hPa. Consequently, compensating upper-level convergence and subsequent low-level subsidence prohibited convection, increasing atmospheric stability and preventing cloud development, enhancing drought conditions. With convection prohibited, the lack of precipitation inhibited the growth of vegetation, contributing to increasing surface temperatures as the lack of evapotranspiration reduced latent heat flux.

2.5.2   *Vertical Velocity*

While dust emission is reliant on strong surface winds, capable of exceeding local wind speed or frictional velocity thresholds (Section 2.3.4.2), strong vertical velocity is required for long-range transport of dust emission. A combination of ground, air and satellite derived lidar operations have given insights into the vertical structure of emitting dust plumes within the atmospheric boundary layer (ABL) (Knippertz and Todd, 2012). These investigations have shown that vertical transport of dust is driven by several mechanisms, including diurnal mixing through the convective boundary layer (CBL) (I in Fig. 2.7), and dynamic lifting of dust layers by cold air intrusions (II.a and II.b) (Cuesta *et al.*, 2009). Vertical transport potential of dust is controlled by the depth of the ABL. In sub-tropical arid environments, such as the Sahara and the Middle East, summer time conditions enable the deepening of this layer, frequently reaching heights of 6 km (asl), far deeper than other locations around the world (Knippertz and Todd, 2012).

2.5.2.1   Diurnal mixing of atmospheric boundary layer

In North Africa, Cuesta *et al.* (2009) observed dust emission in response to both diurnal CBL growth and dynamic lifting mechanisms. Here, CBL dynamics causes the stratifying of the Saharan atmospheric boundary layer (SABL) into a Saharan Residual Layer (SRL) of vertically

stable air and the buoyant Saharan convective boundary layer (SCBL). Critically, while vertically stable, the SRL is prone to have strong horizontal shear, so any dust intrusions are likely to be transported away by advection. Diurnal mixing is especially strong in the summer; the SCBL is created by solar heating of desert surfaces (such as those in many areas across the Middle East) and is found across large parts of the Sahara. Dust emissions are vertically constrained by the height of the SCBL, so that dust emissions in the early morning are concentrated within a relatively shallow SCBL that typically erodes the SRL throughout the daylight hours, filling the SABL to a height of 4 to 5 km by the end of the day. Lidar observations have shown that dust emission is typically observed in three situations within the stratified ABL: (i) in a concentrated layer, elevated within the SABL with clear air below; (ii) a concentrated layer with clear air above; or (iii) a well-mixed profile that extends from the surface to ABL top.
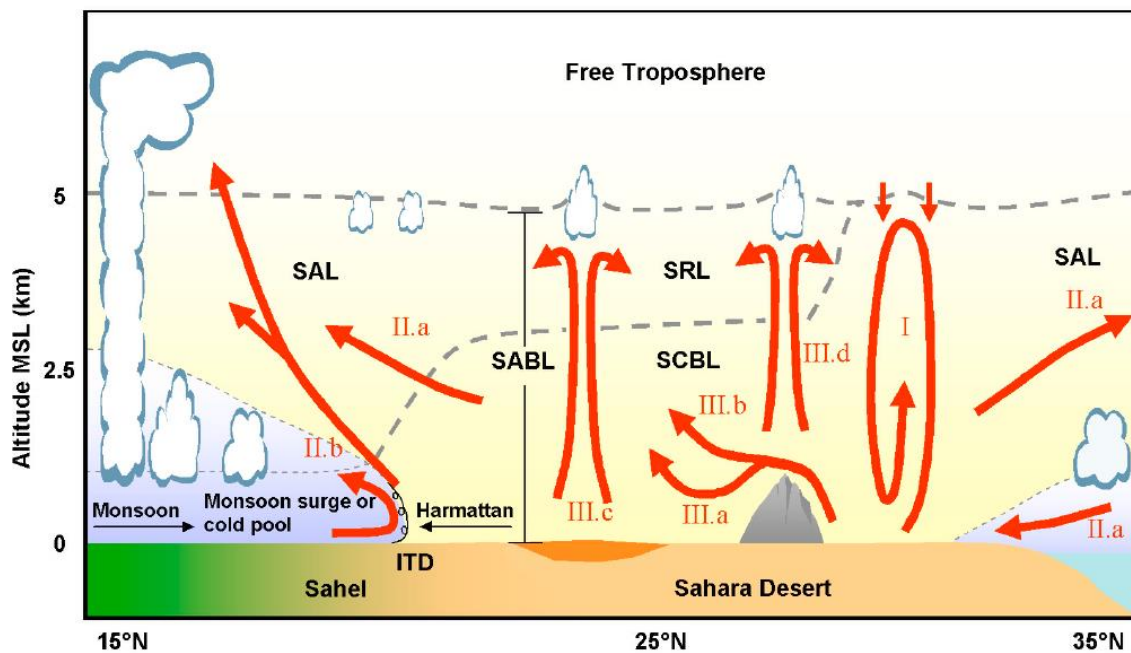
Figure 2.7: Schematic of various mechanisms that control the dynamics of the Saharan ABL, and the vertical distribution of dust in the atmosphere. Abbreviation stand for Saharan air layer (SAL), intertropical discontinuity (ITD), Saharan atmospheric boundary layer (SABL), Saharan convective boundary layer (SCBL) and the Saharan residual layer (SRB). Numerical labels indicate different mechanisms that are explained throughout Section 2.5.2. (Source Cuesta *et al.*, 2009).

An example, whereby a combination of these convective forces have instigated dust storm conditions can be found in Vishkaee *et al.* (2011). During the 3-5 August 2007, visibility in the city of Tehran was reduced to less than 7 km by dust that had been transported from Iraq and Syria (Vishkaee *et al.*, 2011). On the 3rd August, lidar observations from both ground and space borne platforms show a well-mixed dusty ABL advecting east across the Zagros Mountains. MODIS AOD measurements implied that the dust emission was derived from the Tigris-Euphrates basin, while lidar measurements from the Cloud-Aerosol Lidar with Orthogonal Polarization (CALIOP) showed the establishment of a deep CBL, which had elevated the dust layer to a height in excess of 3.5 km. Importantly, this deep CBL enabled the dust layer to be forced over the high terrain of the Zagros Mountains, which sit between source and deposition areas. During the morning of 5th August, the elevated dust layer is seen by surface based Lidar measurements around 2 km above the surface, on the lee side of the mountains. Shown as a concentrated 2 km thick dust layer above a layer of clear air, diurnal observations show the development of a CBL in the late morning, reaching the elevated aerosol layer around 12:30 UTC. Turbulent mixing of the CBL began to reduce the horizontal visibility of the entire CBL vertical profile, as the elevated dust plume is mixed down to the surface by 14:00 UTC.

2.5.2.2 Dynamic lifting of dust layer

Described by Cuesta *et al.* (2009), dynamic lifting occurs across North Africa at the fringes of the Saharan Desert. Here, intrusions of cold clean air originate from both North Atlantic mid-latitude troughs and the seasonal progression of the intertropical discontinuity (ITD), where tropical monsoon surges undercut the SABL (II.a). These air masses undercut the dry and dusty Saharan Air Layer (SAL), dynamically lifting the SAL across slanted isentropes, in a process termed up-gliding (Knippertz and Todd, 2012). Transported high above the surface by a wedge of cold air, this process is very effective at transporting dust over long distances, with the SAL in conjunction with the northerly Harmattan Flow, recognised as an importance source of mineral nutrients for the tropical Atlantic and Amazon Rainforest (Koren *et al.*, 2006).

Dynamic lifting is also associated with density currents (Bou Karam *et al.*, 2010), also known as cold pools (Knippertz *et al.*, 2007), which are associated with mesoscale convective systems

in the development of cumulonimbus clouds (II.b); these are discussed in more detail in Section 2.5.4.

2.5.2.3 Topographic controls and effects of albedo

Surface characteristics such as topography and albedo are known to affect the vertical structure of the ABL. Described again by Cuesta *et al.*, 2009, these include a 'hydraulic jump', caused by the horizontal flow over and around topographic barriers (III.a). Examples from the Hoggar Mountains, North Africa, show horizontal wind speed alterations in response to the contraction of the ABL as it passes over the topographic barrier. As the ABL descends on the lee of the mountain range, wind speed accelerates in response to hydraulic pumping forces. Subsequently, an abrupt decrease in wind speeds occur approximately 1.5 km downstream (12 m s^{-1} to 5 m s^{-1}), as the ABL deepens again. Importantly, this sudden deepening of the boundary layer induces a sudden increase in vertical velocity, causing rapid vertical mixing of entrained dust, instigated by leeward wind acceleration. Topographic barriers can also lead to increased stratification of the ABL (III.b), with a condensed dust layer above a surface layer of clean air, as seen in the lee of the Zagros Mountains on the 5th August 2007 case study (see Section 2.5.2.1) (Vishkaee *et al.*, 2011).

Analysis by low-level flights during the GERBILS (GERB Inter-comparison of Longwave and Shortwave radiation) campaign showed that changes in the surface albedo, on a scale greater than 10 km are linked with changes in land surface temperatures and alterations of the CBL (III.c) (Marsham *et al.*, 2008). Furthermore, dry convective ascent within the SABL was enhanced by the elevated heating over the rocky surfaces of the Atlas Mountains (III.d) (Cuesta *et al.*, 2009). In both cases, increased dry convection caused by changes in albedo can cause increased warming of the SRL above, supressing the growth of the SCBL, and the vertical transport of dust by stabilisation of the temperature profile and compensating subsidence.

2.5.3 *Synoptic Conditions*

Spatial and temporal analysis of dust events around the world have highlighted the importance of synoptic scale patterns (2,000 – 10,000 km), where seasonal differences in

surface temperature frequently produce strong surface pressure gradients in the region of dust source areas (Knippertz and Todd, 2012).
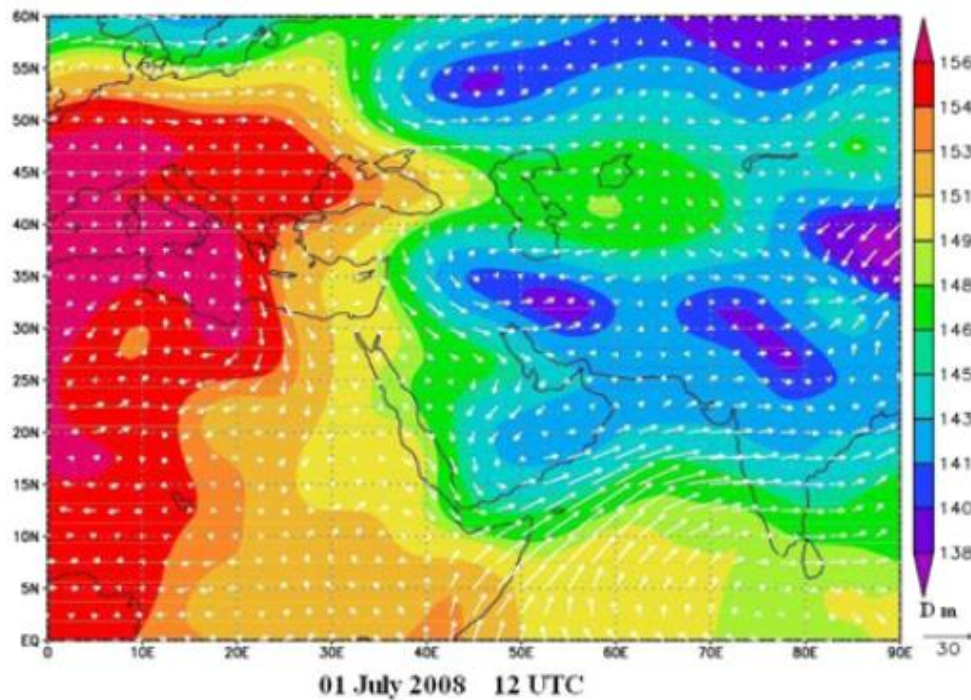
Figure 2.8: A typical synoptic pattern associated with Shamal winds across the Arabian Peninsula on the 1 July 2008 (12:00, UTC). The plot shows the geopotential height of 850 hPa with associated wind vectors in white. Geopotential height is in deka metres. (Source: Hamidi *et al.*, 2013).

The largest, continental-scale circulations are linked to the Indian and West African Monsoons, where seasonal peaks in dust emission coincide with the directional shift in surface winds, accelerating towards continental heat lows over Pakistan, The Arabian Peninsula and Western Sahara (Knippertz, 2014). In the Middle East, summer peaks in dust emission are linked to Shamal winds (Hamidi *et al.*, 2013; Bou Karam *et al.*, 2017; Kaskaoutis *et al.*, 2015a). Shown as geopotential height of 850 hPa in Figure 2.8, this typical Shamal-type synoptic pattern is characterised by a semi-permanent heat low over the Arabian Peninsula and Iran, which forms a powerful pressure gradient against high pressure over northern Africa – eastern Mediterranean, creating strong westerly and north westerly winds across much of the Arabian Peninsula (Hamidi *et al.*, 2013). Some studies suggest that teleconnections between monsoon intensity and variations in El Nino Southern Oscillation (ENSO) can be attributed to inter-annual differences in surface wind intensification (Abish and

Mohanakumar, 2013; Kaskaoutis *et al.*, 2015b; Notaro *et al.*, 2015), this link is not discussed further as it is beyond the scope of this thesis. Further east, summer time dust emission events over the Sistan Basin in eastern Iran are associated with the 'wind of 120 days' (Choobari *et al.*, 2014). These winds are characterised by persistent surface lows, caused by upper level (700 hPa) pressure gradient from the Indian thermal low and the Arabian/Iranian ridge of high pressure (Fig. 2.9.A) (Kaskaoutis *et al.*, 2015a). Recently, temperature driven variations in mean sea level pressure between the Caspian Sea and the Hindu Kush region (Red and black boxes respectively in Fig. 2.9.B) have been recognised as a contributing factor to monsoon acceleration of surface wind speeds (Kaskaoutis *et al.*, 2015a). Kaskaoutis *et al.*, (2015b) identified a positive correlation (r=0.96) between high CasHKI anomalies (increased pressure gradient) and high northerly winds (between 10 and 14 m s^{-1}) across 10 local meteorological stations during the period 1-3 July 2014. Each of these stations observed decreased horizontal visibility as high wind speeds instigated surface deflation of the dry ephemeral lakes across the area. Furthermore, the breakdown of nocturnal low level jets (LLJ) have previously been linked to an intensification of seasonal dust emissions in both Iranian and Arabian dust source areas (Barough *et al.*, 2010; Alizadeh Choobari *et al.*, 2013; Bou Karam *et al.*, 2017; see Section 2.5.5).

Across North Africa, similar large-scale circulations are observed in spring and summer months. Here, the Saharan and West African heat lows generate north easterly flow from the Mediterranean Sea, persistent northerly winds from the Atlantic and southerly monsoon flow over the Sahel (Knippertz, 2014).

Smaller scale synoptic conditions, such as sub-tropical cyclones are prominent near storm track areas, where they drive episodic dust emission events (Kaskaoutis *et al.*, 2015a). The development of these cyclones along the northern coast of North Africa has been linked to multiple mechanisms, including large-scale baraclinity, ABL baraclinity (during spring months, when the temperature gradient between the North African coast and the Mediterranean Sea are highest) and sub-tropical jet stream circulations (Bou Karam *et al.*, 2010; Schepanski *et al.*, 2009). These important winter and springtime synoptic features, known as Saharan depressions or Sharav cyclones, induce high surface wind speeds and dust activity across the Mediterranean Coast of North Africa and Northern parts of the Arabian Peninsula (Bou Karam *et al.*, 2010; Kaskaoutis *et al.*, 2012; Middleton, 1986). Cyclogenesis is typically enhanced by

a deep trough stretching equatorward in the upper layers of the atmosphere (Bou Karam *et al.,* 2010). Deep surface lows occur where the leading edge of high latitude cold air meets warm African air. These cyclones migrate eastward and are characterised by an active warm front along their eastern edges and a well-defined trailing cold front to the south west of the low-pressure centres. The cold fronts act as a density current (see Section 2.5.4), generating surface wind speeds in excess of 10 m s^{-1}. Dust entrainment is high, as convective and dynamic lifting mechanisms are well developed, leading to dust emissions reaching high altitudes (above 500 hPa). Depressions gain energy as they cross the Mediterranean before crossing into northern Arabian Peninsula, where they are often referred to as winter Shamal (Hamidi *et al.*, 2013) or Belat winds (Middleton 1986). As monsoon circulations strengthen during the summer, the mid latitude stormtrack migrates poleward, meaning it has little impact on summer dust emissions in the Middle East (Knippertz 2014).
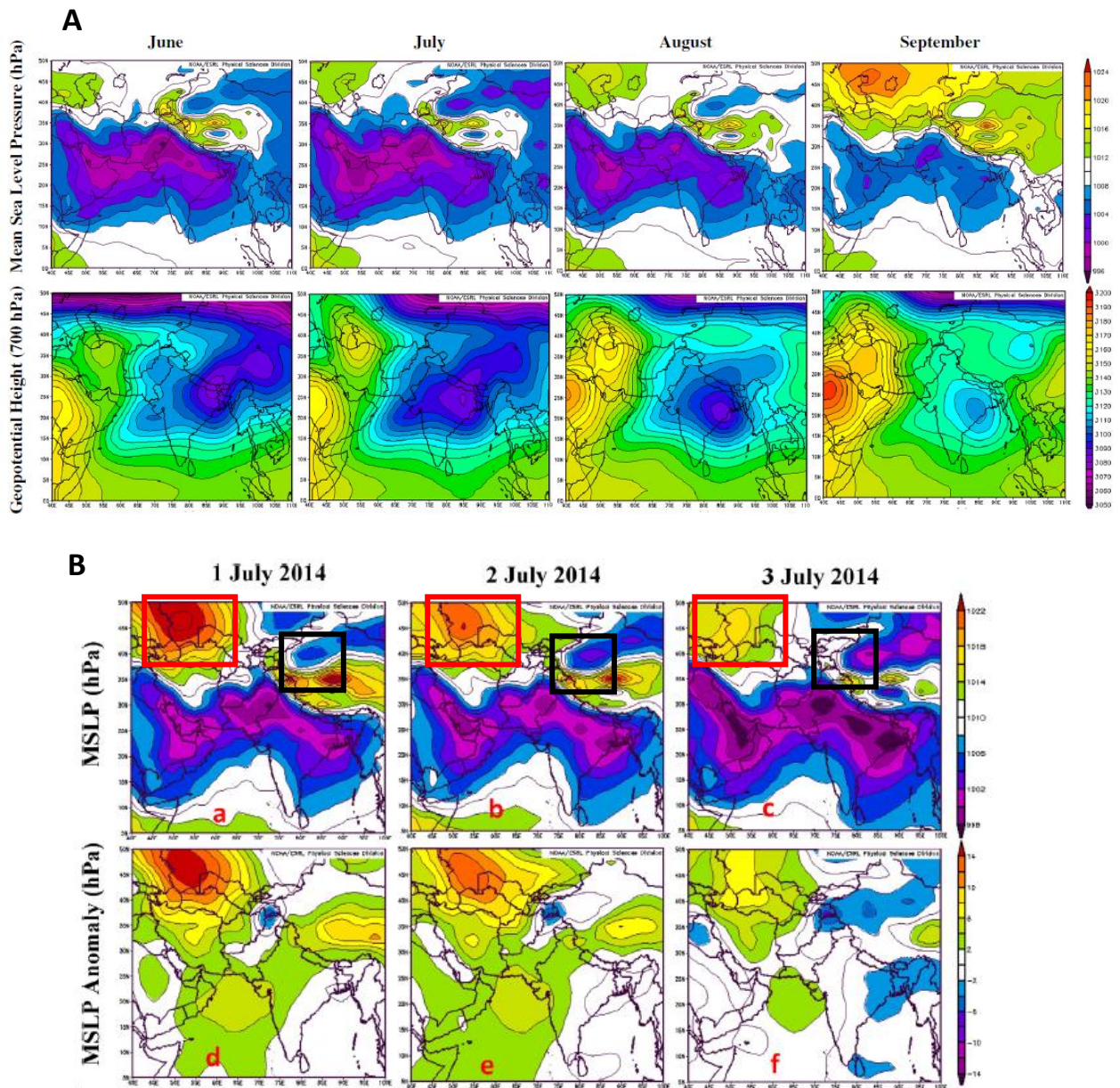
Figure 2.9: Synoptic conditions related to increased surface winds within the Sistan Basin in eastern Iran. A: Composite-mean MSLP and geopotential height at 700 hPa plots of SW Asia between June and September for dust storm days (2001-2012). MSLP range from 1024 (red) to 996 (magenta). Geopotential height (700 hPa) range from 3200 (red) to 3050 (magenta). (Source Kaskaoutis et al 2015a). B: MSLP and MSLP anomaly (from July 1981-2010 climatology) for three consecutive days (1st – 3rd) July 2014 for SW Asia. Red (Caspian Sea) and black (Hindu Kush) boxes indicate locations of synoptic index (CasHKI). (Source: Kaskaoutis *et al.*, 2015b). Both A and B produced from NCEP/NCAR reanalysis data.

2.5.3 Mesoscale Conditions

A number of mesoscale conditions, linked to seasonal processes of moist and dry convection are known to initiate dust emission in drylands (Schepanski *et al.*, 2009). At the scale of several hundred kilometres, haboob events contribute a large proportion of a region's annual dust emission (Miller *et al.*, 2008). These events, also referred to as cold pool outflows are regularly seen throughout the Western Sahara in summer. Here, they typically occur in response to the south easterly monsoon flow, transporting moist air from the Gulf of Guinea into the dry and hot Saharan air (Peters and Tetzlaff, 1988). As deep moist convection propagates, downbursts of precipitation cause cold humid air to descend to the surface. Evaporation of precipitation continues as it falls through the dry and hot ABL, creating an accelerating density current of cold air ahead of the convective core and into the subtropical deserts. The strong gusts at the leading edge of the cold pool create a dramatic 'wall of dust' between 500m to 2 km in height, known to extend a significant distance away from the precipitation area (Knippertz and Todd, 2010). Similar activity is seen over Sudan, where the wall of dust can extend 10-80 km and last several hours (Lawson, 1971). As Figure 2.10 shows, cold pooling not only occurs at the convergence of air masses, but also by topographically forced convection. As a moist air mass propagates southeast over the Atlas Mountains, toward the dry hot Saharan core, the forced uplift and cooling provides the same deep convection required to allow evaporation of precipitation and density currents below (Knippertz *et al.*, 2007). The passing of the gust front involves an abrupt change in wind speed and relative humidity, with meteorological stations in Tinfou (Morocco) recording surface wind speed increase from 3 to 9 ms^{-1} in only 2 minutes, while maximum gusts range from 8 to 15 ms^{-1} (Knippertz *et al.*, 2007). The wall of dust moves at approximately half the gust speed within the front as horizontal motion is redirected vertically into a ring vortex, forcing deflated sediments high into the planetary boundary layer (PBL) (Miller *et al.*, 2008). Given the significant topographic relief across Iran and along the western edge of the Arabian Peninsula, these moist convection events could significantly contribute towards dust emission in the Middle East.
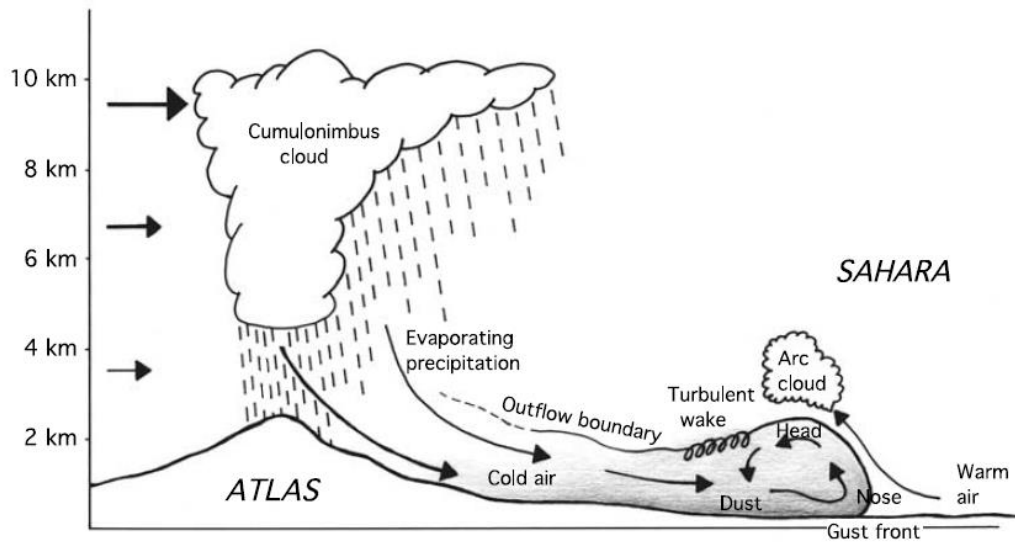
Figure 2.10: Schematic of cold pooling density current around the Atlas Mountains, Morocco. (Source Knippertz *et al.*, 2007).

In the Middle East, Miller *et al.* (2008) observed multiple haboob events south of the Al Hajar Mountains in Oman. Here, they observed simultaneous formation of multiple haboob fronts, typically with an average 10 m s $^{-1}$ increase in winds speed, 2 mb rise in surface pressure, 15% increase in humidity and drop of 7°C within 15 minutes of the front passing. Significantly, haboob generated dust storms were episodic in nature, with peak haboob activity occurring near the centre of multiday periods of convective activity. Indicating that the development of these mesoscale features is dependent on synoptic scale environmental conditions, especially when multiple fronts occur simultaneously. Dust emission from haboobs are frequently underrepresented in global emission models, due to their association with convective clouds and the subsequent difficulty to be observed by daily satellite observations (Knippertz and Todd, 2012). The utilisation of high frequency data (sub hourly) should allow the observation of a larger number of events (see Section 3.2), giving a better account of dust emission events generated by moist convection.

Dry convection events within the ABL occur over desert surfaces when high solar insolation, low background horizontal winds cause high convective vorticity (Ansmann *et al.*, 2009). These dry convective features include nonrotating convective plumes, described as 'dusty plumes' by Koch and Renno (2005), typically around 100 m in diameter, and convective vortices known as dust devils, typically between 3m and 15m in diameter (Koch and Renno,

2005). These features are unlikely to be observed in this study, due to their small scale and the relatively coarse pixel resolution of SEVIRI data (greater than 4 km over the Middle East); however, it is important to recognise their dust emitting potential. Both dusty plumes and dust devils contain strong vertical velocities of about 1 m s^{-1} and 7 m s^{-1} respectively, and over their short lifetime (typically up to 1 hour) can lift up to 15,000 kg of dust into the atmosphere (Koch and Reno, 2005).

2.5.4   *Diurnal cycle of surface deflation*

In Section 2.5.2.1, it was shown how the diurnal regime of the CBL determined the vertical mixing of dust into the ABL. Diurnal regimes also play a key role in the timing of high surface wind speeds, instigating a clear diurnal pattern of dust emission in many arid regions (Choobari *et al.*, 2013; Schepanksi *et al.*, 2009; Washington *et al.*, 2006). Over the Bodélé Depression and much of the Sahara, observations show the strongest winds typically commence around midmorning; a diurnal pattern that has been linked to the breakdown and downward momentum shift of nocturnal low level jets (LLJ) (Schepanski *et al.*, 2009; Washington and Todd, 2005). Nocturnal LLJs describe the formation of maximum horizontal wind speeds, peaking near to 925 hPa geopotential height (Washington *et al.*, 2006). These jets occur in all subtropical desert regions (Knippertz and Todd, 2012) and exhibit out-of-phase relationship to surface winds, with jets peaking during the night and surface winds peaking during the day (Bou Karam *et al.*, 2017). These jets develop under clear skies, where high surface insolation creates a hot and deep CBL (see Section 2.5.2). During nighttime conditions, the air directly above the surface cools, decoupling the daytime CBL from the surface and creating a strong temperature inversion. The decoupled CBL becomes free air, separated from surface related turbulence and frictional forces, allowing the ambient pressure gradient to accelerate winds to supergeostrophic conditions, peaking just before sunrise. With the onset of solar heating at sunrise, convective turbulence begins to erode the decoupled air layer above, frictionally coupling the LLJ with the surface layer, directing its momentum into surface winds (Schepanski *et al.*, 2009). The coupling of the two layers is progressive, with the phase lag in maximum surface winds complete between midmorning and midday (Knippertz and Todd, 2012).

Nocturnal LLJs have been credited with the intensification of dust storms across the Middle East, including the Summer Shamal winds over the Tigris Euphrates Basin (Bou Karam *et al.*, 2017) and the Sistan Winds over Eastern Iran (Barough *et al.*, 2010; Alizadeh Choobari *et al.*, 2013; Choobari *et al.*, 2014). Bou Karam *et al.* (2017) observed large diurnal variability in dust emission during summer Shamal events, with a daily peak around 15:00 UTC, transporting a maximum of 2.5 Tg of dust (within a 3 hour period), similar in magnitude to the maximum flux in the Bodélé Depression 2.7 Tg (Todd *et al.*, 2008). Over the Sistan Basin, Choobari *et al.*, (2014) observed seasonal maximum LLJ velocities during July, coinciding with maximum north-south ambient pressure gradient. In a region 300 – 500 m above ground, night-time velocities exceed 20 m s^{-1}. Here peak surface velocities arrive earlier than those related to the Shamal winds, peaking mid-morning (09:00 local time, 13:00 UTC), with the highest surface winds of 13 m s $^{-1}$ recorded during their study period. The continued expansion of the CBL effectively reduces surface winds throughout the day, as momentum is shifted vertically within the deepening CBL. Surface winds here are enhanced by orthographic features, with winds accelerated by topographic channelling as they pass between the Hindu Kush Mountains and the Palanghan Mountains to the west (Hamidi *et al.*, 2013). A similar process enhances LLJs over the Bodélé Depression, as the caldera-like valley between the Tibesti and Ennedi mountain ranges to the north and east of the depression accelerate the LLJ enhanced Harmatten flow by the Venturi effect, (Koren and Kaufman, 2004), accelerating surface winds speeds in excess of 16 m/s^{-1} (Washington *et al.*, 2006).

2.6   Middle East

The Middle East is, as a region, one of the most dust-affected areas in the world (Washington *et al.*, 2003), second only to Africa (Kutiel and Furman, 2003). While the exact contribution is not known, estimates range from 221 Tg yr^{-1} (Tanaka *et al.*, 2005) to 496 Tg yr^{-1} (Ginoux and Torres, 2003), resulting in a profound impact on the people and environment in the region (Akbari, 2011). Dust activity is described as seasonal by Prospero *et al.* (2002), with low levels of dust in the atmosphere during winter, increasing through spring and peaking during the summer months (Middleton et al. 1986). The climate of the region is dry and hot, with moderate precipitation during its mild winters (Rezazadeh *et al.*, 2013).
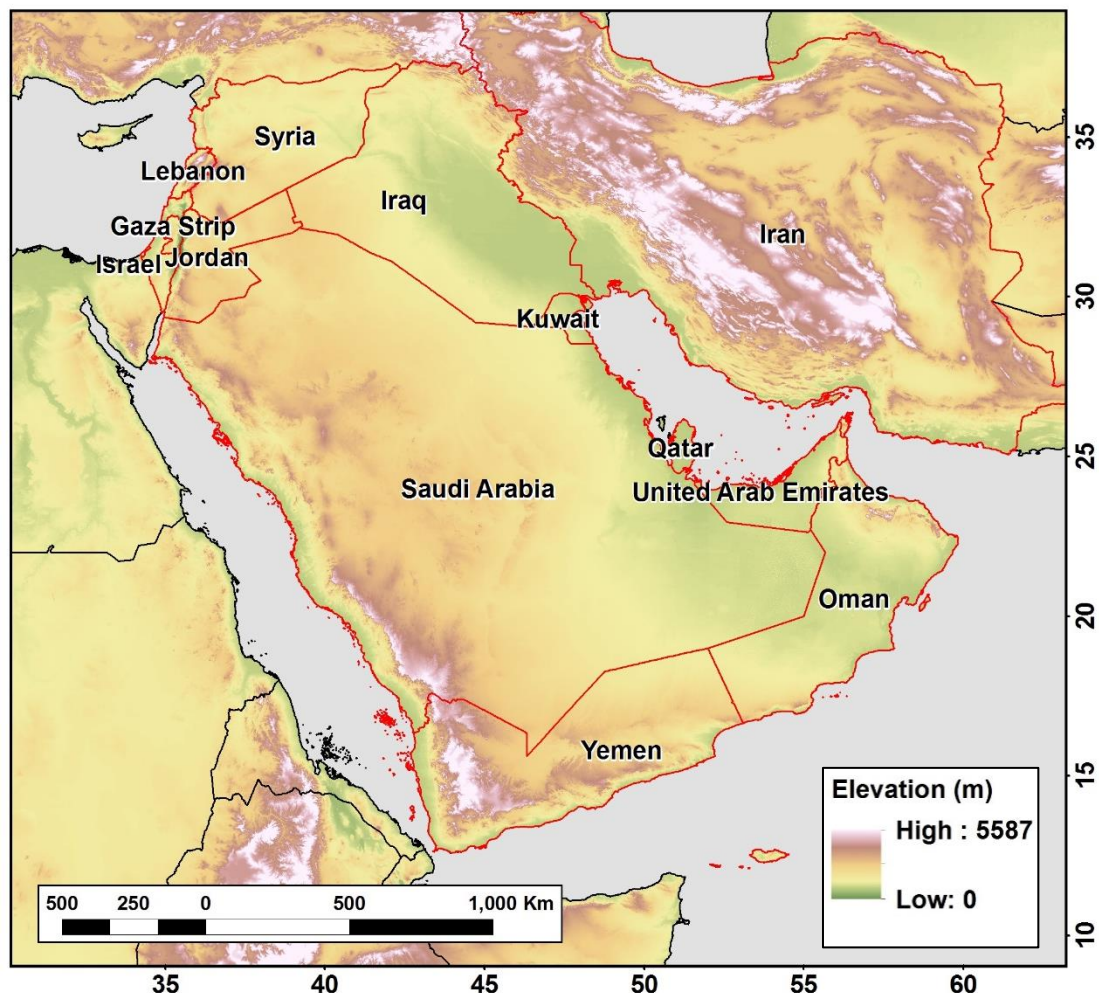
Figure 2.11: Study area map of the Middle East. Red line depicts area of interest and national borders. Background DEM provided by USGS, has a 3 km spatial resolution and is represented as meters above sea level (masl).

The area known as the Middle East sits between 30° to 65° E and 10° to 55°N covering parts of north east Africa and west Asia (Rezazadeh *et al.* 2013). Topographically the region is dominated by large plateaus intersected by mountain ranges and ancient flood plains (Fig. 2.11) (Middleton, 1986). In comparison to the Sahara, the Middle East has a greater population density, with around 30% of all emissions coming from anthropogenic soils compared to only 8% in North Africa (Ginoux *et al.*, 2012). Intensive periods of drought since the beginning of the 21st Century have seriously affected agricultural production and increased desertification (Kelley *et al.*, 2013; Moridnejad *et al.*, 2015), creating increasing levels of dust across large swathes of the region (Notaro et al,, 2015). To date, investigations of dust sources within the Middle East have focussed on country/drainage basin (Choobari *et al.*, 2014; Kaskaoutis *et al.*, 2014), regional (Middleton, 1986; Walker *et al.*, 2009) and global scales (e.g. Ginoux *et al.*, 2012; Prospero *et al.*, 2002). Dust emission data is commonly derived from wide swath, passive, polar orbiting sensors such as MODIS and TOMS/OMI (Washington *et al.*, 2003; Walker *et al.*, 2009) and narrow swath, active, atmospheric profiling Lidar sensors such as CALIOP (Vishkaee *et al.*, 2011). Land surfaces models have estimated areas of potential dust emission from a combination of soil, vegetation and aerosol load data (Gherboudj *et al.*, 2017). In addition, non-satellite data, such as horizontal visibility records, from ground-based meteorological stations are commonly used (Middleton 1986; Miller *et al.*, 2008; Rashki *et al.*, 2017). The merits and limitations of these platforms have been discussed in this chapter, and it is clear that each contains a level of uncertainty (these platforms are discussed in more detail in Chapter 3). Importantly, the SEVIRI dust RGB product has never been used to crerate a dust source inventory of the Middle East; this investigation is the first attempt to apply this method to map dust sources at high resolution and characterise their respective emission frequency. With it's unmatched temporal reolution and ability to monitor 24 hours a day, SEVIRI imagery has already been shown to produce highly accurate maps of dust sources in North Africa (Schepanski *et al.*, 2009), but here it will be used to characterise dust emission processes in another very important dust source region.

For the purposes of this section, known dust source areas are discussed within three separate geographic regions; splitting dust sources on the Arabian Peninsula into Northern (Section 2.6.1) and Southern (Section 2.6.2) regions, with Iranian sources discussed in Section 2.6.3.

2.6.1   *Northern Arabian Peninsula*

Topographically, this area consists of a gently sloping plateau from the upland areas in the west (around 400 m asl) down to the low (less than 100 m asl) alluvial plains of Iraq in the east. Bordered by the Syrian Mountains and the Mediterranean Sea in the West and the Zagros Mountains of Iran in the east and the Mercan and Taurus Mountains of Turkey to the north (Vishkaee *et al.*, 2012). The plateau covers two climatic zones, with the Euphrates River dividing the Syrian Desert to the west and south from the more humid Tigris-Euphrates drainage basin and alluvial sediments to the east and north (Bou Karam *et al.*, 2017). The Tigris-Euphrates river basin occupies the north east of the Arabian Peninsula; dust emissions are thought to emanate from the low level (50-250 m asl) alluvial plains, running north east to south west from the Iraq/Syria border through to Kuwait and the shores of the Persian Gulf (Hamidi *et al.* 2013). Dust emission is frequently linked to the Shamal Winds, peaking during the summer months (Middleton 1986). Also known as Mesopotamia, the basin contains a combination of natural and anthropogenic land surfaces, with northern Iraq and Syria (33 - 36°N; 35 -46°E) dominated by agricultural fields and drainage channels from the Tigris and Euphrates rivers (Ginoux *et al.*, 2012).

Previous studies show that dust emission is concentrated around the upland areas of the Tigris Euphrates Basin, at the beginning of an area known as the 'fertile crescent' (Prospero *et al.*, 2002). Here, soils are made up of fine silt and clay, originating from ancient irrigated fields, resulting from some of the earliest attempts of modern agriculture ~10,000 years ago (Lev-Yadun *et al.*, 2000). This area continues to be an important source of agriculture, with 70-85% of agriculture focussed on cereal crops, specifically winter rain-fed wheat (Gibson *et al.*, 2015). Figure 2.12 shows the seasonality of precipitation and average daytime temperature in Mosul (36.3°N 43.1°'E) on the Tigris River. Summer months receive very little precipitation and the warmer temperatures prevent crop growth, this causes the cultivated areas to be largely barren and vulnerable to surface deflation during the summer.

Increasing desertification across the whole of Mesopotamia has been observed by Normalised Difference Vegetation Index (NDVI) analysis, with approximately 12,218 km^2 of land becoming desert in the past 30 years (Moridnejad *et al.*, 2015). Moridnejad *et al.*, (2015) note that the agricultural lands between Nineveh (Iraq) to Al Hasakah (Syria) have experienced the most intense desertification, linked strongly to the construction of dams and

increased restrictions on water flow into this area (Hamidi *et al.,* 2013). Observations from MODIS AOD show frequent high AOD values from nearby playas (Albu Gharz, al Burghuth and Ar-Rawda), along the Iraq/Sudan border and the farmland regions around Ar Raqqah in northern Syria (Ginoux *et al.,* 2012).
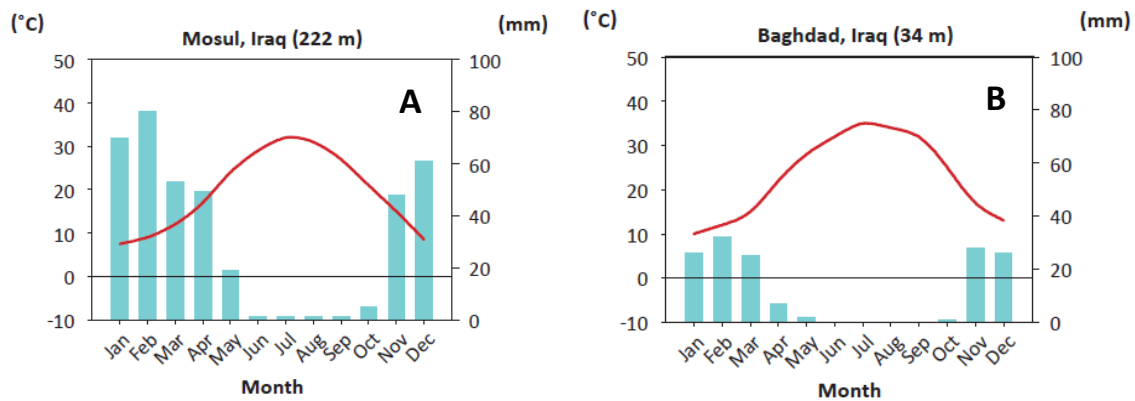
Figure 2.12: Precipitation (mm) and temperature (°C) data for regions of Iraq on different sides of the Upper and Lower Mesopotamia divide Mosul (Upper Mesopotamia) and Baghdad (Lowere Mesopotamia). Source Worldclim (2011) in UN-ESCWA BGR, (2013).

The lowland areas of the Tigris Euphrates basin (less than 100 m asl), were described by Middleton (1986) as the dustiest region of the Middle East. The region is defined by a large alluvial plain, which begins around 100 km northeast of Baghdad, covering large parts of central and southern Iraq and Kuwait. Middleton (1986) observed dust storms on up to 40 dust days per year. This large area (130,000 km^2) is regularly inundated with floodwaters during the winter months (Prospero *et al.* 2002). As Figure 2.12 shows, precipitation in this region (including Baghdad) is much lower than areas in the North, with desert regions occupying 170,000 km^2 in Iraq alone, dominating the landscape in southern and western parts of the country (Bou Karam *et al.,* 2017). Alluvial areas are susceptible to surface deflation during summer months, where high average temperatures and minimal precipitation reduce vegetation cover, leaving much of the land surfaces bare (Ginoux *et al.,* 2012). To the east of the Euphrates River, at the Iran/ Iraq border, dust emission is believed to emanate from the previously discussed Mesopotamian marshes (see Section 2.4.3.2) (30- to 33°N, 45- to 48°E).

Drought conditions have persisted across the Tigris Euphrates basin since 2007 (Notaro *et al.*, 2015), with the period 2008-2010 described as one of the worst recorded droughts in Iraq's history (Gibson *et al.*, 2015), causing widespread crop failure and enhancing socio-political unrest (Kelley *et al.*, 2015). The continuing drought has affected rain fed wheat production the hardest (Gibson *et al.*, 2015), while overexploitation of groundwater and stream flow has impacted soil moisture and water quality downstream (Kelley *et al.*, 2015). These factors have contributed to an increase in dust storm frequency, as observed at multiple meteorological stations across the Arabian Peninsula, which have been backtracked to the Tigris Euphrates Basin by Hybrid Single-Particle Lagrangian Integrated Trajectory (HYSPLIT) model analysis (Notaro *et al.*, 2015).

2.6.2   Southern Arabian Peninsula

The Southern part of the Arabian Peninsula consists of large plateau called Al Hamad, which slopes from its highest elevation (~3 km) along the Hajiz and Asir Mountains in the west, to its lowest elevation at the Persian Gulf in the east (Prospero *et al.*, 2002). The Arabian Desert comprises a large proportion of the Al Hamad plateau, occupying an area of 2,330,000 km^2 and containing one of the largest sand dune systems in the world, the Rub'al-Khali (18 - 22°N; 45 - 52°E) (Rezazadeh *et al.* 2013). The Rub'al-Khali fills the 'Empty Quarter', with its southern extent marking the borders between Saudi Arabia and Yemen/Oman. The Ad Dahna desert (20 - 28°N; 45 -55°E), including the coastal lowlands of the Persian Gulf, experiences frequent dust activity (Prospero *et al.*, 2002; Washington *et al.*, 2003). Dust activity along this 1300 km long sand sea correlates to the hydrological regime of three wadis, Al Batin, Al Rimah and Al Sahba (Ginoux *et al.*, 2012). Here, peak emission occurs during the dry and hot summer months, shown by high levels of TOMS AI (Goudie and Middleton, 2001). Dust activity in the coastal lowlands (50 – 200 m asl), along the Persian Gulf coastline are described as active all year by Prospero *et al.* (2002). These surfaces are characterised by coastal sabkhas, covered by sandy calcareous sediments and evaporites that are up to 30 km wide in places (Prospero *et al.*, 2002). Further south, near the United Arab Emirates (UAE), active dune fields effectively erode the surface crusts of the nearby Sabkha (Matti), sand blasting the salt crusted mud flats into atmospheric dust during periods of high surface wind speeds (Ginoux *et al.,* 2012). These

areas have also been linked to the convective downbursts in the lee of the Al Hajar Mountains (see Section 2.5.4).

At the southern tip of the Peninsula, the coast of Oman is believed to be a highly active dust source (Prospero *et al.*, 2002). It is ranked as the third dustiest region in the world by TOMS observations, behind the Bodélé depression in central Sahara and Mali in Western Sahara (Washington *et al.*, 2003). However, this region is not recognised as a dust source in both Ginoux *et al.* (2012) and Middleton (1986), with the former observing greatest dust activity near the coastal escarpment in Hadramawt (14 – 16°N; 47 - 52°E) instead. Here, dust activity is associated with alluvial fans (Ginoux *et al.*, 2012). Conflicting opinion on the dust potential of this area can be linked to high levels of cloud contamination in this part of the peninsula, linked in part to Asian Monsoon in the Arabian Sea (Hamidi *et al.*, 2013). High levels of cloud will have a large impact on the number of observations made by satellite products, with four of the five investigations using cloud contamination masks, many dust storms can be missed due to cloud contamination.

2.6.3   Iran

The Islamic Republic of Iran (22 - 25°N; 43 -47°E) occupies a high plateau, bordered to the north by the Alborz Mountains and to the west by the Zagros Mountains; these ranges converge in the north west, with a greatest altitude over 4000 m asl (Vishkaee *et al.*, 2012). Dust sources in Iran are clustered into inter-mountain wadis, salt pans and ephemeral lakes and sabkhas (Choobari *et al.*, 2014; Kaskaoutis *et al.*, 2014; Prospero *et al.*, 2002). A significant portion of dust emission comes from the Sistan Basin, on the eastern border with Afghanistan, at the western extent of the Dasht-i-Margo desert (27 - 32°N; 60 - 63°E) (Choobari *et al.*, 2013). This topographic depression is characterised by ephemeral salt lakes including the Hamun-e- Saberi, Hamun-e Puzak and Daryacheh-ye-Hamun (Prospero *et al.*, 2002) and is recognised as the most active dust source in southwest Asia (Kaskaoutis *et al.*, 2015a). Peak activity is associated with summer time, 120 day winds, also known as the Sistan Winds which are intensified by topographic channelling and the diurnal breakdown of nocturnal LLJs (Rezazedeh *et al.,* 2013) (See Section 2.5.5). Like the large portions of the Middle East, the Sistan basin has experienced a prolonged period of drought since 2000 (Ginoux *et al.*, 2012).

Further south, on the Iran / Pakistan border, this sub-region includes the Hamun-i-Mashkel ephemeral lake. Recognised as a prominent dust source in TOMS data, this large ephemeral lake (1950 km^2), is subjected to the 120 days winds and, like the Sistan basin sources, observes peak dust emission frequency during summer (Prospero *et al.*, 2002).

The Jazmurian basin, in the south east of the country is a recently recognised dust source in the region (Rashki *et al.*, 2017). This topographic depression has an average elevation 2000m below the surrounding mountains and contains a seasonal lake (Hammun-e Jaz Murian) that has remained almost continuously dry since the drought of 2000. The dry lakebed surface is made up of silty-clay sediments transported into the depression by the Bumpur (east) and Halil Rud (west) rivers (Rashki *et al.*, 2017). Analysis of dust storm activity between 1990 and 2013 by Rashki *et al.* (2017), showed an increasing frequency during intense drought conditions (2001-2004), recording over 20 dust storm events per year on average. Further dust activity has been reported along the Makran coast, an area dominated by ephemeral rivers and alluvial fans, with large supplies of silt-sized particles transported from the mountains inland (Washington *et al.*, 2003). Dust emission are frequently observed from both locations, blowing out over the Arabian Sea and east towards India (Walker *et al.*, 2009). Dust activity is strongest during June / July, with a substantial reduction in the autumn and winter months (Rashki *et al.*, 2017).

Across the rest of Iran, dust activity is linked to the large salt deserts Dasht-e-Kavir and Dasht-e-Lut (Vishkaee *et al.*, 2011). In the larger of the two, the Dasht-e-Kavir desert (centred around 34.3°N, 55.2°E, covering an area of 77,600 km^2), dust activity is concentrated at the western extremities, near Tehran. Here, fluvial activity has produced a network of ephemeral lakes and channels, marshes and the intermittent salt lake Daryachen-ye Namak (1,825 km^2), also known as Qom Dry Lake due to its proximity to the city of Qom (Vishkaee *et al.*, 2011). Analysis of dust storm frequency in Tehran by Vishkaee *et al.* (2011) showed high levels of atmospheric dust are most frequently seen during summer, linked to foreign dust, predominantly from Mesopotamia, traversing the Zagros mountains to the west in response to Shamal Winds (see Section 2.5.2.1).

The hyper arid Dasht-e-Lut desert valley (centred around 31.3°N, 58.8°E, covering an area 51,800 km^2) is dominated by salt flats (Choobari *et al.*, 2014). Despite this, the desert is not recognised as a major dust source, with dust emission constrained to the western edge of the

desert, adjacent to the slopes of the Central Mountains (Walker *et al.*, 2009). However, where a LLJ forms during stable conditions, the orography of these central valley appears to enhance the northerly LLJ, accelerating north to south winds, which are driven by cold advection, and increasing surface winds to over 14 m s^{-1} (Barough *et al.*, 2010). The existence of these LLJs mean that the Lut valley could become a dust source if a sufficient amount of fine sediment becomes available for deflation. Relatively little information is available on the seasonality of dust emission in the region.

2.7   Conclusion and research questions

The process of dust emission relies upon a complex relationship between many mechanisms, from land surface and basin scale production of fine sediments to seasonal changes in local climate and patterns of atmospheric circulation from the synoptic to mesoscale. This chapter has discussed the current understanding of key environmental conditions involved in dust emission both globally and specifically within the Middle East. In summary, the following important points have framed the research presented in this thesis:

- Global observations of major dust emitting regions have been derived by a host of different remote sensing platforms. Importantly, these data cover a range of spatial and temporal resolutions, with many investigations focussing on dust sources derived from daily distributions of high AOD. The introduction of SEVIRI high frequency data has enabled sub-hourly observations of the surface, these data have the ability to show dust emission *in situ* and determine dust source locations with a high level of accuracy. SEVIRI data have identified inaccuracies with daily observations, which due to their fixed time of day observations; contain an inherent transport route bias in dust source attribution.

- The frequency and volume of global dust emissions change seasonally, with dust emission peaking in response to wind speeds exceeding locally specific surface thresholds. These thresholds are determined by the spatial and temporal controls on sediment texture, soil moisture and surface roughness including vegetation.

- Analysis of known dust sources around the globe has shown a clear link to topographic depressions, specifically those that contain evidence of contemporary or ancient fluvial activity. These topographic depressions show significant heterogeneity in dust emission, with ephemeral lakes and alluvial features regarded as the key emitting surfaces due to the abundance of fine sediment, weathered and transported by rivers.

- Human induced changes to the land surface, by the development of agricultural and channel management practices, have been shown to increase dust activity in some regions. The net contribution of anthropogenic dust is not fully understood due to the complex relationship between human activity and dust emission and the lack of high-resolution dust source data.

- Meteorological conditions connected with dust occur at a large range of scales, from continental scale circulations linked to the seasonal movement of monsoon systems, to

the passing of sub-tropical depressions and mesoscale cold pool density currents in the presence of moist convection cells. Importantly, each of these features produce sufficient surface horizontal wind speeds to deflate material from the surface; and significant vertical velocities within the ABL to inject mineral dust high into the atmosphere, allowing long distance transportation that can extend over continents / oceans.

- The Middle East is recognised as a key dust source area, with dust activity concentrated in specific areas including the Tigris Euphrates Basin, the Sistan Basin and the foothills of the Oman Mountains. In comparison to other important dust emitting regions (e.g. the Sahara), there are relatively few studies carried out on the Middle East. Of the existing studies, dust sources are commonly determined from daily maps of AOD or surface observations of horizontal visibility. There is, therefore, a need to create a high-resolution inventory of dust emissions using sub-daily images to provide an accurate account of dust sources and their emission frequency.

Based on this literature review, this thesis will address the following research goals:

- Identify the location of major dust emitting source regions and investigating their emission frequency by creating an inventory of dust emissions using the SEVIRI Dust RGB product, at sub-hourly resolution.

- Determine the key environmental factors that dictate dust-emission source locations, including changes in land cover type, geomorphology, and land use.

- Examine which factors appear to influence dust emission frequency, including distance from fluvial features and seasonal changes in vegetation / agriculture.

- Investigate the key synoptic conditions that drive dust activity in the region and how this changes seasonally.

Chapter 3: Data and Methods –SEVIRI Dust RGB Product

3.1 Introduction

Satellite derived data is now widely used for the detection of dust in the atmosphere. The spatial coverage offered by spacecraft in either low earth polar or geostationary orbits far exceed aircraft mounted or ground based sensors (Ashpole and Washington, 2013; Choobari *et al.*, 2014). The variety of platforms and sensors used to observe atmospheric dust have increased greatly in the last few decades, providing new insights into atmospheric dust emission processes (Vishkaee *et al.*, 2011), the global aerosol burden (Prospero *et al*, 2002), radiative effects (Tegan *et al.*, 2006) and dust source locations (Schepanski *et al* 2009).

Observation of dust at the source of emission is of key importance, as its physical, chemical and optical characteristics vary between source regions, evolving throughout the life span of each dust plume and across its transportation route (Ackerman, 1997). Knowledge of these properties is necessary to improve dust representation in weather and climate models and thus, accuracy of the estimation of the resulting radiative forcing (Ashpole and Washington 2013). It is, therefore, important to gain precise knowledge of dust sources, their location, emission frequency and how they respond to climate variability (Schepanski *et al.* 2012).

This chapter aims to:

i)   Review existing data and methods for determining the location of dust emission sources, justifying the use of SEVIRI Dust RGB data for this study (Section 3.2).

ii)   Provide an analysis of SEVIRI Dust RGB data including limitations (Section 3.3).

iii)   Describe the back-tracking method utilised in this investigation, discussing the benefits of subjective-manual observations compared to an automated approach (Section 3.4).

iv)   Present an error analysis of the dust source inventory, focussing on the impact of using SEVIRI Dust RGB data at various temporal resolutions (Section 3.5).

v)   Describe the secondary data used to characterise land surface environments of dust emitting sources (Section 3.5.1) and synoptic patterns associated with dust emission (Section 3.5.2).

3.2   Review of existing dust observation data and methods – Three themes

Locating sources of dust emission is an important and challenging task; the scale, emission variability and inhospitable nature of the arid environments is well suited to the use of satellite based remote sensing data and methods. Dust observation platforms (satellites) and sensors utilise a range of wavelengths and orbits to produce global maps of dust emissions at various spatial and temporal resolutions. These methods have been developed by understanding how dust interacts within the electromagnetic spectrum and, more importantly, how its spectral properties differs from the surface and other features in the atmosphere. In the visible wavelengths, lofted dust yields a very similar upwelling radiance to bare soils below, especially in the red (c. 670 nm) wavelengths, making it very difficult to distinguish from the surface below (Hsu *et al.*, 2004). Viewing dust in these visible wavelengths is only possible over dark homogeneous surfaces like the sea or thick vegetation (Hsu *et al.*, 2013). These surface types tend to be infrequent in dust emitting dryland regions. With single or multiple wavelengths, dust observations are now routinely retrieved in the thermal infrared (TIR), ultra-violet (UV) and near UV (deep blue) parts of the electromagnetic spectrum (Ginoux *et al.*, 2012; Prospero *et al.*, 2002; Klüser *et al.*, 2012; Ashpole and Washington, 2012).

Remote sensing methods used to determine dust sources can be categorised into three different types:

Type 1) daily maps of aerosol optical depth

Type 2) observations of emission plumes from source

Type 3) Coupled climate aerosol models based on maps of surface and soil characteristics.

These products and their recent application are shown in Table 3.1, where they are grouped into these three categories. The first two types were briefly discussed in Section 2.2, while land surface processes linked to dust emission models were discussed in Sections 2.3 and 2.4. This section will discuss the theory behind these three methods, discussing the advantages and limitations of each before demonstrating the applicability of SEVIRI Dust RGB product to this investigation.

Table 3.1: List of dust observation studies, detailing which remote sensing products were used and their specific spatial/temporal resolution. Detailing the different spatial scales at which these studies were carried out and from where they were observed on the electromagnetic spectrum.

Approach	Platform	Product / Model parameters (Type 3)	Automated / Manual (emission retrieval)	Spectral Range	Spatial Resolution	Temporal Resolution	Region	Reference
Type 1	TOMS [a]	Aerosol Index (AI)	Automated	UV and nUV	1° at level 3	Daily	Global	**Prospero *et al.*, 2002**
							Global	**Washington *et al.*, 2003**
							West Africa	**Mahowald *et al.*, 2003b**
							Middle East	**Alpert and Ganor, 2001**
	MODIS [b]	Deep Blue, Aerosol Optical Depth (AOD)	Automated	Visible Blue and Red	0.1°	Daily	Western Sahara	**Ginoux *et al.*, 2010**
							Global	**Ginoux *et al.*, 2012**
							Global	**Hsu *et al.*, 2013**
Type 2	MODIS [b]	Deep Blue, Aerosol Optical Depth (AOD) Dust Enhancement Product (DEP) (Miller *et al.*, 2003); Dust differential algorithm (Rskovensky and Liou, 2005); Brightness temperature difference (BTD)(Ackerman, 1997)	Manual	Visible; TIR; SWIR	Various (10 –1 km)	Daily	Lake Eyre, Australia	**Baddock *et al.*, 2009**
	SEVIRI [c]	Dust RGB Product	Manual	TIR	3 km (nadir)	15 minute	North Africa	**Schepanski *et al.*, 2007; 2009; 2012**
		Dust RGB Product	Automated	TIR	3 km (nadir)	15 minute	North Africa	**Ashpole and Washington 2012; 2013**

Type 2 / 3	MODIS [b]	Dust Enhancement Product (DEP) (Type 2); COAMPS [d] model	Manual	Visible and TIR	1 km	Daily	South West Asia – incl. Middle East	**Walker *et al.*, 2009**
Type 3	MENA DEP[e] model	Wind speed; Soil Moisture; Vegetation cover, Soil erodibility, Soil texture	n/a	n/a	0.5˚	n/a	Middle East and North Africa	**Gherboudj *et al.*, 2017**
	DEAD [f] model	Vegetation cover, topography, hydrology	n/a	n/a	1 km	n/a	Global	**Zender *et al.*, 2003**
	Coupled Aerosol-Erodibility model	Soil roughness; Sediment particle size distribution; Soil Texture; Wind Speed; Soil Moisture; Snow Cover	n/a	n/a	0.25˚	n/a	China and Mongolia	**Laurent *et al.*, 2006**
	Tracer transport Model [g]	Soil Texture; Soil Moisture; Vegetation Cover	n/a	n/a	2.5 ˚	n/a	Global	**Tegen and Fung 1994**

[a] Total Ozone Monitoring

[b] Moderate Resolution Imaging Spectrodiameter

[c] Spinning Enhanced Visible and InfraRed Imager

[d] Coupled Ocean/Atmophere Mesoscale Prediction System

[e] Middle East and North Africa Dust Emission Product

[f] Dust Entrainment And Deposition model

[g] (Provided by) Goddard Institute for Space Studies

UV = ultra violet

nUV = near ultra violet

TIR = thermal infrared

SWIR = short wave infrared

3.2.1 Type 1 – Statistical dust load mapping

Many dust observation studies are carried out using sun-synchronous, polar orbiting satellites. With their wide observation swath and daily global coverage, sensors such as TOMS/OMI and MODIS provide the only possibility to produce rapid global maps of dust in the atmosphere using a consistent automated approach. These data have shown large spatial and seasonal heterogeneity of dust emissions around the world (See section 2.2). Satellite observations are taken at a fixed time of day, related to the position within the satellite orbit. Dust source regions are assessed by the statistical correlation of frequently high dust loadings over recognised local dust emitting land surfaces (Prospero *et al.,* 2002: Ginoux *et al*., 2010; Ginoux *et al*., 2012). This approach is determined by the nature of dust emission, which occurs as short episodic events, linked to regular diurnal cycles of strong surface winds (Knippertz *et al*., 2012; see Section 2.5). Where time of observation and time of emission are frequently offset, the short-term existence of dust emission at source dictates the use of the statistical approach, as individual observations of lofted dust plumes will be geographically separated from their source.

The Total Ozone Mapping Spectrometer (TOMS), later replaced by the Ozone Monitoring Instrument (OMI) missions provide measurements of atmospheric absorptive aerosol index (AI) indicating the presence of dust in the atmosphere with a daily temporal resolution and a 1x1° spatial resolution (Prospero *et al.*, 2002). The AI is created by comparisons of the absorptive signature of the atmosphere in the UV wavelengths 340, 360 and 380 nm. At these wavelengths, molecular scattering by atmospheric gases is strong, while radiative backscattering is dominated by sulphate aerosols, sea salt and meteorological clouds (Torres *et al.*, 1998). In the presence of dust and other absorbing aerosols, it is expected that there will be a wavelength dependant reduction in Rayleigh scattering relative to a dust free atmosphere (Hsu *et al.*, 1999). This technique is applicable over both ocean and land surfaces as neither have strong reflectance in the UV (2-8% reflectivity at 340-380 nm) (Torres *et al.*, 2002), meaning that radiance received by the sensor is derived from the atmosphere (Alpert and Ganor, 2001). From this index, AI values greater than 0.7 are taken to indicate the presence of atmospheric dust (Hsu *et al.*, 1999).

With the use of TOMS data, Prospero *et al*. (2002) produced a global representation of high (greater than 0.7) AI areas, averaged across representative months for the period 1980-1992 (Fig. 3.1). The months used were selected to best represent highest emission activity at each dust source region, while the AI threshold was adapted by region. Many areas within the so called 'dust belt' are given a higher AI threshold, as AI is positively biased by fine particles in the atmosphere, such as soot from biomass burning. This is thought to enhance the dust signal in regions such as the Sahel, where biomass burning is frequent (Ginoux *et al*., 2010).

The most significant TOMS/OMI limitation is the coarse spatial resolution (1° x 1°). With dust emission plumes regularly emanating from multiple point sources smaller than 10 km^2 (Mahowald and Luo, 2003; Walker *et al.*, 2009), the 1° TOMS/OMI data can only provide limited information on the spatial variability of emission surfaces, especially at a sub basin scale (Bullard *et al.*, 2011). While regions such as the North Africa may contain large-scale source areas (e.g. Bodélé Depression), identifying emission source within the inter-mountain drainage channels of Iran, will be challenging at this coarse spatial resolution (Vishkaee *et al.* 2011).
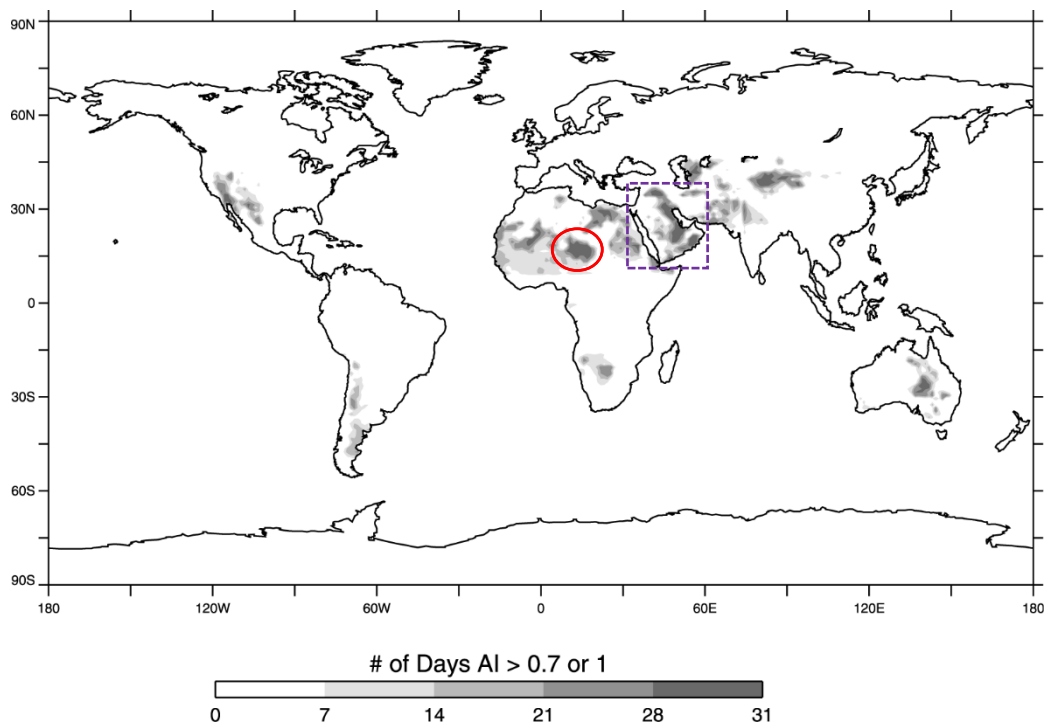
Figure 3.1: Average number of days per month with AI >1.0 through the dust belt regions (0-40° N) and >0.7 throughout the rest of the globe. The red circle depicts the region including the Bodélé depression and Erg du Djourab (Chad). The dashed purple square shows the Middle East. (Source: Prospero *et al.,* 2002).

The Moderate Resolution Imaging Spectrometer (MODIS) provides a higher spatial resolution of up to 250 m at nadir across 36 spectral bands from 0.4 µm to 14.4 µm (Ginoux *et al.*, 2012). Global coverage is completed every 1 to 2 days with a polar orbit and a 2,330 km swath width (Baddock *et al.*, 2009). Originally used specifically over oceans and vegetated surfaces, the development of the Deep Blue algorithm has permitted dust detection over bright surfaces (Hsu *et al.*, 2004). Created to avoid high surface reflectance in the longer visible wavelengths, the Deep Blue algorithm focusses on the blue wavelengths 412nm and 470nm, where the surface absorption is greater over desert surfaces compared to longer wavelengths (Hsu *et al.*, 2004). At these wavelengths dust causes increased backscattering of radiation, represented as a brightening of the image (Hsu *et al.*, 2013). Based aboard NASA Earth Observing System (EOS) Terra and Aqua satellites, MODIS operates on a sun synchronous 705 km altitude orbit. The latest 'Collection 6' Deep Blue aerosol retrievals provide global maps of aerosol optical depth (AOD), with a spatial resolution of 10 km^2 (level 2) or 1° (level 3) (Banks *et al.*, 2013). AOD describes how radiance at that point of the spectrum is attenuated by aerosol particles by either scattering or absorption, with its value varying by the volume of dust in the atmospheric column (Dubovik *et al.*, 2002).

Automated algorithms screen pixels for cloud contamination, before comparing surface reflectance to radiative transfer models, which considers viewing and solar angles (Hsu *et al.*, 2004). The compared radiances are then analysed with a dust aerosol model, which takes into account the non-spherical scattering characteristics of mineral dust and transfers these radiances into values of AOD and particle size (Ångström exponent) (Hsu *et al.*, 2013). Utilising short wavelength solar reflectance omits sensitivity to water vapour absorption, a key limitation of longer wavelength retrievals (Banks *et al.*, 2013). The higher spatial resolution improves cloud screening accuracy over the coarser products such as TOMS, while observing outside the UV wavelengths avoids contamination of the dust signal by other high UV-absorbing aerosols such as carbon from biomass burning (Ginoux *et al.*, 2010). The use of reflected solar radiation prevents night time observations, allowing just one useable observation per day/per satellite, with MODIS Terra crossing the Equator in the morning (10:30 local time) and MODIS Aqua crossing the Equator in the afternoon (13:30 local time) (Hsu *et al.*, 2004). With a maximum of two images per day (one from each satellite), individual emission surfaces are hard to determine due to emission/observation time offset, meaning

sub-daily emission processes are poorly understood. With a low temporal resolution, these data are more vulnerable to cloud conditions, frequently observed with the active warm front of sub-tropical cyclones across North Africa and the Middle East, during non summer months (Bou Karam *et al.*, 2010) - see Section 2.5.

Therefore, to obtain a clearer understanding of dust source locations and their associated seasonality and diurnal cycle, a higher frequency of observations is required.

3.2.2   Type 2 - Dust emission observations

To reproduce data on dust emission source location with the highest accuracy, observations should ideally be taken at the moment of emission. Data with a high temporal resolution will have a greater probability of providing such observations. In the past decade a new product has become available from Eumetsat's SEVIRI instrument aboard Meteosat Second Generation (MSG) satellites; offering unparalleled temporal and spatial resolution (Banks and Brindley, 2013). Operating in a geostationary orbit at 3.5°W, data acquisition of the whole of the African continent and the Middle East comes at a 15 min temporal resolution, with 3 km spatial resolution at nadir and 4-6 km across the Middle East (EUMETSAT, http://oiswww.eumetsat.org). The SEVIRI 'Dust RGB' product does not suffer from the same temporal sampling limitations of MODIS and TOMS/OMI (Schepanski *et al.*, 2012). It has been used by many researchers to determine dust source locations across arid environments in North Africa (Ashpole and Washington, 2013; Schepanski *et al.*, 2007; Schepanski *et al.*, 2009; Banks and Brindley, 2013). The Dust RGB product works in the thermal infrared (TIR) (8.7 µm – 12.0 µm), using the distinctive 'cool anomaly' produced by dust in the atmosphere (Legrand *et al.*, 2001) - see Section 3.3.1. Analysis is performed by measuring brightness temperature differences (BTD) across three bands, in a configuration developed to highlight dust in a RGB colour composite image (Lensky and Rosenfeld, 2008).

The main advantage of the platform is the high temporal resolution offered by the geostationary orbit, and the ability to perform in both day and night-time conditions, through the observation of terrestriaolly-emitted thermal infrared radiation (Ashpole and Washington 2013). From this, it is possible to observe airborne dust plumes and backtrack them through consecutive images to the point of first appearance (Schepanski *et al.*, 2007). Observations in

the TIR are susceptible to number of radiative effects, most notably high absorption by water vapour. Here, the presence of high column water vapour (CWV) is known to limit the cool anomaly in the dust RGB product (Brindley *et al.*, 2012) - see Section 3.3.4. These limitations hamper development of a robust automated detection algorithm, favouring a more subjective manual inspection approach, where human pattern-recognition skills effectively identify individual dust plumes and their associated sources through back-tracking (Schepanski *et al.*, 2012). Applying this method over several years can produce a more accurate identification of frequently emitting land surfaces, their diurnal emission regime, seasonality and reaction to specific climatological and meteorological events such as drought or mesoscale atmospheric circulation (Schepanski *et al.*, 2012).

With its relatively high spatial resolution, MODIS data has also proven effective at determining discrete dust emission sources at a regional scale (Bullard *et al.*, 2008). This type of analysis is only possible when dust emission occurs concurrently with satellite observation time and without cloud contamination (Walker *et al.*, 2009). In these situations, Baddock *et al.* (2009) were able to evaluate a range of MODIS dust detection algorithms, to determine which produced the clearest depiction of dust emitting at source. Focussing on dust emissions from the Lake Eyre Basin, the algorithms tested included MODIS visible wavelengths, (460 nm (Blue), 550 nm (Green) and 650 nm (Red)), and a three individual BTD algorithms from Ackerman (1997), Roskovensky and Liou (2003) and Miller (2003), which use a range of TIR bands (10.78 μm, 11.28 μm and 12.27 μm) and short wave IR (SWIR) (1.38 μm). TIR/SWIR algorithms performed better than both visible wavelengths and MODIS deep blue algorithm at clearly identifying emission source in each of the five cases studies. The dust enhancement product (DEP) from Miller *et al.* (2003) performed consistently well, visualising the data well and making it possible for the viewer to clearly identify the head of the dust plume (i.e. the deflating surface).

Using 5 years of MODIS DEP data (2001-2005), Walker *et al.* (2009) extracted dust source locations subjectively across the Middle East. DEP analysis was carried out in areas and days when local meteorological stations indicated reduced horizontal visibility at the surface. Quality of DEP imagery depends on the presence of cloud and the dust emission/satellite observation time offset, with only cloud free images of recently emitted dust plumes (where plume head is clearly visible) used for source detection. Despite this significant limitation,

results demonstrated that large layers of lofted dust (greater than 100 km in length) originate from multiple small-scale sources around 1-10 km^2.

In both SEVIRI and DEP analysis, subjective techniques are predominantly used to derive dust emissions manually (Schepanski *et al*., 2007; Baddock *et al*., 2009). These data can be applied to land surface characteristics, where the emission behaviour of those surfaces can be extrapolated to improve regional dust emission models (Walker *et al*., 2009).

3.2.3   Type 3 - Climate Aerosol Models

Coupled climate-aerosol models are an important tool in identifying dust emission surfaces, and simulating a regions dust fluxes and associated climate impact (Todd *et al*., 2008). Utilising a suite of land surface information from satellite retrievals, atlases and field based observations; these models apply knowledge gained on the emission thresholds of different land cover types to determine maps of erodible soils (Shao *et al*., 2002; see Section 2.3). These models simulate dust flux using a combination of multiple parameters, including vegetation cover, soil texture and land cover type, including landforms (Gherboudj *et al.*, 2017; Laurent *et al.*, 2006; Tegen and Fung, 1995; Walker *et al.*, 2009; Zender *et al.*, 2003). Meteorological data from either surface stations or re-analysis data are then used to determine seasonal dust fluxes at a regional scale.

Few models are directly configured on the basis of AOD emission data. These data are considered too coarse in spatial resolution and unrepresentative of land surface patterns or mesoscale meteorological events such as cold-pool density currents (Walker *et al*., 2009). Importantly, the accuracy of these models is dependent on the quality of the input data and our understanding of dust emission behaviour of each land characteristic unit (Liu *et al.*, 2007). Recent analysis has shown that large uncertainties exist in model estimates at both regional and global scales (Johnson *et al.*, 2011; Todd *et al.*, 2008). In analysis of the Met Office's Crisis Area Mesoscale (CAM) model, Johnson *et al*. (2011) noted that observations taken from the Geostationary Earth Radiation Budget Inter-comparison of Long-wave and Short-wave radiation (GERBILS) campaign were spatial separated from the model. They attributed this bias to poorly understood source locations, specifically the lack of information on preferential soil texture and geomorphological features. This factor was demonstrated by

Todd *et al*. (2008) when comparing multiple dust emission during a 3-day dust event over the Bodélé Depression, coinciding with the Bodélé Dust Experiment (BoDEx 2005, Washington *et al.*, 2006). Here, soil texture data indicated pure sand soils within the depression, failing to recognise the large range in particle size present in the diatomite soils. Consequently, the models only crudely represent the complex nature of dust emission from the ancient lakebed, with estimates of dust flux separated by a factor of 30 across five models. Furthermore, land surface characteristics are continuously changing, especially within anthropogenic land use areas (Tegen and Fung, 1995), this necessitates the constant updating of land surface data to remain relevant to current emission potential. Despite these limitations, Gherboudj *et al*. (2017) argue that simulations of dust emission surfaces, provide a better representation of surface conditions than satellite based aerosol products such as TOMS/OMI and MODIS (Section 3.2.1). They maintain that modelled data are independent of seasonal cloud conditions, contamination by other atmospheric aerosols and poor temporal resolution. It can be argued, however, that model skill can be improved by the inclusion of dust emission observations (Section 3.2.2). By including dust source information, determined by DEP dust source database (DSD) (Section 3.2.2), Walker *et al*. (2009) re-configured the erodible land index of the Coupled Ocean/Atmospheric Mesoscale Prediction System (COAMPS) model. Compared to the standard COAMPS model, configured with United States Geological Survey (USGS) land characteristics data, the DEP COAMPS model performed closer to observations, with the USGS model producing erroneous emissions from upwind areas. For this reason, there is a large demand for 'Type 2' dust emission data, as improved understanding of dust emission surfaces and their characteristics will fundamentally improve the accuracy of emission models.

3.2.4   Comparison and summary

MODIS and TOMS/OMI 'Type 1' style mapping carries distinct limitations originating in their temporal sampling rate. With a maximum of two images per day (1 for OMI), retrievals of dust plume position and composition can be affected by up to 21 hours transport from the original emission location time (maximum offset between Terra and Aqua MODIS satellites).

Recognising this, Ginoux *et al.* (2010) aimed to quantify the age of each dust plume by introducing a minimum particle size threshold, limiting the retrieval to plumes that contain

coarser particles only. Once emitted, dust plumes contain a large distribution of particle sizes that changes during transport, with the majority of the coarser particles removed by dry deposition within a matter of hours (Tegen and Fung, 1994). To acquire a measure of particle size within a plume/pixel, AOD measurements at 440 nm and 870 nm are compared using equation 1, extracting the Ångström exponent (α) particle size distribution (Klüser *et al.*, 2011).

$$\frac{AOD\ 0.44\ \mu m}{AOD\ 0.87\ \mu m} = \left(\frac{0.44\ \mu m}{0.87\ \mu m}\right)\alpha \qquad \text{(equation 1)}$$

Size distribution is inversely related to the value of α, thus the larger particle size mode, the smaller α (Kluser *et al.*, 2011). Ginoux *et al.* (2010) use an Ångström exponent threshold of less than α = 0.3. In theory, constraining α will limit the transport bias in the retrieval, with older (smaller α mode) plumes screened out, leaving only recently emitted dust (within a few hours before observation). These plumes are thought to represent dust emission source areas more accurately. However, a significant amount of time is still required for a plume to develop, before it is large enough to make a notable contribution to automated plots of global/regional AOD. During this time, advection will continue to remove plume horizontally from source area. Furthermore, the omission of finer mode α plumes could induces biases towards coarser sediment type source areas and sources downwind, which initiate emission near to observation time. Given the spatial and temporal variability of dust plumes (Kahn *et al.*, 2009), these limitations must be taken into consideration, especially when discussing global dust sources or assessing anthropogenic influence on dust emission (e.g. Ginoux *et al.*, 2012; see Section 2.2).

A comparison study by Schepanski *et al.* (2012) demonstrates how the different approaches used by 'Type 1' (AOD mapping) and 'Type 2' (dust emission observation) data produce a spatial offset in dust emission source. Focussing on North Africa, Type 1 data were represented by daily MODIS Deep Blue AOD and OMI AI data. Type 2 data were derived from subjective inspection of SEVIRI Dust RGB images at 15 minute temporal resolution, and marked on a 1°x1° dust source activation frequency (DSAF) grid. Analysis was performed with each data type from March 2006 to February 2010. Figure 3.2 shows that all data agree that the Bodélé depression in Western Chad is a frequent source of dust, with dust activation occurring in up to 40% of observations. Elsewhere, there appears to be a significant offset

between the different 'Types' of analysis, with MODIS and OMI data highlighting areas further south of the SEVIRI data. This offset can be explained by the transport element inherent in 'Type 1' analysis, which is much less significant in the high temporal resolution SEVIRI data. Here, the northerly Harmattan flow (described by Bou Karam *et al.*, 2010) is an important factor, driving the offset seen between the two 'Types' of data. These winds are consistently observed in ECMWF ERA interim wind field data, transporting the predominantly mid-morning emissions south of the SEVIRI source areas, where they are frequently observed over the Sahel regions by the time of MODIS (13:30 local time, MODIS Aqua) and OMI (13:45 local time) observations (Fig. 3.2).
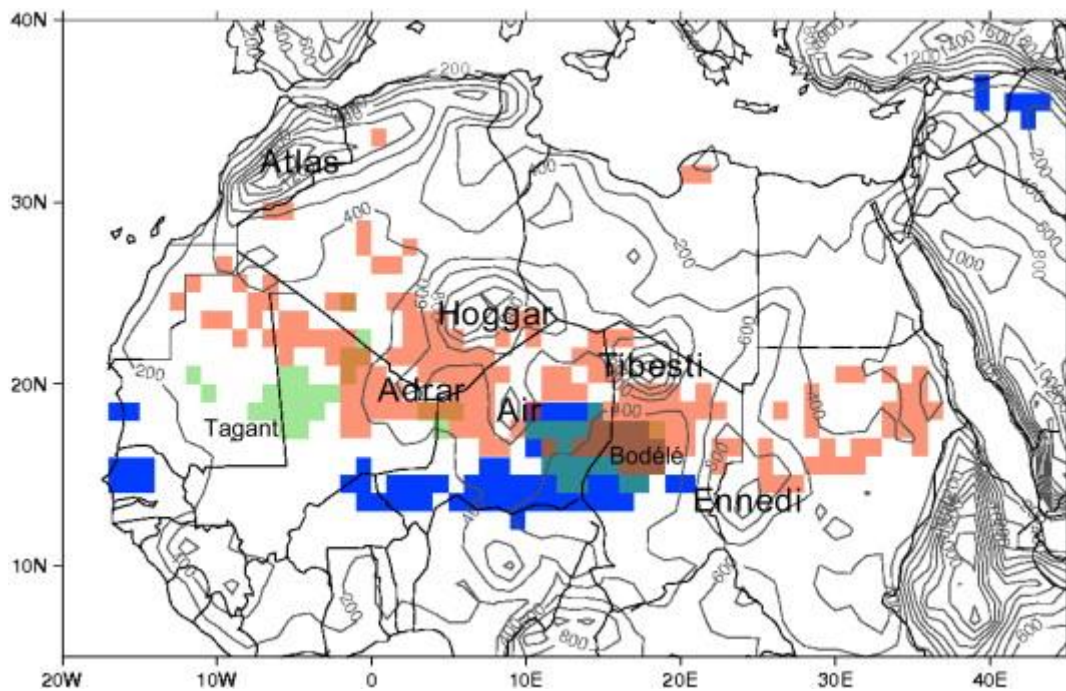
Figure 3.2: Product comparison showing dust emission frequency from SEVIRI, MODIS and OMI over North Africa (2006 -2010). Highlighted areas represent > 6% (SEVIRI (DSAF) – Red); > 40% (MODIS (AOT) – Blue); >40% (OMI (AI) – Green) (Source: Scepanski *et al.*, 2012).

In review of satellite data used to determine dust emission sources, three regularly applied method 'Types' have been identified. Analysis of these data and their applications can be summarised as follows:

- Observations of dust emission can be separated into two types, with Type 1 data produced by automated maps of persistent high areas of AOD, statistically derived from daily resolution polar orbiting satellites.

- Most significantly, Type 1 data provide an account of dust in the atmosphere only, they do not describe dust emission from the source, with areas of high AOD likely removed by time of emission/observation offset.

- Type 2 data are generated by subjective interpretation of dust emission data, taken during an emission event where the deflation surface can be identified at the head of emission plume.

- Type 2 analysis are performed with data at various temporal resolutions, with the 24-hour, high-temporal resolution (up to 15 minute) data from TIR geostationary data providing the best opportunity to observe emission at source.

- Satellite-based dust observations tend to rely on non-dynamic retrieval algorithms, which are required to work in all surface and atmospheric conditions. These data are susceptible to changes in surface brightness (Deep Blue), fine aerosol particles (TOMS/OMI) and high CWV conditions (SEVIRI). These limitations present a significant challenge when trying to develop robust automated emission detection algorithm, supporting the preferential use of a subjective approach, where human interpretation can overcome false positives in the data.

- Coupled climate-aerosol models provide the third Type of dust source analysis. Produced through the combination of land surface classification data and the application of wind speed deflation thresholds. These models provide a useful tool for applying empirically derived knowledge of land–atmospheric emission processes to predict probable dust emission surfaces and emission fluxes.

- Type 3 dust sources that do not use dust observation data are highly susceptible to poor or coarsely derived data on surface characteristics. The addition of more Type 2 data has proven to aid the development of model configurations and thus improve the accuracy of dust emission simulations.

- Comparisons between Type 1 (AOD) and Type 2 (emission) data has highlighted the transport offset of dust sources mapped using averaged plots of AOD, revealing a

significant improvement in dust source accuracy where high temporal resolution (SEVIRI) data are used.

To date, several global and regional studies have attempted to identify source locations in the Middle East (Table 3.1). So far, none of these studies has used SEVIRI dust RGB product to track dust plumes back to the point of first emission. As this product has proved very successful in monitoring dust sources in North Africa (Schepanski *et al*., 2012; Banks and Brindley, 2013; Ashpole and Washington, 2012), the aim of this study is to observe and locate the source of all identifiable dust emissions from the Middle East using the SEVIRI dust RGB data series (2006-2013).

3.3   SEVIRI – characteristics and applications

This section discusses the features of the SEVIRI dust RGB product, describing the technical specification (3.3.1), its performance against surface observations from the Aerosol Robotic Network AERONET (3.3.2), advantages and current applications (3.3.3) and known limitations (3.3.4).

3.3.1   Technical specification

Operating within the narrowband TIR wavelength (8.7 µm – 12.0 µm), the SEVIRI dust RGB product utilises the cooling anomaly created by mineral dust in the atmosphere. The use of these wavelengths is long established as a suitable method in which to extract the atmospheric dust signal (Ackerman, 1997; Volz, 1973). The signature drop in radiance is caused by a double effect on the net radiation of the atmosphere. Firstly, surface insolation is reduced by both the absorbing and scattering of short wave (SW) radiation by the dust layer above (Claquin *et al.*, 1998). The net reduction in surface insolation over land is determined by surface characteristics including albedo, soil moisture and vegetation (Wald *et al.*, 1998). Bare dark soils will experience the greatest reduction compared to clear sky conditions, with a drop of approximately 10 K observed during dusty conditions over parts of the Western Sahara (Legrand *et al.*, 2001). Secondly, the attenuated SW insolation emits as long wave (LW) terrestrial radiation, where it is strongly absorbed in the thermal wavelengths (8 – 12 µm) by the silicate material within the elevated dust plume (Klüser *et al.*, 2012). This absorption of both SW and LW radiation causes heating of the dust layer in the lower atmosphere, redirecting the energy flux from the top of the atmosphere and decreasing thermal emission by the surface (Dubovik *et al.*, 2002). The re-emitted energy (described as brightness temperature (BT)) from the dust layer is lower than that of the Earth surface BT below; creating the distinctive cooling effect relative to clear sky emission in the narrow thermal bands (Zhang and Christopher, 2003).
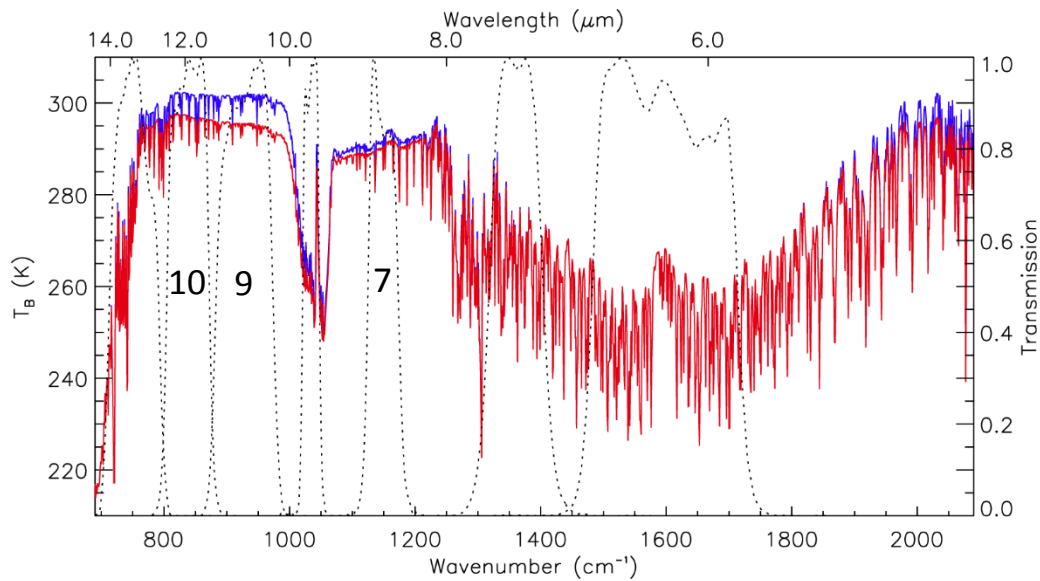
Figure 3.3: SEVIRI filter transmission functions in the mid-IR (4.5 – 14.5 μm) wavelengths (dashed black line); highlighting the three SEVIRI channels used: 7 (8.7 μm), 9 (10.8 μm) and 10 (12.0 μm). Simulated brightness temperature (T$_B$) over barren soils with clear skies (solid blue line) and dusty conditions (solid red line) are shown using mean June 2006 atmospheric profiles of Niamey (Niger). (Source: Brindley *et al.*, 2012).

In clear sky conditions, Figure 3.3 shows how emissions in the IR wavelengths (BT), are highest over desert surfaces in the 10.8 – 12.0 μm channels (Brindley *et al.,* 2012). Here, thermal emissivity peaks over desert surfaces (Sokolik, 2002). A comparison of BT shows both 10.8 μm (Ch.9) and 12.0 μm (Ch. 10) wavelength regions have a relatively greater thermal emissivity over desert surfaces than the 8.7 μm (Ch. 7) wavelength region (Schepanski *et al.,* 2007). In the presence of mineral dust (red line), a distinctive reduction in BT is clearly visible across these three channels, with maximum absorption around 10.8 μm (Fig. 3.3). Dust extraction with Dust RGB product is therefore performed by the comparison of BTDs within these three SEVIRI channels (Table 3.2) (Lensky and Rosenfeld, 2008). The use of multi-channel analysis helps to isolate dust aerosols from other (non-dust) atmospheric features, which could contaminate the IR signature in any individual channel (Ashpole and Washington, 2012).

Table 3.2: SEVIRI dust RGB product channel combinations and associated beam thresholds.

Beam	Channel	Measurement	Range
Red	12.0 μm (Ch. 10) – 10.8 μm (Ch.9)	BTD (K)	(Range -4 to 2 K)
Green	10.8 μm (Ch.9) – 8.7 μm (Ch.7)	BTD (K)	(Range 0 to 15 K)
Blue	10.8 μm (Ch. 9)	BT (K)	(Range 261 to 289 K)

The strength of each of the RGB signals are determined within a range of possible values (Table 3.2), with the red and green signals a function of BTDs between 10.8 μm (channel 9) and the adjacent channels (Ashpole and Washington, 2012). The blue signal is defined by the BT within a given range 261 – 289 K at 10.8 μm. Throughout normal daytime conditions, the surface BT at 10.8 μm will eventually exceed the 289 K threshold, saturating during both dusty and dust free conditions (Ashpole and Washington, 2012). Brindley *et al.* (2012) observed saturation in the blue signal (emissivity greater than 289 K) in 92% of midday observations from the Sahara.
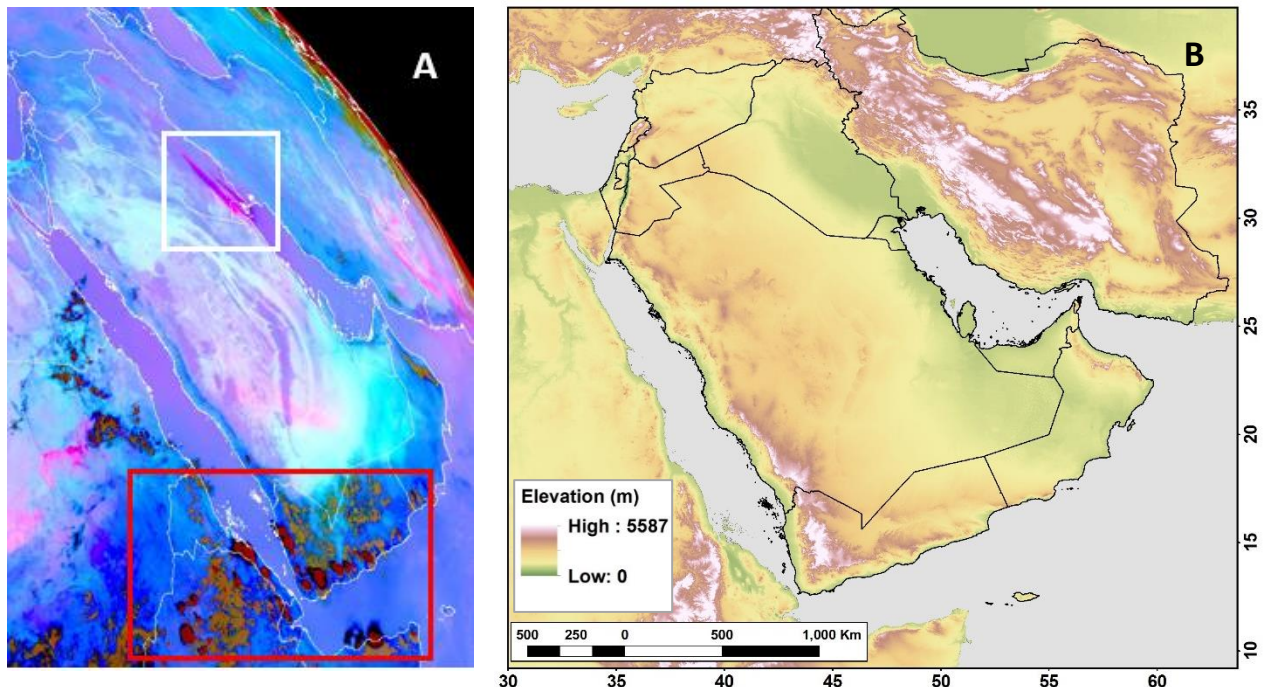
Figure 3.4: A) An example of SEVIRI dust RGB imagery used in this study (11/07/2006 - 11:00 UTC) Dust is shown with pink colours (white box), meteorological clouds show up as red or orange (red box). (Source EUMETSAT). B) The Middle East study region.

With the blue signal saturated, the daytime RGB output will only differ in the green and red signals, with strong red/weak green indicating dust contamination (which shows as pink in the RGB display) (Fig. 3.4). This pattern is a consequence of the 10.8 μm channel being suppressed more rapidly than the 8.7 μm and 12.0 μm channels (Fig. 3.4), decreasing ΔT_{BG} (10.8 μm − 8.7 μm), and increasing ΔT_{BR} (12.0 μm − 10.8 μm) (Brindley *et al*., 2012). More frequent atmospheric features such as cirrus clouds are distinguishable by red and orange colours as their opacity supresses surface emission, and their cold cloud top temperature combine to significantly reduce BT (10.8 μm), causing a decrease in blue and green signals while increasing red (Ashpole and Washington, 2012).

3.3.2   Comparison with AERONET

All remote sensing systems, including SEVIRI rely on measurements of either SW reflectance or LW emission from the Earth's surface and extraction of the atmospheric dust component can be susceptible to changes in land surface properties (Dubovik *et al*., 2002). It is therefore important to validate satellite-derived radiance with a network of ground based radiometers provided by the Aerosol Robotic Network (AERONET) (Holben *et al.*, 1998). The network uses radiance inversion algorithms to extract quantitative description of dust in the atmosphere (AOD) and particle size distribution (Holben *et al*., 1998; Dubovik *et al*., 2002), using ground based automated sun-photometers from over 100 sites (Banks *et al*., 2013);.

Dusty conditions are designated when AOD at 1.02 μm is greater than 0.2 and α is less than 0.6 (Dubovik *et al*., 2002). AOD from each AERONET site is deemed representative of a radius of 25 km^2 (Banks *et al*., 2013) while uncertainties are calculated to be between 0.01 and 0.02 (Holben *et al*., 1998).

Comparisons between SEVIRI dust RGB data and AERONET measurements were made during dusty and non-dusty conditions in North Africa by Ashpole and Washington (2012). The results appeared to be 'completely consistent' with what would be expected, as AOD increases, ΔT_{BR} increased, while ΔT_{BG} reduced in turn producing the signature pink hue in the pixels surrounding the AERONET site.

Schepanski *et al.* (2007) observed a r = 0.77 correlation coefficient between positive SEVIRI RGB and AERONET observations. Reduced visibility (<5000m) at seven meteorological

monitoring stations across the Sahara, coincide with dusty conditions observed in the SEVIRI Dust RGB imagery in 75% of cases analysed between March 2006 – February 2007. It must be acknowledged that the Dust RGB product does not offer a quantitative measure of actual dust load, instead it provides a suitable tool for observing and understanding dust source activation and is far more appropriate for this task than daily repeat, polar orbiting satellites or ground based optical sensors.

3.3.3   Advantages and recent applications

As outlined in Section 3.2.4, the greatest advantage of this platform is the high temporal resolution imagery it provides. In combination with the use of TIR wavelengths and a broad field of view (the entire Middle East region presented here, see Fig. 3.4), dust emission observations can be retrieved 24 hours a day, at the precise time and location of emission source (Schepanski *et al.*, 2012). Section 3.2.2 described the manual approach used by Schepanski *et al.* (2007) (and in subsequent papers: Schepanski *et al.*, 2009; 2012). Here, the high temporal resolution reduces the probability of atmospheric contamination, from either meteorological cloud or upwind dust emission; as multiple images provide greater information on dust plume evolution, allowing the viewer to make a correct assessment of emission source (see Section 3.5).

Throughout this chapter, attention has been paid to the contrasting approaches of manual and automated dust source retrievals. It can be argued that the Schepanski *et al.* (2009; 2012) approach, of manually backtracking dust emission through consecutive 15-minute images presents a number of challengers to the reproducibility of the results. Firstly, the time and data storage requirement in manually digitising each dust emission 'event', over an extended period, is considerable (35,040 images, from 105,120 individual wavelength images, per year). Secondly, the subjective nature of the approach may suffer from individual observer biases (Ashpole and Washington, 2012); especially during challenging atmospheric conditions (see Section 3.3.4).

Ashpole and Washington (2012) pioneered an automated algorithm based specifically on the Dust RGB product. Known as the SEVIRI Dust Flag (SDF); it was possible to extract 'pink dust' pixels from each image across the Sahara, for the summer months of 2005-2009. This was

achieved by applying thresholds to each of the RGB channels: ΔT_{BR} (red channel) greater than zero, ΔT_{BG} (green channel) less than 10 and blue channel BT greater than 285 K (Fig. 3.5).

While this approach produced results quickly, the automated algorithm is unable to determine the evolution of the dust plume, preferentially mapping evolved dust plumes, which are made of multiple smaller plumes that have moved some distance from source. Furthermore, with no quantitative value of dust AOD in this version of SEVIRI data, old 'multi-day' plumes which persist in topographic or synoptic depressions will be indistinguishable from newly emitted dust, overestimating those locations dust emitting contribution. This automated approach therefore negates the main advantage of the SEVIRI database, encompassing the same transport bias seen in 'Type 1' daily maps of AOD.
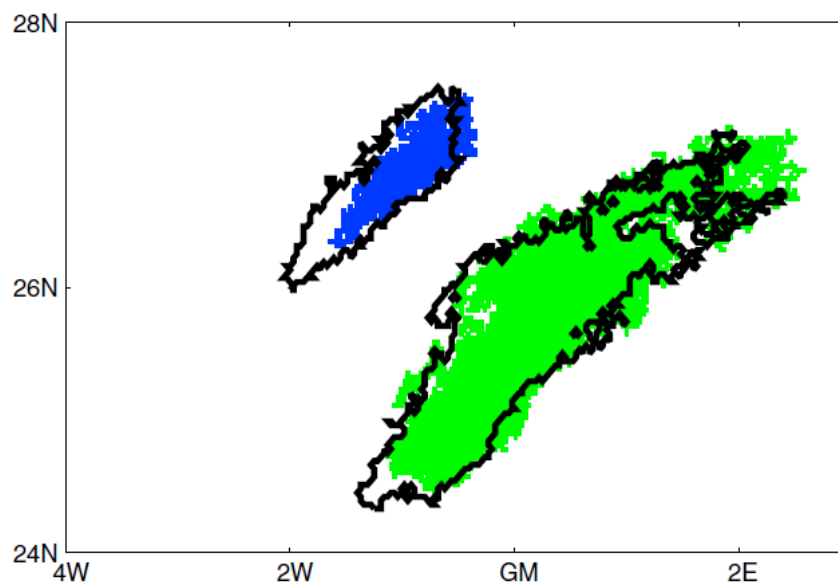
Figure 3.5: Illustration of Dust plume tracking algorithm over the Saharan Dessert. The example shows two distinct clusters of SDF pixels, representing dust plumes at consecutive time steps. The extent, shown by black outline represents the transport of the plume from the previous time step (shaded area). Source Ashpole and Washington (2013).

To improve the accuracy of the SDF algorithm, Ashpole and Washington (2013) applied an automated dust plume-tracking algorithm, in an attempt to replicate the manual back tracking process used by Schepanski *et al.* (2007). Identifying dust plumes by the clustering of pixels identified as dust by the standard SDF retrieval. Clusters are identified as a dust plume

when they exceed a threshold of 250 spatially connected pixels (approximately 0.5° x 0.5°). Plumes are then backtracked through their entire evolution through the preceding images by a cloud-tracking algorithm. This algorithm considers the spatial overlapping of a plume cluster, in the two adjacent time-steps, as the transport function (Fig. 3.5). A similar approach has been previously applied to track mesoscale convective cloud systems. Dust source is attributed to the area where plume extent (number of pixels) drops below the same minimum threshold. These source 'clusters' are averaged at pixel resolution (~0.03°), providing a high resolution plot of dust source locations, improving on the 1° spatial resolution used in Schepanski *et al*. (2007) manual dust source maps.

The use of the cloud-tracking algorithm provides an improvement on previous automated approaches; however, a transport bias is inherited by the use of a minimal threshold in determining source location. At the point that dust plume extent drops below the minimum threshold, the plume is likely to remain a distance downwind of discrete source area/s. The use of this threshold is a necessity, as the uncertainty in the SDF algorithm is greatest where the dust signal (thermal contrast to the surface) is weakest, this includes where the dust plume is close to the surface (emission source). Like many automated retrievals, the SDF method suffers from the dynamic BT signature of dust in the thermal IR wavelengths, especially over heterogeneous surface types of different emissivity and changes in atmospheric conditions (Section 3.3.4) (Brindley *et al*., 2012). These inconsistencies can prevent the clustering of sufficient SDF pixels, potentially creating a negative bias to dust emissions in unfavourable conditions. In each of these cases, human judgement is better at pattern recognition, compensating for inconsistencies in the RGB rendering and providing a more robust scheme for identifying precise dust source locations (Schepanski *et al*., 2012).

Ashpole and Washington (2013) compared the automated results with those from manual (Schepanski *et al*., 2007, 2009, 2012) back-tracking techniques. The largest difference was in the number of observations made, with the subjective approach recording nearly double that of the automated data. Spatial distribution of frequently emitting dust source areas were similar; however, the increased number of results demonstrates the improved accuracy of manual analysis, enabling the observer to differentiate multiple discrete emission surfaces within the automated 0.5° threshold area. Furthermore, the downgrading of the spatial resolution of the automated data, to the 1° grid data used in Schepanski *et al*. (2007)

potentially obscures the expected transport bias in the automated approach. Manual detection allows greater freedom in determining the spatial resolution of the final dust source plot, with the maximum resolution determined by the pixel size (3 km at nadir).

3.3.4   Limitations

As previous applications of the SEVRI dust RGB product have shown, the main challenges relate to the dynamic emissivity of the surface and atmospheric constituents across the TIR. These relate to climatic conditions including water vapour and cloud cover, diurnal temperature ranges and changing emissivity of different surface types observed in dust producing regions (Sokolik *et al.*, 2001).

Brindley *et al.*, (2012) aimed to analyse the performance of SEVIRI dust RGB imagery during variable dust and atmospheric conditions, with the aim to discover which conditions would make identification unlikely. Their analysis can be used to advise observers using the subjective method. SEVIRI dust RGB renderings were simulated using clear sky (non-dusty) mean temperature and dew point vertical profiles, calculated from radiosonde data over Niamey (Niger) (Fig. 3.6).   Importantly, atmospheric profiles of Niamey demonstrate a high seasonality in atmospheric moisture content, with the onset of the West Africa Monsoon between May and October, and dry north easterly Harmattan flow during non-monsoon months. These conditions are represented in the two-dimensional plots (Fig. 3.6), where a fourfold reduction in total atmospheric moisture content (CWV) is simulated between June (~40 mm) to December (~10 mm) (Figure 3.6a and 3.6b respectively). Differences in temperature profile are represented by early morning (05:30 UTC) and mid-morning (10:30 UTC) measurements, with a 5.2 K increase in surface temperature in the later profile. Increasing dust storm intensity is simulated by AOD (measured in the 10 μm range) levels, shown in 0.1 increments from 0 – 1. Referred to as τ_{10}, the simulated plume has a dust top height of 3 km and all particles are assumed to be spherical (Mie scattering), which is unlikely. Variability in surface emissivity, caused by different percentages of vegetation coverage were simulated at 0%, 50% and 100% in each simulation.

Due to high surface emissivity in the 10.8 μm channel during clear sky conditions, the blue signal (BT 10.8 μm) is assumed to reach saturation (289 K), with the RGB rendering a function of the relative strengths of just the red (ΔT_{BR} 10.8μm – 8.7μm) and green (ΔT_{BR} 12.0μm –

10.8μm) signals. The automated dust flagging criteria are defined by the dashed box, with the thresholds set by Ashpole and Washington (2012). These thresholds were built from subjective visual interpretation of the imagery and then applied to an automated retrieval technique (see Section 3.3.3).
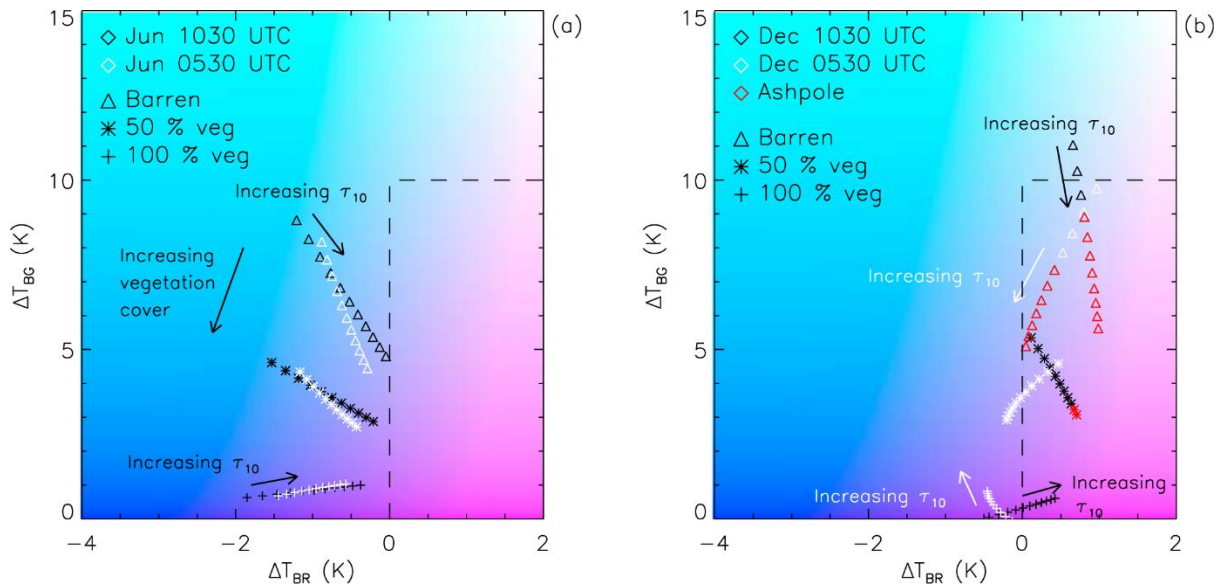
Figure 3.6: Two-dimensional graphical depiction of SEVIRI Dust RGB rendering, simulating the response to variations in AOD (τ_{10}), at different times of day over varying vegetation cover. Simulation assumes blue signal (BT 10.8 μm) is at saturation, with variations in RGB rendering defined by strength of red (ΔT_{BR} / 12.0μm – 10.8μm) and green (ΔT_{BG} / 10.8μm – 8.7μm) signals. Simulation based on clear sky atmospheric profile of Niamey (Niger) - see text for details. Monthly mean atmospheric profiles for (a) humid-June and (b) dry-December, demonstrate variations in humidity. Dashed box indicates Ashpole and Washington (2012) automated dust-flag thresholds with the red symbols calculated against 15-day rolling mean clear sky ΔT_{BG} data. Source: Brindley *et al.* (2012).

3.3.4.1 Evaluation of SEVIRI dust RGB – Variations in humidity and temperature

The position within the RGB rendering of all AOD retrievals (independent of time of day and vegetation coverage) is evidently different between seasons in Figure 3.6. The reduction in CWV, described in the December simulation (Fig. 3.6b) is represented by a significant shift in the observations into the pink area of the ΔT_{BG} (10.8μm – 8.7μm) and ΔT_{BR} (12.0μm – 10.8μm) plot and within the Ashpole and Washington (2012) threshold. This effect is a function of the

dominating absorptive characteristic of CWV in the TIR (Hsu *et al.*, 2004), significantly reducing ΔT_{BR} / 12.0μm – 10.8μm in all (dusty/clear sky) conditions. This is a crucial factor during periods of increased humidity, but also in dust storms associated with moist convection, such as mesoscale convective systems (Knippertz and Todd, 2010: see Section 2.5). Comparisons with AERONET observations demonstrated that dusty pixels, adjacent or mixed with cloud cover were undetected by automated dust storm recognition algorithms (Ashpole and Washington, 2012). Importantly, dust detection was invariably undetectable in several time steps (15 minute) prior to and following the passing of the cloud. The presence of cloud appears to not only mask the dust plume but also alters the atmospheric moisture content, altering the IR signal of that specific pixel and inhibiting the distinctive cool anomaly required to identify dust.

Comparison between early and late morning simulations demonstrate the impact of temperature variability, with BTDs for each τ_{10} step reduced in the cooler 05:30 UTC simulations. Temperature variations have the greatest effect on 8.7μm BT, with warmer temperatures increasing the 8.7μm BT more rapidly than the rest of TIR. This results in a larger decrease in ΔT_{BG}, relative to ΔT_{BR} in the later morning simulations, distinguishing dust more readily in its characteristic pink hue.

AOD simulations (τ_{10} increments) are distributed over a greater range in the 10:30 (UTC) time steps. Here, enhanced lower tropospheric lapse rates (compared to temperature inversion frequently observed at 05:30 UTC) maintain a cooler air temperature at dust plume top (3 km), relative to the surface. This increases the temperature contrast of the elevated dust plume to the surface, causing an increase in both ΔT_{BG} and ΔT_{BR} with each increment of τ_{10}, extending the simulations closer to the pink dust threshold.

The 'cool anomaly', commonly experienced during daytime conditions is frequently inverted during the night. With the cessation of solar insolation, the dust layer quickly becomes an insulator of surface BT, increasing the downward long-wave energy flux and reducing the thermal contrast seen in daytime conditions (Ashpole and Washington, 2012). Under clear sky conditions, lower night time skin surface temperatures reduce the BT at 10.8 μm, resulting in an inversion of ΔT_{BG} and ΔT_{BR} relative signal strengths (Fig. 3.7). Furthermore, reduction in 10.8 μm BT will result in a less than saturated blue signal, giving much of the bare surfaces

the same spectral response as daytime dusty conditions. Currently, the Ashpole and Washington (2012) automated algorithm does not alter its dust flagging thresholds for night-time conditions. Relaxing the thresholds will only induce more false positives, while the inversion from day-time spectral signature will result in negligible returns should the thresholds be tightened. This automated issue is systematic of the dynamic radiative properties of dust over a range of atmospheric conditions, represented in only a 31% agreement between manual and automated positive-dust flags.
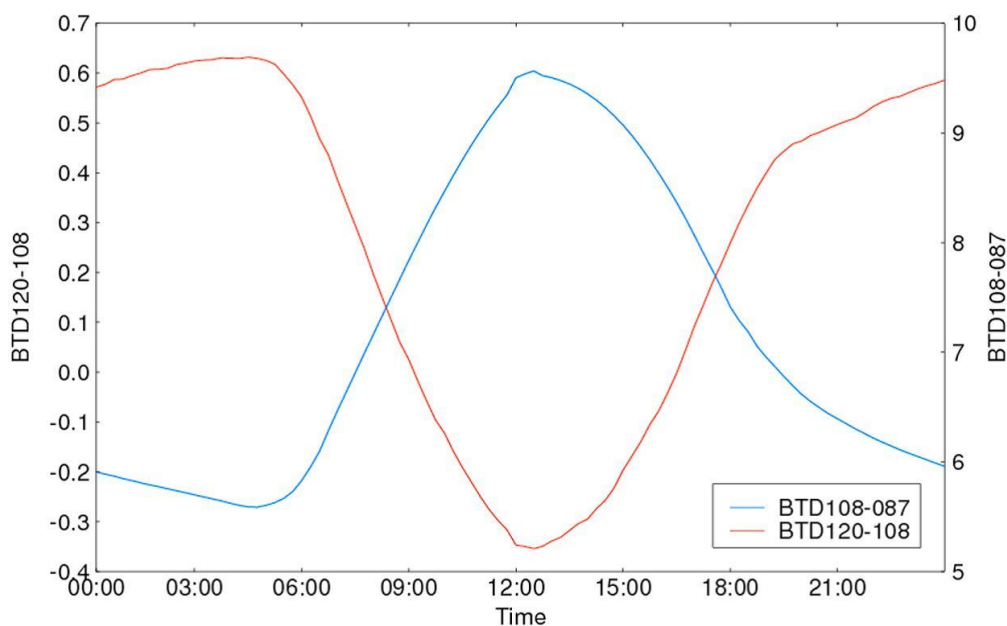
Figure 3.7: Variable signal strength of clear sky SEVIRI red (12.0 – 10.8 μm) and green (10.8 - 8.7 μm) BTD's signals during diurnal cycle, averaged during a 15 day period over Western Saharan region (green signal = blue line here). Source Ashpole and Washington (2012).

3.3.4.2 Evaluation of SEVIRI dust RGB – Land cover changes

During less-humid conditions (Fig. 3.6b), low AOD dust plumes (minimal τ_{10}) are also identified as dust in the Ashpole and Washington (2012) automated thresholds. The low sensitivity to AOD increases the probability of false-positive detection, especially over heterogeneous land surfaces, where surface emissivity (and thus BTD) can varying considerably around the 8.7 μm wavelengths in arid environments (Fig. 3.8). Over dark bare surfaces, such as rocky outcrops and ancient lava flows of Libya and Saudi Arabia (white boxes), 8.7 μm BT is greater than the surrounding sand or sediment surfaces (Seemann *et al.*, 2008). This decreases the clear sky

ΔT_{BG} (10.8 − 8.7 µm), mimicking the dust signal in the RGB renderings and creating a false positive in the retrieval. To ameliorate false-positive detection, Ashpole and Washington (2013) applied a 15-day rolling-mean clear sky ΔT_{BG} (10.8 − 8.7 µm) filter to each pixel. The ΔT_{BG} filter value is subtracted from the retrieval, with only pixels that return values less than -2 considered being representative of atmospheric dust. This filter was applied to the December simulation (red symbols, Fig. 3.6b), demonstrating the necessity of up-to-date surface emission data (15-day rolling mean), highlighting only the dust plumes of significant τ_{10} and omitting the lighter dust loadings (white and black symbols).
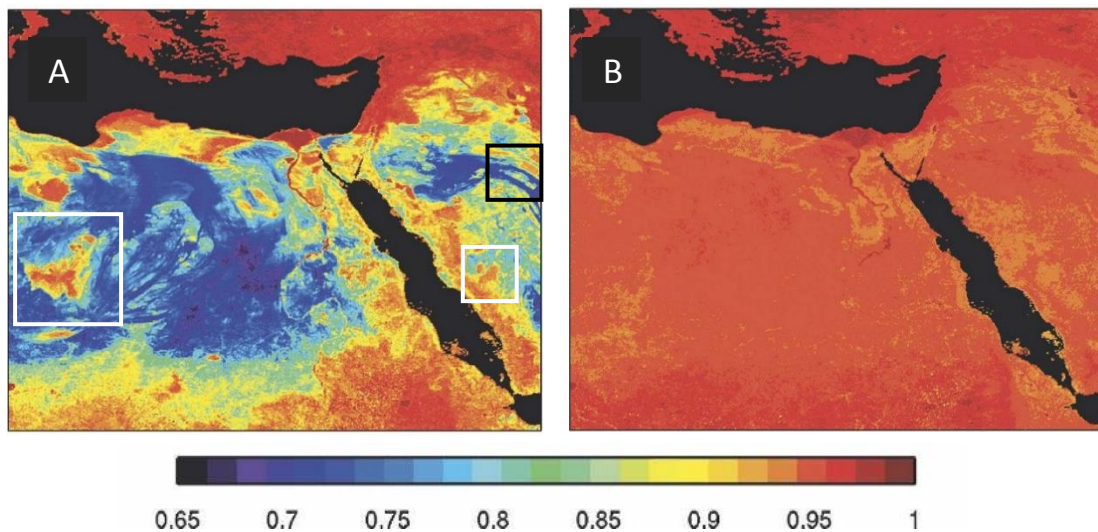
Figure 3.8: Surface emissivity of north east Africa and the Arabian Peninsula derived from the MODIS spacecraft at two thermal IR channels (a) 8.3 *µ*m and (b) 10.8 *µ*m. Black square shows the northern areas of the Ad Dahna Sand Sea. Source: Seeman *et al.* (2008).

Importantly, subjective analysis must also take into consideration this enhancement of the dust signal, especially in regions located close to transition surfaces like the Ad Dahna Sand Sea in Central Saudi Arabia (black square, Fig. 3.8). Here, the use of sequential images is key to understanding the evolution of the dust plume, with human judgement and consideration of known dust RGB limitations offering a distinct advantage to subjective analysis (Schepanski *et al*., 2007).

Increasing vegetation density is shown to increase surface emissivity across the TIR wavelengths, especially in 8.7µm channel (Fig. 3.9). This culminates in a reduction in both

ΔT_{BG} and ΔT_{BR} signals, affecting the greatest drop in ΔT_{BG} (10.8 μm – 8.7 μm) (Fig. 3.6). As τ_{10} increases, the vegetation influence reduces, bringing all three vegetation emission values closer together in both ΔT_{BG} and ΔT_{BR}. These trends are independent of variations in humidity with the pattern replicated in both June and September simulations. In the simulations, there is little difference in the relative 'pinkness' of each vegetation type, resulting in minimal impact on subjective analysis.
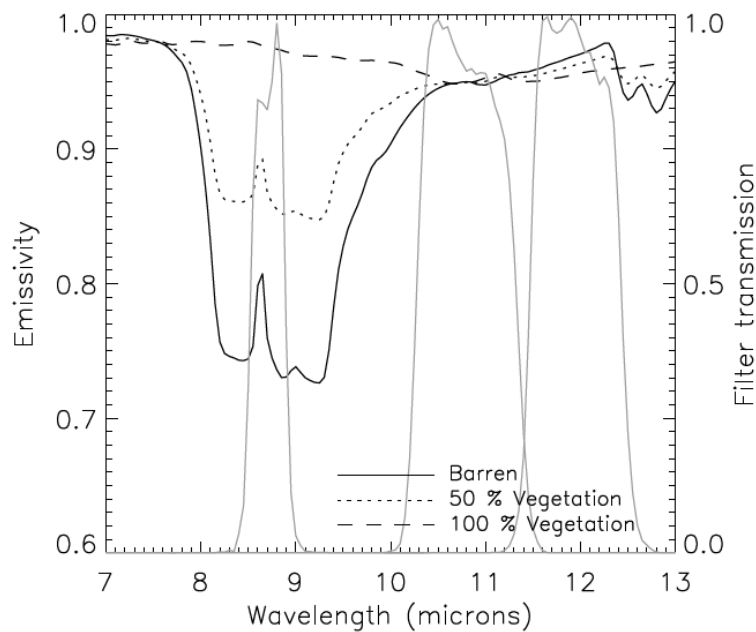
Figure 3.9: Simulated spectral surface emissivity of variable vegetation cover in the TIR. Superimposed over the SEVIRI filter transmission windows of the channels used in the Dust RGB product. Source Brindley *et al*. (2012).

3.3.4.3 Evaluation of SEVIRI dust RGB – Viewing zenith angle

Over the Middle East the viewing zenith angle (θ_v) of the SEVIRI sensor ranges from 45° to 75°. As the θ_v increases further from nadir, both the pixel footprint and the path length increasingly expand. Pixel resolution increases from 3 km at nadir to over 5 km at the highest θv, while the increased path length increase the atmospheric contamination. The increased atmospheric path length amplifies the influence of CWV (Fig. 3.10), creating the largest divergence in spectral response during the humid June simulation. Consequently, with no data on atmospheric state, specifically CWV, observations made in the Middle East and

especially in Eastern Iran will be more susceptible to atmospheric state, accordingly, observations from these areas will carry greater ambiguity.
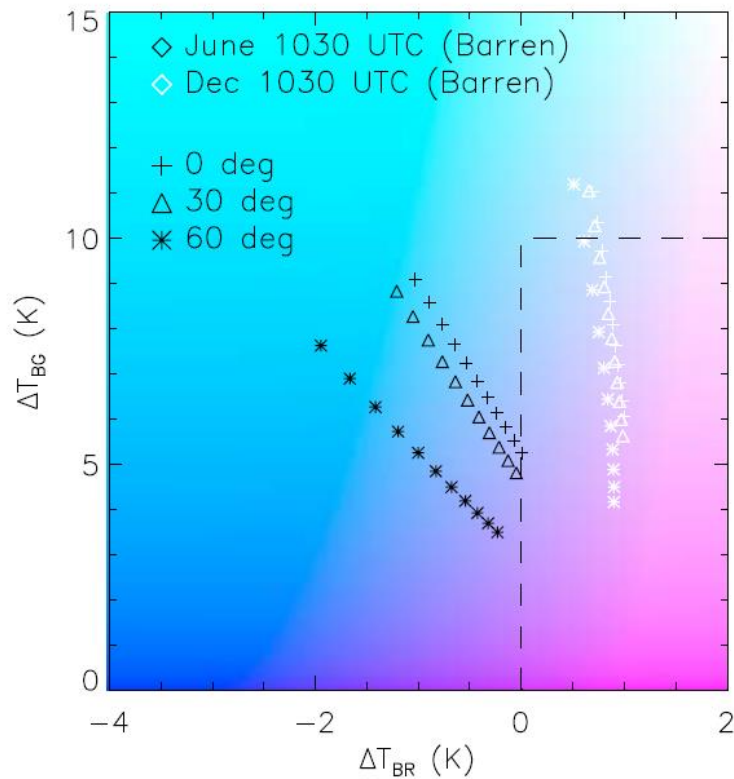
Figure 3.10: Sensitivity analysis of Dust RGB rendering with regard to viewing zenith angle over barren soil during June and December conditions typical of Niamey, Niger. Source: Brindley *et al*., 2012

3.2.4.4 Limitations synthesis

A comprehensive analysis of the SEVIRI dust RGB product by Brindley *et al*. (2012) has demonstrated the key limitations inherent in observing within the TIR wavelengths 8.7 µm – 12.0 µm), these can be summarised as follows:

- Absorption in the TIR by water vapour dominates the spectral response, reducing the cooling trend normally presented by atmospheric dust. This anomaly is especially effective at the longer 10.8 µm and 12.0 µm channels, significantly reducing the red (ΔT_{BR}, 12.0 µm – 10.8 µm) signal, providing the greatest challenge to accurately identifying dust in the RGB rendering.

- Diurnal temperature variability produces differential alterations to the BTs of the three channels used in the RGB rendering. During dusty conditions, the greatest impact is seen at shorter wavelengths, with reduced temperatures in the early morning increasing the green (ΔT_{BG}, 10.8 μm – 8.7 μm) signal away from the recognised pink rendering of the RGB image.

- Clear sky conditions at night can produce an inversion of daytime red and green signal strengths, with the emissivity signature of dark surfaces mimicking the high red / low green signal strengths pertinent to dusty pixels.

- Rocky surfaces, including dark basalt of ancient lava flows emit strongly at the shorter TIR wavelengths, reducing ΔT_{BG} (10.8 μm – 8.7 μm) compared to the more restrictive emissivity of soils surfaces. Dust emissions over dark surfaces therefore produce a stronger pink rendering than those over fine sediment surfaces.

- Increasing AOD produces stronger pink signal, while vegetation density alters surface emissivity, particularly at 8.7 μm. However, the relative pinkness of the RGB rendering remains relatively consistent across all vegetation densities.

- Large viewing angles over the Middle East (45° to 75°) increase the spatial extent of pixel footprint from 3 km (nadir) to >5 km. Importantly, the increased path length from source to sensor increases the influence of atmospheric CWV, showing greater variability in RGB rendering in more humid atmospheres.

3.4   Middle East dust source inventory 2006 - 2013

In this project, dust emissions sources over the Middle East are manually located by subjective analysis of SEVIRI dust RGB images (Lensky and Rosenfeld, 2008). A full description of the data can be found in Sections 3.2.2 and 3.3.1. Data were provided by Imperial College London and processed on IDL software to the required channel combinations and thresholds, developed by EUMETSAT, to construct the dust RGB colour composite imagery (Table 3.2). Due to data acquisition problems, the years 2008 and 2009 were only available at a 30-minute temporal resolution, all other data were available at 15 minute intervals.

This inventory will describe the dust climatology of the region from January 2006 to December 2013, as defined by images at 15 min (2006-2007; 2010-2013) and 30 min (2008-2009) temporal resolutions. The subjective method follows that of Schepanski *et al*. (2007; 2009; 2012) over North Africa, whereby images are viewed consecutively to identify lofted aerosol dust emissions, and then backtracked through consecutive images to the point and time where it is first visible in the imagery. In an improvement of the Schepanki *et al*. (2007; 2009; 2012) method, each discrete dust emission (referred to as a 'dust event') are continuously monitored through plume evolution, characterising each event with the duration of emission and trajectory from source. Furthermore, dust sources will be located at the full spatial resolution available of 0.03°, providing a higher accuracy than the 1° DSAF map of Schepanksi *et al*. (2007). This represents the first time that this method has been applied to the Middle East.

Results are presented as a gridded map - with cubic convolution resampling applied, using Arc GIS 10.1 software, whereby dust events are binned into an appropriate spatial scale (maximum 0.25°) for each analysis. In addition to a record of dust events, the inventory will also include monthly and annual records of dusty days, defined by the number of days with at least one observed dust event.

Regional analysis is completed by the separation of the inventory into sub-regions, defined by a combination of the spatial distribution of dust emissions, natural geographic boundaries (i.e. mountain ranges, drainage basins desert areas) and distinctions made in literature. Analysis at a regional scale will help to define the different land surface and synoptic characteristics associated with dust emission across the Middle East.

Discrete source areas of frequent dust activity (hot spots) will be defined in the results and studied in greater depth, paying particular attention to land surface characteristics (see Section 3.6).

3.4.1 *Characterisation of uncertainty – degree of confidence*

Subjectively retrieved dust source locations contain a certain level of ambiguity, especially in conditions where the rendering of the dust signal becomes difficult, such as in the presence of meteorological clouds, high atmospheric water vapour, diurnal surface temperature ranges and high viewing zenith angles (Brindley *et al*. 2012). To take account of these ambiguities, a degree of confidence (DOC) is attributed to each dust emission event (Fig. 3.11). The uncertainty is evaluated on a scale from 1 to 3 (1 = high confidence to 3 = lowest confidence) and recorded alongside the registered emission events.

Level 1

Level 1-dust events occur where there is zero cloud cover; Figure 3.11 shows three individual dust plumes over Tigris Euphrates basin in Iraq, generated from individual source areas. The image shown is taken several hours (time steps) after first observation.

Level 2

Level 2-dust events describe moderate cloud conditions in the proximity of dust emission. These type of events are defined by the presence of cloud down-wind of emission source with clear sky conditions up-wind. Here, the deflating surface should be visible during the hour prior and after dust emission. In these conditions, the potential for increased CWV in the proximity to the dust emission sites have the potential to influence the RGB signal and thus the accuracy of the subjective analysis (see Section 3.3.4). With this in mind, dust emissions from coastal source areas are attributed level 2 (DOC), where dust emissions are predominately generated by onshore flows (indicated by trajectory of emanating dust plume).

Despite these limitations, these data are still considered representative of dust emission and are factored in all analysis without distinction. In Figure 3.11, dust emission from the North West Iraq can be seen in the wake of bank of cloud (red and orange features). Level 2

confidence can also apply to emission during night time hours, where atmospheric temperature inversion and reduced skin temperature reduce the BTD across the SEVIRI thermal range, reducing the pinkness of atmospheric dust (see Section 3.3.4.1). All dust emission observations made in the eastern reaches of Iran (e.g. Sistan Basin) are given Level 2 confidence due to the high viewing zenith angles and increased atmospheric path length, increasing the influence of variability in atmospheric state (see Section 3.3.4.3).
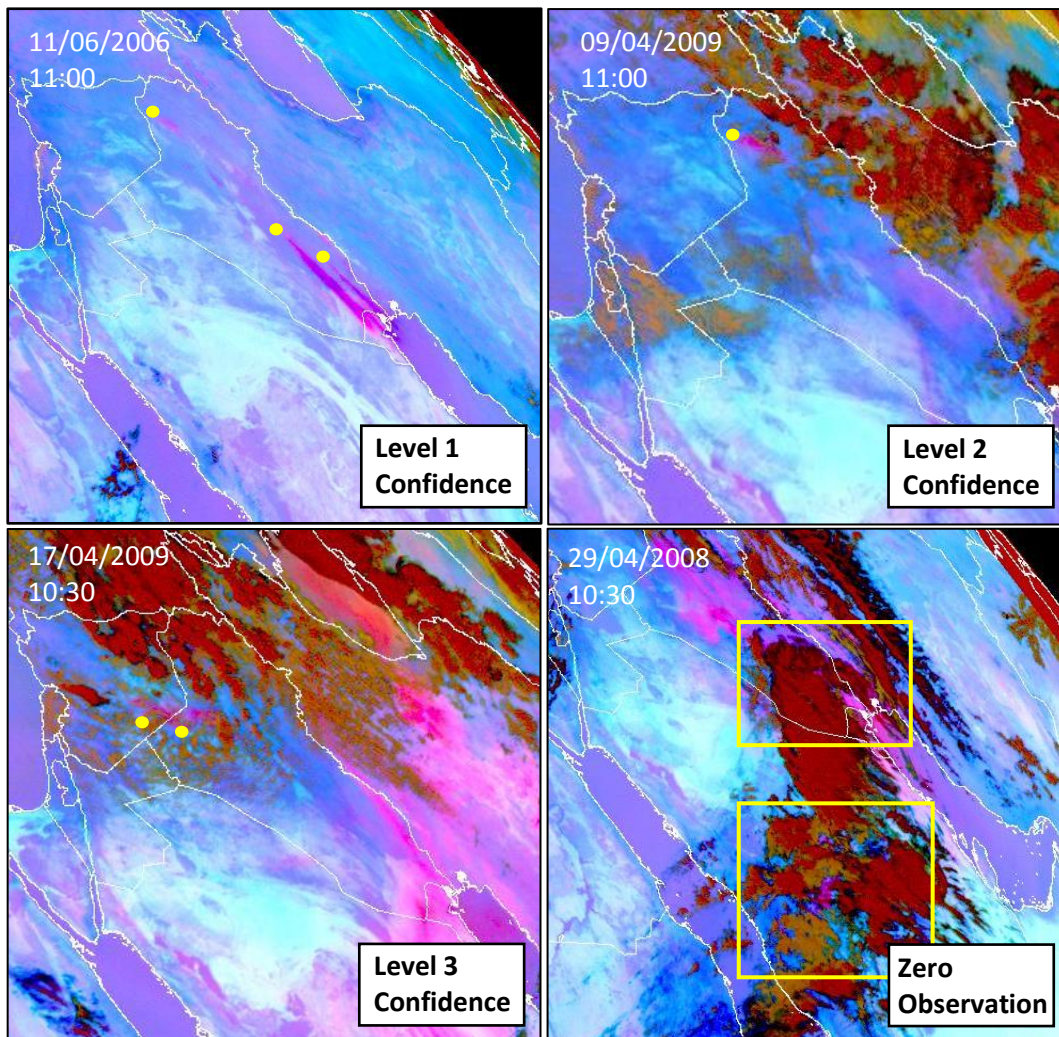
Figure 3.11: Examples of SEVIRI dust RGB imagery where dust emission surfaces (yellow circle) are observed at different degrees of confidence (DOC). DOC determined by cloud conditions – see text for full description of level criteria (Section 3.4.1).

Level 3

Level 3-dust events describe dust emissions which occur within/under sufficiently thin banks of cloud where emission surface is visible at the moment of dust emission. These type of events will typically have meterological cloud up-wind and down-wind of emission source. Determination of these emissions are only possible through careful inspection of dust emission evolution through the backward and forward tracking of plume in sequential images. An example of these conditions is shown in Figure 3.11, where emission sources are detected on either side of the Iraq/Syria border within a discontinuous layer of cloud to the south of heavy cloud. Due to the reduced confidence of these dust source observations, their contribution is only considered in regional source area frequency analysis and are omitted from precise surface feature analyses.

Beyond Level 3

Should an observed dust plume fail to meet the criterion of level 3 confidence, then it will be omitted from the dust source inventory. Such events includes (i) dust emerging under a large convective system or active front, and (ii) blowing dust that appears into the study area from an outside source (i.e. North Africa).

3.4.2 SEVIRI dust source inventory - Summary

The methodology detailed above is expected to produce: (i) an accurate database, locating all the observable dust emission sources, throughout the Middle East over the entire study period of 2006-2013. Identifying features about each event, including time of emission and duration and trajectory after emission. (ii) A robust method by which to monitor dust sources using SEVIRI, taking into consideration the challenges of identifying dust in the thermal infrared discussed above, and applying a degree of confidence to each recorded emission event.

3.5   Error analysis

To evaluate the uncertainty from using less frequent imagery, a further study was carried out where subjective analysis of 2006 data was completed at three different temporal resolutions (15 minutes, 30 minutes and 60 minutes). Due to the large data storage requirements of monitoring data at a 15-minute temporal (approximately 35,000 images per year), this analysis provided an opportunity to critically assess the impact of using lower temporal resolutions on the results. This was necessary because data for 2008 and 2009 were only available at 30 minute intervals.

Each dataset is completed following the same methodology (see Section 3.4), with the results described in Section 3.5.1 and discussed in Section 3.5.2. Unlike the dust source inventory, results are plotted on a 0.5° grid to aid visual comparison. To avoid bias in observations, the operator trained on 6 months of data prior to the compilation of the data set, these earlier data are not included in the results. The analysis will help in planning future work with this method, demonstrating the relative accuracy associated with each frequency of observation.

3.5.1   Frequency analysis – results

The monthly results (Fig. 3.12), shows a reduction in the total number of dust events with each step decrease in temporal resolution. Dropping the resolution from 15 minute to hourly data reduces the total number of events by 50%. 30 minute observations recorded 17% fewer events than the 15 minute data. Differences in observations vary considerably by season, with JJA showing both the peak and the greatest divergence in dust activity across all resolutions. Here, the number of dust events reduced by 34% and 64% when using SEVIRI at the 30 minute and hourly time steps instead of 15 minute time steps. Observations converge during autumn months (SON) and Winter months (JFD). The 15 minute and 30 minute data is relatively consistent through the spring months (MAM) while the hourly data records a significant decrease (45% reduction (15 minute – hourly). The monthly peak in dust events occurred during July in all three resolutions, but predictably mimicking the seasonal trend, with different recorded frequencies: 492, 316 and 195 events at 15 minute, 30 minute and hourly intervals respectively. June produced the highest percentage of dust days in both sub-hourly results (100% and 97% respectively); hourly observations saw a peak dusty days in July (87%).
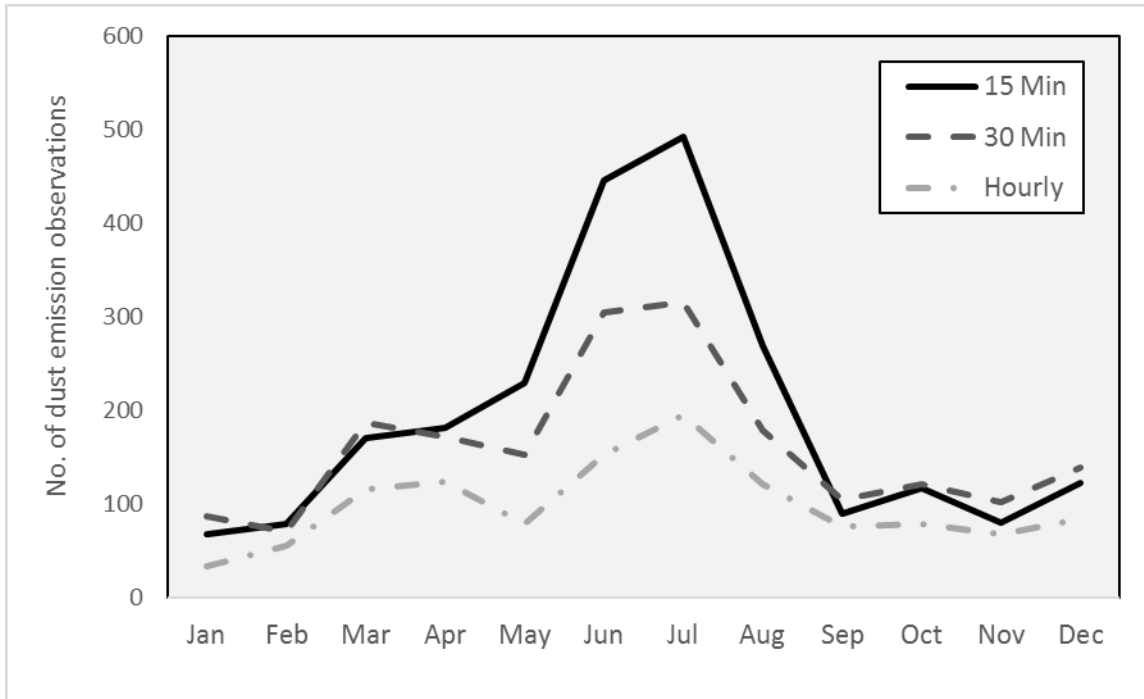
Figure 3.12: Comparison of 2006 dust emission events (per month) in the Middle East recorded using SEVIRI dust RGB data with 15 minute, 30 minute and hourly temporal resolution.

The use of three different time steps affects spatial statistics of the detected dust sources, specifically when an hourly time step is used. Figure 3.13 shows the spatial distribution and emission frequency of dust emissions sources across all three datasets (indicated by number of dust event within a 0.5° x 0.5° grid cell). Both sub-hourly data are largely in agreement, with the significant difference shown in the hourly data, especially at the coast lines of the Arabian and Red Seas (red outline) where, in contrast to the 15 minute and 30 minute data, the hourly data fails to highlight these areas as a source entirely.

In all three datasets, four large clusters of frequent dust activity emerge, but with different emission frequencies, reducing significantly in the hourly time step. These include: the northern reaches of upper Mesopotamia, on the border of Iraq and Syria (35 - 36°N; 40 - 42°E); in lower Mesopotamia, at the confluence of the Tigris and Euphrates rivers (30 - 32°N; 43 – 46°E); at the piedmont of the Asir Mountains in central Saudi Arabia (20 -22°N; 42 - 43.5°E); and the Sistan Basin in eastern Iran (30 -31.5°N; 61 - 62°E).
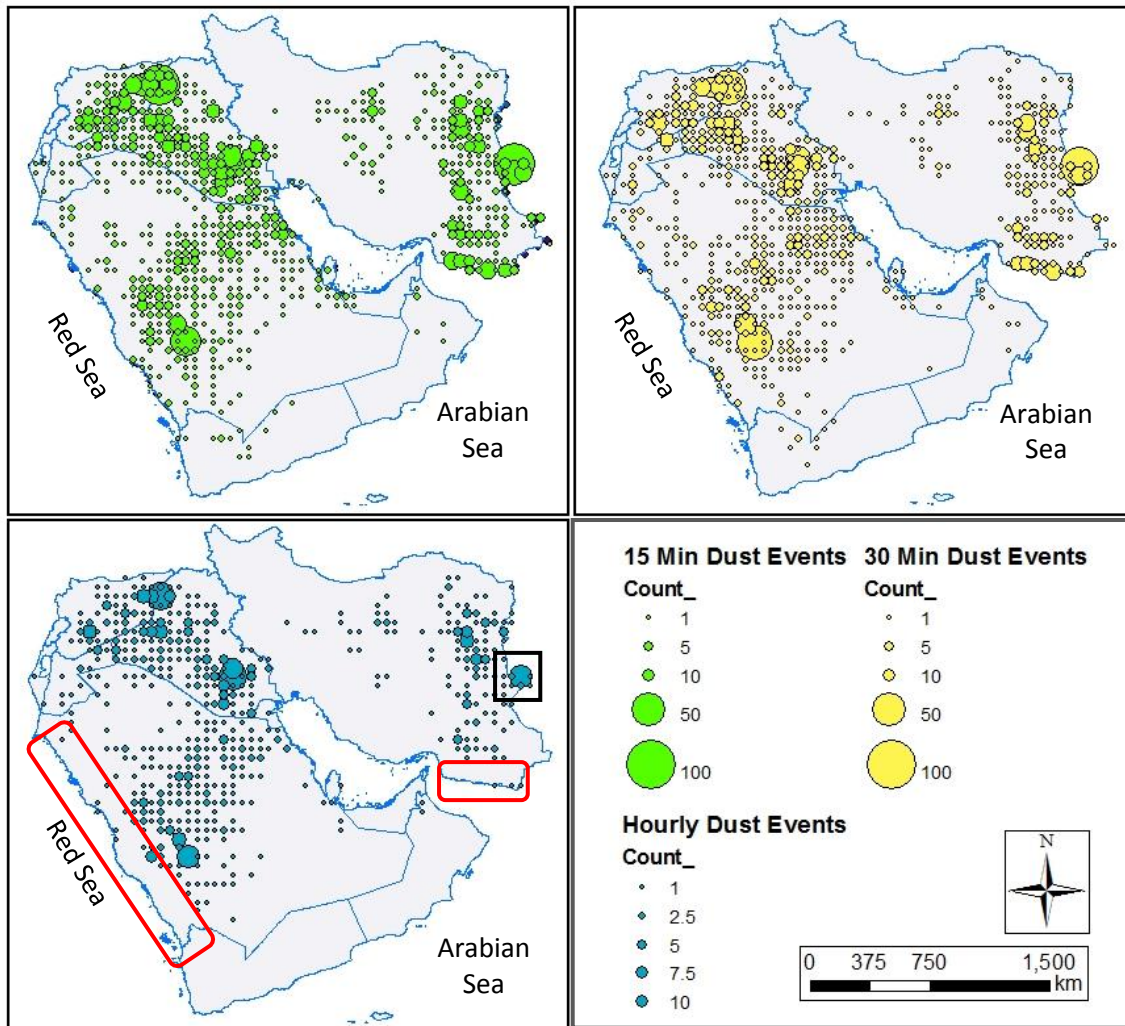
Figure 3.13: Spatial distribution comparison of SEVIRI dust emission sources at 15 minute (green), 30 minute (yellow) and hourly (blue) temporal resolutions. Observations are binned into 0.5° x 0.5° grid; circle size represents count of observations made within the grid cell it is centred within.

3.5.2   *Frequency analysis – discussion*

The difference in number of dust emission events observed across the three temporal resolutions is due to three critical factors. These are (i) spatial distribution of sources, (ii) time of emission, and (iii) seasonal cloud conditions.

Spatial distribution

A large proportion of the dust emissions are concentrated into a few 0.5° grid cells in all three data sets (Fig 3.13). In total, 849 grid squares register at least 1 dust event in each of the three frequencies, accounting for 41% (2.1 million km^2) of all land surfaces within the Middle East.

However, the concentration of events means that 51 % of all dust sources occur within only 6 % (0.28 million km^2) of the total land area. This clustering of source areas is typical of dust emitting landscapes in drylands, representing the preferential accumulation of fine sediments within fluvial channels and ephemeral and / or seasonal lakes (Bullard *et al.*, 2011) (see Section 2.4). With most dust sources emitting in small zones of deflation, the probability of downwind sources being obscured by an upwind-derived dust plumes are increased.

Figure 3.14 illustrates the clustering of dust sources within a dust source area at the commencement of a dust storm and demonstrates how the number of recognised dust emission events changes when observing at three different temporal resolutions (15 min, 30 min, 1 hour). Each Tn represents a 15 minute time step (the highest temporal resolution available), within a 60 minute observation window. At hourly resolution, only T1 and T5 would be observable; 30 minute resolution observes T1, T3 and T5; 15 minute resolution observes all images.

Large dust storms are typically created by the contributing emission from multiple discrete point dust sources (Mahowald *et al.*, 2003). Figure 3.14 schematically represents a typical dust source area, with several discrete emission sources. Surface deflation will commence as the north-westerly winds exceed a surface cohesion threshold of wind speed. In this example, all point sources are assumed to have the same wind speed threshold. At T1, wind speed does not exceed surface threshold across the region, with no dust emission and zero dust events observed at each temporal resolution. As wind speeds increase in the north west of the region (T2), the two most north westerly point sources (S1 and S2) start to deflate and are observed in the 15 minute dataset. Each source is distinguished by the point (red circle) most upwind of the emission cone (brown triangle), neither are obscured by atmospheric dust at this time (T2). At T3, the high north westerly winds have propagated south east and initiated dust emission at point source S3, to the east of the source area. This is observed in both sub-hourly resolutions, with the 30 minute resolution observing S1 for the first time. Emission from S2 is now obscured by atmospheric dust emanating upwind form S1 and is not recorded in the 30 minute results. At T4, no new sources are visible, while dust propagating from S1 now visibly obscures S2 and S3. T5 signifies the first image at hourly resolution that includes dust. With S2 and S3 obscured, hourly resolution only records one point source for entire region and hour of observation.

Temporal Resolution	Number of Dust Events observed		
	15 Minute	**30 Minute**	**Hourly**
T1	0	0	0
T2	2	No Image	No Image
T3	1	2	No Image
T4	0	No Image	No Image
T5	0	0	1
Total	**3**	**2**	**1**
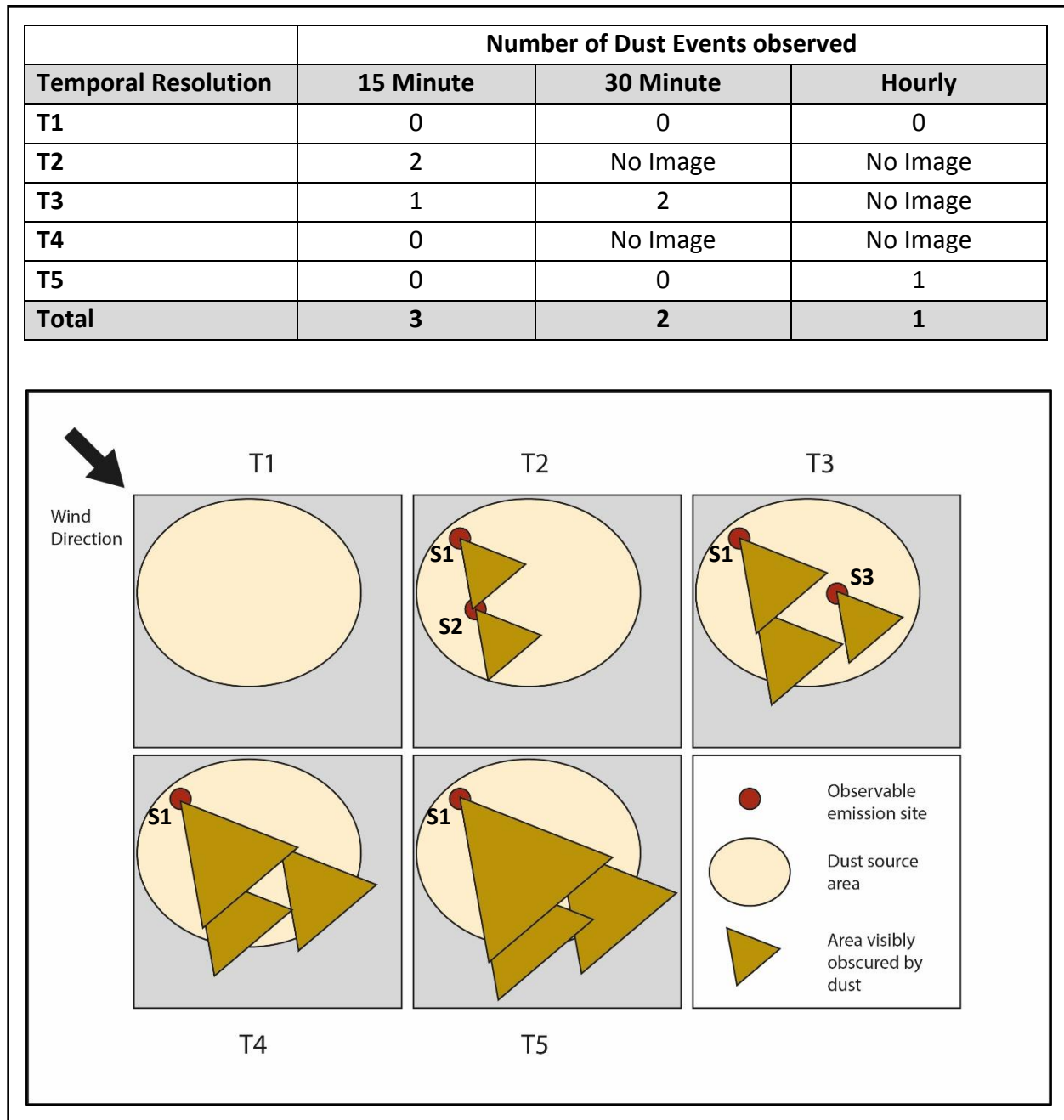
Figure 3.14 (overleaf): Schematic illustrating the formation of dust point sources (Sn - red circles) within a dust source area at different time step intervals. (Tn = 15 minute steps). T1:T5 observable only by 15 minute resolution; T1,T3,T5 observable at 30 minute resolution; T1, T5 observable at hourly resolution. Dust source (red circle) only visible when not entrained by dust emission upwind (brown triangle).

Geometric progression infers that the divergence in dust event frequency (of the three data sets) will be greatest during peak dust activity, as a larger number of dust storms multiplies the clustering effect. JJA observes a 33.7% (30 minute) and 61% (hourly) reduction in dusts

events. This percentage difference is not seen in all months, with non-summer months showing a closer correlation in all data sets. Actual differences in the number of observations is dependent on the distance between the point sources, the wind speed and direction, as well as the number of dust storms. The most active dust region (the Tigris Euphrates Basin) peaks in dust activity in JJA, as Figure 3.13 shows, dust sources across the Tigris Euphrates Basin are clustered together in a NE to SW corridor. Here, an average of 94% (across all three data sets) of JJA dust emissions take a SE trajectory. In these conditions, the lower resolution data are unable to detect all discrete sources downwind of propagating dust plume. Across central Saudi Arabia, where dust emissions sources are more evenly distributed, the clustering effect has a reduced impact on lower temporal resolution data. This area peaks during the non-summer months, where the divergence in number of dust events also reduces.

Diurnal cycles and seasonal cloud conditions

As Figure 3.14 demonstrates, simultaneous or similar emission times of dust plumes from spatially clustered deflation surfaces also increases the difference between the datasets. This is especially apparent, when a surface deflates in a reaction to specific diurnal atmospheric circulation conditions such as nocturnal LLJs (See section 2.5), emitting only once during a specific period of the day. During this period, the higher resolution data allows the observer to determine more discrete emissions. Over eastern Iran, nocturnal LLJs are strongly linked to an intensification of mid-morning dust emission over the Sistan Basin (Barough *et al.*, 2010; Alizadeh Choobari *et al.*, 2013). The hourly data in Figure 3.13 shows a large reduction in the number of dust events over this basin (black outline) in comparison to the sub-hourly data sets. Throughout the entire Middle East, Figure 3.15 describes the domination of mid-late morning dust emissions, with an average of 76% of all observations occurring between 06:00 and 12:00 coordinated universal time (UTC). The Middle East covers four different time zones, with range of +2 UTC in the East to +4 UTC in Oman. The concentration of dust emissions during these hours highlights the need to use SEVIRI images at a sub-hourly resolution.
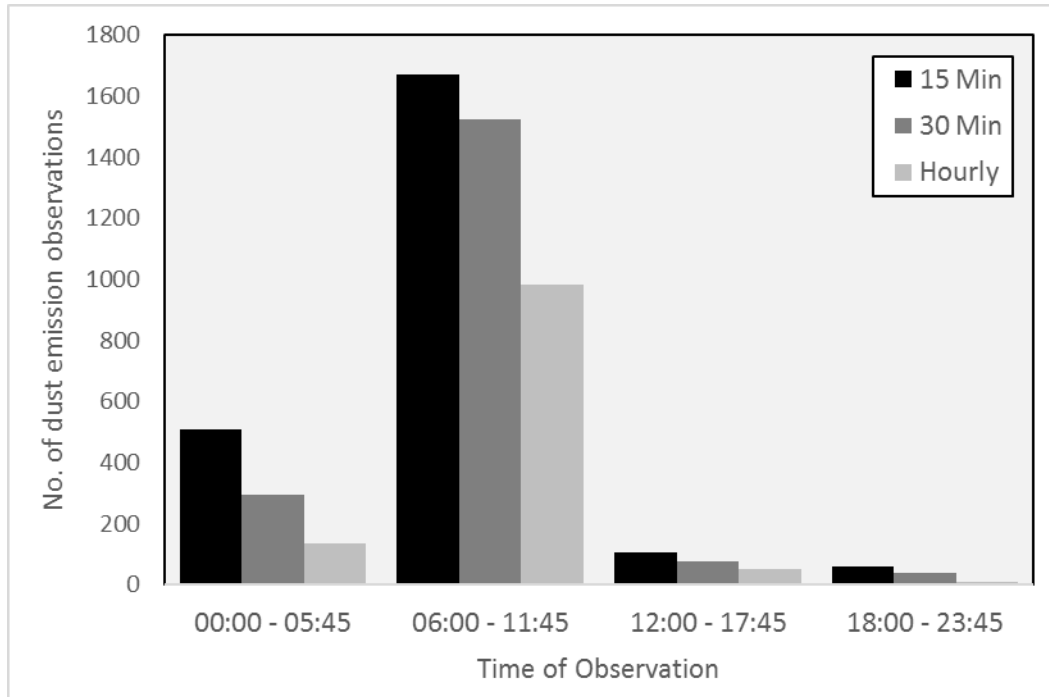
Figure 3.15: Diurnal plot of dust emission observations binned into 4 (6 hour) time segments at each 15 minute, 30 minute and hourly temporal resolution.

The convergence in the number of dust events, seen across each data set in the non-JJA months, can be attributed to increased cloud conditions associated with dust emission processes in those months. These seasons are dominated by travelling depressions from the eastern Mediterranean and northern Africa, bringing increased cloud cover, thunderstorms and high wind speeds as they progress eastward along their transport channel (Kutuzov *et al.*, 2013; Middleton, 1986) - see Section 2.5. Meteorological cloud presents multiple challenges to the subjective analysis of dust emission (see Section 3.3.4); while their presence obscures emission, the associated increase in column water vapour is of equal importance, potentially masking the dust signal in the RGB rendering. Degree of confidence (DOC) scores are therefore attributed to each event, with level 2 and 3 observations demonstrating increasing levels of cloud contamination. The increased percentage on level 2 and 3 dust events in non-JJA months (Fig. 3.16), is indicative of increased cloud conditions. During cloudy conditions, the number of observable sources, in all temporal resolutions is reduced, as clouds form and move independently above dust emissions. This diminishes the ability to distinguish smaller dust emission events found downwind of more frequently observed emitting surfaces, reducing the benefit of higher resolution data. The result is a bias in observations towards the

more readily defined point sources, most-upwind of a dust storm (S1 in Figure 3.14), leading to a convergence in the number of observations across the three temporal resolutions.
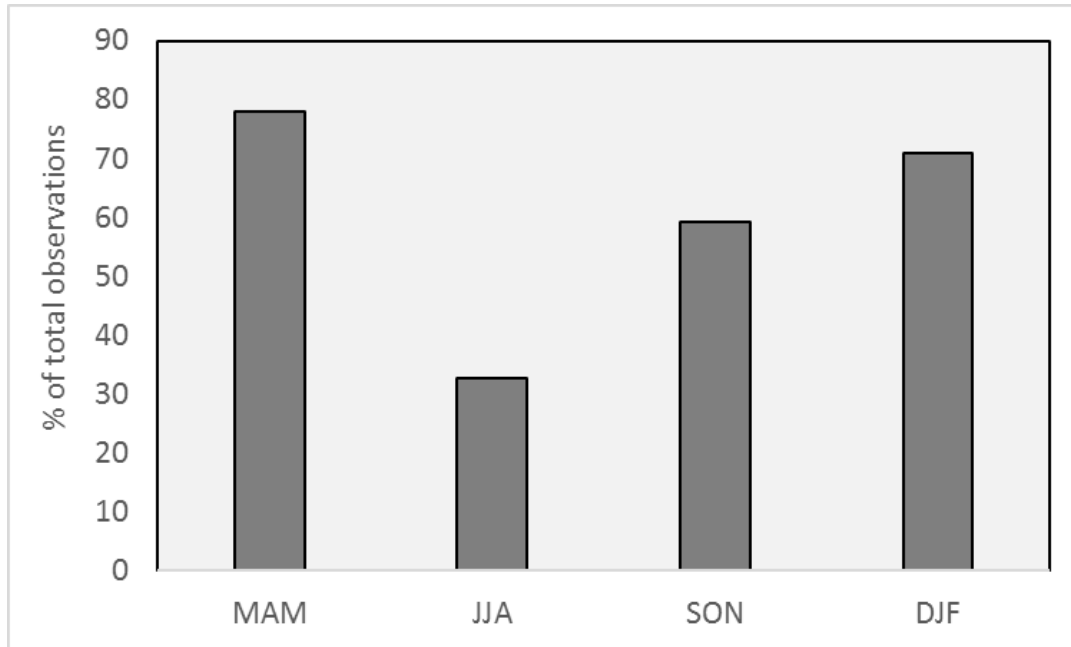
Figure 3.16: Percentage of dust events with degree of confidence level 2 or 3. Values shown represent the average percentage between all temporal resolutions.

Subjective interpretation

It is important to remember the subjective methodology used to make these observations, with low probability of exact replication of results. When digitising the entire aerial extent of dust clouds in SEVIRI dust RGB data, Ashpole and Washington (2012) compared the results of two experienced independent viewers, finding only a 77% agreement during daylight hours and only 52% at night. Importantly, the low agreement in their study is due to the use of single snapshot analysis, with only one image digitized of North Africa for each day (12:00 UTC) and night (03:00 UTC) of observation. By using sequential images in this investigation over the Middle East, it is expected that the differences will be more representative of the increased accuracy derived from sub-hourly image analysis. However, it is evident that a proportion of the difference will relate to the subjective method being used.

3.5.3   Frequency analysis - synthesis

Analysis of one year of SEVIRI dust RGB data over the Middle East, at three different temporal resolutions has shown that the number of dust emission events observed reduced with each step reduction in temporal resolution. The magnitude of these differences depended on the spatial and temporal clustering of dust emission events and the presence of meteorological cloud. In summary, this investigation showed that:

- These results suggest that the highest resolution data (ideally sub hourly), be used where emissions frequently develop from multiple discrete deflation surfaces within a small source area, frequently seen in parts of the Tigris Euphrates Basin.

- Sub-hourly data also performs best where emission is instigated by diurnal atmospheric processes such as the breakdown of nocturnal LLJs, where the daily total emission, occurs within a few hours of the day.

- During both conditions, higher resolution data provide the best opportunity to observe all deflating surfaces prior to their entrainment by the propagating dust plume.

- Uncertainty caused by meteorological cloud contamination reduces the divergence in results between datasets. Only the most frequently observed emissions are available for detection, these are predominately visible at each temporal resolution, reducing the advantage of higher resolution data.

- Given the scale of the study region, the small number of discrepancies and the high correlation seen in Figures 3.10 and 3.11, the two sub hourly observations are comparable, with each capable of producing accurate locations of dust emission in the Middle East.

3.6   Secondary data and methods

To complete the second aim of this project (see Section 1.2), each dust emission event is compared to multiple land surface datasets using ESRI Arc GIS 10.1 software. These data are described in the following sections and include: information on elevation and slope from a digital elevation model (DEM) (Section 3.6.1), soil texture of deflation area (3.6.2), proximity to fluvial features (3.6.3), palaeohydrology (3.6.4), vegetation cover (3.6.5), landforms (3.6.6) and monthly normalised difference vegetation index (NDVI) data (3.6.7). Finally, Section 3.6.8 describes the ERA-interim re-analysis data from the European Centre for Medium-range Weather Forecasts (ECMWF), used here to determine the synoptic conditions associated with dust emission in the most active sub-region. Compared to monthly dust event totals, each of these data will highlight the influence of land surface and atmospheric environmental conditions on dust emission frequency at both a regional and sub-basin scale.

3.6.1   Digital Elevation Model

Elevation and slope information are derived from the GTOPO30 digital elevation model (DEM) (USGS). The GTOPO30 DEM produces a global map of surface elevation, at a resolution of 3-arc seconds (approximately 90 m) (Kiamehr and Sjöberg, 2005). The GTOPO30 DEM was successfully applied by (Miliaresis, 2001) for mapping in the Zagros Mountains in Iran, where accuracy is reduced in complex terrain, to ± 30 m, which for the purposes of this investigation is deemed acceptable.

3.6.2   Soil texture

Soil texture data for the top 1-metre soil horizon was provided by the Webb-Rosenzwig global soil profile database (http://www.daac.ornl.gov). With a spatial resolution of 1°, soil texture is categorised by the percentage of sand, silt, clay and loam into 12 soil types defined by the U.S. Department of Agriculture (USDA) (Webb *et al.*, 1992). These data have previously been used to model dust emission sources in the Middle East (Hamidi *et al.*, 2017), where dust emission volumes were simulated during Shamal dust events (3-8 July 2009) by combining estimated wind speed thresholds for specific soil textures and other surface characteristics, with re-analysis wind speed data. While the coarse resolution prevents a high-resolution

characterisation of all dust emission sites, these data will provide useful insights into the more prominent soil textures across the dust emitting regions.

3.6.3   Fluvial features

River networks are presented in shapefile format, taken from the global polygonal drainage basin database (PDBD) (Masutomi *et al.*, 2009). The PBDB was derived from DEMs with a high spatial resolution (100 m – 1 km). Automated methods such as 'stream burning' and non-automated manual corrections, including the use of geographic data collected by local governments were applied. These data will show how dust emission frequency varies with proximity to rivers and lakes.

3.6.4   Palaeolakes

Information on palaeohydrological features in the Arabian peninsula were derived from Breeze *et al.* (2015), who used automated GIS methods to identify the location and spatial extent of closed basin palaeolakes. Firstly, endorheic basins were identified from Shuttle Radar Topography Mission (SRTM) DEM topographic data, with a spatial resolution of 90m. Potential paleolakes were then identified within these endorheic depressions, by applying a supervised multispectral classification of known palaeolake deposits in Landsat Thematic Mapper (TM) data. Finally, palaeolake shorelines (area of maximum extent) are modelled by filling the basin to the elevation of the highest detected deposit, thus simulating the more humid climate and hydrological regime of the Mid-Late Pleistocene. These data are available for the Arabian Peninsula only, however this represents the first attempt to compare these data with dust emission observations.

3.6.5   Land use

Land cover data is produced by Broxton *et al*. (2014) and is derived from 10 years (2001 to 2010) of collection 5.1 MODIS Land Cover Type (MCD12Q1) data. This land cover product provides 0.5 km spatial resolution information of vegetation-type land cover. Each pixel is classified into one of 16 land cover types by a supervised decision-tree algorithm (for a full list of classifications see Friedl *et al*., 2002). Each decision is given a confidence score, with inter-

annual changes in land cover solved by the weighting of the corresponding confidence scores of each land cover type observed, and assigning the highest to that pixel. This multi-year approach is believed to give a better account of land surface type than single year analysis; with 40% of non-water pixels showing inter annual variability between 2001 and 2010 (Broxton *et al.*, 2014). Using these data, six different land cover types were identified across the Middle East (Table 3.3).

Table 3.3: A description of the MODIS MCD12Q1 land cover types observed over the Middle East. Source: Friedl *et al*. (2002)

Land Cover type	Description
Urban and built up	Land covered by buildings and man-made surfaces (concrete and asphalt).
Barren	Exposed soil, sand or rocks, with less than 10% vegetation in all seasons.
Grasslands	Surface with herbaceous coverage, with less than 10% tree and shrub coverage.
Open shrublands	Wooded vegetation less than 2 m tall, canopy coverage between 10% and 60% of either evergreen of deciduous foliage.
Mixed forest	Wooded area with trees greater than 2 m tall and vegetated coverage over 60%. Tree communities include a mixture of evergreen and deciduous species.
Cropland	Land surfaces with seasonal rotation between temporary crops, harvest and bare soil of single or multiple cropping systems.

3.6.6   Landforms

A high-resolution database of landforms are provided by Parajuli *et al*. (2014). Landforms are assigned by the visual interpretation of ArcGIS/Basemaps and Google Earth Professional, which range from 1 m to several meters spatial resolution. This subjective interpretation is believed to be appropriate, given the clarity in which different landforms are distinguishable by a trained viewer. Automated approaches, which apply spectral reflectance signatures to supervised classification schemes, were not used due to potential false classifications in spectrally similar features (e.g. savannahs and croplands), and the variation in spectral contrast presented by the mosaic of images that form the base imagery. Landform types mimic those of Bullard *et al*. (2011) (see Section 2.4), with 12 different landform types (Table 3.4). Of the 12 landforms, 10 were represented in the Middle East, with Savannah/grassland and Forest the only two omitted. In comparison to Bullard *et al*. (2011), these data consider anthropogenic landforms (Agriculture and Urban Areas, Table 3.4), an important factor for

the Middle East due to the increased population density compared to other arid regions (See section 2.4.4).

Table 3.4: Landform classification as described by the Parajuli *et al*. (2014) database and the relative classification in Bullard *et al*. (2011).

Landform	Bullard *et al*. (2011) classification	Description (Parajuli *et al*., 2014)
Bedrock	Low emission surface (Section 2.4.2)	Bedrock surface with no sediment deposits. This type is relief independent, although predominantly found in mountain areas. Also includes volcanic formations including lava flows.
Bedrock with sediment	High Relief alluvial systems (Section 2.4.3.3)	Areas with a discontinuous cover of sediment deposits over bedrock. This includes high relief bedrock uplands with incised river channels and wadis.
Sand deposit	Aeolian sand dunes (Section 2.4.3.4)	Active sand dunes, with no bedrock visible
Sand deposit on bedrock	Sand sheet (Section 2.4.3.4)	Active sand dunes over thin layer of sand deposits, with bedrock intermittently visible.
Sand deposit, stabilised	Aeolian sand dunes (Section 2.4.3.4)	Inactive dunes, potentially vegetated
Agricultural and urban	Not considered	Anthropogenic / disturbed surfaces, includes areas of agriculture independent of relief and urban settlements. Agricultural areas are typically found near fluvial features including rivers, lakes and floodplains.
Fluvial system	Low relief alluvial (Section 2.4.3.3)	Hydrological basins that contain multiple streams, normally in areas of low relief. Frequently mixed with agricultural areas.
Stoney surface	Stoney surface (Section 2.4.3.4)	Wind deflated surfaces, characterised by a surface layer with closely packed gravel and ventifacts, over a layer of fine sediments.
Forest	N/A	Forest areas – not represented in Middle East data
Playa/sabkha	Ephemeral Lakes (Section 2.4.3.2)	Includes playas, chotts, pans, coastal sabkhas and ephemeral lakes (with or without agricultural features).
Savannah/grassland	N/A	Grassland areas typical of the Sahel – not represented in Middle East data
Water body/wetland	Wet Lake (Section 2.4.3.2)	Areas permanently covered by open water or wetlands.

3.6.7   NDVI

Monthly MODIS NDVI (MOD13A3, collection 5) data (Didan, 2015) are used to provide information on vegetation cover of dust hotspots. MOD13A3 data has a spatial resolution of 1 km on a 16 day repeat cycle. NDVI retrieval is performed by daily, atmosphere-corrected, surface reflectance data, using the Advanced Very High Resolution Radiometer (AVHRR) 'continuity index' algorithm (Huete *et al.*, 1999). This algorithm follows standard NDVI, demonstrating the normalised reflectance ration of NIR (0.7 – 1.1 μm) and visible red (0.6 – 0.7 μm) (ρNIR/ρRED*)* reflectance ratio between values of -1 and +1, where negative values indicate non-vegetated surfaces such as snow and water (Lee and Kim, 2012). Pixel value is defined by the highest NDVI value, recorded during low cloud and low viewing angle conditions within the 16 day cycle. Monthly average MOD13A3 data is collected from January 2006 to December 2013 and stacked in ERDAS Imagine 2013 software to produce a 96-point time series. The most active dust hot-spots over the Tigris Euphrates Basin are defined by number of dust events within a 0.25° grid. Monthly NDVI values are produced for the 20 most active grid cells, calculated from the average pixel value contained in each grid cell subset. Pearson correlation coefficient (*r*) values are presented for Monthly NDVI / dust event frequency values.

NDVI analysis is widely used to represent the vegetation regime in all climates including drylands (Shahriar Pervez *et al.*, 2014), and have helped to demonstrate the role of seasonal changes in vegetation and changes in dust emission frequency (Kim *et al.*, 2017). MODIS MOD13A3 data has also been used as an indicator of precipitation variability (Formica *et al.*, 2017). Here, the MOD13A3 NDVI data will define the seasonality and inter-annual variability of vegetation coverage in different dust hot spots across the Tigris Euphrates Basin and provide an insight into its influence on dust activity in an important dust emitting region.

3.6.8   Mean Sea Level Synoptic conditions

Prominent synoptic patterns, linked to dust emission across the Middle East are determined from averaged mean-sea-level-pressure (MSLP) data for dusty days, calculated using ECMWF ERA interim data. Data are produced at a 0.5° spatial resolution, with values averaged at a daily temporal resolution. 10 m surface wind data are calculated from daily averages, describing direction and velocity in ms^{-1}. Dusty days are defined (sub) regionally, by a dust

activity threshold, whereby the number of dust events in any given day must surpass the 75th percentile of the seasonal average (sub-regions are determined by the method in Section 3.4). This threshold is chosen to highlight only the synoptic conditions associated with the most intense dust activity, reducing the contamination by non-dust meteorological events. The application of a local threshold removes any bias caused by unequal distribution of dust events between regions, highlighting the specific synoptic conditions which instigate dust emission during that season and within that area of the Middle East.

3.7   Summary

The primary focus of this thesis is to produce a high resolution, dust emission inventory of the Middle East, showing the locations of frequently emitting surfaces and describing the seasonal dust climatology of an important dust-emitting region. This inventory provides the basis for the subsequent investigations set out in this thesis, where the research question put forward in Section 2.7 will be answered. The main points from this chapter can be summarised as follows:

- A comparison of current data and methods has highlighted three distinctive approaches to determine dust emission sources. These include, (i) automated averaging of daily maps of high-AOD, (ii) subjective backtracking of dust emissions to the point of first emission, and (iii) coupled climate-aerosol models based on land surface classifications.

- Examination of these approaches demonstrated the improvement in accuracy, when subjectively backtracking dust plumes to the point of first emission, especially when using high temporal resolution SEVRI Dust RGB data.

- Taken from a geostationary orbit, these data provide a 15-minute temporal resolution and 3 km spatial resolution at nadir (4 – 5 km over the Middle East). Using TIR wavelengths, the SEVIRI Dust RGB product offers 24 hour observations of the surface.

- Analysis of SEVRI dust RGB product demonstrated its sensitivity to high levels of humidity and changes in surface emissivity caused by different surface materials and variability in vegetation cover. In comparison with automated retrievals, it was shown that human interpretation is best equipped to differentiate the dust signal during weak dust signal conditions.

- To create a dust source inventory for the Middle East, SEVIRI dust RGB data are subjectively analysed from 2006 – 2013 at a minimum of 30 minute temporal resolution. Dust plumes are backtracked through sequential images to point of first emission. Each dust event is described by location, date, time, duration and trajectory; with a degree of confidence score given to provide an account of atmospheric cloud conditions at time of emission.

- Performance analysis of SEVIRI dust RGB data, at three different temporal resolutions (one image every 15 minutes, 30 minutes, and hour) showed the improved accuracy in source detection in sub-hourly over the hourly data. The higher resolution data performed

better, where multiple discrete sources are clustered into small land formations such as ephemeral lakebeds. These data also performed better where dust emission is confined to a few hours of the day, typically in response to specific atmospheric circulation conditions, such as nocturnal LLJs.

- Further analysis is performed using the dust source inventory and a suite of land surface data. These analyses are carried out by spatially attributing the dust events with information on surface topography, soil texture, contemporary and paleo hydrology, land cover and geomorphological land formations.

- Typical synoptic conditions, linked with dust emission in the Middle East are described by averaging (MSLP) re-analysis data for representative 'dusty days'. These Dusty days are defined through the application of regional and seasonal threshold for the number of dust events per day.

Chapter 4: Results - Middle East dust emission inventory

4.1   Introduction

This chapter presents the results of the dust emission inventory for the Middle East from January 2006 to December 2013. The primary objective is to examine the frequency and temporal variability of dust emission, along with a detailed geographical distribution of dust sources in the Middle East. Importantly, the results presented here do not include dust load or associated aerosol optical depth (AOD).

The inventory describes inter-annual and seasonal variability in both number of dust events and percentage of dusty days (Section 4.2). The spatial distribution of emission sources are described in Section 4.3, which are split into nine sub-regions in Section 4.4. Further characteristics attributed to each event, including time of emission, duration and trajectory are described in Sections 4.5 to 4.8. Potential errors, especially those associated with cloud contamination, are analysed using the degree of confidence scores attributed to each dust event observation in Section 4.9. Finally, Section 4.10 gives a summary of all results.

4.2   Inter-annual variability and seasonality

In total, 27,680 events were observed between January 2006 and December 2013, with an average of 3,460 events per year. Figure 4.1 shows the inter-annual variability in the total number of dust events and dusty days. Both series show a bi-modal peak, dusty days peak in 2008 and 2012, dust events peak in 2009 (and 2013, with a significant reduction of dust events in 2010. 2013 produced the highest number of dust events (4800), while 2006 recording the fewest (2342). The maximum percentage of dusty days was observed in 2012 (89%), and the lowest in in 2006 (77%).
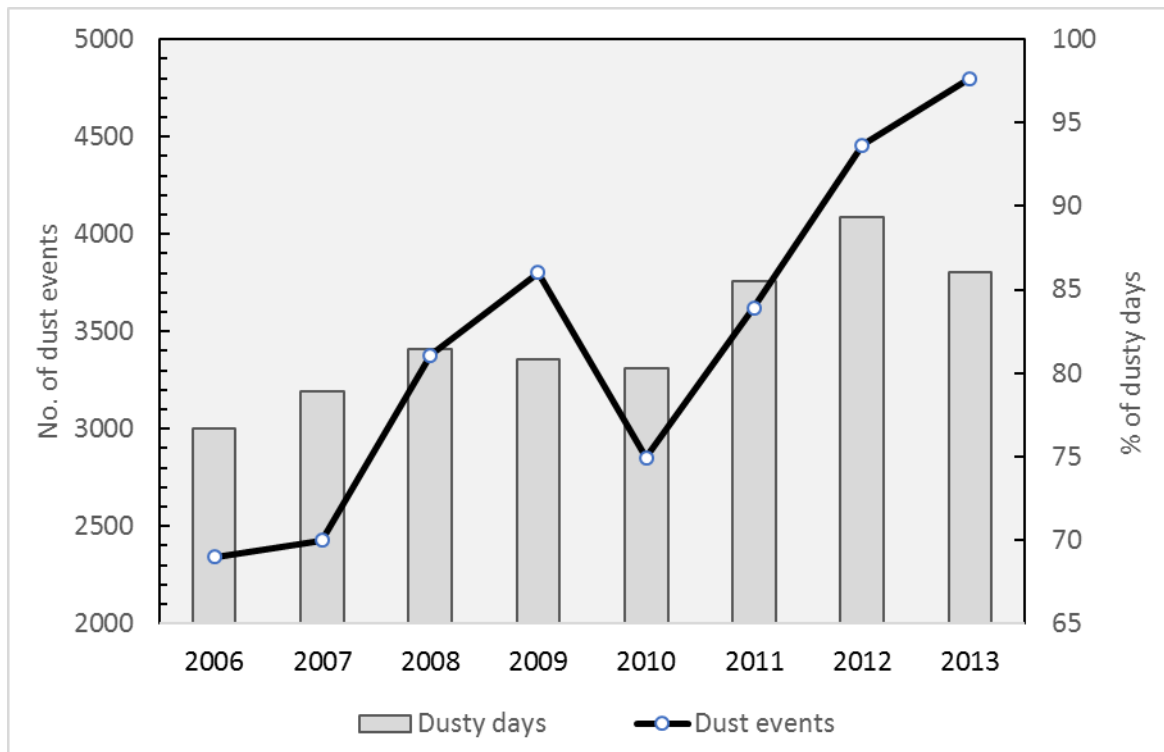
Figure 4.1: Number of dust events and percentage of dusty days in the Middle East between 2006 and 2013. Observations derived from SEVIRI Dust RGB data. Dusty days, shown as percentage of total days, indicate days where >1 dust event was observed.

Monthly mean values of dust events and percentage of dusty days from 2006 – 2013 are described in Figure 4.2. The results demonstrate a clear seasonality, with a maximum in both series during JJA. A secondary peak appears in March, followed by a reduction/plateau in dust events in April/May. The largest percentage of all dust events (39%) was recorded in JJA, followed by MAM and SON with 28% and 17% respectively, with DJF recording the fewest (16%). June produces the highest monthly mean in both series, with an average of 573 dust events and 99% dusty days. Across the time series, June only failed to record 100% (30 days) dusty days over two years (2007 and 2010). November produced the lowest monthly mean in dust events (120) while December had the lowest mean dusty days (57%).
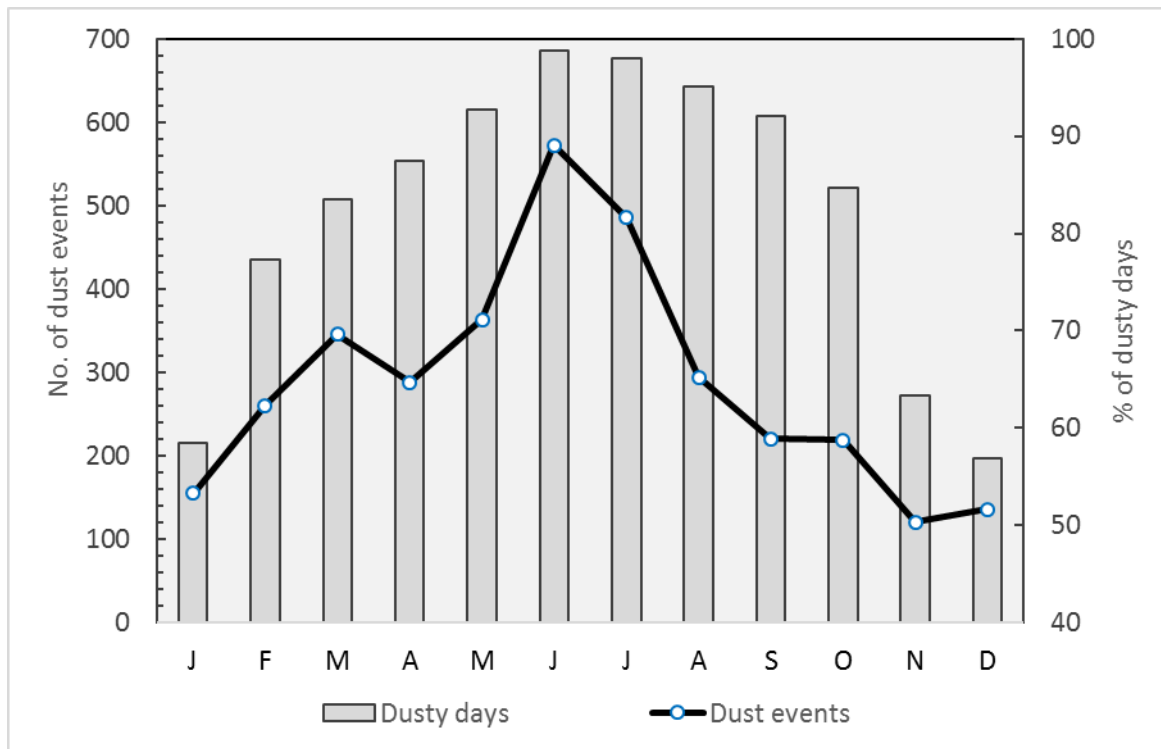
Figure 4.2: Monthly mean values of dust events and dusty days per month between 2006 and 2013.

The monthly time series of dust events and percentage of dusty days are presented in Figure 4.3, where the distinct bi-modal seasonality exhibited by the mean values (Fig. 4.2) is evident in most years. In each year, the number of events peaks in either June or July except in 2012, which sees an exceptional increase in dust emission frequency during the (typically) secondary springtime peak. The March of that year exceeded the monthly average by 89%, producing 653 dust events. June 2013 produced 931 dust events, the greatest number of dust events in any single month, with a 37% increase over the next highest monthly total (May 2013). June 2013 was unprecedented in the time series, exceeding the June average (573) by 78% and is more than double the monthly average for JJA (451). November 2010 generated the fewest events (57), 57% fewer than the November average (120). December 2009 had the lowest percentage of dusty days (32.3%), 24% less than the December average.
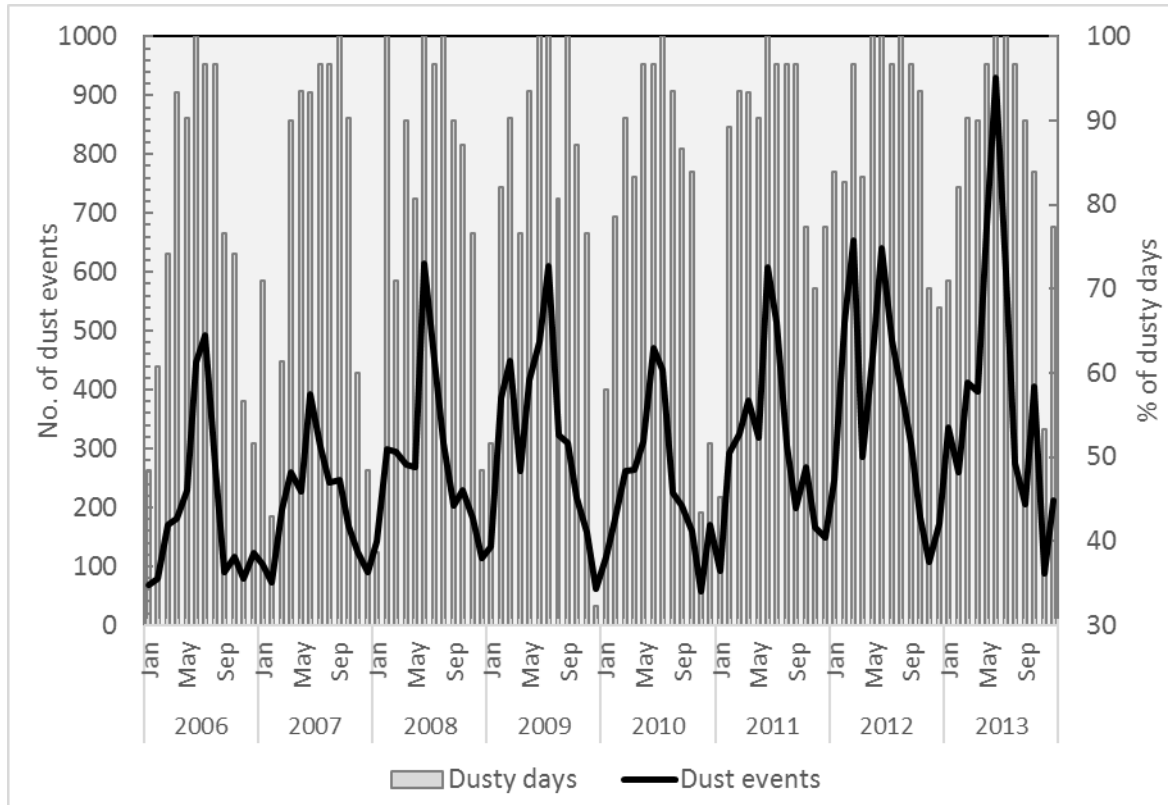
Figure 4.3: Time series showing number of dust events and percentage of dusty days per month from 2006 to 2013.

Monthly variability is described by coefficient of variation (CV) statistical analysis of both the number of dust events and percentage of dusty days (Fig. 4.4). Typically, the greatest variability (highest CV) occurs during the least dusty months – between November and March. April has a relatively low CV in number of dust events compared to the other spring months. Both March and May produce exceptional dust emission frequencies in certain years (2012 and 2013 respectively) resulting in higher values of CV. JJA shows very little variability in percentage of dusty days, regularly recording close to 100% dusty days. July and August record the lowest dust event CV, while June's variability is inflated by the exceptionally large value of June 2013 (Fig. 4.3).
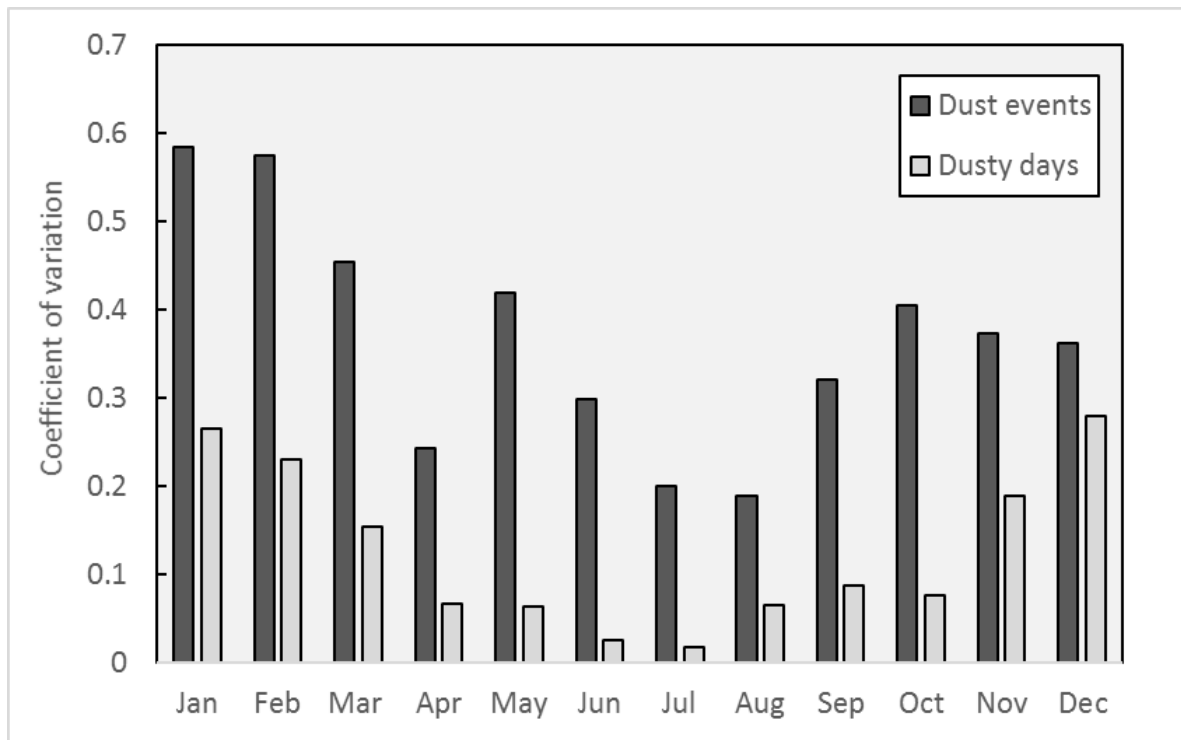
Figure 4.4: Variability of dust events and dusty days by month between 2006 and 2013, shown by coefficient of variation (CV) values.

4.3   Spatial Distribution of dust emission sources

The spatial distribution of all dust events from 2006 – 2013 are shown as point sources in a 0.25° x 0.25° grid (Fig. 4.5). This high-resolution map of dust sources shows several 'hot spots', where dust is emitted at a higher frequency relative to the rest of the region. Of the 27,680 dust events, 23% emanate from an area covering just 1% of the total land area in the Middle East.

The majority of the dust sources lie within the gently sloping plateau of the Arabian Peninsula, with 37% of all events within the Tigris-Euphrates River basin alone (red outline in Figure 4.5). Central areas of the peninsula appear moderately active, including sources along the Persian Gulf coastline, to the foothills of the Asir Mountains in south western Saud Arabia / Yemen. Dust sources in Iran are concentrated in the east of the country, following the flat inter-mountain valley (Dasht-e-Lut) and topographic depressions of the Sistan Basin and Jaz Moorian dry lake basin. Coastal areas are moderately active dust sources, especially around the Makran coast in south eastern Iran and the Red Sea and Persian Gulf coastlines of Saudi

Arabia. Dust source areas are limited to areas of little relief, with no dust sources emanating from mountainous areas, including the Zagros and Alzorz mountains of northern and western Iran, and the Asir Mountains of western Saudi Arabia / Yemen. Similarly, the sandy An Nafud desert in northern Saudi Arabia shows very few dust source areas, shown by an arc of inactivity to the south west of the Tigris Euphrates basin in Figure 4.5. In contrast to many previous dust source inventories (e.g. Ginoux *et al*., 2012; Prospero *et al*., 2002; Washington *et al*., 2003), very few dust sources appear in the southern extent of the Arabian Peninsula - including the Rub'al-Khali sand sea (18 - 22°N; 45 - 52°E), Omani coastal areas and Al Hajar Mountain foothills. Here, it is believed that persistent northerly winds frequently transport Mesopotamian dust south, where they are interpreted as source locations in daily-frequency satellite platform (MODSI / TOMS) used in the previously mentioned studies. In the SEVIRI analysis, human interpretation of high frequency imagery prevents such false-positive dust source area attribution, thus providing a more robust account of dust activity (see Section 6.2).
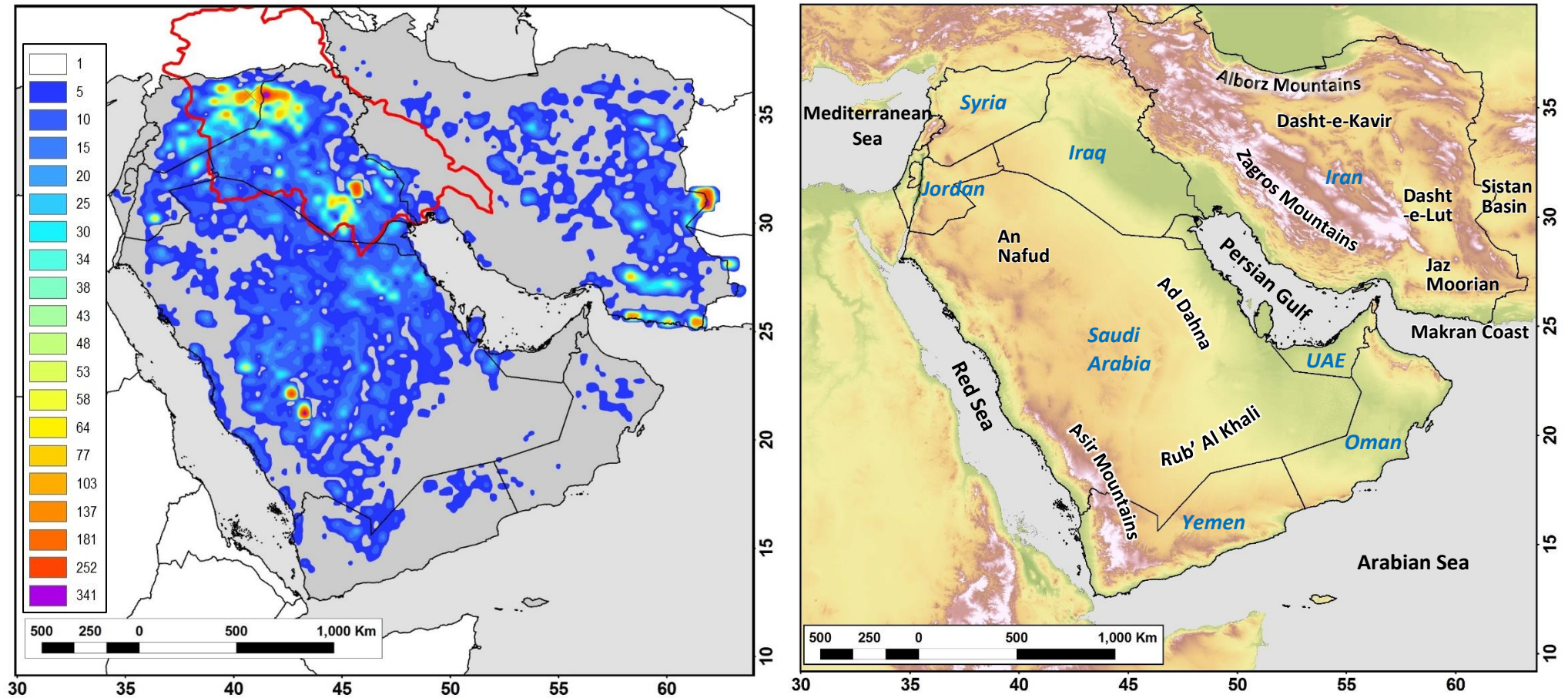
Figure 4.5: Spatial distribution of dust emission events across the Middle East in 2006 – 2013. Dust events indicate dust point source (i.e. point of first emission), displayed in a continuous raster format with 0.25° resolution. Red outline depicts the topographic boundaries of the Tigris-Euphrates Basin.

4.4   Sub-regions of dust activity in the Middle East (2006 -2013)

Based on the result of the inventory of dust emissions, the Middle East has been divided into nine sub-regions of dust activity (Fig. 4.6). Each region is defined by a combination of the spatial distribution of dust emissions (Fig. 4.5), natural geographical boundaries (i.e. mountain ranges, drainage basins desert areas) and distinctions made in research literature (Walker et a., 2009; Middleton, 1986).   As both Figure 4.5 and Figure 4.6 show, frequency of dust emission varies considerably across the nine sub-regions. Upper Mesopotamia is the dustiest, producing 29% of all dust events. The South East Arabian Peninsula produced the fewest dust events (1%). A clear East to West difference in emission frequency exists, with 78% of dust observations emanating from the Arabian Peninsula. The Sistan Basin and Hamoon Jazmoorian are the most active sub-regions in Iran, with each accounting for 6% of all dust events despite being the two smallest sub-regions.

4.4.1   *Upper Mesopotamia*

Upper Mesopotamia includes the northern and western areas of Iraq, the Syrian Desert and the basalt Badia of Jordan and northwestern Saudi Arabia. Importantly, this sub-region makes up the upland area of the Tigris-Euphrates basin, with extensive areas of agriculture (see Section 2.6.1). As shown by Figure 4.6, this area emitted the largest number of dust events of all sub-regions (8076), equalling 29% of all dust events across the Middle East. Several concentrated areas of frequent dust emission are clearly visible on either side of the Iraq-Syria border (Fig. 4.5). Dust activity in this sub-region shows a clear seasonality (Fig. 4.7), increasing in early spring, peaking in JJA before decreasing in late summer through to DJF.

4.4.2   *Lower Mesopotamia*

Referred to as the dustiest area of the Middle East by Middleton (1986), Lower Mesopotamia includes the lower elevations (less than 100 m a.s.l.) of the Tigris Euphrates River Basin and the northern reaches of the An Nafud Desert, Saudi Arabia. This region is climatically distinct from Upper Mesopotamia, with far less annual rainfall (UN ESCWA; see Section 2.6.1). This sub-region produced 20% of all dust emissions in the Middle East. A significant proportion of dust events are concentrated into two dust hot spots in the south-east of Iraq, in the lower

reaches of the Tigris-Euphrates basin. Dust emission frequency is seasonal, increasing in late spring and peaking during JJA (Fig. 4.7). Dust activity decreases through SON to minimal in DJF.
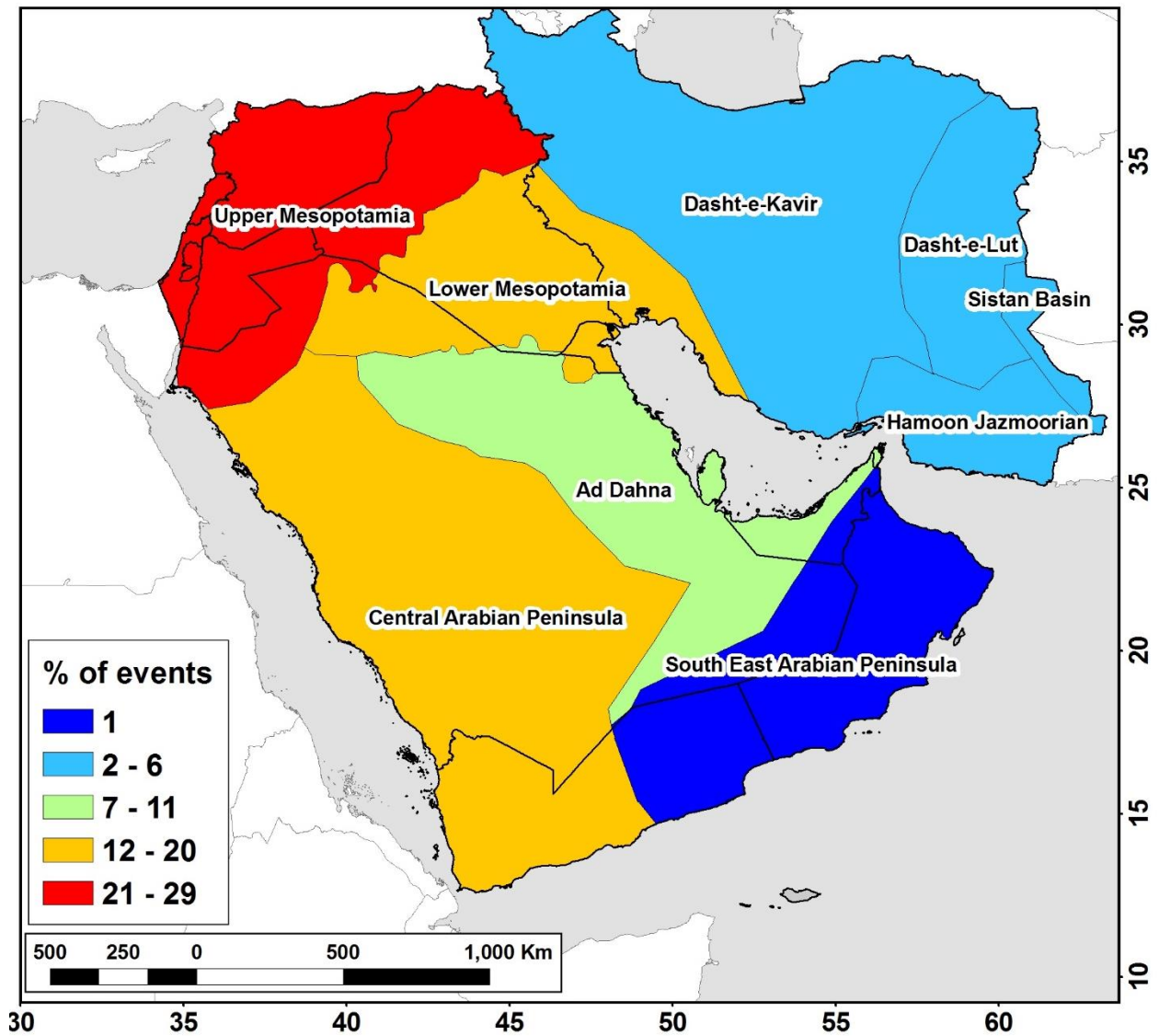
Figure 4.6: A map of the Middle East and the boundaries of the nine sub-regions discussed in section 4.4 Graduated colours show relative percentage of dust events generated in each sub-area.
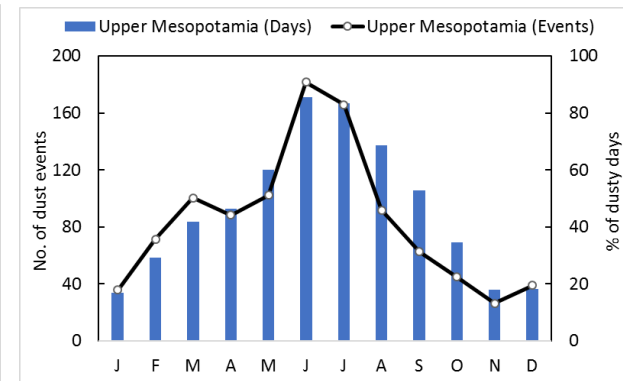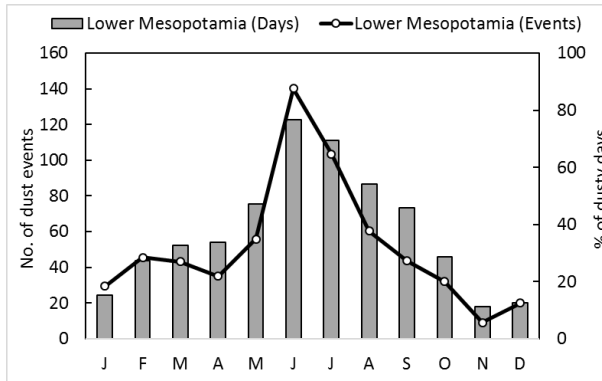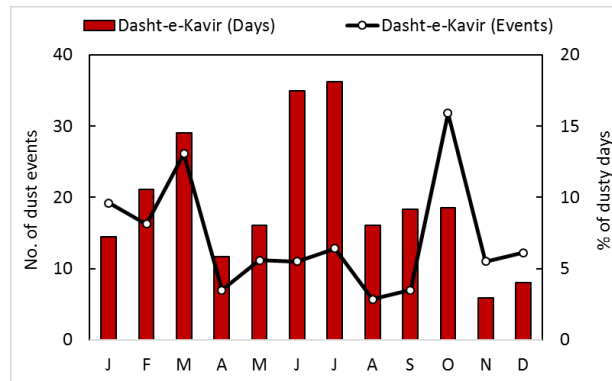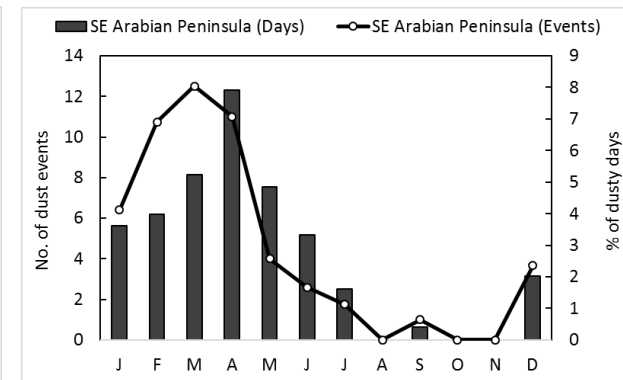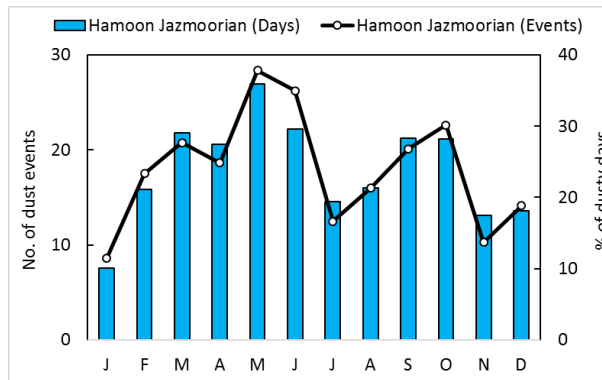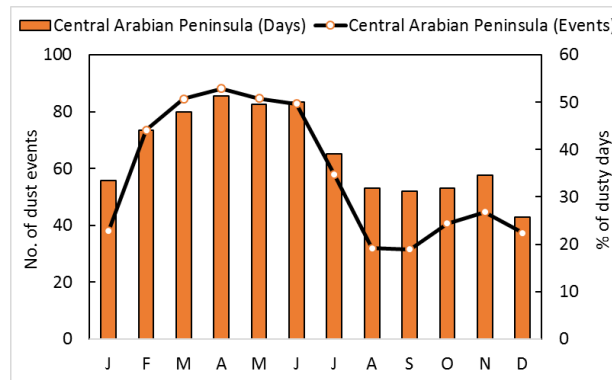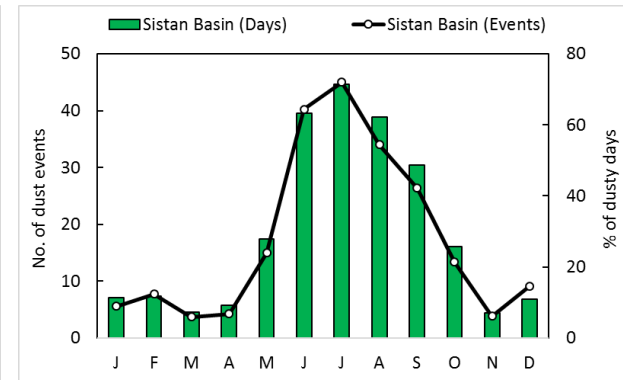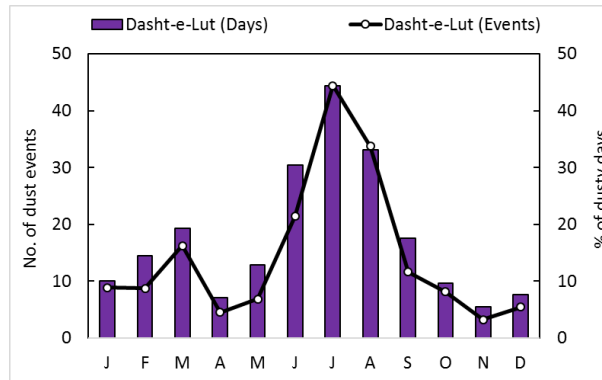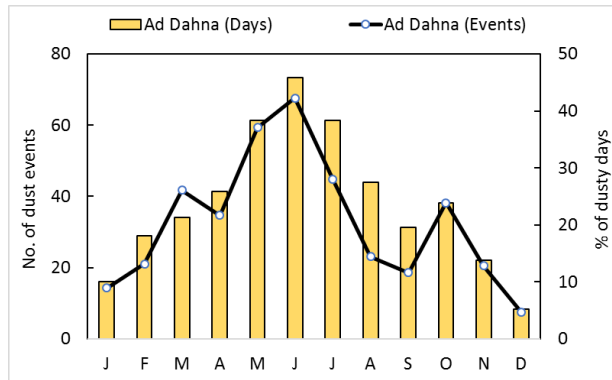
Figure 4.7 (Overleaf): Monthly means of dust events (black line) and dusty days (coloured bars) of the nine sub-regions of the Middle East (shown in Figure 4.6) between 2006 and 2013.

4.4.3   Ad Dahna

The Ad Dahna sub-region includes the southern and western coast of the Persian Gulf and the Ad Dahna sand sea, extending from the Rub Al-Khali in the south to the Syrian Desert in the north. Recognised as an active dust source in research literature (Prospero et al., 2002; Walker et al., 2009; Washington et al., 2003), this area accounts for 11.2% of dust emission events in the 2006-2013 period. The most active dust sources are concentrated north of 21°N, in the north of the Ad Dahna sand sea. Here, dust emanates from the inland wadis Al Batin, Al Rimah and Al Sahba (Ginoux *et al.*, 2012) and to the sandy calcareous sabkhas on the coast (Prospero *et al.*, 2002). The dust source inventory shows activity throughout the year, with two distinct peaks in JJA and SON (Fig. 4.7).

4.4.4   Central Arabian Peninsula

The Central Arabian Peninsula sub-region (12 - 28°N; 35 - 45°E), is the largest of the nine sub-regions, covering most the Al Hamad plateau. This area includes a mixture of fluvial channels originating from the Asir Mountains, ancient lava flows and human settlements. Geomorphologically, the region is defined by an extensive network of paleolakes and river channels (Breeze *et al.*, 2015). These areas include large parts of the Dawadami region (22 - 25°N; 43 - 47°E) of the central Arabian shield peneplain, the Shuwaynis region of Harrat Khabar (25 - 28°N; 37 - 42°E) to the north near the An Nufud Desert and the Mundafan region (15 - 18°N; 43 - 48°E) to the west of the Rub' al-Khali (Breeze *et al.*, 2015). The results show emission surfaces covering most of the sub-region, except the Rub al Kahli and the Asir Mountains (Fig. 4.5). Most activity is confined to a chain of hotspots, running adjacent to the Asir Mountains. This region accounts for 20.1% of all dust events, with dust activity highest between February and June (Fig. 4.7).

4.4.5   South East Arabian Peninsula

The South East Arabian Peninsula sub-region is the least active, producing only 271 dust events accounting for around 1% of all dust events in the Middle East. Dust sources are concentrated in a few deep wadis at the base of the Omani upland areas (1,500-3,000 m), and the lowlands to the north of the Hadramawt coastal escarpment in Yemen, an area dominated by ephemeral rivers and lakes (Prospero *et al* 2002). Dust activity is highest during MAM, with very little activity during JJA and SON (Fig. 4.7). These results contrast with previous investigations; this region is regularly described as the most active dust source in the Middle East, with Prospero *et al.* (2002) recognising it as the third dustiest location in the world.

4.4.6   Dasht-e-Kavir

The Dasht-e-Kavir sub-region covers a large portion of central Iran (25 - 40°N; 45 - 63°E in the north and 48 - 52°E in the south), producing 3.7% (1003) of all dust events. This sub-region encompasses the Zagros and Alborz mountain ranges and the Dasht-e-Kavir salt desert. Dust emissions are predominately generated from the flat, inter-mountain valleys and salt pans, including a dry lake bed within the Kuh Rud Mountains (33.1°N, 52.9°E) and at the centre of the large Dasht-e-Kavir desert. The seasonality of dust activity is bi-modal, peaking during March and October (Fig. 4.7), with minimal emissions in all other months. In contrast to frequency of events, the number of dusty days peaks in JJA, albeit with reduced dust storm intensity (see Section 4.5).

4.4.7   Dasht-e-Lut

The Dasht-e-Lut sub-region (28 - 37°N; 55 - 60°E) is defined by the hyper-arid Dasht-e-Lut desert valley and the surrounding mountain regions to the north and east. This region produced 4.9% (1354) of all dust events, with the largest concentration of sources in the dry flood plains in the Khorassan Razavi Province of north eastern Iran (34.9°N, 58.4°E) and the Dash-e-Lut Desert, at the base of the Kuh-e Deneband (31.5°N, 57.5°E) and Kuh-e Bagh-e Bala (30.5°N, 57.7°E) Mountains. Dust activity is seasonal, with an initial peak in March, followed by a larger peak in JJA when 58.8% of all event occurred (Fig. 4.7).

4.4.8   Hamoon Jazmoorian

The Hamoon Jazmoorian sub-region (24 - 27°N; 57 - 62°E) includes two distinct dust emitting areas, including a cluster of sources along the Makran Coastline and the large dry Jazmurian Lake basin further inland (centred around 27.5°N, 58.7°E). These areas are separated by the Central Makran Mountains. Hamoon Jazmoorian is the most active sub-region in Iran, producing 1710 individual dust events and 6.2% of all events. Dust activity continues all year, with a peak in activity during MAM (May) and SON (October) (Fig. 4.7).

4.4.9   Sistan Basin

The Sistan Basin sub-region is the smallest of all the sub-regions; and includes Iran's eastern borders with Pakistan and Afghanistan. Dust sources are in two distinct locations, the largest being at the base of the Sistan Mountains to the west, an area of ephemeral salt lakes (Prospero *et al.*, 2002). Further south, a (smaller) cluster of dust sources exist near the Hamun-i-Maskel ephemeral lake, on the Pakistan border. This sub-region records the second highest dust activity of all sub-regions in Iran (1627 events). Dust activity is very seasonal, increasing from late spring to JJA, with 59% of all dust events occurring between June and September, before decreasing to minimal activity from late autumn to MAM (Fig. 4.7).

4.5   Comparison of dust activity across Middle East sub-regions

Seasonal peaks in dust events differ significantly between sub-regions. Specifically, dust events peak in JJA over Iran and both Upper and Lower Mesopotamia, in contrast to a MAM peak in both the Ad Dahna and Central Saudi Arabia sub-regions (Fig. 4.8).
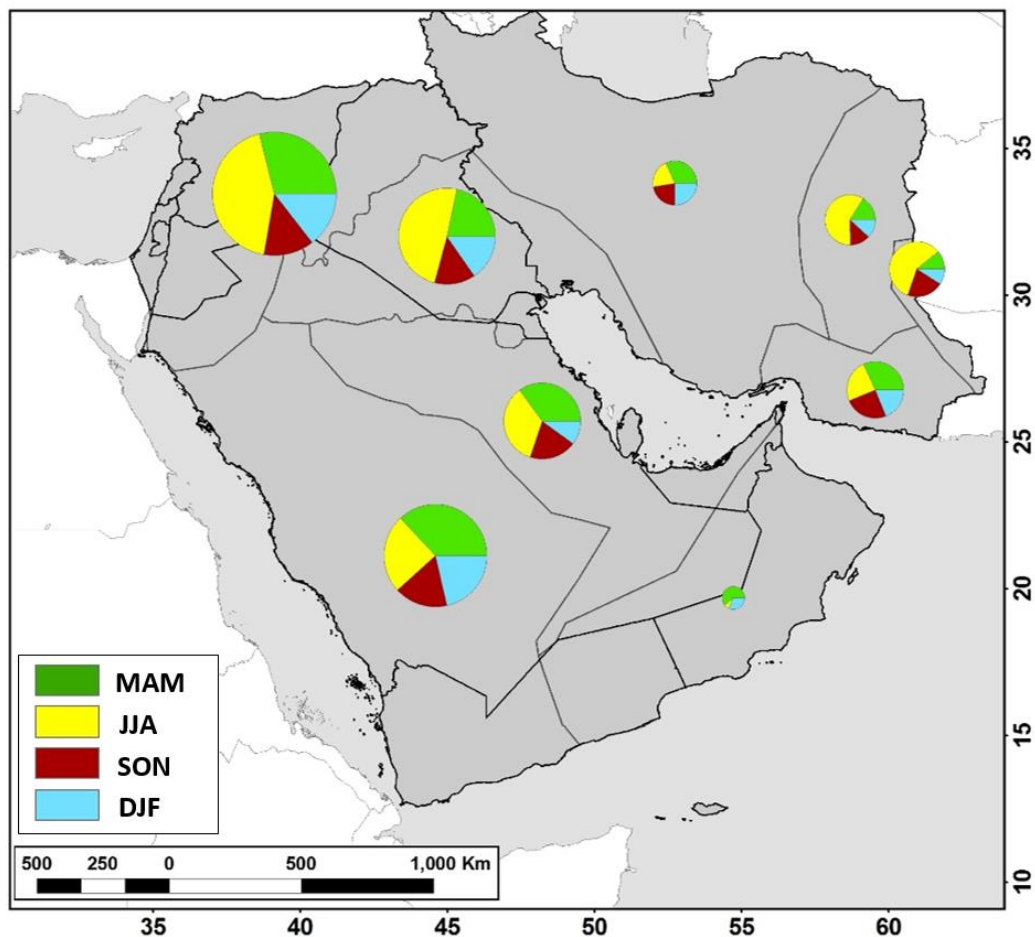
Figure 4.8: Seasonality of dust activity in the nine sub-regions of the Middle East between the years 2006 – 2013. The size of the pie chart depicts the magnitude of the number of events.

Seasonal peaks in dusty days follow a similar pattern to that of dust events (Fig. 4.7), except in the Dasht-e-Kavir sub-region in Iran. Here, JJA produces on average, both the fewest number of dust events and the highest percentage of dusty days. Indicating a relatively large number of low intensity dust events, with an average of 2.2 dust events per dusty day. In

comparison, Upper Mesopotamia produces nearly a three-fold greater average intensity during the same season (6.2 dust events per dusty day).

Annual observations of sub-region dust activity (Fig. 4.9); including the number of dust events (A) and percentage of dusty days (B) demonstrate greatest activity in Upper Mesopotamia (2013), with the highest annual total of any region (1462 events) in 2009. In all but one year (2007) the South East Arabian Peninsula sub-region generated the fewest dust events, with a minimum of one event in 2008. The results show a geographical separation in the magnitude of dust events across the time series. With the four most active sub-regions on the Arabian Peninsula producing increasingly, more dust events than all other sub-regions, with their combined number of events increasing by 135% (comparing 2006 and 2013 figures).

These four sub-regions, including Upper and Lower Mesopotamia, Ad Dahna and Central Arabian Peninsula, show a similar inter-annual pattern, increasing and decreasing in the same years (albeit with different magnitudes), with the exception of 2010 and 2013. The latter produced the highest dust activity (events and days) in both Central Arabian Peninsula and Ad Dahna sub-regions, with the former increasing by 54% from 2012. This increase coincides with decreasing dust activity in both Mesopotamia sub-regions. The four regions show an uneven decrease in activity from 2009 to 2010, with Upper Mesopotamia exhibiting the highest relative decrease (44.8%), while Ad Dahna remained relatively stable (4.8% reduction).

Among the Iranian sub-regions, the inter-annual variability of Dasht-e-Kavir stands out, producing the highest number of events of all Iranian sub-regions in 2013 (272), and the fewest in 6 of the 8 years of observation (2010 = lowest, 47). The Hamoon Jazmoorian sub-region produces the highest annual total of dust events, with 302 events in 2012.

Inter-annual patterns of dusty days (Fig. 4.9) are comparable to the number of dust events in each sub-region, exhibiting the same trends already described in the dust events data. The most significant difference between the two data sets is the relative magnitude in each region, with the Iranian sub-regions far more comparable to those of the Arabian Peninsula in the dusty days data. This is most evident in the Sistan Basin, which records on average, only 17% fewer dusty days than the most active sub-region (Upper Mesopotamia) and a higher annual percentage than Ad Dahna in all but one year (2013).
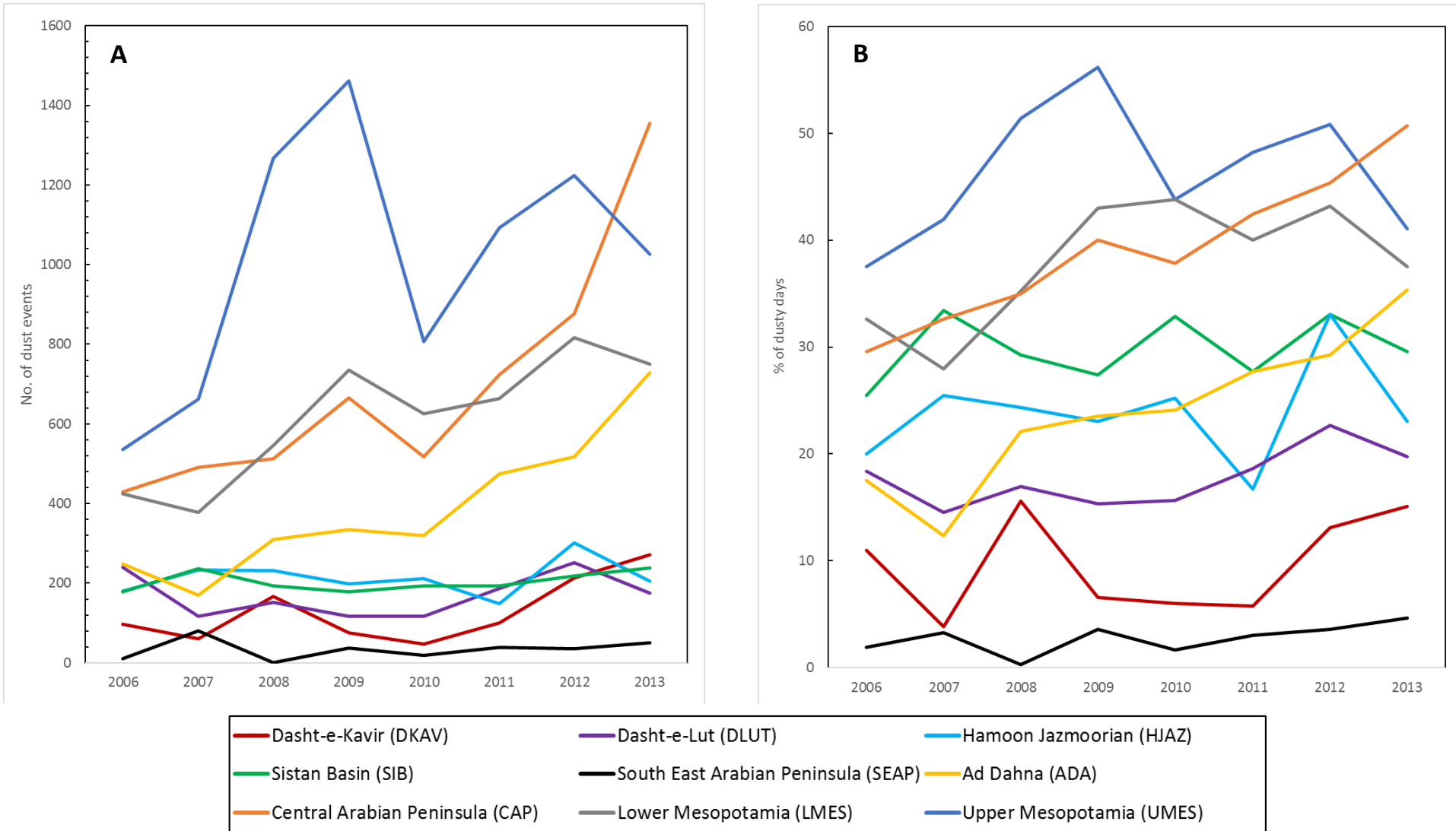
Figure 4.9: Sub-region inter annual comparison of (A) number of dust events and (B) percentage of dusty days from 2006 to 2013. Nine sub-regions defined in Figure 4.6.

The annual and seasonal variability of each of the sub-regions have been normalised by the mean using coefficient of variation and compared in Figure 4.10. Seasonal and inter-annual variability is highest in South East Arabian Peninsula, where the relatively few dust events are constrained to MAM in 2007. The relatively high, inter-annual variability of the Dasht-e-Kavir is evident here, contrasting with the other Iranian sub-regions. The Sistan Basin is characterised by the lowest inter-annual variability and the highest seasonal variability (outside of SEAP), consistently peaking every year in the JJA with limited activity in DJF.
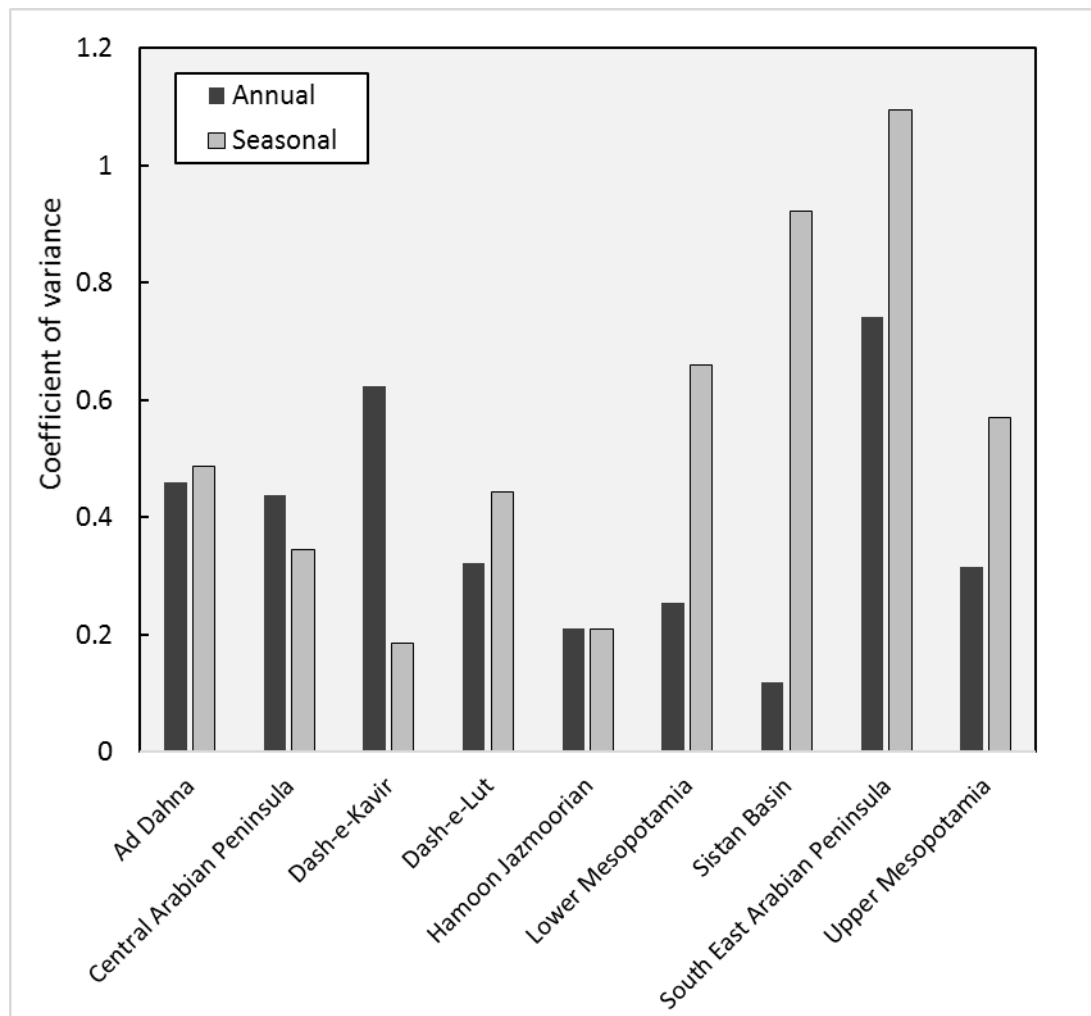
Figure 4.10: Inter-annual and seasonal dust emission variability of Middle East sub-regions. Variability described by coefficient of variation values.

4.6   Diurnal regime of dust activation in the Middle East

The diurnal regime of dust activity in the Middle East (Fig. 4.11) shows a clear link to daylight hours. Converted into local time (+3/4 UTC, split across four time zones), 96% of all dust events start between 06:00 and 17:45, with 62% commencing before midday. This pattern is representative of all regions in the Middle East, with a 09:00 to 11:45 peak in emissions in six of the nine sub-regions. The diurnal regime of the Iranian sub-regions differ from those on the Arabian Peninsula, with both the Dasht-e-Kavir and Hamoon Jazmoorian sub-regions peaking in the early afternoon (12:00 to 14:45). Dust emissions in the Sistan Basin commence earlier than any other sub-region, peaking mid-morning (06:00 to 08:45), potentially driven by the early breakdown of nocturnal temperature inversions, and the redirection of LLJs towards the surface (Choobari et al., 2013; see Section 2.5.5). Nocturnal dust activation is limited to only the Sistan Basin, where 17% of dust emissions occur between 21:00 and 05:45.

4.7   Duration of dust storms across the Middle East

The duration of dust emission, defined by the moment the dust plume appears to detach from source location in the SEVIRI dust RGB imagery – dust storm length may appear different at the surface, produces a range of storm lengths from less than 1 hour to a maximum of 4 days, 9 hours (Sistan Basin, 10/06/2008). The majority (89%) of events last less than 9 hours, with an average of 5.5 hours (Fig. 4.12). dust storms, lasting less than 9 hours, dominate across the Middle East. The highest percentage (33.4%) of longer dust storms occurs in the Sistan basin. Here, the mean duration of dust storms of 7.8 hours is the highest among all sub-regions. Hamoon Jazmoorian has the lowest average duration of dust storm of just 4.3 hours.

4.8   Direction of dust transport from emission source

Direction of dust transport is defined by observation of plume movement and evolution in the period (3 hours) directly after emission. Overall, 56% of all emission events follow a southerly trajectory (S, SW, SE), with only 2% travelling west. Dust plume trajectory also appears to vary by sub-region; each of the sub-regions having their own transport characteristics while bordering regions share similar trajectory patterns (Fig. 4.13). Dust emissions from the Sistan Basin have the most consistent transport route,   with 96% of all dust emission events transported south. Peak JJA dust activity responds to enhanced

northerly winds, referred to as Sistan winds (Choobari et al., 2014), with 99% of emissions transported south. Dust emissions from both Mesopotamia regions are regularly transported south-east apparently in response to the frequent northerly (north westerly) Shamal winds, reported in many previous studies (see Section 2.5) Accordingly, 69% of dust emission in Lower Mesopotamia are transported south east towards the Persian Gulf and Ad Dahna sub-region . Dust emissions from Upper Mesopotamia has a more complex transport pattern, with records 52% of events travelling SE and 25% transported E (25%). Typically, dust plumes, which are transported east directly after emission, merge with emissions down-wind, where they are subsequently transported southeast. Combined with dust emissions from Lower Mesopotamia, these plumes are transported over long distances, covering large areas of the Arabian Peninsula and continuing towards the Arabian Sea, potentially interacting with the Asian Monsson cycle (Zhu *et al.*, 2007). Central Arabian Peninsula records the most variable trajectories, with dust emission peaking slightly to the northeast (22%). A large proportion of dust events from the Ad Dahna sub-region are transported southeast or northeast, mimicking the transport routes of both neighbouring sub-regions. Dust emission are transported in opposing directions from the central Iranian sub-regions Dasht-e-Kavir and Dasht-e-Lut, with the former transporting the majority (48%) of events northeast, while 53% of events are transported south from the latter .
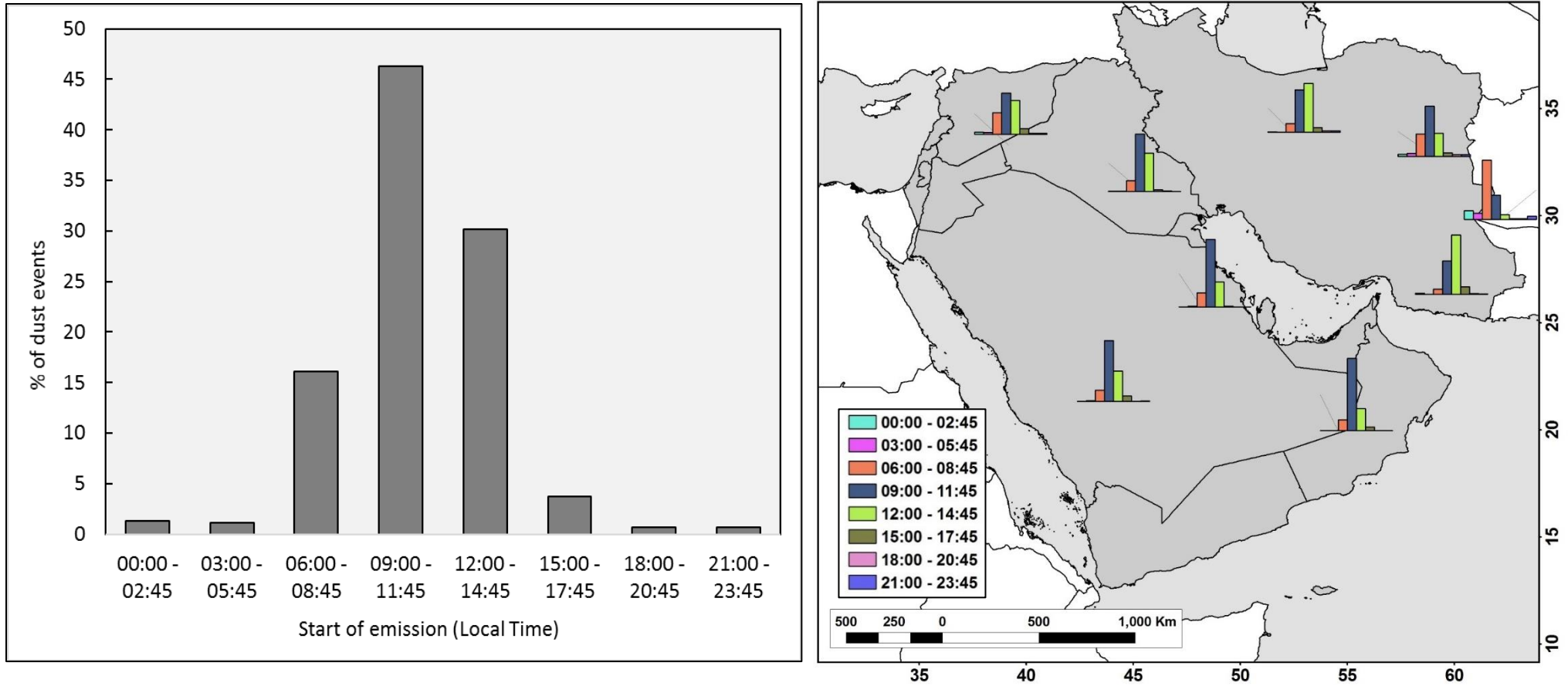
Figure 4.11: Diurnal characteristics of dust storms in the Middle East (A) and the nine sub-regions (B) from 2006 to 2013. Start time of each dust event is binned into one of eight time segments (Local time) (Local time = +3/4 UTC).
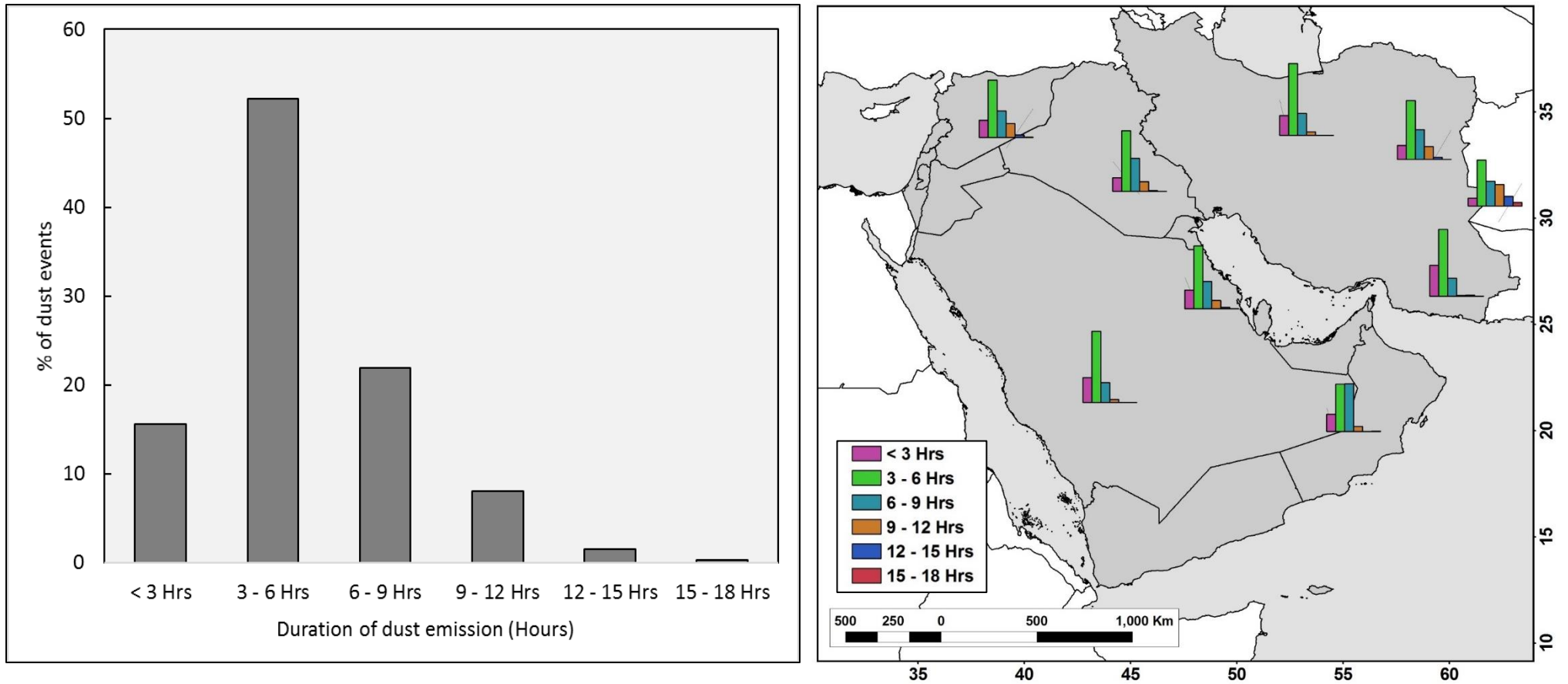
Figure 4.12: Duration of dust emission in the in the Middle East (A) and the nine sub-regions (B) from 2006 to 2013. Dust emissions are binned into six duration periods (shown as % of total emissions). Dust events over 18 Hrs in duration equal 0.3% (94 events) of total events (not shown).
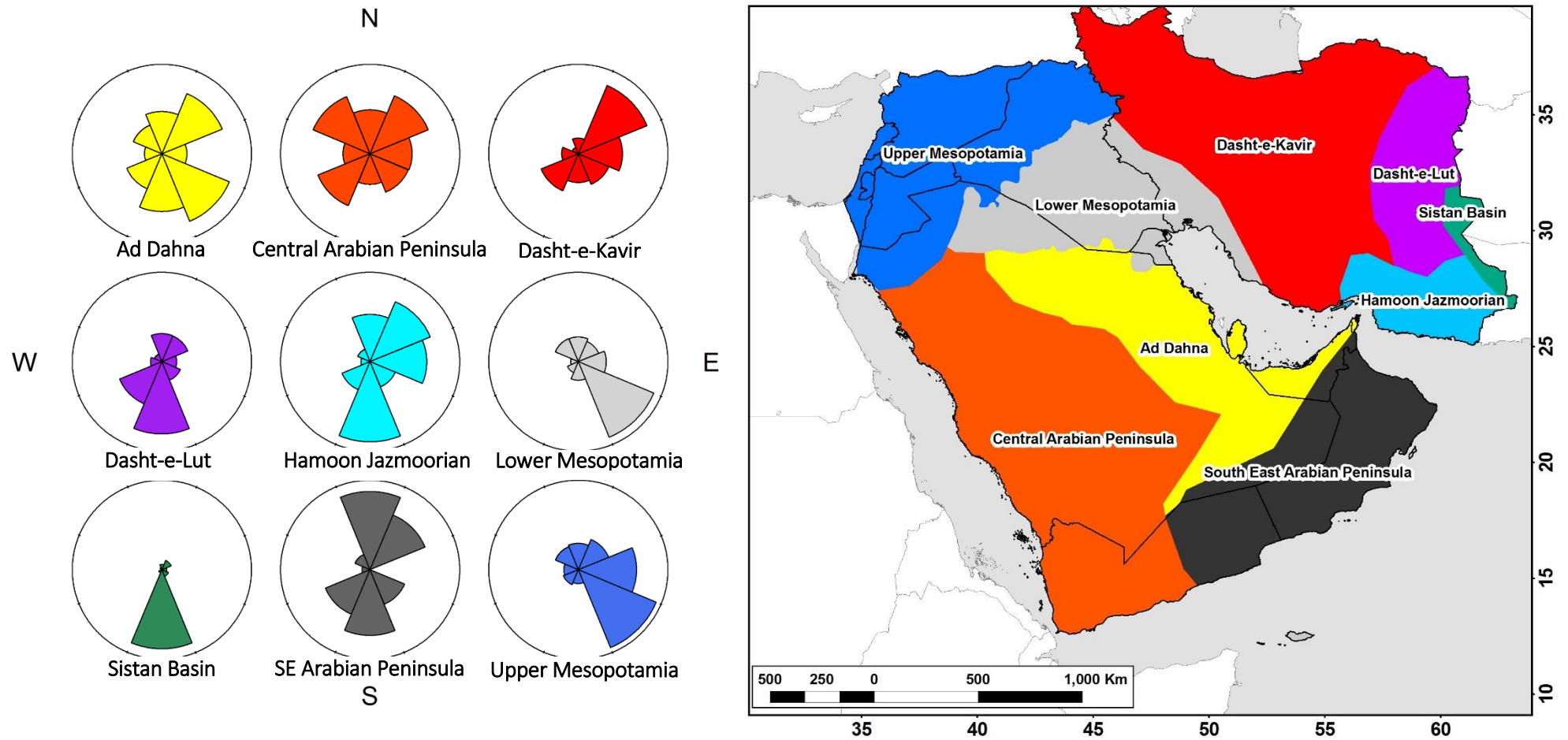
Figure 4.13: Rose plots showing the direction of transport of dust plume directly after emission. Segment size indicates the relative number of dust events that travel in each direction within each of the sub-regions. The colours of each plot depict the respective sub-regions in the insert map (right).

4.9   Degree of Confidence

To assess the influence of cloud conditions on the results, dust events observed at high viewing angle (greater than 60˚E) are excluded (see Figure 4.14). Dust events along the Red Sea coast originate from a narrow strip of coastal plain at the foot of the Asir and Mountains. Here, observations of SEVIRI RGB data show frequent dust emission transported across the Red Sea from the Sudanese coast. Consequently, a low degree of confidence (DOC) score results from contamination of dust of external origin and suspected high column water vapour (CWV) levels, driven by the proximity to coastal winds. Similarly, dust emission generated from coastal winds along the narrow coastal plain of the Makran Coast, also record a lower confidence score. DOC scores in these areas are, therefore, not indicative of cloud conditions and are excluded from the subsequent cloud analysis. Dust emission from sources close to the Persian Gulf are typically generated by offshore winds - as demonstrated by Figure 4.13, and are therefore, less influenced by humid coastal air. DOC scores are therefore, related to cloud conditions only.
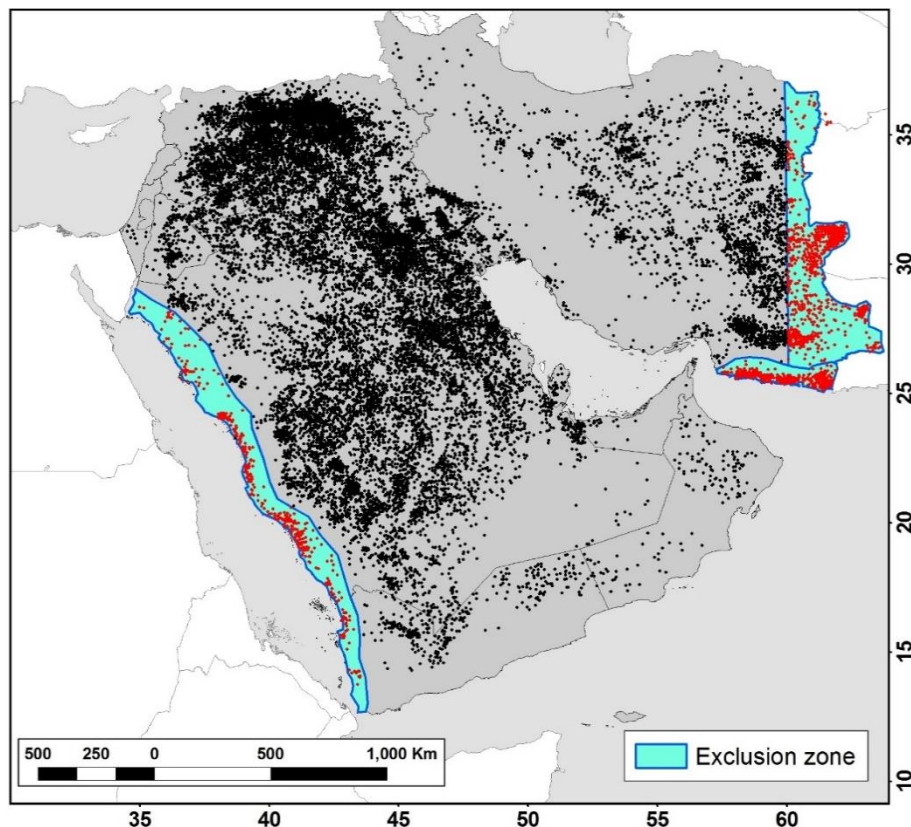
Figure 4.14: Degree of confidence exclusion zones described by distribution of dust emission events from 2006 – 2013. Red points indicate emissions not considered in cloud contamination study, due to influence of high viewing angle (area beyond 60° E) and high column water vapour (Makran and Red Sea coastlines).

Excluding dust events with DOC related to non-cloud related conditions (see Figure 4.14), the total number of events reduced by 11% to 24,692.
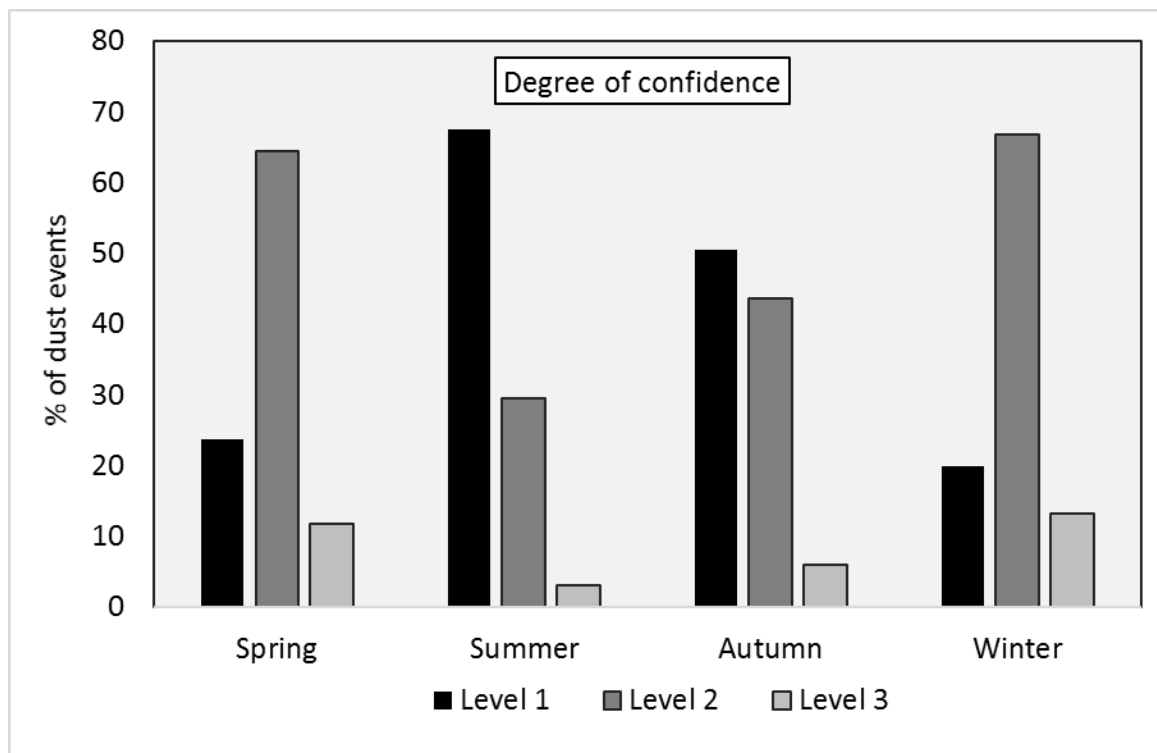
Figure 4.15: Attributed degree of confidence scores, as a percentage of total seasonal dust emissions from 2006 - 2013.

Seasonal changes in DOC result from changing synoptic patterns and atmospheric conditions. Figure 4.15 shows clear sky (Level 1) dust emissions dominate during JJA, representing 68% of all emissions. These months are defined by the Shamal winds (see Sections 2.5.3 and 2.6), created by a strong northwesterly flow in response to persistent positioning of synoptic high and low pressure systems. In contrast, DJF and MAM months are characterised by cloud contaminated dust emission, with 65% and 67% of emissions categorised as DOC level 2 emissions respectively. These seasons are synonymous with travelling sub-tropical depressions (Middleton 1986; see Section 2.5.3). These depressions frequently bring high levels of cloud, especially associated with their warm front (usually to the east of the low centre), with a trailing cold front (usually south or south west of depression centre) which generates significant dust emission (Bou Karam *et al.,* 2010). These conditions characterise level 2 (DOC) type events and explain their dominance during these months. Dust emission tends to be recirculated throughout these storms, sometimes for days at a time; the resulting opacity of the atmosphere makes it difficult to observe new emissions underneath the

depression. The increased number of Level 3 DOC events during these months also appear to be related to this factor, and it is only possible to determine emissions within breaks in the dust and meteorological cloudbank (See Section 3.4.1). SON appears to be a transitional season, with roughly the same number of DOC level 2 and 3 events.
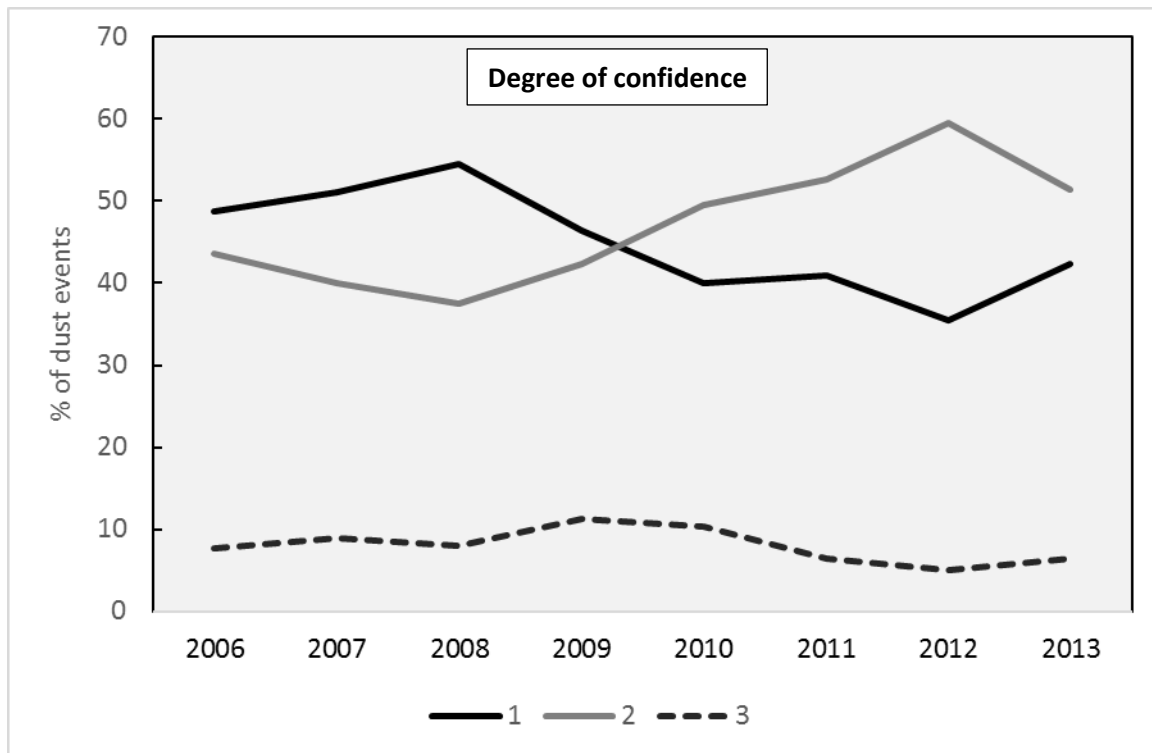
Figure 4.16: Attributed degree of confidence scores, as a percentage of total annual dust events per year.

Inter-annual comparisons of DOC (Figure 4.16) suggests that, compared to the preceding years, dust events after 2009 are more frequently associated with cloudy conditions. 2012 sees the largest reversal from the pre-2009 conditions, this year is unique in the time series, as it sees a strong springtime peak, with maximum number of events occurring in March (See Fig. 4.3). As previously mentioned, MAM dust events tend to occur with migrating sub-tropical depressions, explaining the increased percentage of level 2 (DOC) events. Level 3 DOC events remain low in each year, peaking slightly in 2009 and 2010. Further analysis concerning synoptic and other meteorological factors will be discussed with ECMWF re-analysis data in chapter 6.

4.10   Summary

The results of a new dust emission inventory of the Middle East have been presented here. By using SEVIRI Dust RGB images at a sub-hourly frequency, a high resolution record of dust emission sources and their emission frequency has been produced. In summary, the main findings from these data include the following:

- In total, 27,680 individual dust emissions were identified at source (referred to as dust events) in the Middle East from 2006 to 2013.

- Maximum annual totals of dust events occur in 2013 (4800 individual dust events, 39% greater than the annual mean across the study period). Maximum percentage of dusty days occurs in 2012, with dust emissions observed on 89.4% of all days.

- Dust events in the Middle East peak during JJA season, accounting for 39% of all dust events. Monthly averages peak in June, with an average of 572.7 dust events and 98.8% of dusty days. Maximum dust activity occurred in June 2013, with 931 dust events, 78% higher than the average June (572.7), with 100% dusty days.

- Dust emission is concentrated into specific areas across the region, establishing a clear east to west difference, with 78% of all events originating from the Arabian Peninsula. The alluvial plains of the Tigris Euphrates Basin generated 37% of all events, with greatest activity emanating from the upland areas (150-250 m a.s.l.).

- Distinctly low dust activity was generated from the An Nafud and Rub Al Khali sand seas, all mountain ranges and the southern Arabian Peninsula.

- The regions was divided into 9 sub-regions, defined by the spatial distribution of dust events, prominent dust source areas in academic literature and geographical features such as drainage basins, deserts and mountain ranges.

- Upper Mesopotamia, including the upper reaches of the Tigris Euphrates Basin was the most active sub-regions, with 29% of total dust events.

- Seasonality of dust events vary between sub-regions, with dust activity peaking during JJA in the northern Arabian Peninsula and Eastern Iran, while the southern Arabian Peninsula peaks in MAM.

- Multiple discrete 'hot spots' of frequent dust activity were identified in several sub-regions, which together accounted for 23% of all dust events emanating from 1% of total land area.

- Inter annual comparison of the sub-regions show dust activity increasing in the Arabian Peninsula, especially in the Central Arabian Peninsula and Ad Dahna sub-regions, with the latter producing more dust events than Upper Mesopotamia in 2013. Iranian sources remain relatively consistent, with dust activity in the Dasht-e-Kavir salt desert showing the most inter annual variability.

- The diurnal pattern, duration and trajectory of dust events show some inter-regional differences. The Sistan Basin stands out, with dust emissions lasting longer and commencing earlier in the day than all other regions. Persistent southward transport of dust emission is linked to the known Sistan Winds, peaking in JJA It is thought that the known effect of topographic channelling and early morning breakdown of nocturnal LLJs, linked to the Sistan wind, are demonstrated here by peak dust activity in the early morning hours (06:00 - 8:45 local time).

- In both Mesopotamia regions, the north-westerly (Shamal) winds control dust activity, with each region persistently transporting dust southeast.

- Degree of confidence (DOC) scores attributed to each dust event give an indication of the local cloud conditions at the time of emission. Seasonal patterns of DOC scores illustrate the seasonal cycle of synoptic conditions, synonymous with dust emission in the Middle East. JJA events are linked to summer continental-scale atmospheric circulation, with no active fronts and little cloud contamination, indicated by a high proportion of level 1 DOC. Non-summer events are driven by sub-tropical cyclones, with an active warm front associated with moist convection and high cloud levels, indicated by high proportion of level 2 DOC.

Chapter 5: Land surface characteristics

5.1   Introduction

Understanding dust emission processes in relation to land surface characteristics has many important benefits. Firstly, where dust emission causes a problem to public health or agricultural production (e.g. Tigris Euphrates Basin) (Al-Awadhi and AlShuaibi, 2013; Notaro *et al.*, 2015), correct determination of preferential emission surfaces and the processes driving emission, allow the development of appropriate adaptation methods. Secondly, there currently exists a need for more emission observations, at a high enough resolution to provide a reliable reference for current aerosol-climate models (Todd *et al.*, 2008). In combination with land surface characteristic information, these data will aid in better constraining the emission potential, and thus emission thresholds, for particular land surface types (Walker et al., 2009), improving model performance both in the study area and elsewhere.

In this chapter, land surface processes commonly linked to dust emission (see Section 2.3 and 2.4) are analysed. Firstly, Section 5.2 uses multiple datasets to characterise the dust emission surfaces (determined in Section 4), by land surface data (see Section 3.6) including: vegetation and land use, proximity to rivers and lake basins, topography and geomorphology. Areas of frequent dust emission, described here and elsewhere as 'hotspots', are discussed with regard to land surface processes in Section 5.3. Finally, Section 5.4 summarises the main findings, defining which characteristics appear the most important for dust emission and what additional data could improve the analysis.

5.2   Land surface characteristics of dust emission surfaces in the Middle East

Land surface data have been collected for each of the 27,680 dust events from the 2006-13 dust emission inventory (Section 4). The methodology used to create these data are described in Section 3.6. These data are spatially attributed to each of the dust events using Arc GIS 10.1 software and the results are presented in the following section.

5.2.1 Vegetation and land use

Vegetation cover is known to inhibit surface deflation, increasing the aerodynamic roughness function and thus reducing the inertia of surface winds (Harrison *et al.*, 2001). Seasonal vegetation growth can significantly reduce the deflation potential (Tegen *et al.*, 2002), with inter annual emission flux often controlled by the success of annual vegetation growth (Bryant et al., 2003; see Section 2.3.2).
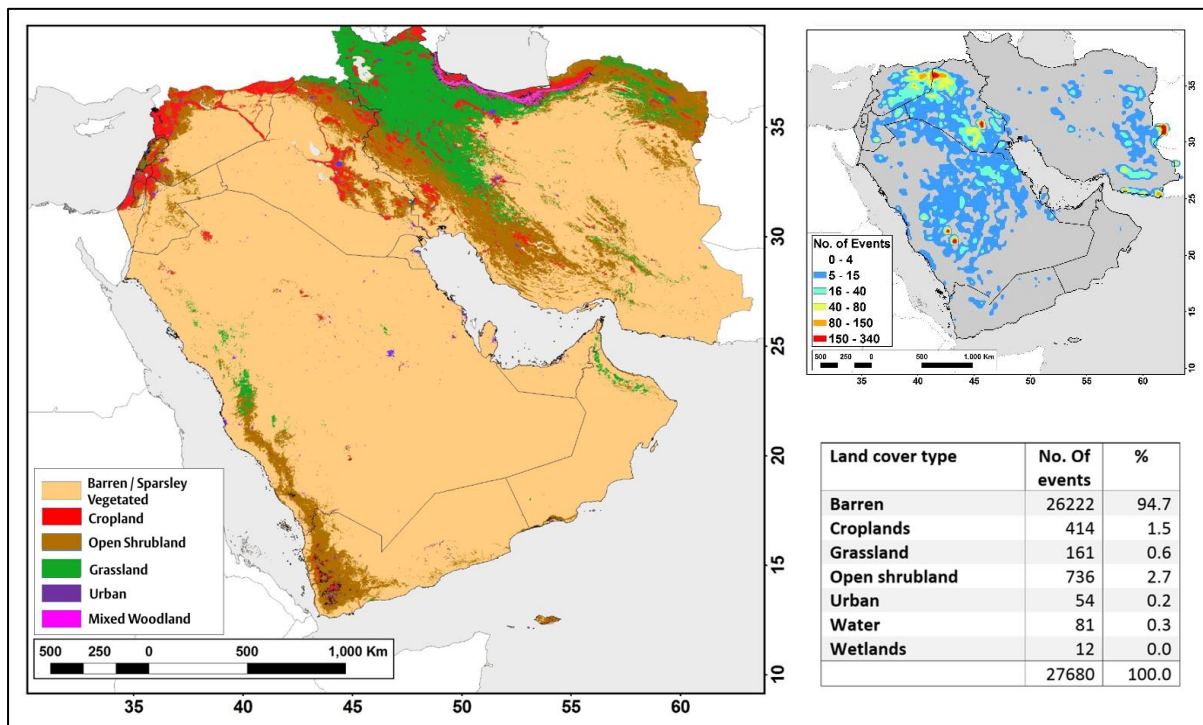
Figure 5.1: MODIS (MCD12Q1) land cover distribution for the Middle East. Insert map: Spatial distribution of dust events shown at 0.25° grid resolution. Insert table: dust emission distribution by land cover type. Land cover data source: Broxton et al. (2014).

The MODIS (MCD12Q1) land cover data (Fig. 5.1) classifies a high proportion of the Middle East as Barren/Sparsely vegetated. Dust emission surfaces reflect this distribution, with 94.7% of all events occurring within this land cover type. Both Open Shrubland and Cropland land cover types show a small proportion of dust events (2.7% and 1.5% respectively), with the majority of these events coming from the Tigris Euphrates basin and along the western edges of the Syrian Desert. Emission frequency appears highest on the margins between barren surfaces and both shrubland and cropland land cover types, particularly within the Tigris Euphrates Basin. Inspection of these margin areas reveals a higher proportion of agricultural

activity than the data in Figure 5.1 describes. Agricultural activity in this region is highly seasonal (Gibson *et al.*, 2015), with winter wheat accounting for up to 80% of local crop production. These surfaces are often left barren during summer months, which may account for the incorrect classification of these surfaces as barren, and resulting in underestimation of dust events from agricultural land cover type.

5.2.2 Fluvial Activity

Dryland river channels are recognised as playing an important role in the transport and accumulation of fine sediment (Kocurek, 1998), depositing this material on alluvial surfaces in the river catchment (Bullard et al., 2011; see Section 2.4.3). The network of river channels in the Middle East is shown in Figure 5.2. Dust emission frequency is presented here on a 0.25° grid, while spatial analysis is carried out at the highest (around 0.03°) resolution offered by the SEVIRI data. To determine the dust emission potential of the land surfaces surrounding river channels, a 10km (0.1°) buffer is projected. This simplistic approach is intended to encompass all riparian land surfaces, including surfaces that are inundated during high flow events. In total, 57% of dust events are found within 10 km or a river channel, and dust events can be found originating adjacent to river channels in all recognised dust emitting drainage basins (Tigris-Euphrates, Sistan and Hamoon Jaz Mourian) and the chain of sources near the Makran Coast. Seasonal trends from these riparian sources are very similar to the non-riparian sources, with each peaking in JJA, with a minimum in DJF.

The simplistic approach suffers from the omission of a topographic model in the 10 km buffer zone. The 10 km buffer radius is not a robust method for classifying riparian land surfaces, especially where river channels flow through steep terrain. To improve the accuracy of results, a hydrological model should be applied that accounts for changing topography, giving a more realistic geomorphological map of riparian land surfaces.

5.2.3 Soil texture

Airborne dust emission and transport are driven by three key physical processes known as saltation, suspension and creep (Gherboudj et al., 2017), the effectiveness of these processes is determined by the particle size range, described here as soil texture (see Section 2.3.1).
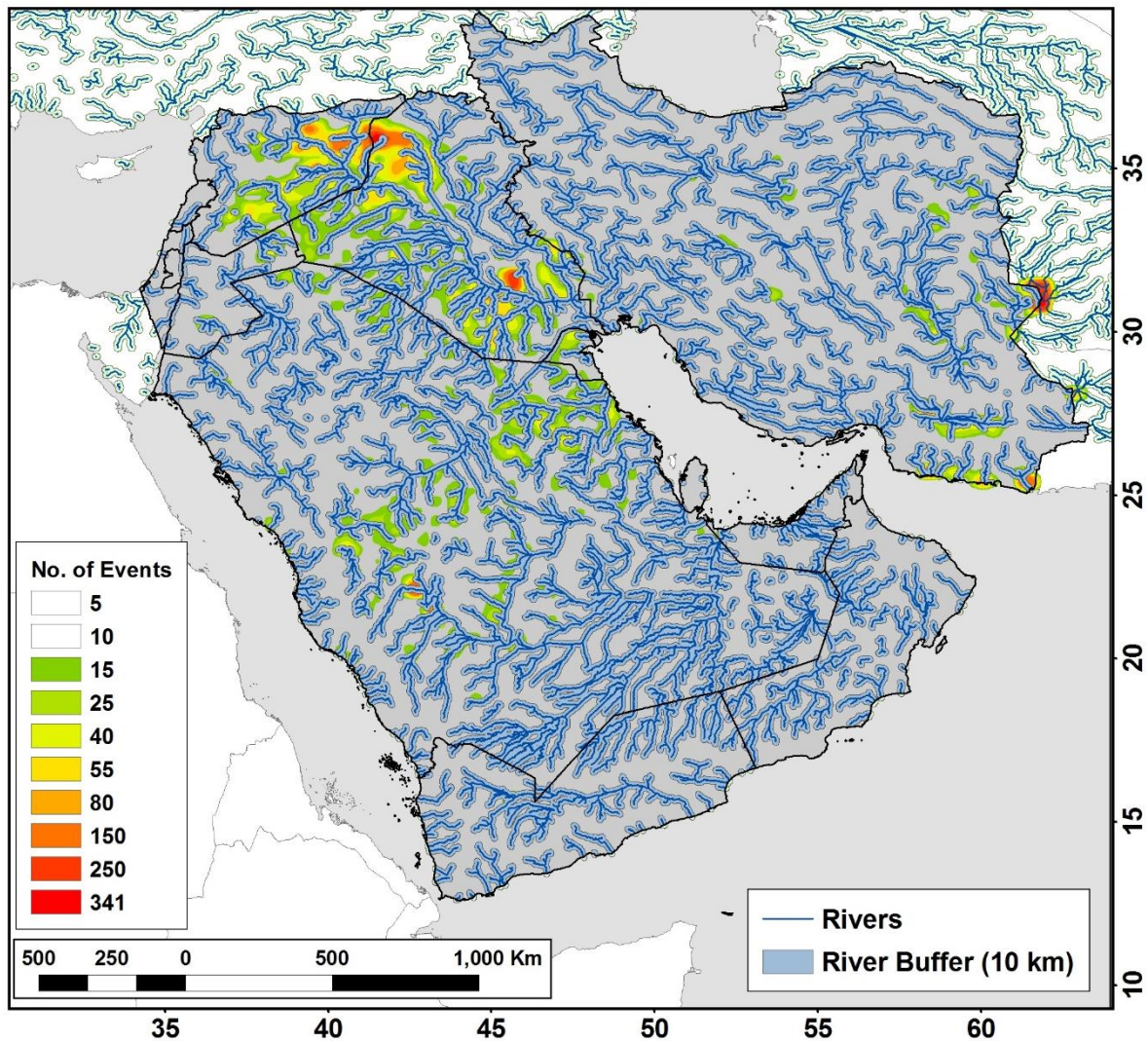
Figure 5.2: River networks of the Middle East, superimposed over dust emission frequency distribution at a 0.25° grid resolution. River channels are buffered to 10km to describe potential alluvial surfaces. River data source: Matsutomi *et al.* (2009).

Soils texture data are provided at a coarse 1° resolution in Webb et al. (1992). While these data provide useful information on the dominant soil types across the Middle East, it is important to recognise that sub-pixel variability is likely. These data indicate a large proportion of the region is made up of loamy soils, which accordingly is demonstrated in the dust source inventory, with 93% of all events originating from a mixture of loamy soils.   Soil texture data for the Middle East (Fig. 5.3) show. This dominance is represented in the dust inventory data, with 93% of all events originating from a mixture of loamy soils. Clay loams are particularly effective, producing 39% of all events, with these soils dominating the lower elevations of multiple drainage basins including the Tigris-Euphrates, Sistan and Hamoon Jazmourian Basins. Soils described simply as loam are the most effective dust emitting soil,

relative to the number of grid squares where it occurs in the Middle East, with frequent emissions in Upper Mesopotamia and Central Saudi Arabia. These soils are preferentially used in agriculture, where their high water retention properties, adequate drainage and organic matter content produce good cropping conditions (Harrison *et al.*, 2001). The mixture of sand and clay sized particles contain enough coarse mode particles (sand / loam) to initiate saltation bombardment and sufficient fine mode particles (clay) to be suspended in atmosphere for long range horizontal transport (Zender, 2003). For this same reason, soils with a significant proportion of sand (sandy loam, loamy sand) are also effective dust emitters, producing frequent dust emissions in northern Syria, the Jordanian Desert and Ad Dahna sand sea. The results support the findings of Bullard et al. (2011), where dust emission is preferentially linked to mixed soils, especially those that contain minimal silt sized particles.
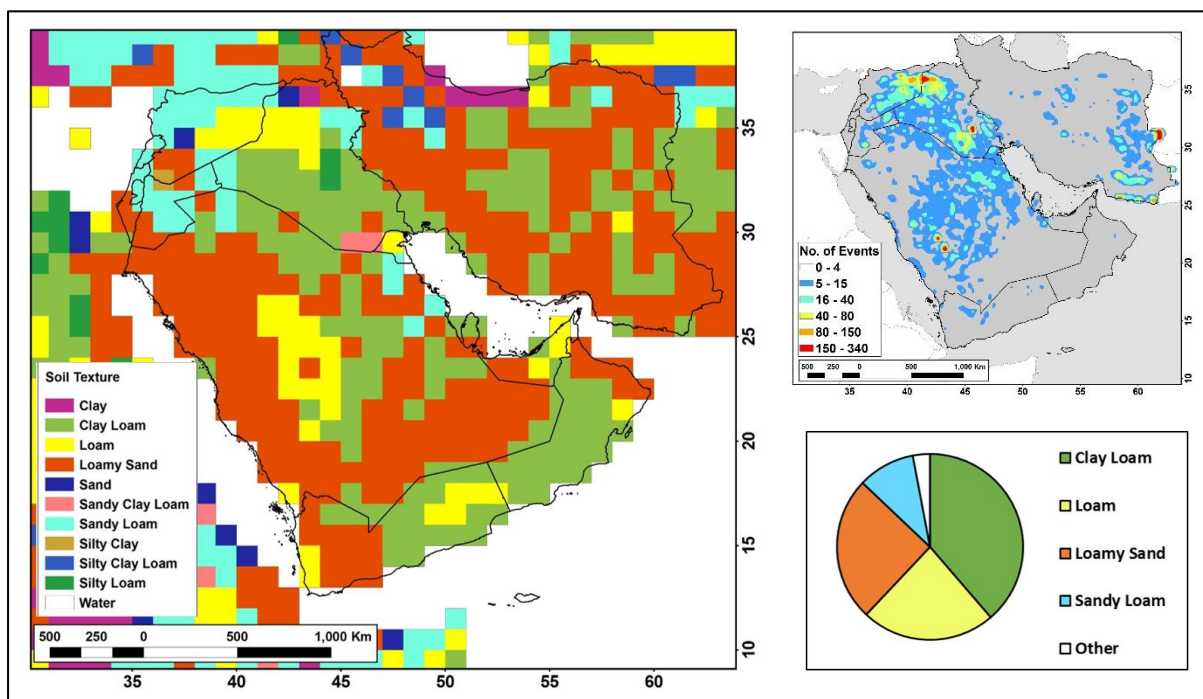
Figure 5.3: Coarse resolution (1°) soil texture distribution of the Middle East using the USDA soil texture classification. Insert map: Spatial distribution of dust events shown at 0.25° grid resolution. Insert graph: Percentage of dust events generated from each of the soil texture types. Source Webb-Rosenzwig global soil profile database (Webb *et al*., 2000).

5.2.4   Land forms and topography

Analysis of sub-basin geomorphology has shown how emission frequency can be dependent of the topographic and geomorphological characteristics of the land surface, resulting in heterogeneous emission flux within any given drainage basin (Baddock et al., 2011; Bullard et al., 2009; see Section 2.4). To enable inter-basin comparisons of the emission frequency from different landform types, a simple classification framework has been produced by Bullard et al. (2011) and adapted by Parajuli *et al*. (2014), where land surfaces are grouped into seven broad landform types (see Section 3.6.5). The Parajuli *et al*. (2014) database identified ten different landform types in the Middle East, with the number of dust events varying considerably between them. Low relief alluvial surfaces were split between agricultural and fluvial surfaces, producing 19% and 17% of events respectively. Combined, these surfaces were the most effective dust emitting landform types in the Middle East, generating frequent dust emission throughout the Tigris Euphrates Basin. Elsewhere, these surfaces do not appear as effective, with fluvial landforms in much of western Iran, Yemen and Oman showing reduced emission frequency.

Ephemeral lakes, including playa and sabkha surfaces generated only 8.5% of dust events in the study area. However, these surfaces are the most effective dust emitters relative to their land area, producing the highest number of dust events per km^2 (0.017), four times greater than agricultural surfaces. A similar pattern was found in Lake Eyre Basin (Bullard et al., 2011) and the Chihuahuan Desert (Baddock et al., 2011; see Section 2.4.2), with emissions frequently emanating from dry lake beds at the base of topographic basins (e.g. Sistan Basin) and along coastal sabkhas (e.g. Makran Coast).

The landform type 'Bedrock with sediments' produced the highest number of events of a single landform type (29 %). This landform type is made up of alluvial sediments over gently sloped or complex bedrock terrain, these surfaces produced a large number of dust events over eastern Iran, Western Saudi Arabia and the Jordanian Desert. These emissions are evenly distributed over a large area relative to other landform types, with few hotspots (Fig. 5.4).

Landform	Area (km²)	% of Study area	No. of events	% of events	No. of events per km²
Low relief agriculture	1,051,323	18.5	4872	17.6	0.0046
Bedrock	775,635	13.6	539	1.9	0.0007
High relief alluvial	1,584,575	27.9	7968	28.8	0.0050
Sand dunes	793,732	14.0	1138	4.1	0.0014
Sand sheet	18,293	0.3	76	0.3	0.0042
Consolidated sand dunes	56,446	1.0	416	1.5	0.0074
Low relief alluvial	955,295	16.8	6435	23.2	0.0067
Stoney surface	298,229	5.2	3780	13.7	0.0127
Playa / Sabkha	136,894	2.4	2356	8.5	0.0172
Water body / Wetlands	14,052	0.2	100	0.4	0.0071
	5,684,474	100.0	27,680	100.0	0.0049

Figure 5.4: Geomorphological landform classification of the Middle East. Inset map: Spatial distribution of dust events shown at 0.25° grid resolution. Inset table: Landform type and dust emission statistics for the Middle East 2006 – 2013. Source: Parajuli *et al*. (2014).

Aeolian surfaces produced fewer dust events relative to alluvial surfaces, with dust emission generated mostly from stone (pavement) surfaces. Stone pavements produced 14% of all events, and contributed a significant proportion of dust events across the Tigris Euphrates Basin and in the northern reaches of the Ad Dahna Desert, with the second highest emission rate per km^2 (0.012). Dune fields and Sand Seas characterise both stabilised and unconsolidated sand deposit landform types, occupying large parts of the Rub Al Kahli, An Nafud and Ad Dahna Deserts. Combined, these three sand deposit types account for only 6% of dust events, despite covering large areas.

Seasonal emission frequency varies between different landform types, most prominently in low relief alluvial surfaces (agricultural and fluvial). Agricultural surfaces produce a significant peak during JJA, generating 51% of all events, reducing to 10% in DJF. Fluvial surfaces have a reduced seasonality, peaking with only 35% of dust events in JJA, with 19% of events in DJF. These results indicate the importance of vegetation cover, with the greater seasonality shown by agricultural surfaces mimicking the growing-harvest cycle of winter wheat, which is commonly grown in the region (Gibson et al., 2015; see Section 2.6). Reduced precipitation and increased temperatures / evaporation prevent crop growth during JJA, leaving unirrigated surfaces barren and susceptible to surface deflation. Post-harvest (MAM – JJA), agricultural surfaces are largely barren, with dust emission frequency increasing as aerodynamic roughness decreases with significant vegetation loss (Notaro *et al.*, 2015). A similar seasonal cycle occurs for playa / sabkha surfaces, producing 41% of events during JJA and just 11% in the winter. Here, reduced ephemeral / seasonal channel flow during JJA conditions result in the desiccation of lakes, exposing fine grained lacustrine sediments to surface winds (see Section 2.4).

Analysis of slope data indicates preferential dust emission from gently sloping surfaces, with 63% of events emanating from surfaces with a slope angle less than 5° (Fig. 5.5). These surfaces accounted for 74% and 61% of all dust events from agricultural and fluvial landform types respectively. Dust events from high relief alluvial features (Bedrock sediments in Figure 5.4), are also limited by surface slope angle, with 87% of these events generated from surfaces with less than 15° slope angle.
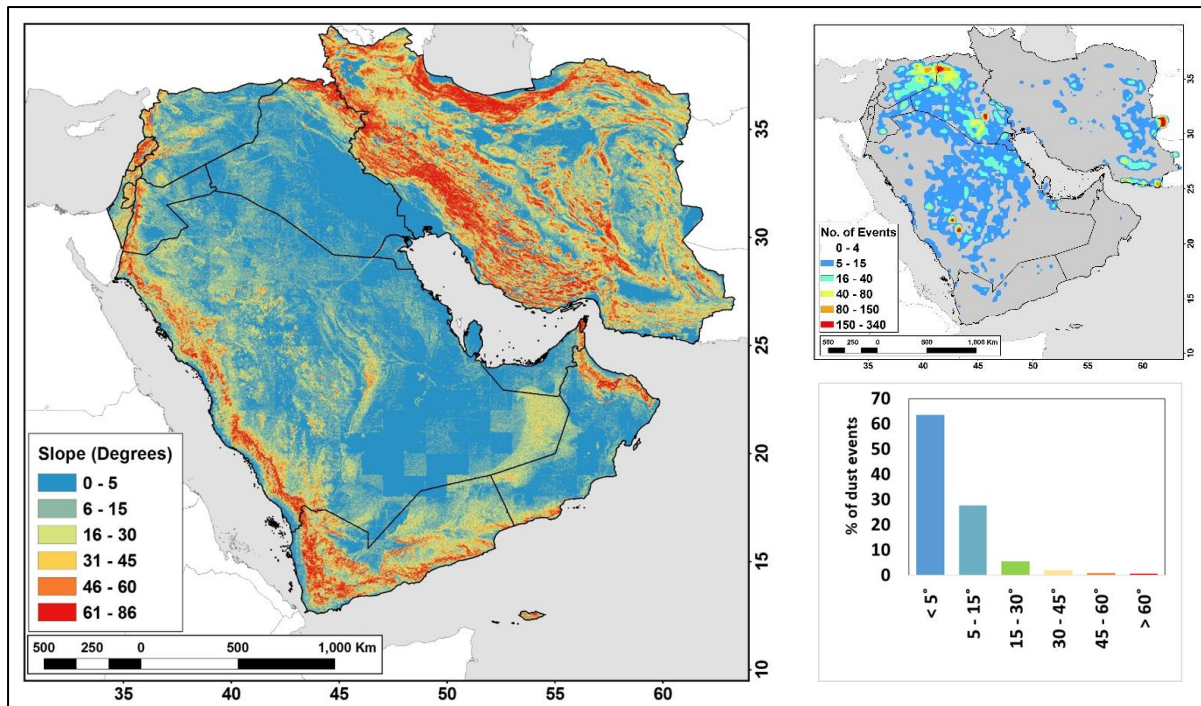
Figure 5.5: Land surfaces slope angle across the Middle East described by GTOPO30 DEM data at 3 arc-seconds (90 m) spatial resolution. Inset map: Spatial distribution of dust events shown at 0.25° grid resolution. Insert chart: Emission frequency of surfaces binned into 6 slope classes. Source: USGS.

Elevation data in Figure 5.6 demonstrates the concentration of dust sources within many of the topographic depressions in the region. These include the large Tigris Euphrates Basin (~1,600,000 km^2) in the north west of the region, bordered by the high (over 2,500 masl) Zagros Mountains to the east and Taurus Mountains to the north. Here, dust emission is confined to the elevations below 500 masl. These emissions account for a high proportion of the dust events below 100 masl, and the peak around 300 masl in the Figure 5.6 elevation histogram. Other prominent topographic features include the smaller Hamoon Jaz Mourian and Sistan Basins in Eastern Iran, with the latter producing a substantial number (940) of dust events over a relatively small range of altitudes (470 and 480 masl). Dust emission across Iran is constrained to flat inter-mountain wadis and topographic sumps, shown especially along the Dast-e-Lut valley desert in eastern Iran, where dust emission is confined to the lowest elevations (250 – 500 masl) at the base of the Kuh-e Deneband (31.5°N, 57.5°E) and Kuh-e Bagh-e Bala (30.5°N, 57.7°E) Mountains. Further north, the spatial distribution of emission surfaces follow the inter mountain valleys in the Khorassan Razavi Province, an area not previously recognised as a dust emitting region.
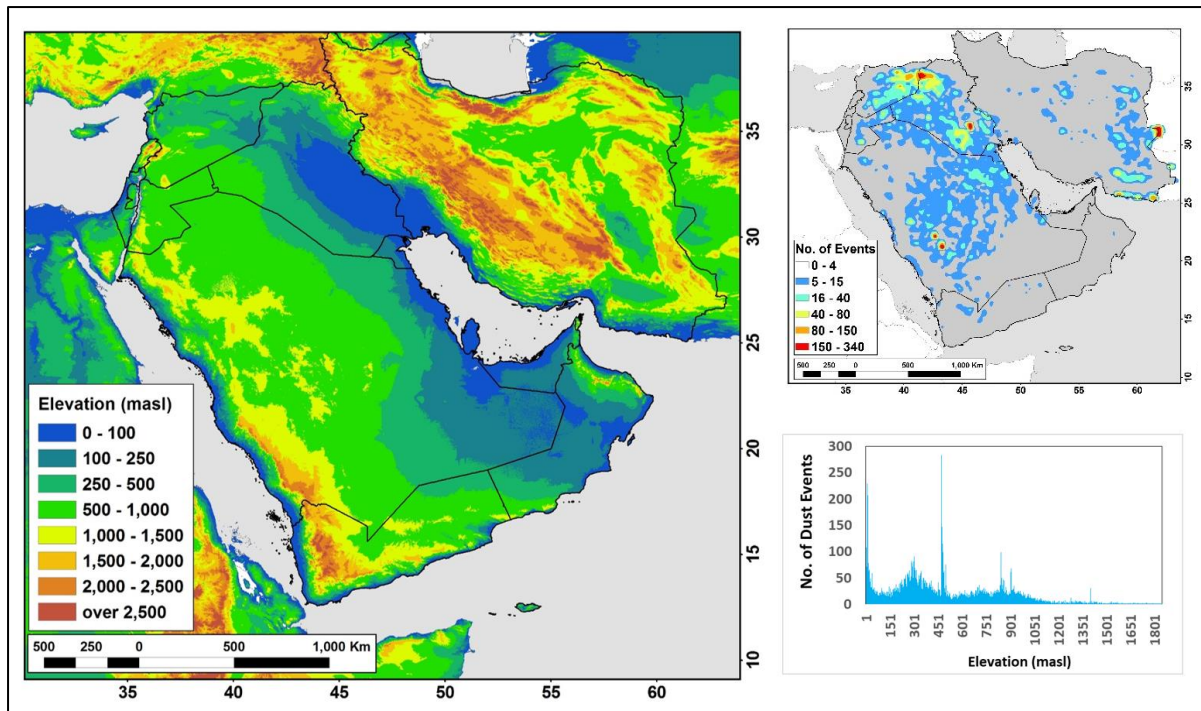
Figure 5.6: Elevation data across the Middle East described by GTOPO30 DEM data at 3 arc-seconds (90 m) spatial resolution. Inset map: Spatial distribution of dust events shown at 0.25° grid resolution. Inset chart: Histogram of dust event elevation. Source: USGS.

Typically, the peaks shown in the elevation histogram (Fig. 5.6) represent the elevation of areas of frequent dust emission (i.e. hotspots) in Figure 5.7, with two further hot spots identified by the increase in dust events at 841 and 904 masl, signifying the height of the two hotspots in western Saudi Arabia (location F in Fig. 5.7).

The highest peak occurs at 1448 masl, representing a dry lakebed in centre of the Kuh Rud Mountains in Central Iran. This small area produces 31 dust events, too few to be considered a hot spot but active enough to be of note.
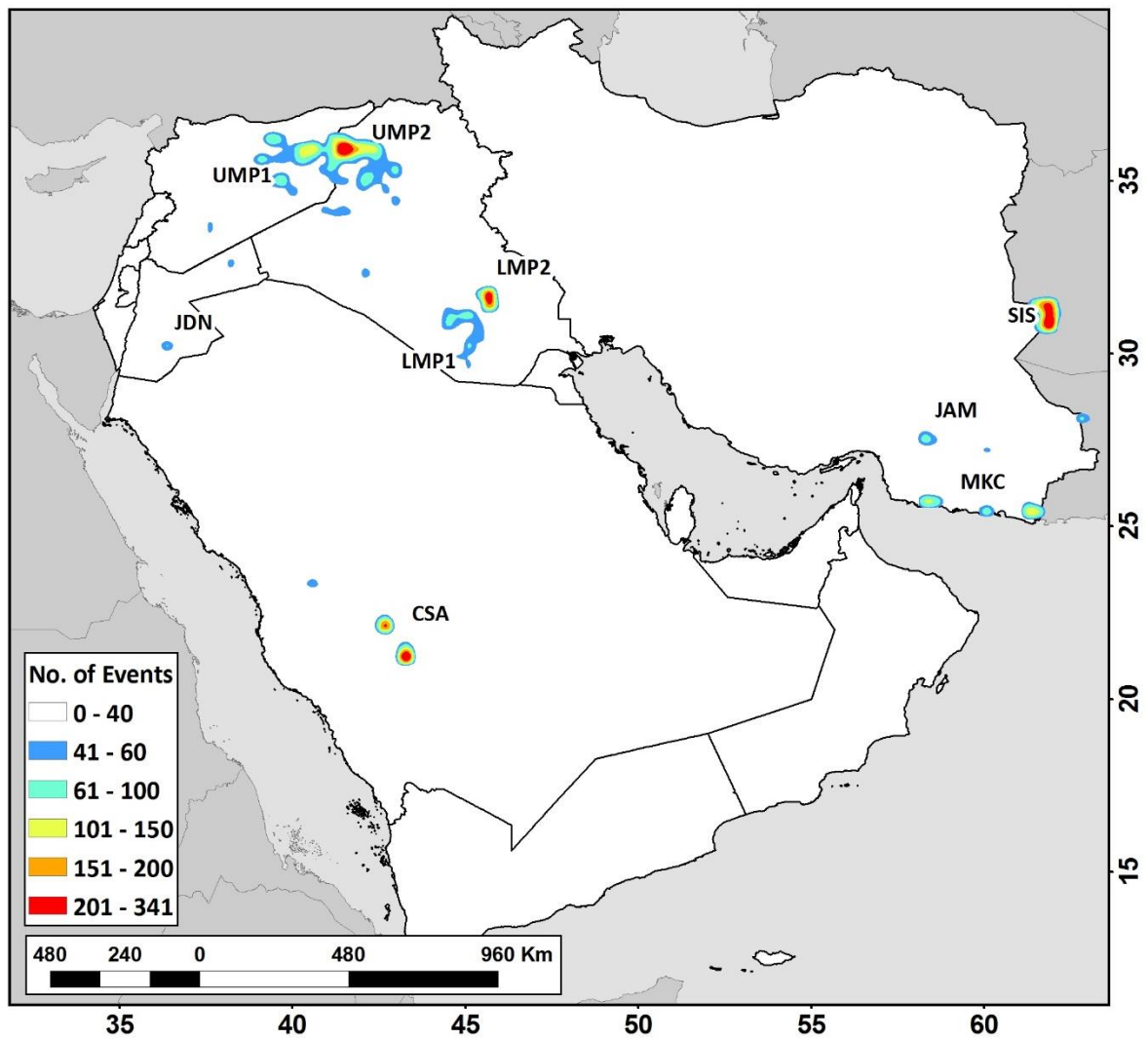
Figure 5.7: Areas of frequent dust emission (Dust Hotspots) - determined by subjective analysis of SEVIRI imagery during the period 2006 – 2013. Frequency of dust emission events are binned into 0.25° grid, with only those areas producing more than 40 dust events shown.

5.3   Dust Hot Spots

As noted in Section 4.3, concentrated areas of frequent dust emission are typically linked to specific land surface features. From the dust emission inventory (Section 4), nine individual regions have been identified in the Middle East (Fig. 5.7). By area, these hotspots account for just 0.9% of all dust-emitting surfaces, yet produce 4135 dust events, 15% of total dust emissions during 2006 – 2013 period. Each hotspot produces its own seasonality (Fig. 5.9), which typically corresponds to the sub-region it belongs to (see Section 4.4). These hotspots are defined by specific land surface features including agricultural land use, aeolian sand dunes and fluvial features including ephemeral lakes, river flood plains and palaeolakes. In the following section, the dust emission frequency of these hotspots are analysed with regard to land surface characteristics, described by the data in Section 5.2 and aerial imagery.

5.3.1   Upper Mesopotamia agricultural surfaces

The Upper Mesopotamia sub-region produced the highest number of dust events of all sub regions in this study (Section 4.4), a large proportion of these events were located in the upland areas between the Tigris and Euphrates Rivers in northern Iraq and northern Syria. The source of highest emission frequency is close to the Iraq/Syria border (Fig 5.8a), near the town of Baa'j (35.9˚N, 41.5˚E); this location is the most active dust source in the entire Middle East. The area is characterised by loamy soils over gently sloping terrain, with aerial imagery showing a large network of agricultural fields, and river channels draining from the northwest. Agriculture is dominated by rain fed winter wheat (see Section 5.2.4) with monthly observations showing a distinct increase in dust activity in late Spring, before peaking in June in the post-harvest period (Fig. 5.9). The JJA peak in emission is also driven by increased summer Shamal winds (see Section 2.5).

This area, described as UMP2 (Upper Mesopotamia 2) in Table 5.1, covers approximately 6,639 km^2, producing 1,163 dust events in total, from predominately agricultural and fluvial surfaces (45% and 40% respectively). Dust emission frequency peaks in 2008/09 and 2012, with a noticeable drop in dust events in the following years 2010 and 2013.

West of UMP2, dust emissions emanate from a mixture of gently sloping agricultural and barren surfaces, surrounding a group of playas (Albu Gharz, al Burghuth, and Ar-Rawda)

surrounding the Syrian city of Al Raqqah, on the northern banks of the Euphrates River (Fig. 8b). The landform type here is described as fluvial in the Parajuli *et al*. (2014) database, but 38% of dust emissions appear to emanate from the playa surfaces. Evidence from aerial images confirm the importance of aeolian processes in this area, with clear wind streaks – deposited fine sediment dust, forming in the wake of low topographic features (Fig. 8b), indicating the prevailing north-westerly winds.

The hotspot called UMP1 in Table 5.1, comprises three individual areas with a combined area of approximately 4,217 km^2, producing a total of 440 individual dust events. The most active hotspot lies in the east (Fig. 5.8), generating 137 dust events. Like UMP2, dust activity in UMP1 peaks in JJA, with minimal dust activity between September and May. These source areas were most active between 2007 and 2009, and relatively less active between 2010 and 2013.
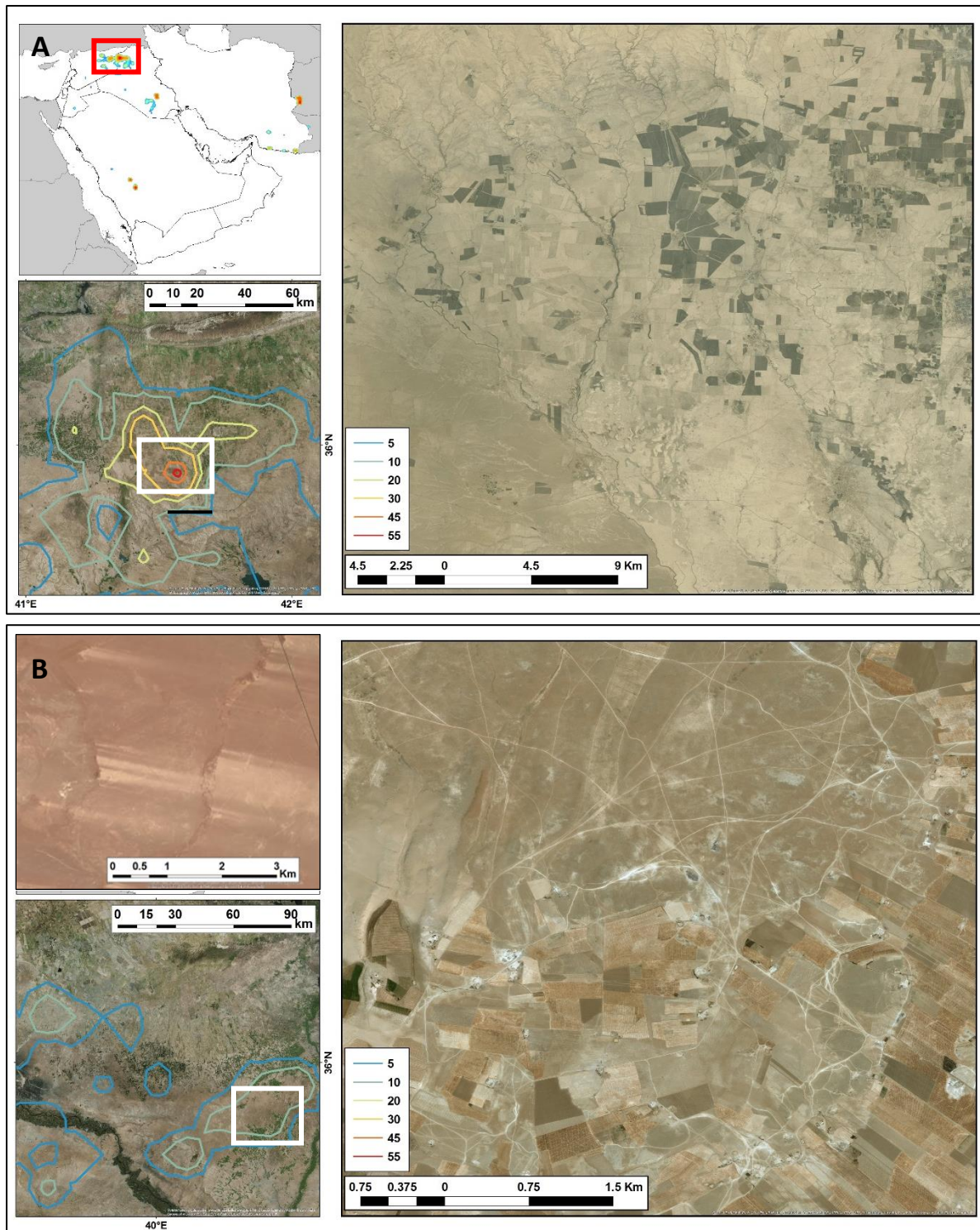
Figure 5.8: Surface features of dust emission hotspots in Upper Mesopotamia (red box), including: A: Agricultural fields in northwest Iraq. B: Agricultural (main panel) and wind streaks (top left) in northeast Syria, north of the Euphrates River. Contour data describes dust emission frequency data at 0.1° resolution. White box describes location of image in the respective main panel. Source: ESRI Digital Globe.
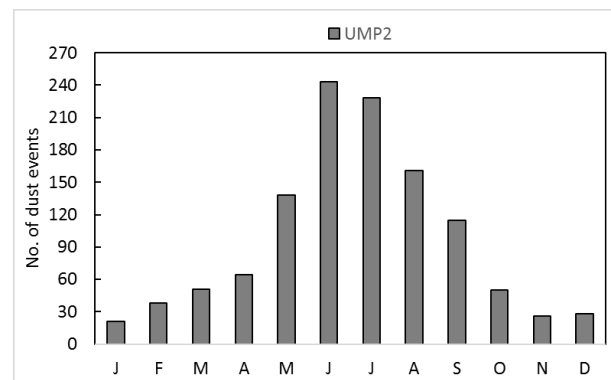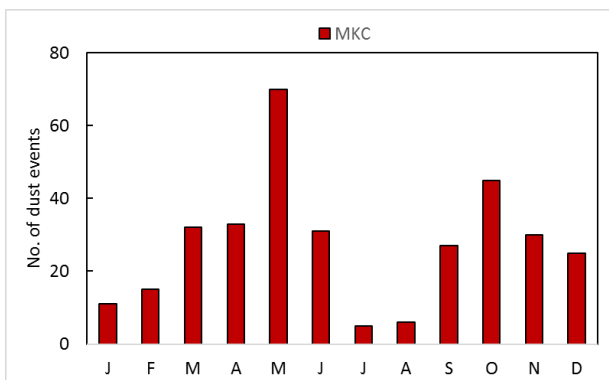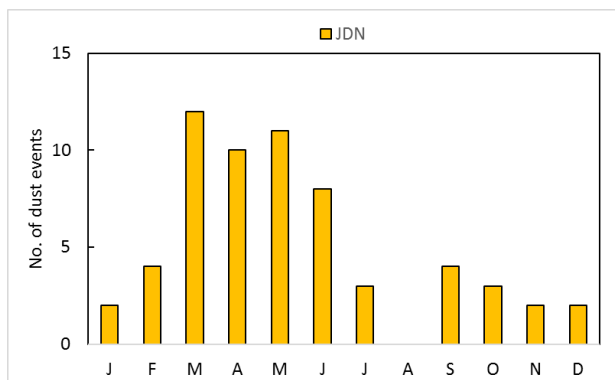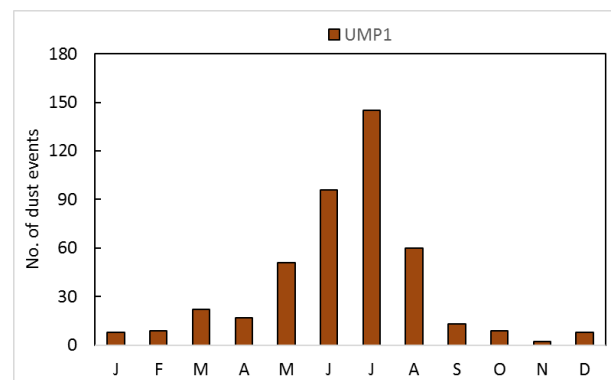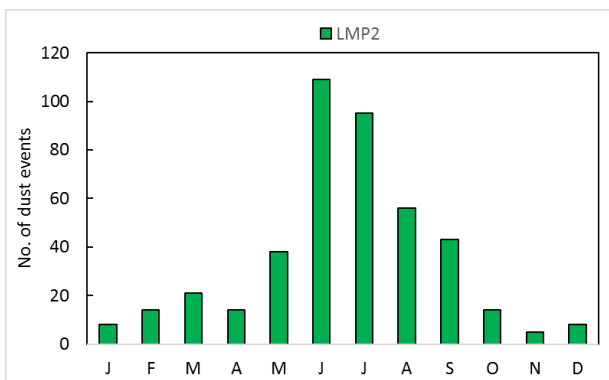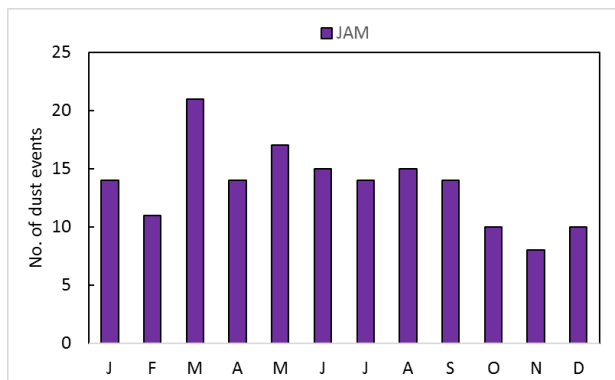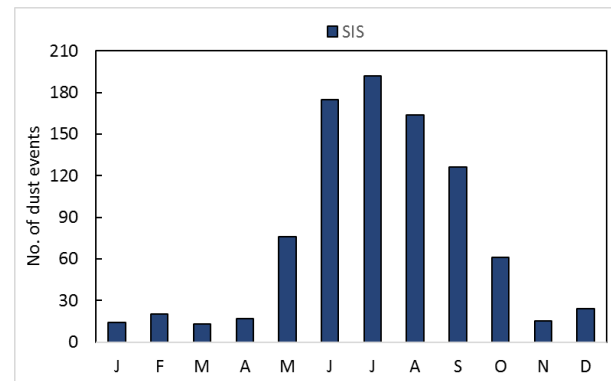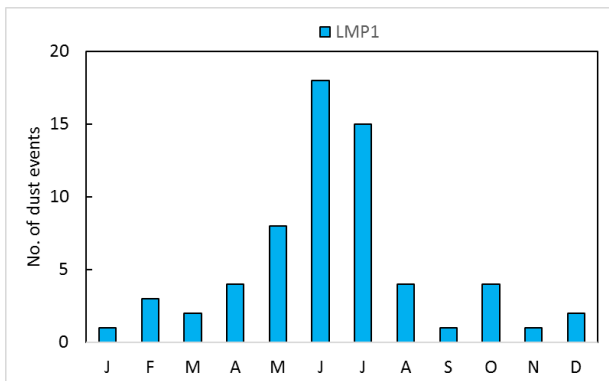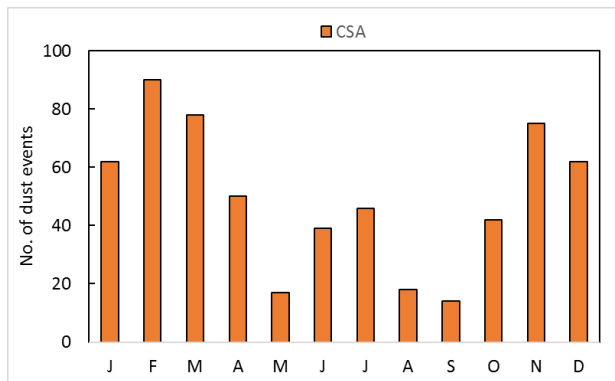
Table 5.1: Statistical data of the number of dust events produced by the nine dust hotspots highlighted in Figure 5.7. The source of topographic and landform type data are described in Section 3.6. The top two landform types are shown where dust emission come from more than one type.

Dust Source Reference	Figure	Location	Area (km²)	No. of Events Total	No. of Events Average (per km²)	Dust source average height (masl)	Average slope (%)	Land form Type	% of events
CSA	5.12a	21.1˚N, 43.2˚E; 22.5˚N, 42.7˚E	6951	593	0.09	873	2.3	Bedrock (Sediments)	100
JAM	5.13a	27.5˚N, 58.3˚E	452	163	0.36	395	1.4	Agricultural	75
								Fluvial	15
JDN	5.12b	30.2˚N, 36.2˚E	563	61	0.11	847	1.9	Fluvial	100
LMP1	5.11a	31.1˚N, 45.1˚E	1385	63	0.05	224	5.1	Stoney Surface	100
LMP2	5.11b	31.5˚N, 45.6˚E	2982	425	0.14	10	0.6	Agriculture	100
MKC	5.13b	25.2˚N, 61.2˚E; 25.2˚N, 60.0˚E; 25.5˚N, 58.5˚E	7356	330	0.04	330	3.7	Playa	72
								Bedrock Sediments	18
SIS	5.14	30.6˚N, 61.5˚E	2466	897	0.36	477	0.9	Playa	57
								Agricultural	25
UMP1	5.10b	35.9˚N, 39.0˚E	4217	440	0.1	315	3.61	Agricultural	62
								Fluvial	38
UMP2	5.10a	35.9˚N, 41.5˚E	6639	1163	0.18	311	4.5	Agricultural	45
								Fluvial	40

Figure 5.9 (overleaf): Monthly averages of dust events in each of the nine dust hotspots highlighted in Figure 5.7
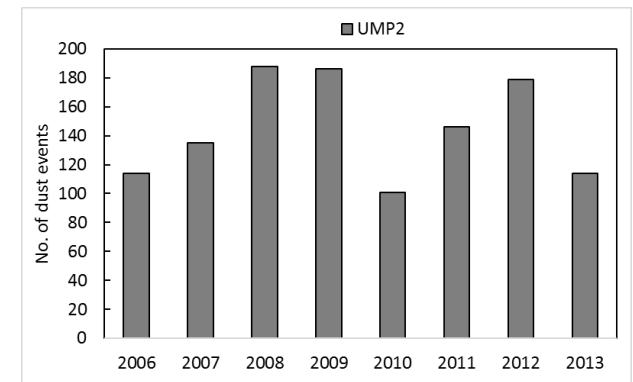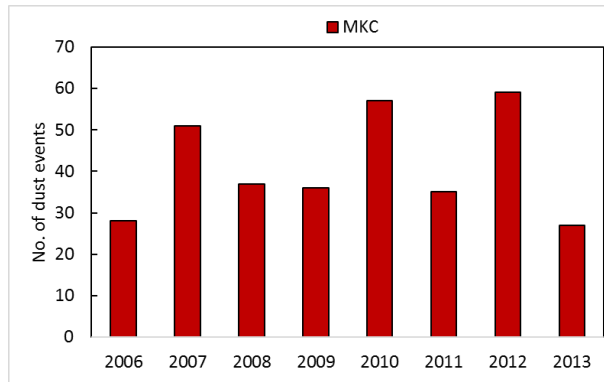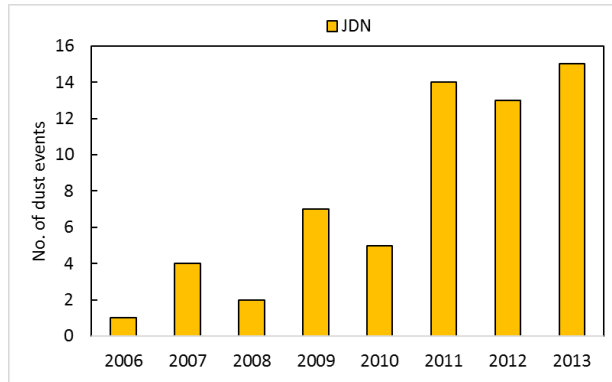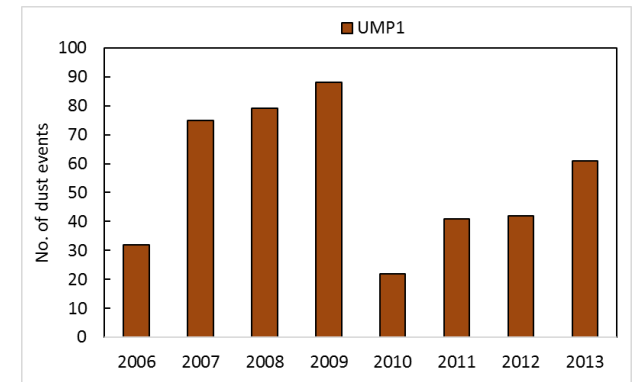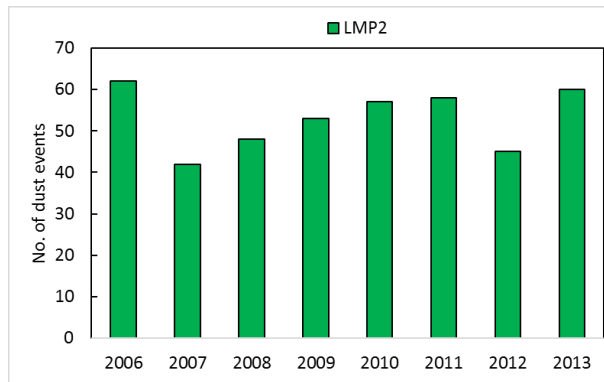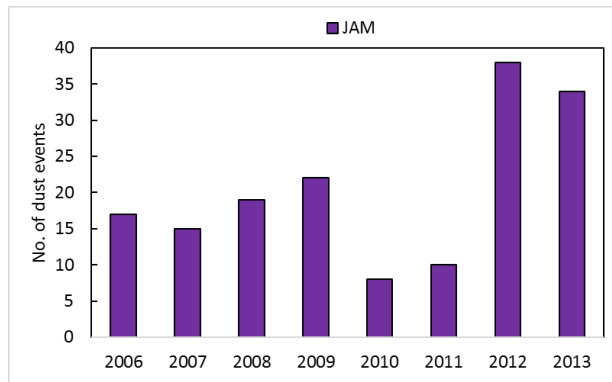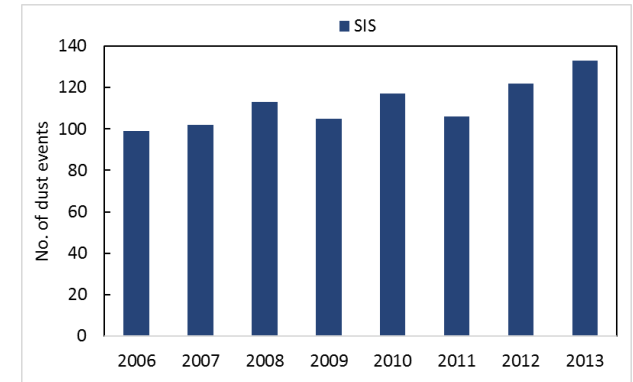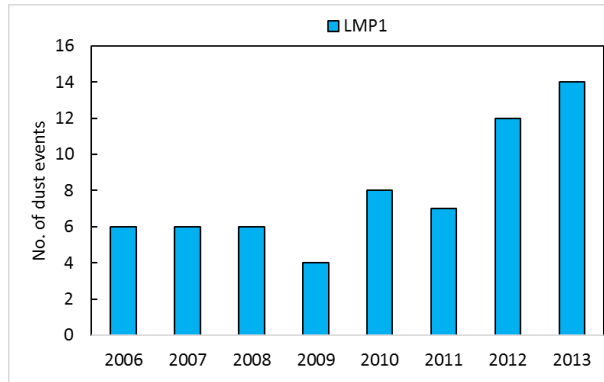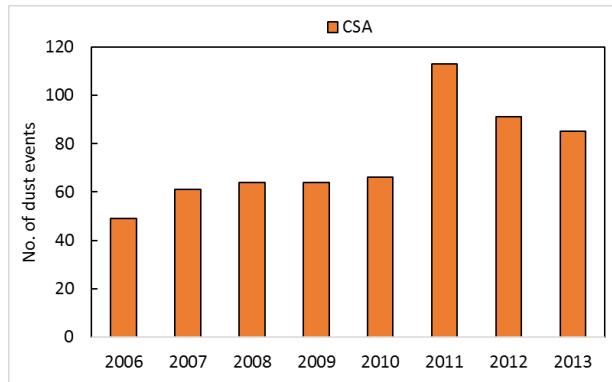
Figure 5.10 (overleaf): Inter-annual comparison of the number of dust events in each of the nine hotspots highlighted in Figure 5.7.

5.3.2   Stone Pavements in Lower Mesopotamia

In the lower elevations of the Tigris Euphrates Basin, an area of bare ground which appears to have once been agricultural, appears now as an aeolian landscape with migrating barchans dunes travelling southeast (Fig. 5.11a). The cause of agricultural abandonment is unknown; however, implementation of extensive upstream river control and increased demand on agricultural irrigation since the 1980's is recognised as the leading cause of increased desertification in the area (Richardson, 2005). The land surfaces surrounding the hotspot are extensively cultivated, and is classified as agricultural in the Parajuli *et al*. (2014) database. This flat area is located just north of the Euphrates River, and is intersected by multiple river channels, lakes and irrigation canals, along with a road with flood protection infrastructure. The lighter coloured sediment near the dunes indicate fine sediments, which may have formed during seasonal flooding events.

This hotspot, called LMP2 in Table 5.1, covers 2,982 km^2, producing a total of 425 dust events, with greatest concentration to the north. Dust activity is highest during JJA, peaking in June (109 events), and reducing to minimal activity from September until May (Fig. 5.9). Inter annual variability is low, with a maximum number of dust events in 2006 (Fig. 5.10).

There is another hotspot further southwest in the Al Muthanna province of southern Iraq, in the Samawah Desert. Figure 5.11b shows this to be a barren environment, with fine sediments (light coloured patches) on the gently sloping lands (locally known as Marhab) between areas of low relief. This area is defined as stoney surface (stone pavement) in the Parajuli *et al*. (2014) database, a surface normally associated with low dust emission potential (Bullard et al., 2011). Close inspection of aerial imagery shows evidence of vehicle tracks across the mud flats (Fig 5.11b). Vehicular disturbance of mud crusts and stone pavements could expose loose sediments to surface winds.
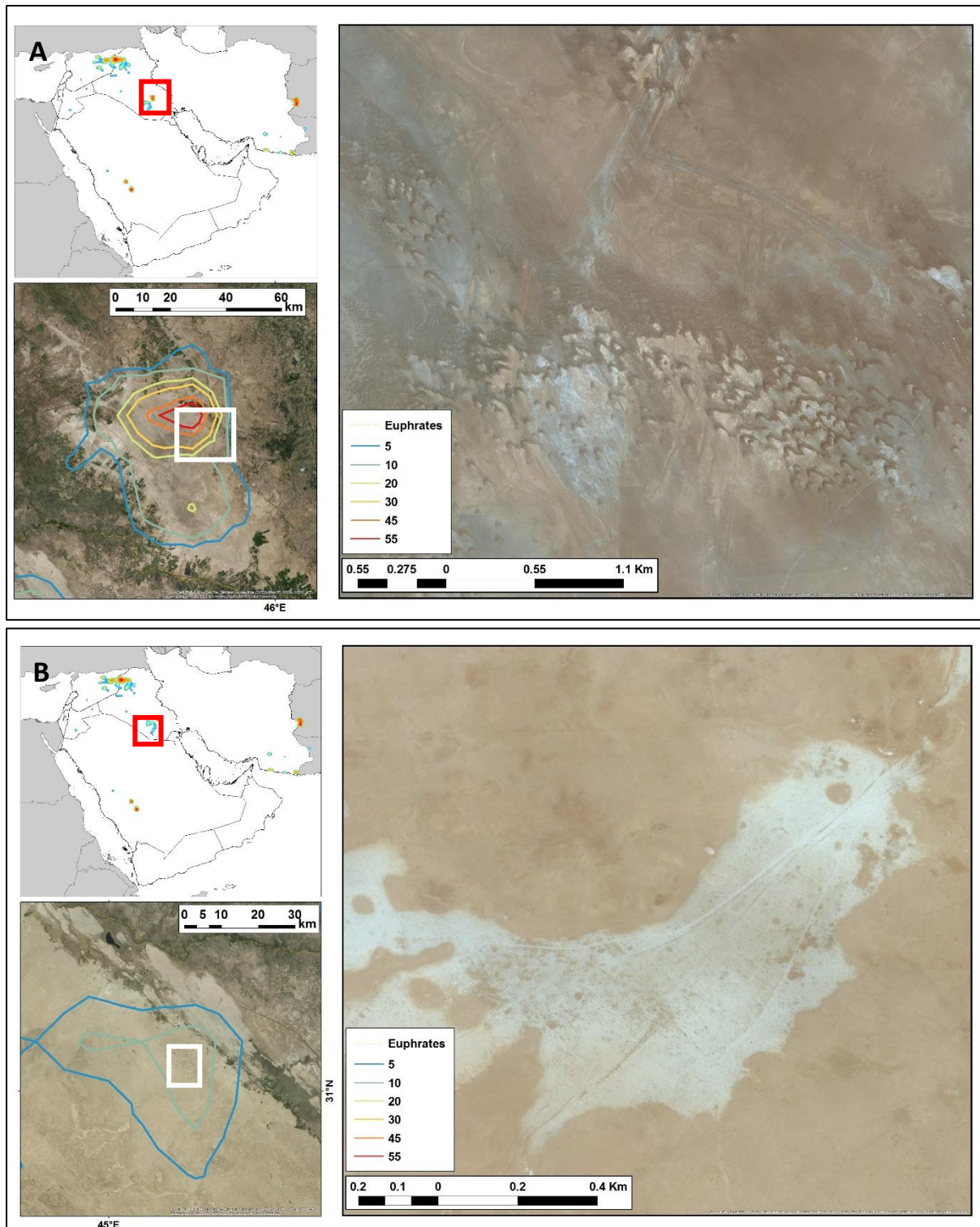
Figure 5.11: Surface features of dust emission hotspots in Lower Mesopotamia (red box), including: A: Barchans sand dunes near abandoned agricultural fields in southeast Iraq. B: Disturbed mud flats in the Al Muthanna province of the Samawah Desert, in southern Iraq, with evidence of vehicle tracks. Contour data describes dust emission frequency data at 0.1° resolution. White box describes location of image in the respective main panel. Source: ESRI Digital Globe.

This area is called LMP1 in Table 5.1, covering approximately 1,385 km^2, producing 63 dust events in total. The seasonality is similar to LMP2, with increased dust activity in late Spring (May) before peaking in June (Fig. 5.9). Dust activity quickly reduces, with minimal activity between August and April. Unlike LMP2, dust activity has been increasing during the last 5 years (2009-2013), up by 250% (Fig. 5.10).

5.3.3   *Palaeolakes and contemporary dust emission*

A map of palaeolake and palaeochannel distribution is given in Breeze et al. (2015), covering the Arabian Peninsula south of 32°N. In comparison to North Africa, the Arabian Peninsula does not show evidence of extensive palaeolakes at the scale of the Bodélé Depression, but there is a large number of small-scale palaeolakes, averaging 6.1 km^2 in area. Dust emission events do not correlate directly with palaeolake areas; they mostly originate from larger-scale geomorphological and contemporary fluvial features (see Section 5.2). An exception to this is the largest of the Breeze et al., (2015) palaeolakes, in the Jordanian desert close to the city of Ma'an. Dust emission is concentrated in the northeast corner of the 1221 km^2 palaeolake, producing 61 dust events, with peak activity in MAM (Fig. 5.9). Aerial imagery identifies multiple vehicle tracks within the flat palaeolake bed, with the area appearing as a frequently used transport route (Fig. 5.12a). While individual vehicles are incapable of producing dust plumes at the scale observed in the SEVIRI Dust RGB imagery, vehicular disturbance of the top soil could alter the soil roughness and infiltration properties of the surface, increasing the proportion of fine material available for surface deflation (Frank et al., 2007; Gill, 1996). The landform type is described as fluvial in the Parajuli *et al*. (2014) database, with numerous contemporary drainage channels around the lake perimeter (Fig 5.12a). Positioned on the edge of a basalt desert (Gherboudj *et al.*, 2017), these fluvial channels will be rich with fine sediments liberated by basalt weathering, providing the area with a seasonal / ephemeral supply of dust sized particles. Dust activity was minimal prior to a sudden increase in 2011, with dust activity peaking in 2013 (Fig. 5.10).
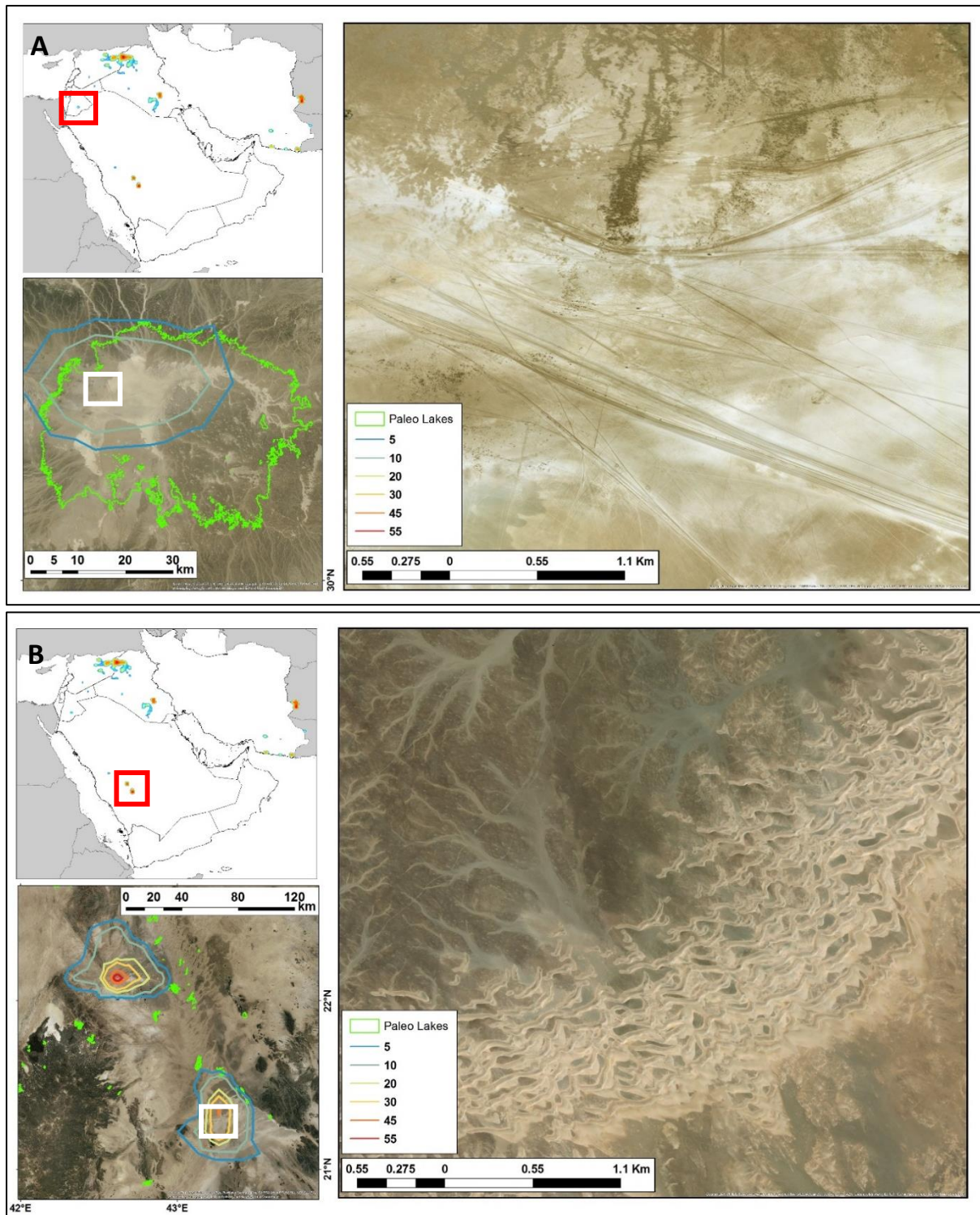
Figure 5.12: Surface features of dust emission hotspots in Jordan and Saudi Arabia (red box), including A: Palaeolake bed in the Jordanian Desert (green outline) near the city of Ma'an (main panel). B: Aeolian-fluvial margin area in western Saudi Arabia, east of the ancient lava flows of the Asir Mountains, with active sand dunes crossing fluvial channels. Contour data describes dust emission frequency data at 0.1° resolution. White box describes location of image in the respective main panel. Source: ESRI Digital Globe.

In Saudi Arabia, a chain of discrete emission hotspots runs adjacent to the Asir Mountains, in close proximity to ancient lava flows. The two most active sit in a valley interspersed with multiple small palaeolakes (Fig. 5.12b). Dust emission does not appear to emanate from these palaeolakes, deriving instead from a network of fluvial channels at the margins of local sand dunes in the valley sump (Fig. 5.12b). Satellite imagery shows evidence of ephemeral channels draining into each emission hotspot, carrying silt rich flood waters from the basalt deposits of the ancient lava flows in the surrounding hills. Dust emission is likely enhanced by the saltation bombardment of sediment crusts from local sand dunes during high wind speeds, in a process commonly seen in other arid environments such as the Taklamakan Desert, China (Wang *et al.*, 2014).

These hotspots, referred to as CSA in Table 5.1, cover a combined area of 6,9510 km^2, producing 593 dust events. These sources have a complex seasonality (Fig. 5.9), peaking in February and November potentially in response to a higher frequency of high wind speeds and ephemeral flows during the non-summer months. Minimal dust activity takes place during late Spring and late Summer. The number of dust events peaked in 2011 with 113 dust events (Fig. 5.10), 53% more than the average.

5.3.4   Agricultural and Fluvial sources in South East Iran

Two areas of frequent dust activity are found in the south east of Iran, on either side of the Central Makran Mountain range (Fig. 5.13). The Jaz Moorian basin to the north of the range sits in a depression and contains a semi-permanent lake, with annual precipitation ranging from 100 – 200 mm a^{-1} and average evaporation approximately 250 mm a^{-1} (Rashki *et al.*, 2017). Dust activity is minimal around the lake bed at the centre of the basin (black square), with emission surfaces concentrated on the gently sloping agricultural surfaces surrounding the silt and clay rich Bampur and Halil rivers (from the east and west respectively) (Fig. 5.13 and Fig. 5.14a). Referred to as JAM in Table 5.1, dust emission is generated from multiple surfaces, with a combined area of 452 km^2 compared to the total 69,600 km^2 basin. These surfaces generating a total of 163 dust events. Dust activity continues throughout the year, peaking in early Spring, supporting the findings of Rashki et al. (2017). Dust activity more than tripled in the last two years of observation, from 8 events in 2010 to 28 events in 2012.

South of the Central Makran Mountains, a chain of discrete emission sources lie along the Makran coast. Emission surfaces are described as sabkhas in the Parajuli *et al*. (2014) database, with each dust emission hotspot occurring where upland river channels drain onto the relatively flat coastal plains (Fig. 5.13 and Fig. 5.14b). Aerial imagery shows significant evidence of agricultural fields and coastal sand dunes close to each hot spot (Fig. 5.14b). Referred to as MKC in Table 5.1, dust emission surfaces cover 7,356 km^2, producing a total of 330 dust events. Dust activity is highest during MAM, peaking in May, with a noticeable reduction in activity during the JJA, where only 12% of dust events occurred. Dust activity varies from year to year with no apparent trend, peaking in 2012 (59 dust events), with a minimum in 2013 (27 dust events).
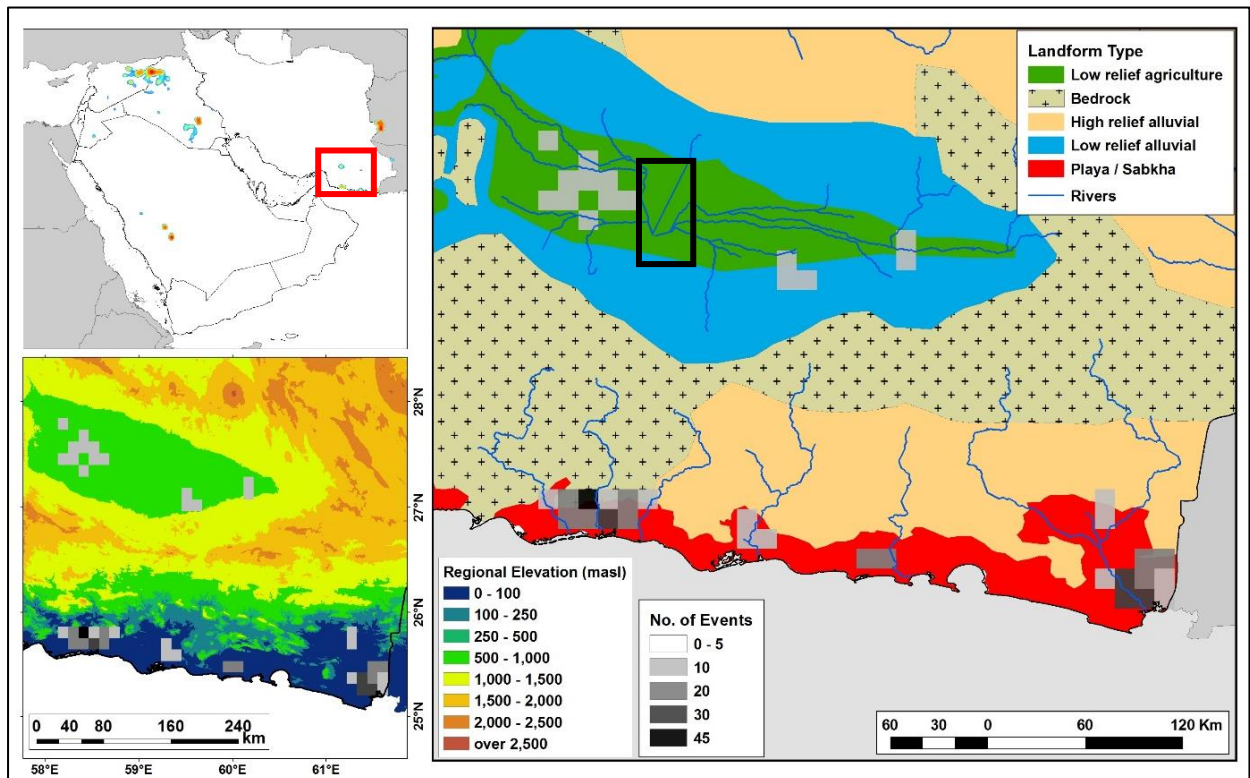
Figure 5.13: Dust emission frequency in the Hamoon Jazmoorian basin and Makran coastline of southeast Iran (red square). Elevation data is shown in the bottom left pane with landform type data in the main pane. Emission frequency is depicted on a 0.1° grid (grey shading) with fluvial channels shown as blue lines. Black box describes the area of the semi-permanent Jaz Moorian dry lake. Source: ESRI Digital Globe.
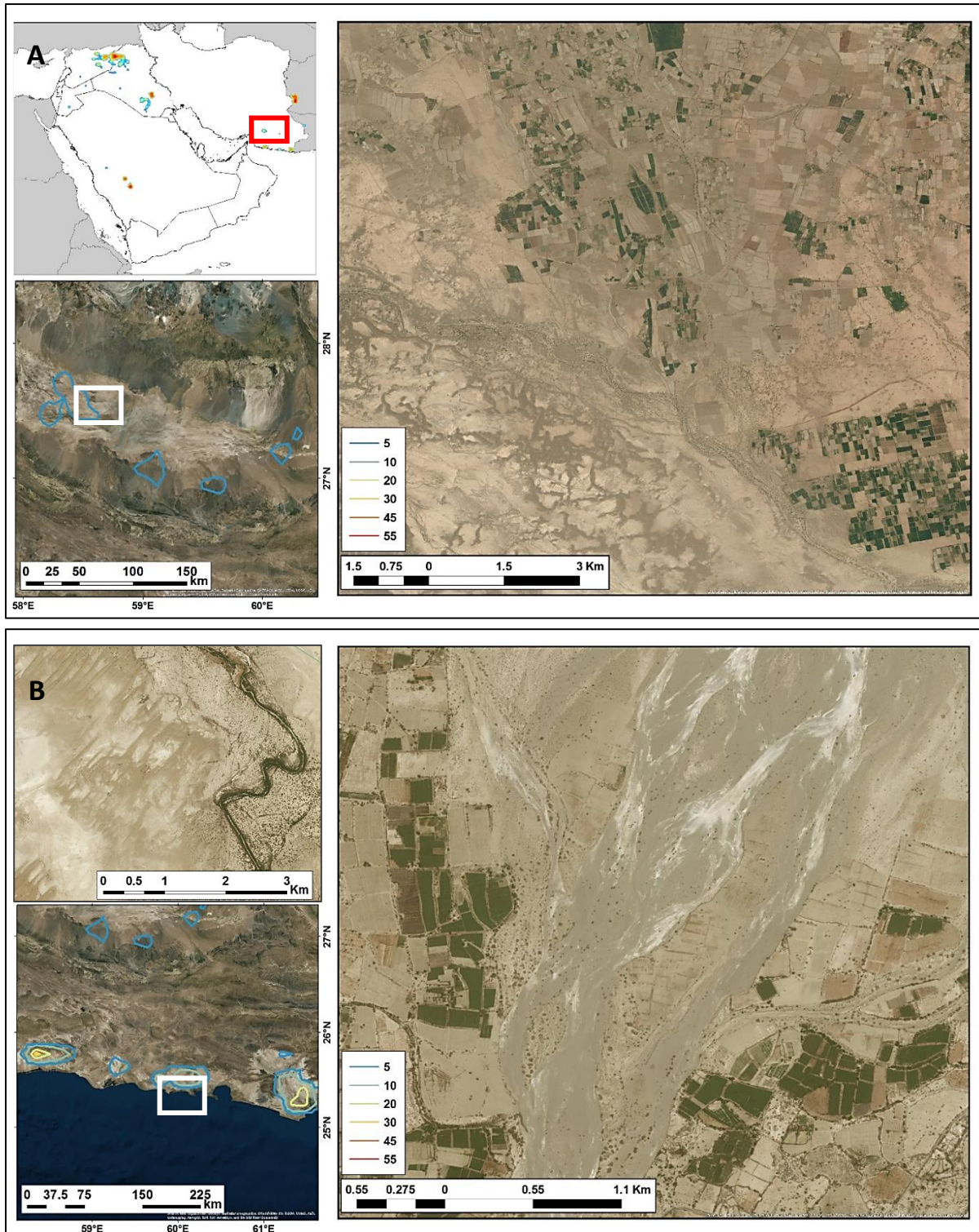
Figure 5.14: Surface features of dust emission hotspots in southeast Iran (red box), including: A: Fluvial and agricultural alluvial surfaces near the Halil River in the Hamoon Jazmoorian Basin. B: Fluvial and agricultural alluvial surfaces as mountain rivers discharge onto the coastal plain along the Makran coastline. The coastline contains multiple sabkhas, with evidence of coastal dunes (B: top left). Contour data describes dust emission frequency data at 0.1° resolution. White box describes location of image in the respective main panel. Source: ESRI Digital Globe.

5.3.5   Ephemeral Lakes in the Sistan Basin

The Sistan Basin is a topographic depression at the base of the Sistan Mountians in eastern Iran. The basin is a major dust emitting area, producing 897 dust events from emission surfaces covering 2,466 km^2. Several river channels drain into the Sistan Basin, including the Helmand, Khash, Farah and Hãrūt Rivers from the Dasht-i-Margo desert to the east. Dust emission is concentrated in areas within and surrounding three ephemeral lakes to the north and east of the city of Zabol (Fig. 5.15a). Emissions surfaces are predominantly characterised as playas in the Parajuli *et al*. (2014) database, while a smaller proportion are generated from agricultural surfaces to the east of Zabol.

Dust emission from the basin is extremely seasonal, increasing concurrently with reduced channel flow and increasing strength of the Sistan Winds during JJA (Choobari et al., 2014; see Section 2.5). The number of dust events peak in July, with an average of 24 dust events (Fig. 5.9), only four less than the most active dust source in the Middle East (UMP2). Analysis of aerial imagery shows an aeolian landscape in the south east of the basin (Fig. 15b), characterised by fast moving barchan dunes, with a southeast trajectory (determined by dune shape), driven by the Sistan Winds. Dust emission observations describe a southerly trajectory for 98% of observations, which could represent a south easterly trajectory given the curvature of the Earth surface at such a high viewing angle (Fig. 5.15b).

The results of this study do not support the increase in AOD observed in 2008 by Kaskaoutis et al., (2014). Data from this study demonstrate that the number of 2008 dust events is no higher than other years. Indeed, inter-annual variability is relatively low, with a minor increase in dust activity in the later years of observation (2011 – 2013) (Fig. 5.10). As AOD and emission frequency are separate measurements, one is not entirely dependent on the other. The events observed in 2008 in this study may have been of higher intensity, producing a larger flux of deflation material due to higher (15 – 20 m s^{-1}) than average wind speed for June (Kaskaoutis et al., 2014).
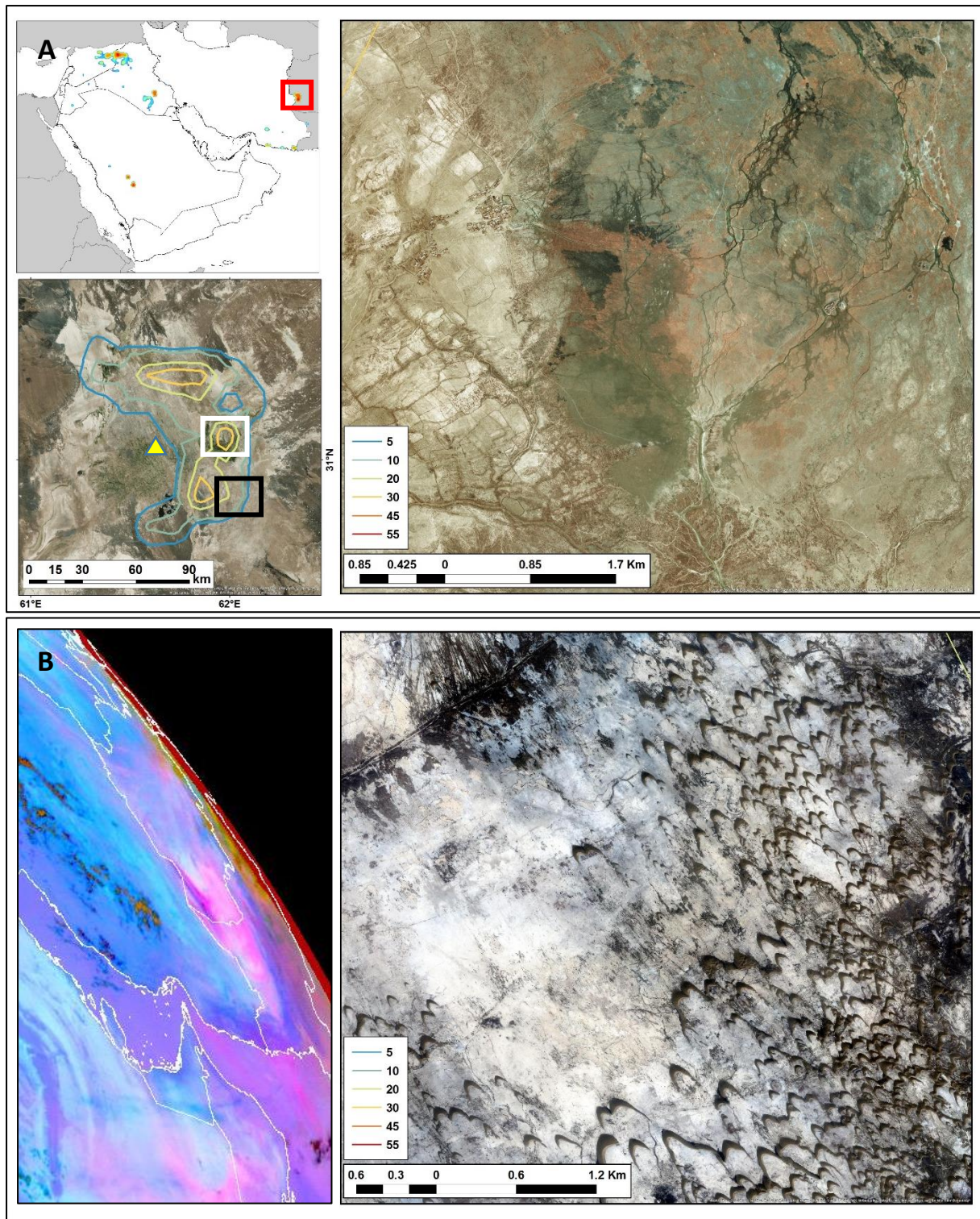
Figure 5.15: Surface features of the Sistan Basin dust emission hotspots in eastern Iran (red box), including: A: Ephemeral Lake beds to the east of the city of Zabol (yellow triangle).   B (main panel): Barchans dunes in the southeast of the basin (black square in 15A), showing a southwest trajectory. B (small panel): An example of southerly Sistan dust emissions from SEVIRI RGB imagery (03/07/2011, 06:15 UTC), see Section 3.3 for technical specification. Contour data describes dust emission frequency data at 0.1° resolution. White box describes location of image in the respective main panel. Source: ESRI Digital Globe.

5.4   Conclusion and synthesis

Analysis of dust emission models has demonstrated a need for more dust emission observations as a reference to improve dust emission thresholds for specific land surface types. In this chapter, land surface data describing vegetation cover, river networks, soil texture and landforms have been spatially attributed to the dust emission events recorded in the Middle East dust source inventory 2006 -2013 (see Section 5). Analysis of emission frequencies from different land surface types can be summarised by the following:

- Dust emissions preferentially derive from barren or sparsely vegetated surfaces (greater than 98%). However, the MODIS (MCD12Q1) land cover database does not fully account for the observed pattern of dust events, with many dust emissions emanating from surfaces that appear agricultural in aerial imagery. These are expected to have significant vegetation cover during growing seasons, remaining barren during hot and dry periods post-harvest.

- Fluvial emissions (i.e. emissions emanating within 10 km of river channels) account for 57% of all dust events, reflecting the increased emission potential associated with fluvial processes.

- Coarse resolution (1˚) soil texture data shows the Middle East is dominated by loamy soils, with a higher proportion of dust emission coming from clay loam soils, found most frequently at the base of topographic depressions. Agricultural loam soils are the most effective soil texture for dust emission, producing the greatest number of events per grid square unit.

- Landform classification describes preferential emission (over 70% of observations) from alluvial surfaces of varying relief, while topographic data show 63% of events emanate from flat or gently sloping surfaces (less than 5˚). These data confirm the previously inferred link between agricultural surfaces and areas of frequent dust activity, with these surfaces present in many of the Middle East emission hotspots.

Overall, these data suggest that gently sloping alluvial surfaces, with loamy soils near to river channels presents the highest probability of surface deflation. The results can be summarised as follows:

- Dust hotspots generally appear in close proximity to rivers, where peak seasonal flow resupplies deflation material to the surrounding area. These areas often show evidence of agricultural activity, with a distinct dust emission seasonality which correlates with cropping practices.

- The most active hotspot is found in the upland reaches of Upper Mesopotamia, in the agricultural lands between the Tigris and Euphrates Rivers, close to the Iraq/Syria border. This one area generated 1163 dust events in 8 years, peaking in 2009. Dust activity appears to be linked with the agricultural cycle, with dust emission supressed during winter growing season, and increased activity following the Spring harvest. Dust events peak in JJA, with June averaging 243 dust events.

- Other emission hotspots relate to the episodic flooding and desiccating of endorheic lakes (e.g. Sistan Basin), or the saltation bombardment of migrating dunes at the margins of alluvial surfaces (central Saudi Arabia, Lower Mesopotamia).

- These data compare well with known land surface dust emission processes, derived from other dust emitting regions around the world. Providing the highest-resolution, regional scale comparison of land surface properties and emission observations for the Middle East, showing the importance of alluvial surfaces, and highlighting the significance of seasonal agricultural practices.

- For future work, additional quantitative data of emission flux, potentially from SEVIRI Dust AOD retrievals (Banks and Brindley, 2013) added to surface wind speed data, would further help in the 'training' of emission thresholds of different land surface types, in global and regional aerosol-climate models.

Chapter 6: Discussion – Dust emissions in the Tigris Euphrates Basin

6.1 Introduction

This investigation has produced a detailed inventory of dust emission sources and their respective dust emission climatology in the Middle East during the period (2006 -2013). Analysis of the spatial and temporal distributions of dust emission has revealed highly localised peaks in dust emission frequency, with multiple areas of persistently high dust emission frequency (i.e. hotspots) linked to specific land surface characteristics (Chapter 5). In this chapter, meteorological conditions and their effect on the land surface characteristics of dust emitting surfaces will be explored in detail. Using the Tigris Euphrates Basin as a case study, environmental controls such as landform type, drought indices, vegetation cover and synoptic climate patterns will be compared with the spatial variability of dust emissions across the basin. This chapter discusses the research questions, summarised in Section 2.7.

Firstly, in Section 6.2, the relative emission frequency of the nine sub-regions in the Middle East, as described by the SEVIRI data, are compared to previous work, while section 6.3 compares the results from three different techniques. Section 6.4 describes dust emission in the Tigris Euphrates Basin, discussing how land use techniques and meteorological conditions effect dust emission frequency in an important dust source area. Finally, Section 6.5 summarises these findings.

6.2 Comparison with other studies

The manual derivation of dust emission sources from SEVIRI RGB imagery has successfully produced an inventory of dust emissions from the Middle East during the period 2006 – 2013 (see Sections 4 and 5). To assess how this new database compares to previous attempts at identifying dust emission surfaces in the Middle East, Table 6.1 has been adapted from Walker et al., (2009) to describe dust activity in the sub-regions identified in Section 4.4, as described by previous work. These assessments utilised different methodologies, from various platforms (i.e. satellite and land based observations) and were performed over various

periods. Each of these products have been discussed in detail in Section 3.2, with the exception of Middleton (1986) and Cao *et al.* (2015).

Table 6.1: Major dust sources in the Middle East identified by different studies using different data sources: Middleton (Meterological stations); Prospero (TOMS); Washington (TOMS); Walker (MODIS); Ginoux (MODIS); Cao (HYSPLIT). X = recognised as a source of dust / O = area of greatest dust activity. (Adapted from Walker *et al*., 2009)

Region	Selection of Studies						
	Middleton (1986)	**Prospero et al., (2002)**	**Washington et al. (2003)**	**Walker et al. (2009)**	**Ginoux et al., (2012)**	**Cao et al. (2015)**	**This work**
	Met. Stations	*TOMS*	*TOMS*	*MODIS DEP*	*MODIS Deep Blue*	*HYSPLIT*	*SEVIRI*
	1950s – 1970s	1980 – 1992	1978 – 1993	2001 – 2005	2003 – 2009	2000-2013	2006 – 2013
	-	1°	1°	0.25°	0.1°	-	0.1°
North Arabian Peninsula							
Upper Mesopotamia	X	X	X	X	O	O	O
Lower Mesopotamia	O	X	X	X	X	O	X
South Arabian Peninsula							
Ad Dahna	X	O	O	O	X	X	X
Central Arabian Peninsula		X	X	X	X		X
Southern Arabian Peninsula		O	O	O		X	
Iran							
Dasht-e Kavir		X		X	X		
Dasht-e Lut				X	X		
Hamoun-e Jaz Murian	X	X	X	X	X	X	X
Sistan Basin	X	X	X	X	X	X	X

The results of this study (Section 4) are also included in the table, with Upper Mesopotamia recognised as the greatest producer of dust, while all other sub-regions are accepted as a major dust source areas, with the exception of Southern Arabian Peninsula and the desert regions of Iran (Dasht-e-Kavir and Dasht-e-Lut). These sub-regions were discounted as major sources due to the low number of dust events produced in relation to all other sub regions.

From the selection of studies in Table 6.1, Middleton (1986) is the sole database to be derived only from ground observations alone - Cao et al. (2015) also utilise this type of data to validate

their findings. Middleton (1986) report dust emission frequency (signified by reduced horizontal visibility) from 135 meteorological stations from across the Middle East during the 1950s to the 1970s. Although ground observations, including AERONET sites, are not capable of defining exact dust source locations, these data provide a useful proxy for emission flux from a given area, especially at the sub-region scale. Middleton (1986) reports dust activity by the number of dust storm (visibility less than 1 km) and blowing dust (visibility less than 11 km) days per year. Using these data, dust activity is highest within the Tigris Euphrates Basin, with up to 33 dust storms and 208 blowing dust days per year in Lower Mesopotamia. Interestingly, all studies agree that the Mesopotamia sub-regions are dust source areas; however, there is a significant disparity in the respective frequency of emissions from these sub-regions. In fact, only the MODIS Deep Blue analysis by Ginoux et al. (2012) agree with the SEVIRI data, ranking Upper Mesopotamia as the most active sub-region in the entire Middle East.

This disparity is explained by southerly emission transport routes and the relative limitations of each dust emission retrieval method. This, in part, explains the high number of blowing dust events across the southern extent of the peninsula (up to 187 per year in the Ad Dahna sub-region) in Middleton (1986). His results suggest a north / south divide in dust activity, with a higher proportion of dust storm days (i.e. lower horizontal visibility) in the north of the Arabian Peninsula, while stations south of Kuwait record predominantly blowing dust days, especially in the Ad Dahna and Southern Arabian Peninsula sub-regions. These results further support the importance of the Mesopotamia sub-regions, as stations that record a higher frequency of dust storms are likely to be closer to dust source areas. The high frequency of blowing dust in Ad Dahna stations are, in part, products of the northerly Shamal winds transporting dust emissions from Mesopotamia across the southern part of the peninsula. Indeed, the SEVIRI results indicates a high proportion of the Mesopotamian dust events (73%) taking a southerly (including SE) trajectory along the east coast of the peninsula during peak in emissions in JJA. These months are synonymous with such continental-scale monsoon-flow (Hamidi *et al.*, 2013; Bou Karam *et al.*, 2017; Knippertz, 2014) - see Section 2.5.3. This transport mechanism has been attributed to the increase in air pollution across much of Saudi Arabia, responding to an increase in dust emission from the Tigris Euphrates Basin during a significant drought period 2007 - 2013 (Notaro et al., 2015).

SEVIRI
10/07/2006 – 06:15 UTC (09:15 local time)

TOMS – Nimbus 7 equator crossing time
10/07/2006 – 09:00 UTC (12:00 local time)

SEVIRI
11/07/2006 – 06:15 UTC (09:15 local time)

TOMS – Nimbus 7 equator crossing time
11/07/2006 – 09:00 UTC (12:00 local time)
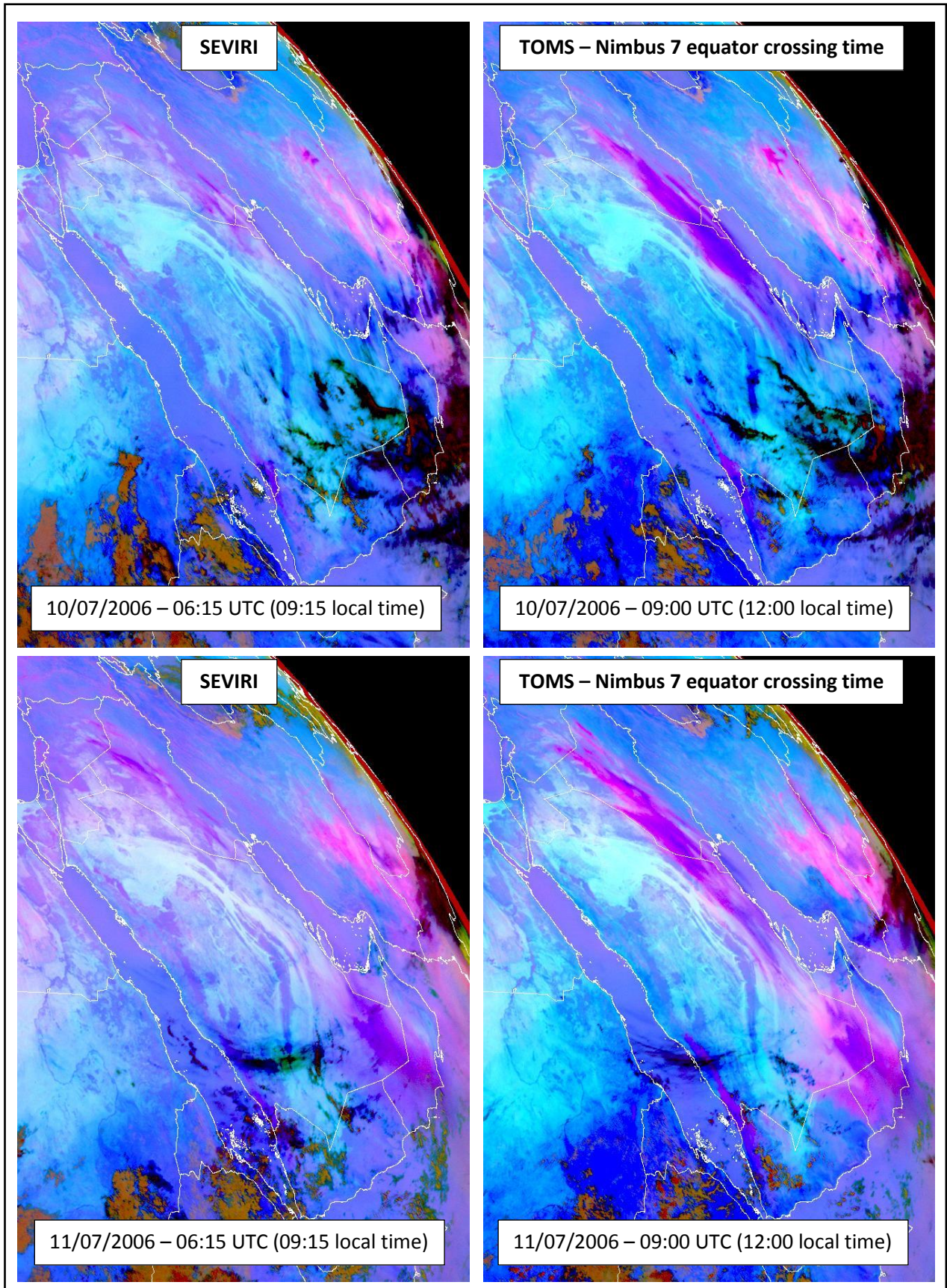
Figure 6.1 (overleaf): Comparison of atmospheric dust conditions at the time of dust emission, as shown by SEVIRI Dust RGB data, dust appear as pink or magenta (for full description see Section 3.3). Left side panels show equatorial crossing time (12:00 local time) of the Nimbus 7 satellite (right side panels), which carried TOMS from 1978 to 1993.

As Table 6.1 shows, the two TOMS based approaches highlight both the Ad Dahna and Southern Arabian Peninsula sub-regions as the greatest producers of dust activity. These results contrast with the SEVIRI data, where the Ad Dahna sub-region produces far fewer dust events compared to the Mesopotamia sub-regions (see Section 4.4), while the Southern Arabian Peninsula is not recognised as an important source of dust, producing less than 1% of all events. These differences are produced by the timing of TOMS observations (midday) and typical early-midmorning dust emission times in the Middle East (see Section 4.6).

With the exception of SEVIRI, all satellite observations in Table 6.1 are limited to one image per day. The probability of the dust plume observation being offset from the source area increases with lower temporal resolution retrievals (Schepanski et al., 2012; see Section 3.2). This effect is clearly shown in Figure 6.1, where multiple dust events commence in the morning hours of 10th and 11th July 2006. Each of these images are from the SEVIRI dust RGB product, with the right side panels describing conditions at the Equatorial crossing time of TOMS - Nimbus 7, used in both Prospero et al. (2002) and Washington et al. (2003) analyses (note – Nimbus 7 ceased operating in 1993). In the earliest image (top left), multiple individual plumes can be seen emanating from the Tigris Euphrates Basin in the north west of the scene (09:15 local time - Iraq). Substantial evolution of the dust plume can be seen in the midday (TOMS – representative) observation of the same day. Significantly, the plume has propagated further south-east, covering much of the Ad Dahna sub-region. This same pattern is observed the following day, with the addition of a large plume situated at the southern extent of the peninsula. Importantly, inspection of sequential images fail to identify any new emission within this southern plume; instead, revealing it to be the residual dust cloud from the previous days emissions in the north. This mid-morning emission and southerly transport pattern is repeated through much of JJA, potentially creating a false impression of significant dust emission in these areas.
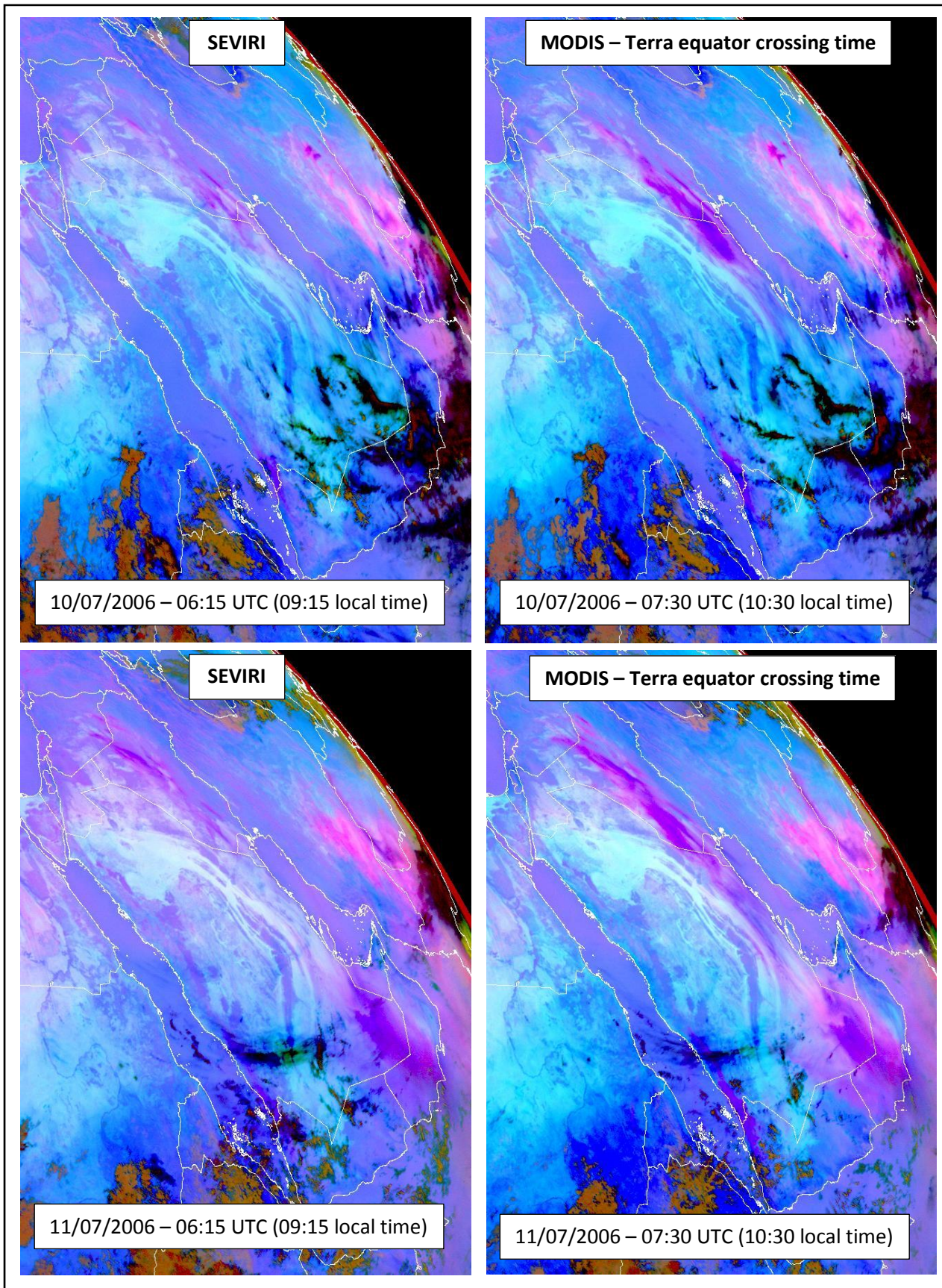
Figure 6.2: Like Figure 6.1 but with the Equatorial crossing time (10:30 local time) of the Terra Satellite (right side panels), which has carried MODIS from 1999 to present day.

The Ozone Monitoring Instrument (OMI) is continuing the TOMS record aboard the Aura satellite. Positioned within the A-train (afternoon train) constellation of NASA satellites, OMI crosses the Equator close behind the Aqua satellite (13:30 local time), increasing the emission-observation offset by nearly two hours (compared to Nimbus 7) and decreasing the accuracy of the results further.

In comparison to TOMS/OMI data, MODIS observations are taken from the Terra satellite, crossing the Equator at 10:30 local time, much closer to the typical emission times of the region (Fig. 6.2). Furthermore, the Deep Blue (Level 2) dust retrieval product (Hsu et al., 2006) used in Ginoux et al., (2012) constrains the Angstrom component to filter out fine mode dust plumes, thus reducing potential false-retrieval caused by old (multi day) plumes (see section 3.2.4). As a result, these data show the greatest similarity with the SEVIRI database, reducing the importance of the Southern Arabian Peninsula region as a dust source, and with greatest activity in the Mesopotamia regions (Table 6.1). While decadal changes in dust emission behaviour could explain the similarities between these data sets (the Ginoux et al., 2012 analysis is the only one to overlap with the SEVIRI inventory), the evidence presented here would suggest that the time of observation and sorting of the fine mode plumes is the primary reason for apparent similarity. Indeed, the Ginoux et al. (2012) and SEVIRI records only appear to disagree in two sub-regions (Dasht-e-Kavir and Dasht-e-Lut), where as previously stated, the SEVIRI records still observe emission, just not enough to record them as major sources.

The COAMPS modelled distribution of erodible surfaces, as defined by manual inspection of MODIS DEP images by Walker et al (2009) (see Section 3.2.3), has a similar distribution to the TOMS databases, highlighting the Ad Dahna and Southern Arabian Peninsula sub-regions. Here, the erodible potential of all surfaces is based on the dust emission frequency of different land surface types; these types are determined by the United States Geological Survey (USGS) land cover index and include variables such as vegetation cover and soil texture. The erodible potential of these surfaces are extrapolated across all similar types in the region, where in conjunction with climatic conditions, dust emission flux is forecasted (Walker et al., 2009). A similar dust source area index was produced by Cao *et al.* (2015), where land surface types linked to dust storm activation between the period 2000 – 2013 are extrapolate across the entire Middle East. In these data, MODIS data is used to recognise 27 atmospheric dust plumes, which are backtracked to a singular point source at ground level

using the HYSPLIT air-mass trajectory model. These data demonstrate the importance of the northerly Shamal winds, with 18 of the 27 dust plumes originating in the Mesopotamia sub-regions. However, as the results from the SEVIRI inventory demonstrate, large dust plume events typically originate from multiple point source locations over a wide area. With a single point source ascribed to each HYSPLIT trajectory simulation, underestimation of source areas included within this plume are unavoidable. Instead, like the meteorological station data used by Middleton (1986), these data help to determine the general source area of dust emission. Observations at a higher resolution are required to define source areas at a landform scale, which is capable of recognising sub-basin features such as ephemeral lakes. As shown by the land surface analysis in Section 5.2, land surface emission processes are dynamic, with multiple environmental factors producing apparent inconsistencies, whereby specific land cover types generate frequent emissions in one area and zero in another. As a result, this kind of analysis is extremely complicated (Todd et al., 2008), and is strongly dependent on the quality of the input data. With only one daytime image per day, the MODIS DEP imagery is highly susceptible to both dust, water and ice cloud contamination (Walker et al., 2009). This is especially important in areas of frequent emission, such as the Mesopotamia sub-regions. As the image frequency analysis showed (Section 3.5.1), where multiple plumes occur in a small source area (e.g. agricultural field / dry lake bed), low frequency data will tend to omit downwind sources. This could result in underestimation of the relative emission potential of agricultural landscapes and alluvial features, when compared to larger barren aeolian landscapes. The latter dominate across the Ad Dahna and the Rub' Al Khali (Southern Arabian Peninsula sub-region) sand seas in the Walker et al. (2009) analysis, potentially leading to an overestimated emission potential. Therefore, the incorporation of the SEVIRI inventory will likely increase the accuracy of the COAMPS erodible surface index.

6.3   Product comparison – SEVIRI and MODIS DOD

With the exception of the MODIS Deep Blue analysis, all previous studies fail to reproduce the spatial accuracy of the SEVIRI database (Table 6.1). Furthermore, the 0.1° resolution offered by MODIS Deep Blue only offers a statistic average of atmospheric dust loading (see Section 3.2), not specific point sources as derived in the SEVIRI dataset. These data are therefore unable to reproduce the same amount of spatial information on specific dust events or

emission surfaces. To determine how these data compare, MODIS Deep Blue data are compared with the SEVIRI inventory and the Ashpole and Washington (2013) automated dust-tracking algorithm for the Arabian Peninsula (Fig. 6.3). The automated SEVIRI results follow the same method stipulated in Ashpole and Washington (2013), presented as frequency of occurrence, at a 0.1° spatial resolution (with cubic convolution resampling applied). The MODIS data follow the same method as Ginoux et al. (2012), with measurements of AOD screened by the Ångstrom component to discriminate dust from all other aerosols (see Section 3.2.4). Referred to as dust optical depth (DOD), the results are presented as number of days that exceed the DOD threshold (greater than 0.2) at 0.1° spatial resolution (with cubic convolution resampling applied). Importantly, both the automated SEVIRI and MODIS data do not highlight point sources, with the dust tracking SEVIRI data defined by its pixel cluster threshold (approximately 0.5° x 0.5°) area. Similarly, the values of each 0.1° MODIS pixel are statistically driven by the positioning of large scale plumes and do not define precise point sources. Accordingly, to aid visual comparison, the manual SEVIRI inventory data is presented here at 0.25° resolution (with cubic convolution resampling applied). Each dataset is taken from 2011, with both SEVIRI datasets representing the entire year, while the MODIS data is from JJA only. This represents the most active period of the year (see Section 4.2), producing 40% of all observations in the manual SEVIRI analysis and is, therefore, deemed representative for this comparison.

Visually, significant differences can be identified between the three datasets (Fig. 6.3). In most cases, the automated SEVERI data is spatially offset from the manual observations, this is shown most clearly in Figure 6.3a, where the two hotspots of dust activity in the NW and SE of Iraq (UMP2 and LMP2 in Section 5.5), are shown several degrees SE in the automated data. This is thought to result from the transport element caused by the use of pixel cluster thresholds (see Section 3.3); with the predominantly north-westerly Shamal winds transporting plumes SE, before they extend to the required number of pixels. Across the southern extent of the Arabian Peninsula (Fig. 6.3b), both automated datasets disagree with the manual observations; specifically, describing dust sources in the eastern reaches of the Rub Al' Khali sand sea (centred around 22°N, 52°E), again downwind of the more frequent sources in the manual observations (northern Ad Dahna). This is especially notable in the MODIS deep blue analysis, with a large continuous area of frequently high DOD (greater than

60 days per season) appearing in an arch from the northern Ad Dahna (28°N, 48°E) to the Rub Al Khali sand seas. This is likely due to both the transport function described in Section 6.2 and the persistent sensitivity to bright surfaces (i.e. sand seas), inherited from the collection 5 Deep Blue algorithm, artificially enhancing the dust signal (Loría-Salazar et al., 2016).
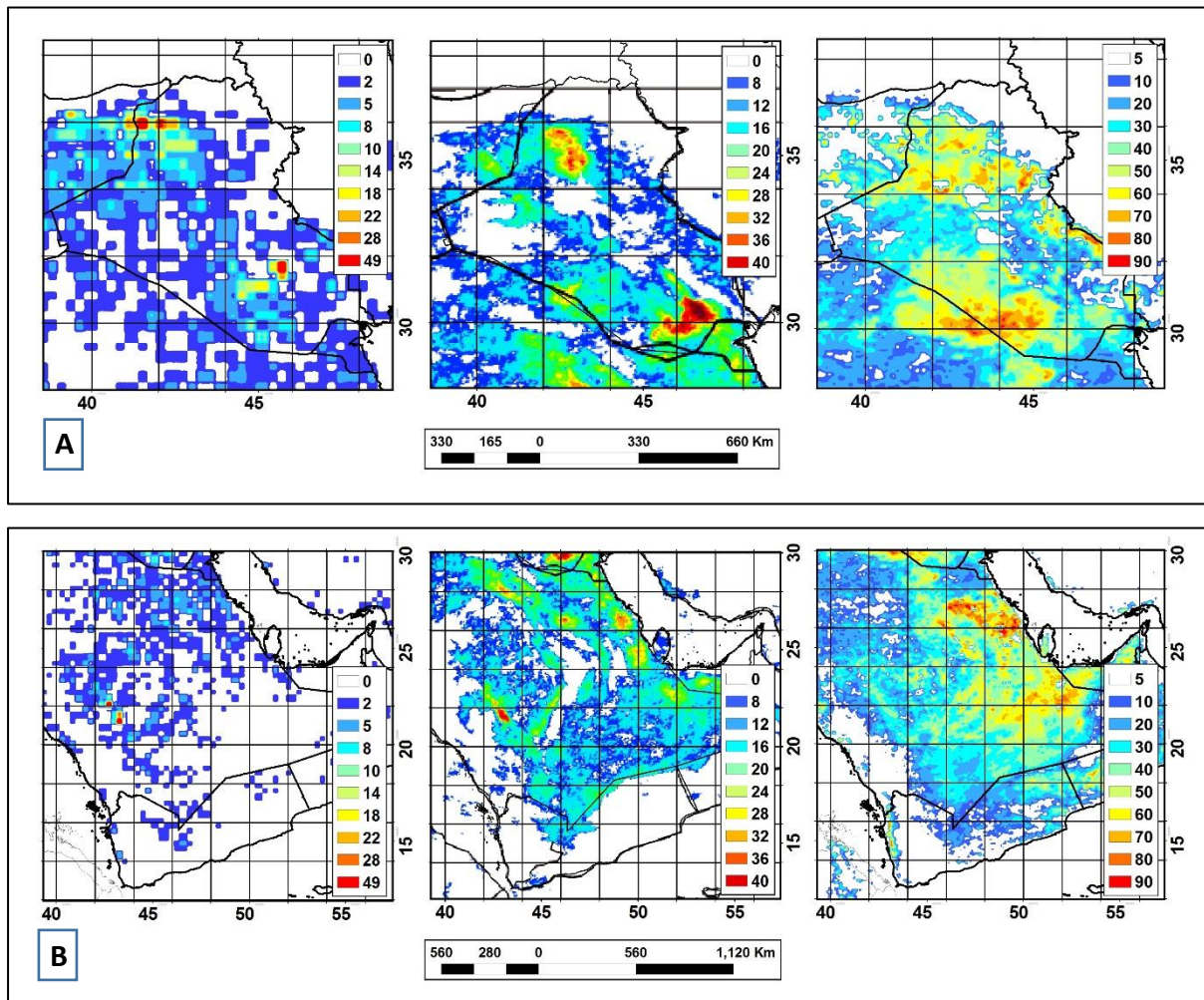
Figure 6.3: Satellite product comparison between manually observed emission sources from SEVIRI Dust RGB imagery (left panels), automated SEVIRI Dust RGB retrievals using the Ashpole and Washington (2013) dust tracking algorithm (middle) and MODIS Deep Blue DOD retrievals (right). All products describe atmospheric dust conditions for 2010, covering the entire year (both SEVIRI products) or JJA (MODIS). Manual observations describe number of dust events within 0.25° grid square; automated data describe frequency of occurrence, whereby dust emission exceed a given threshold within 0.1° grid cells (see text for full details). Comparisons focus on A: Iraq B: Arabian Peninsula.

Further west, the two hotspots running parallel with the Asir Mountains (CSA in Section 5.3) are shown as a single hotspot in the automated SEVIRI data (21°N, 43°E), failing to depict the highly localised emission characteristics. This effect is endemic in automated approaches, where the potential noise in the data is greatest where the dust plume is at its smallest extent (i.e. at source). Thus, manual observations are the only product capable of producing accurate enough results, to resolve landscape scale analysis of preferential emission frequency.

6.4   Sub-basin variability in dust emission frequency - Tigris Euphrates Basin

The high-resolution dust source inventory has been shown to perform better than alternative methods in assessing the precise source locations of dust emission. Therefore, these data are well suited to resolve the relative emission frequencies of various landscape-scale surface characteristics. With arid drainage basins recognised as the most prominent dust emission sources around the world (Prospero et al., 2002, Ginoux et al., 2012), it is important to understand the emission characteristics of these dynamic environments. As described in Section 2.4, drainage basins are heterogeneous in character, typically made up of different geomorphological features and land cover types (Baddock et al., 2011; see Section 2.4). Within the Middle East, several drainage basins exist (e.g. Sistan basin, Hamoon Jaz Mourian basin), with many of them producing frequent dust emissions (see Section 5.2). The southern extent of the Tigris Euphrates Basin is the largest and most active drainage basin in the study region, covering ~1.6 million km^2 (south of the Turkish border) and producing 10,285 dust events during the study period (2006 – 2013). Compared to other prominent surface-depression-type dust sources (Lake Eyre, Bodélé Depression), the Tigris Euphrates basin stands out on two aspects: i) the basin is not endorheic, with channel flow draining externally (via the Persian Gulf). ii) The area contains a large number of human settlements, with more than 37 million people in Iraq alone (The World Bank), consequently a large proportion of the land surfaces are subject to anthropogenic activities. For these reasons, this region was specifically chosen to discuss dust emission frequency in response to multiple land surface and climatic conditions. Firstly, Section 6.4.1 uses the Parajuli et al. (2014) database to discuss the relative emission characteristics of geomorphological features within the basin, providing a useful comparison to the endorheic basins of Lake Eyre and Chihuahua Desert in Bullard et al. (2011). Next, Section 6.4.2 considers the importance of environmental conditions, discussing how dust emission responds to recent drought conditions and changing patterns of vegetation cover. Section 6.4.3 examines human induced changes to the environment, focussing on the Mesopotamia Marshes in SE Iraq and how upstream channel management policies have affected the emission potential of these once permanent wetlands. Finally, Section 6.4.4 uses emission frequency data to describe the synoptic conditions prevalent during days of high dust activity.
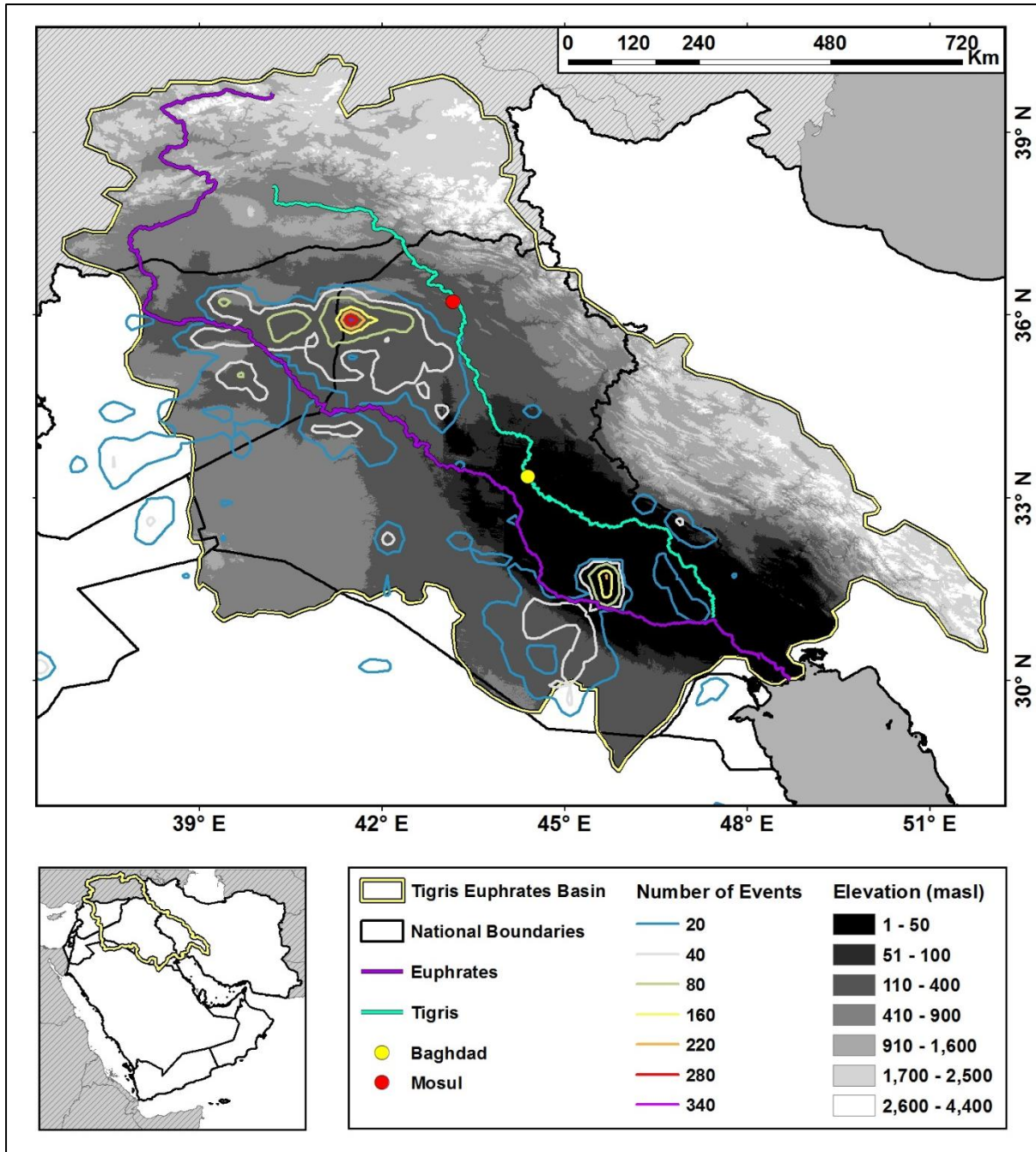
Figure 6.4: Topographic map of the Tigris Euphrates Basin, dust emission sources represented by 0.25° contour overlay of number of dust events.

6.4.1 *Tigris Euphrates Basin – Geomorphological features*

Drainage basins are typically comprised of multiple geomorphological features, typically containing bedrock, alluvial and ephemeral surfaces, with a proportion of aeolian surfaces in arid environments (Baddock et al., 2011; see Section 2.4). Previously, several attempts have used dust emission observations to describe the deflation potential of each landscape type, with Bullard et al. (2011) demonstrating the effectiveness of ephemeral lake beds and aeolian surfaces in generating dust emission in the Lake Eyre and Chihuahua Desert basins (see Section 2.4.2). By using dust emission observations, the authors were better able to determine the emission potential of different landscapes, thus providing information at a far higher resolution than is typically present in climate-aerosol models. Importantly, their results did not include anthropogenic surfaces such as cultivated agriculture. By combining the high-resolution dust emission inventory presented in this thesis, and the Parajuli et al. (2014) landform classification data, the relative importance of anthropogenic dust sources can be more accurately estimated.

Here, the aim is to produce a similar analysis of the Tigris Euphrates Basin (referred to as TEB), discussing the emission frequency of each of the landscape units and comparing them to results from the Lake Eyre Basin (LEB) and the Chihuahua Desert (CD) in Bullard et al. (2011); testing the hypothesis that their simplified scheme is replicable in the Middle East.

The TEB covers a variety of terrain, with a large elevation range from the Zagros and Taurus Mountains (over 4,000 m) in Iran and Turkey to the coastal plains in Kuwait (Fig. 6.4). During the study period, dust emissions derived predominantly from the lower elevations of the basin (84% below 400 m), with zero emission observed from the Taurus Mountains north of the Turkish border (Fig. 6.4). The TEB is significantly larger in area than both LEB and CD (Table 2), with their respective areas covering approximately two thirds (LEB) and one fifth (CD) of the TEB study area (area south of the Turkish border, shown in Figure 6.5). Dust emission observations from these three basins were made over different durations and during different periods; however, each analysis incorporates a full range of seasonal conditions (i.e. is longer than 12 months), accounting for any seasonal bias in emission patterns. Furthermore, differences in emission frequency, relating to specific climatological events, are assumed regionally dependent; each basin is spatially distinct from one another, negating the need for observation overlap. Importantly, there is a difference in the number of dust emission

observations, due to the different observation techniques. Both the LEB and CD observations were made using a variety of MODIS products (see Bullard et al., 2011 for full specification), where discrete source detection is limited by environmental conditions, making observations only possible during specific conditions (i.e. zero cloud / dust emission cover; see Section 3.2.2). Comparisons are therefore made by the percentage of results within each of the given landscape units.
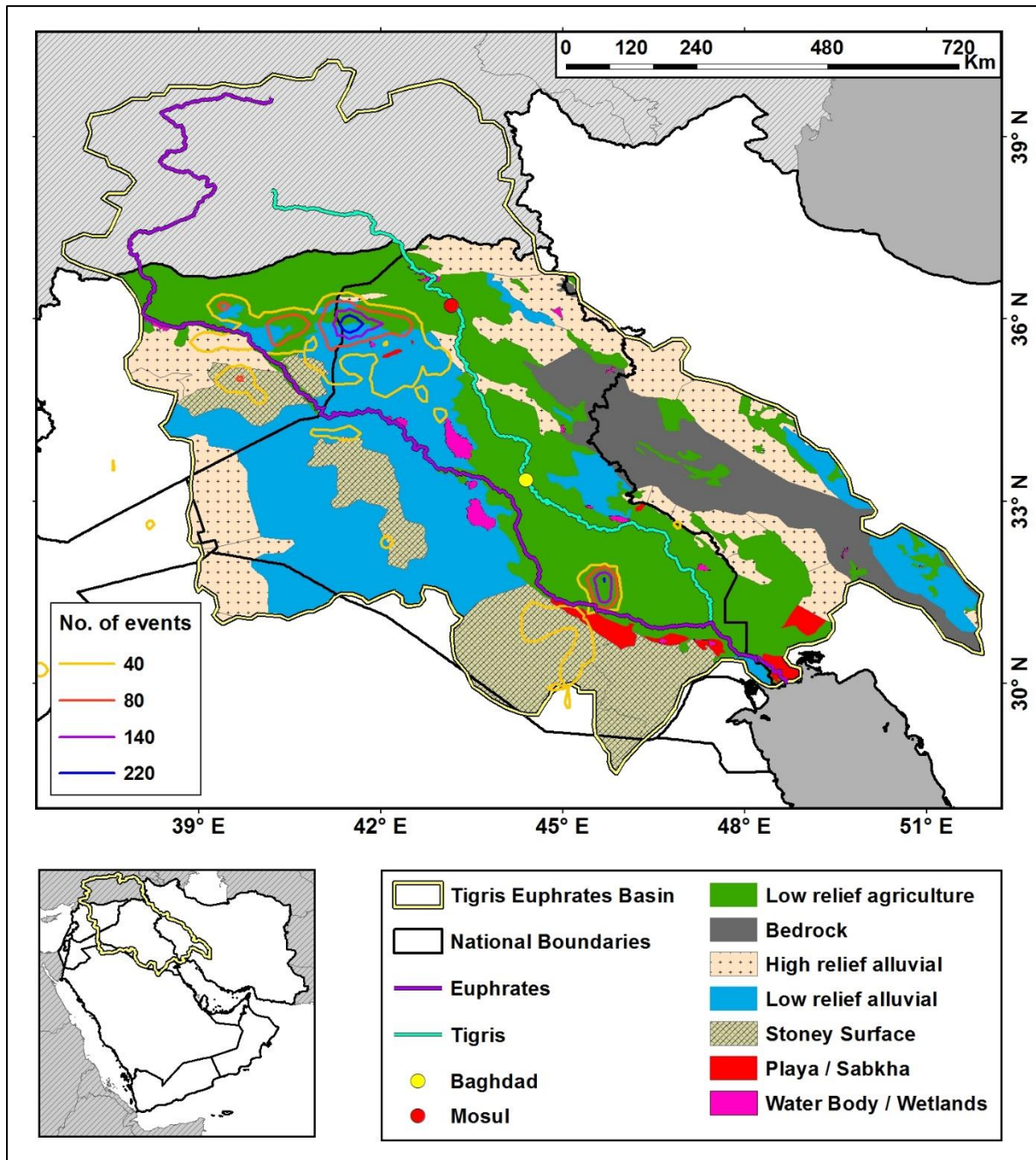
Figure 6.5: Distribution of geomorphological landforms of the Tigris Euphrates Basin. Dust emission frequecy described by 0.25° contour overlay of number of dust events.

Each of the three basins described in Table 6.2 have significantly different landscapes. The Tigris Euphrates Basin, as defined by Parajuli et al. (2014), is a largely alluvial environment, with 83% of the land surfaces classified as either agriculture on low relief alluvial surfaces or uncultivated alluvial surfaces of various relief (Fig. 6.5). Accordingly, dust emission is largely generated from these two surfaces, with uncultivated low relief surfaces the most effective producer of dust, producing 35% of emissions while covering nearly a third less land than agricultural surfaces. In comparison, LEB is a largely aeolian environment (68%), with 35% of emissions generated by sand dunes. The complex topography of CD is dominated by a high proportion of low emission (bedrock) surfaces (28%) and high relief alluvial surfaces (44%). Unlike TEB and LEB, dust emission frequency from CD does not reflect the dominating landscape unit, with the highest proportion of events coming from wet and dry lakes (48%), described predominantly as ephemeral lakes in Bullard et al. (2011).
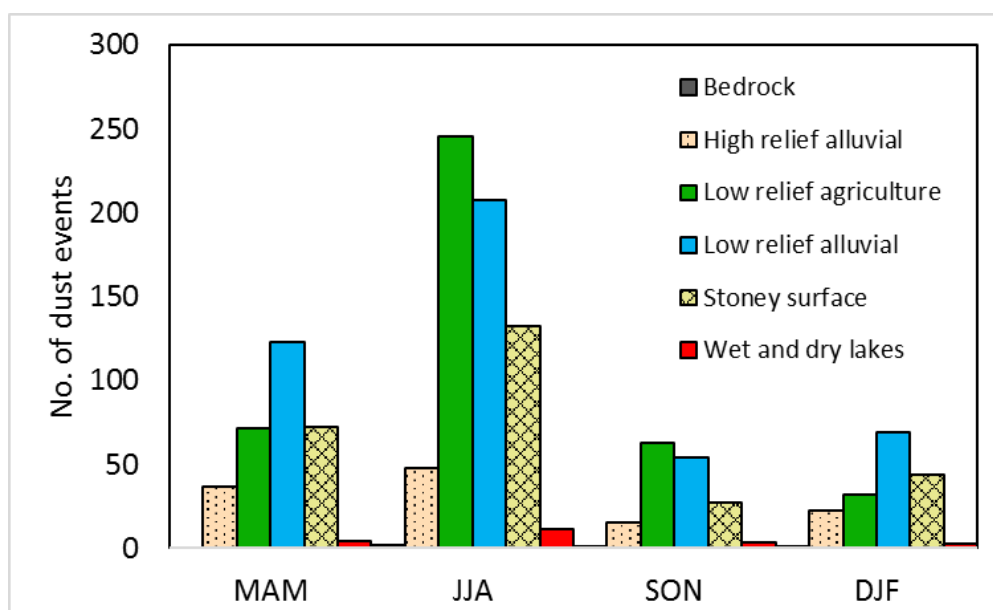
Figure 6.6: Seasonal frequency of dust emission events from various geomorphological landform types in the Tigris Euphrates Basin (see Fig. 6.5).

Within the TEB, a large proportion of low relief alluvial surfaces exist within a central corridor from the Persian Gulf coastline to northern Syria, with both the Tigris and Euphrates Rivers running at its centre. Both rivers originate in Turkey, where 40% and 90% of river discharge is produced respectively (Yürekli, 2015). Combined, these rivers discharge approximately 82

billion m^3 a^{-1} from the basin (Yürekli, 2015), depositing a large supply of fine alluvial material on their floodplains (Parajuli and Zender, 2017). Irrigation waters derived from these channels are crucial in sustaining agriculture in the much drier climate of Iraq and Syria, especially in the lower extents of the basin (Kelley et al., 2015). Agricultural surfaces consist of both irrigated (riparian) and rain-fed cultivated areas (Gibson et al., 2015). Rain-fed agriculture contribute up to 90% of cereal production in the more humid north (Jaafar and Woertz, 2016), producing wheat and barley during the winter rainy season (October – May) (Trigo *et al.*, 2010). Irrigated croplands enable crop production in the drier south, adjacent to the major rivers, where grain production occurs as both winter and summer crops (Gibson et al., 2015).

Alluvial surfaces have long been recognised as potential dust sources, primarily due to the large volumes of fine alluvial material deposited during overbank events (Prospero et al., 2002). These floodplains are present in all three basins, where they are recognised as effective emission surfaces, producing proportionally more dust respective to high relief alluvial surfaces.

Agricultural surfaces are differentiated from non-agricultural low-relief alluvial surfaces by their seasonal dust emission frequency (Fig. 6.6). While both surfaces peak in JJA, agricultural surfaces have a far greater range (38%) in seasonal average dust events, peaking in JJA with an average of 245 dust events compared to just 32 events in DJF. This acute seasonality is expected from the rain-fed winter wheat and barley fields in the north. These surfaces are typically limited to a single harvest per year (March / April) and remain largely barren for long periods of the summer months, before being disturbed by tilling prior to winter growing seasons (Trigo et al., 2010). These sudden changes in vegetation cover and soil roughness are expected to increase the dust emission potential of these soils (see Section 2.3.2). The more extensive irrigation systems across agricultural surfaces in the lower extent of the basin (south) typically maintain agriculture through the dry summer months (Gibson et al., 2015), producing a more consistent vegetation cover, reducing summer dust emission potential. Unexpectedly however, these surfaces produce the same seasonal distribution, with dust emission peaking during JJA. While appearing to contradict previous results, the JJA peak in dust emissions can be explained by the concentration of deflating surfaces in the southern-lowland areas and the simplified land surface classification. Here, the majority of agricultural dust emission events emanate from the centre of the largely barren LMP2 dust emission

hotspot (see Fig 5.11). This area shows evidence of recent agricultural abandonment (see Section 5.3.2), potentially explaining its incorrect classification in the Parajuli et al. (2014) dataset. Indeed, large expanses of irrigated agriculture south of Baghdad are relatively inactive dust emitters. Interestingly, dust emission is highly variable across both agricultural and non-cultivated alluvial surfaces, with the frequency increasing in specific locations (Fig. 6.5). This heterogeneous emission pattern is likely caused by meteorological and socio-political conditions that are beyond the scope of this simplified classification and are explored in more detail in Section 6.4.2.

Table 6.2: Surface area and dust emission frequency statistics of geomorphological landform types in three separate dust source areas. Lake Eyre Basin and Chihuahuan Desert data described in Bullard et al.(2011).

Emission surface	Tigris Euphrates Basin 2006-2013				Lake Eyre Basin 2003-2006				Chihuahuan Desert 2001-2009			
	Area (km²)	Area (%)	Emis. Freq	%	Area (km²)	Area (%)	Emis. Freq	%	Area (km²)	Area (%)	Emis. Freq	%
Lakes												
Wet and dry lakes	16,438	1	183	2	43,818	5	58	11	12,712	4	104	48
Alluvial												
Low relief agriculture	489,404	31	3293	32	-	-	-	-	-	-	-	-
Low relief alluvial	316,655	20	3626	35	179,972	20	87	16	65,119	21	26	12
High relief alluvial	504,886	32	968	9	35,251	4	3	1	138,760	44	45	21
Aeolian												
Stoney surface	152,028	10	2198	21	132,531	15	20	4	141	0.05	1	>0.1
Sand sheets	-	-	-	-	161,747	18	30	6	7,178	2	4	2
Sand dunes	-	-	-	-	305,888	35	304	58	9,450	3	30	14
Low emission surfaces												
Bedrock	96,394	6	17	0.2	330,404	37	26	5	89,090	28	7	3
Total	**1,575,805**	**-**	**10,285**	**-**	**1,189,611**	**-**	**528**	**-**	**322,450**	**-**	**217**	**-**

Agricultural surfaces are not defined in the LEB or CD datasets; however, it is likely that any such surfaces are included within the low relief alluvial landscapes class, as in the TEB.

Stoney surfaces are the only aeolian surfaces across the TEB, thus representing the only aeolian unit common to all three basins. Consisting largely of stone pavements, known locally (in the Middle East) as either *hamada* or *reg* (Cooke *et al.*, 1993), these surfaces cover large parts of the arid Samawah and Syrian Deserts to the SE of the Euphrates River. The high percentage of emissions from these surfaces (21%) is surprising, as the abundance of coarse lag material on the surface typically prevent the emission of the finer material beneath, as shown in both LEB and CD. It is believed that here, dust emission is enhanced by regular surface disturbance, caused in part by local transport networks. This was demonstrated by the emission hotspot (LMP1) in the Samawah Desert in southern Iraq (see Section 5.3.2). The compression and shear forces inflicted by off-road vehicles have been shown to remove or displace clast-sized particles, while also decreasing soil infiltration rates, allowing sediment-rich overland flow to pool within vehicle tracks (Prose *et al.*, 1987). Thus, increasing deflation potential by removal of soil stabilisers and increased supply of fine material by preferential deposition (see Section 2.3). Vehicle tracks have a long term impact, with the natural restoration of stone pavements thought to take centuries (Belnap and Warren, 2002), meaning disturbed areas are likely to remain as dust sources for many years to come.

Ephemeral and permanent lakes, including playa and sabkha surfaces, are not abundant in the TEB according to the Parajuli et al. (2014) database, with the largest concentration along the Euphrates River at the lower elevations of the basin. Interestingly, known features of this type, including the Mesopotamia marshes or the Albu Gharz, al Burghuth, and Ar-Rawda playas in northern Syria, are not recognised as separate features within the larger alluvial (low relief alluvial and agricultural) landscapes they are found in. This suggests that the size of these relatively small features, results in an underestimation of their contribution to the landscape. Indeed, the area at the lower part of the basin has proved difficult to classify, with a recent supervised (automated) classification scheme reclassifying much of the stoney surface as playa / sabkha (Parajuli et al., 2017). The Parajuli et al. (2017) supervised classification scheme is based on reflectance data from the Blue Marble seamless mosaic of the entire Earth, produced by visible wavelengths from MODIS Terra during 2004. Supervised classification is performed on a pixel-by-pixel basis (~500 m^2 pixel), with training reflectance

data taken from the Parajuli et al. (2014) landscape classes. This higher resolution classification is more likely to detect small landscape units such as playas and ephemeral channels; however, the spectral similarity of land surfaces in the visible wavelengths makes it extremely challenging to differentiate the geomorphological process domain of many of these arid environments (Hsu et al., 2004). This is especially apparent over floodplain areas, where seasonal activity frequently alters the dominating land surface process. The ambiguity in these regions is resolved simplistically in the scheme used here (Parajuli et al., 2014), where visual inspection of Google Earth Pro imagery is used to determine the dominant classification over a large landscape unit (see Section 3.6.6). With a degree of uncertainty in each method, possible errors are expected in ambiguous areas. In the classification scheme used in Figure 6.5 (Parajuli et al., 2014), wet and dry lake surfaces only account for 2% of dust emissions, far lower than both Lake Eyre (11%) and Chihuahua (48%) regions (Table 6.2); however, this figure is likely underestimated due to previously stated issues in the dataset.

Low emission surfaces, defined here as bedrock, represent only a small proportion of the TEB, predominantly found on the steep slopes of the Zagros Mountains to the east of the Tigris River. Similar to the LEB and CD, these surfaces are not frequent emitters of dust, with only 17 (0.2%) emission events produced.

In summary, the use of a simple geomorphological landscape unit classification, along with dust emission data, has produced the first high-resolution analysis of the dust emission potential of contrasting landscape units across the Tigris Euphrates Basin. As a known dust-emitting drainage basin, the TEB stands out for its relatively high population density and abundance of agricultural surfaces. The use of a simple landscape classification allowed the results to be compared with the largely aeolian Lake Eyre Basin and the mountainous Chihuahuan Desert, previously analysed in Bullard et al. (2011).

In the TEB, low relief alluvial surfaces are the most effective producers of dust emission, although dust emission potential is highly variable, with areas of frequent emission concentrated into relatively small areas. These results are consistent with the results seen in Bullard et al. (2011), where alluvial surfaces in both LEB and CD produce a significant proportion of dust emissions, with distinct spatial variability. Agricultural surfaces consist of both irrigated and rain fed croplands, and provide a significant proportion of dust emissions

(32%), with a highly seasonal emission frequency, peaking in the warm and dry JJA. These surfaces are not accounted for in either the LEB or the CD analyses; however, land management practices are known to exist within each basin. Within the LEB, agricultural surfaces consist of mostly rangeland, used for cattle and sheep grazing (Aubault *et al.*, 2015), while the CD has seen an increase in both irrigated agriculture and grazing rangeland over the past 40 years (Currit, 2005). For future research, it will be interesting to see how the emission potential of these surfaces compares to those in the TEB.

Like non-cultivated alluvial surfaces, the dust emission distribution of agricultural surfaces are also highly variable. Environmental conditions, not considered in this classification scheme, including drought conditions and varying vegetation cover, are possible causes of this variability, and are explored in more detail in Section 6.4.2.

Wet and dry lakebeds in the TEB, including ephemeral playas and sabkhas are relatively inactive dust emitters. These results contrast to Bullard et al. (2011), especially in CD, where 48% of emissions are generated by these features. This is likely due to the size of these features, and their relative impact on the large-scale alluvial landscapes they are found in, with many known ephemeral lakes overlooked in the Parajuli et al. (2014) dataset. To resolve the emission frequency of these important features more clearly, a higher resolution account of geomorphological landforms is required.

6.4.2   Tigris Euphrates Basin – Environmental conditions

The results of the landscape unit analysis in Section 6.4.1 demonstrate the high dust emission potential of both agricultural and non-cultivated low relief alluvial surfaces surrounding the Tigris and Euphrates Rivers. In this corridor, the margins between agricultural and non-agricultural surfaces have changed during the past 20 years. In Iraq, during the 1990s, croplands were largely expanding across much of this area as a response to sanctions placed on food imports. This expansion subsequently declined following the removal of the Saddam regime in 2003; with the lifting of sanctions, demand for local agriculture subsided and crop production declined (Gibson et al., 2015). These areas have since seen significant abandonment of agricultural land (on average 18,581 ha a^{-1}), due in part to the increase in food imports, but also through continued drought and social-political influences such as

sectarian violence and foreign river channel management programmes (Gibson *et al.*, 2015; Jaafar and Woertz, 2016; Kelley *et al.*, 2015). Through change detection analysis of 32 Landsat Thematic Mapper (LTM) images from 1984 to 2011, Moridnejad et al. (2015) were able to determine significant desertification across Iraq and eastern Syria, which in Figure 6.7, are overlain by the SEVIRI dust source data. Desertification has occurred primarily within this alluvial corridor, most prominently along the Euphrates River, which since the 1990 construction of the Ataturk dam in Turkey has seen flow reduce downstream into Syria and Iraq (Beaumont, 1996; Moridnejad *et al.*, 2015). Furthermore, these lands are thought to have suffered from high soil salinity, in response to years of overexploitation of dwindling groundwater supplies and poor management (Gibson et al., 2015; Kelley et al., 2015). Interestingly, aerial imagery from the two prominent emission hot spots in the upland areas (UMP1 / UMP2; see Section 5.3) clearly show contemporary agricultural fields, within the most active hotspot (UMP2) located within an area classified as 'serious desertification' (Fig. 6.7). This apparent contradiction can be explained by the method used by Moridnejad et al. (2015). To avoid seasonal bias in their land cover change-detection analysis, only September LTM images were used, depicting the minimal vegetation cover in each year of observation. This creates a potential bias, where winter rain-fed croplands have encroached onto previously undisturbed vegetation during the study period (1984 - 2011). During September, these areas will typically be cleared of any vegetation in preparation for the winter growing seasons (Trigo et al., 2010). This explains the greater desertification observed in the upland areas (UMP1 / UMP2), despite their recent agricultural activity. Indeed, these data will likely show the impact of agricultural practices on summer vegetation cover as well as increased desertification, and thus the increased exposure during the driest period of the year.
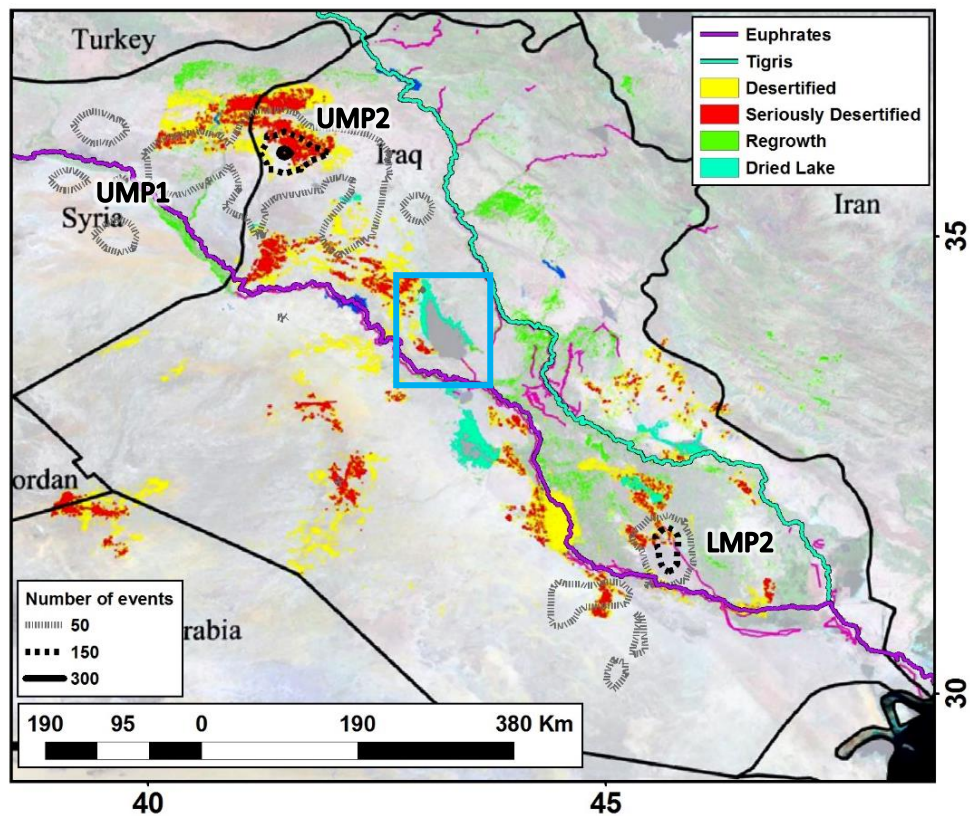
Figure 6.7: Recently desertified areas in Iraq as described by change detection analysis of Landsat Thematic Mapper (LTM) data during the period 1984 – 2011 in Moridnejad et al. (2015). Dust emission frequency represented by 0.25° contour overlay of number of dust events.

Dust activity across the TEB increased dramatically from 2007 to 2009 (Fig. 6.8), coinciding with one of the most severe droughts in the period of instrumental record (Kelley et al., 2015; Trigo et al., 2010). Effective precipitation in the TEB occurs predominantly between October and May (Kelley et al., 2012), with drought conditions characterised by precipitation in these months (Trigo et al., 2010). The inter-annual and decadal variability in precipitation regularly induces drought in this part of the Middle East (Morid *et al.*, 2006), with multi-year droughts occurring in the 1950s, 1980s and 1990s, with the most severe drought previously occurring between 1998 - 2000 (Kelley et al., 2015). During the 2007 – 2009 drought event, winter precipitation levels only reached approximately 40% of 1940 - 2009 mean, between 10 and 20 % less than the 1998-2000 drought (Trigo et al., 2010).

This period can is described by Standardised Precipitation Index (SPI) figures, calculated by the National Climatic Data Centre (NCDC). These data infer short (3 month) to medium (24

month) scale precipitation deficits through comparisons of precipitation and potential evapotranspiration. Notaro et al. (2015) show SPI (12 month) drought conditions starting in August 2006, and persisting through much of the 2006 – 2013 study period (Fig. 6.8). April 2008 and February 2009 recorded exceptionally dry conditions (<-2.0; the highest SPI rating), while moderate drought conditions (-0.8 to -1.29 SPI) routinely appear during the period 2011 – 2013.
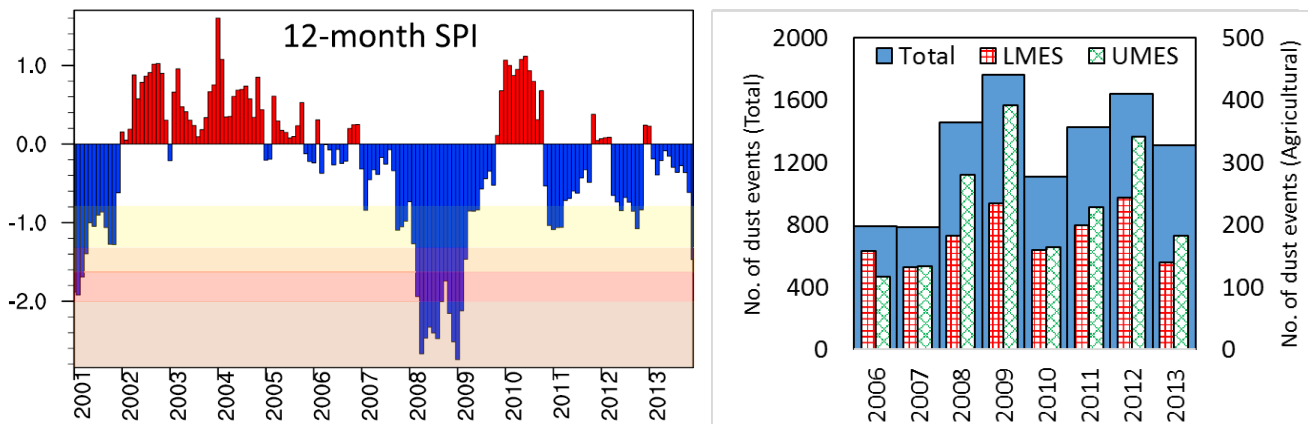
Figure 6.8: Comparison between drought conditions and dust emission frequency within the Tigris Euphrates Basin. Drought conditions described by 12-month Standard Precipitation Index figures from the Global Precipitation Climatology Project (GPCP), published in Notaro et al. (2015). Colour gradient describes the SPI thresholds for moderately, severely, extremely and exceptionally dry conditions. Dust emission frequency described as total dust events for the Tigris Euphrates Basin (blue bars) and agricultural surfaces in Upland (UMES) and Lowland areas (LMES) (secondary axis).

During these periods of drought, the response in number of dust events varied between the predominantly rain-fed crops in Upper Mesopotamia (UMES) and irrigated fields in Lower Mesopotamia (LMES) (Fig. 6.8). The number of dust events produced by each agricultural type remains relatively equal in mild or non-drought years of 2006, 2007 and 2010, while the rain-fed croplands of UMES produce progressively more dust events as droughts prolong, with the greatest difference seen at the peak of the 2007 – 2009 drought. These differences are most readily explained by the availability of water during these periods of drought. Annual precipitation across the entire basin was below long-term norms during the entire (2006 – 2013) study period (Notaro et al., 2015). Importantly, winter precipitation reduced by up to 70% over northern Iraq (UMES) during the most severe drought year (2008 – 2009), severely

affecting the germination period of rain-fed winter crops and causing widespread failure (Trigo et al., 2010). Crops irrigated by channel flow in southern Iraq (LMES), are likely to have had greater access to fresh water for a longer time during these periods of drought, reducing crop loss relative to those reliant on direct precipitation.

Monthly vegetation growth during these drought periods indicate a link to dust activity (Fig. 6.9). Here, monthly mean Normalised Difference Vegetation Index (NDVI) data are calculated for a 1° grid square area at the centre of the three TEB dust emission hotspots (UMP1/2 and LMP2). As described in Section 5.3, both UMP1 and UMP2 show contemporary agriculture, while the lowland LMP2 appears largely barren, with evidence of some irrigated and recently abandoned agriculture. As expected, NDVI values in each area peak in opposite seasons to dust emissions, with maximum vegetation cover during DJF and minimum cover during JJA, producing negative Pearson's Product Moment Correlation Coefficients with dust events of $r(94)$ = -0.34, -0.43 and -0.46 at UMP1, UMP2 and LMP2 respectively. In each case the negative relationship between NDVI and dust emission frequency is significant to $p < .001$.

NDVI values are both higher and more variable in the cultivated hotspots in the north (UMP1/UMP2). NDVI peaks in the winter months, predominantly driven by the growing season of rain-fed wheat and barley (Gibson et al., 2015). These results highlight the impact of drought conditions during the winter growing seasons of 2008, 2009, 2011 and 2012, with NDVI dropping in each of these years compared to the more humid conditions of 2010 and less intense drought of 2007 (Fig. 6.8). Importantly, peak NDVI in these years are similar to those of the largely barren LMP2. Indeed, this period showed a collapse of the local agriculture, with harvested land surface area falling by up to 40% below normal levels, remaining below average until 2013 (Notaro et al., 2015).

Dust emission appears to be more strongly affected by increased winter vegetation / precipitation, with a clear drop in emission frequency in 2010. In comparison, emission frequency during drought years is generally higher, albeit variable, with decreased emission frequency during 2009 in both UMP1/2 despite producing the lowest winter (peak) NDVI figures (of all years) during the preceding rainy season. While the exact cause of this is unknown, it is likely linked to the supply of fine sediment. Dust emission sources that do not contain a localised store of fine material require a persistent supply of fine material by overland flow (Kocurek, 1998). It is probable that in 2009, the cumulative effects of multi-year

drought could have limited the supply of fine sediment to the centre of these hotspots, thus limiting dust emission. Subsequently, dust emission frequency does not recover to pre-2009 values until 2011, following increased precipitation during 2010. It is also important to note that the dust emission frequency presented here only represents emissions from the 1° area at the centre of each emission hotspot, across the entire TEB, dust emission frequency increased during 2009 (Fig. 6.8), while the total area of each hotspot recorded a similar emission frequency to 2008 (see Section 5.3.1).

The largely barren LMP1 hotspot produces lower NDVI values than those in the north, while still demonstrating a reaction to the prolonged drought period of 2008 / 2009. Dust emission frequency appears independent of vegetation cover, with increased dust events during the more humid 2010. This is potentially linked to the increased flow of the Euphrates River, with the largest peak in NDVI (DJF 2012/2013) followed by peak dust activity (JJA 2013), likely triggered by the regeneration of sediment reserves in this low-lying riparian zone.

Drought in the eastern Mediterranean develops in response to teleconnections with naturally occurring oscillations in atmospheric circulation (i.e. North Atlantic Oscillation (NAO) and El-Nino Southern Osciliation (ENSO)) (Notaro *et al.*, 2015; Yürekli, 2015; Yu *et al.*, 2015). However, further analysis using the Coupled Model Intercompariosn Project phase 5 (CMIP5) climate model, has shown that the severity of more recent dry periods exist beyond natural variability, responding instead to anthropogenic climate change (Kelley et al., 2012). Should global warming continue as expected (Reynolds *et al.*, 2007), many global climate models agree on the region becoming drier throughout the 21st Century (Kelley et al., 2015). Indeed, high resolution (20 km) simulations on the Japanese Meteorological Agency's general circulation model (GCM) show a reduction in precipitation over the eastern Mediterranean, predicting a significant streamflow reduction in both Tigris and Euphrates Rivers, culminating in the potential disappearance of rain-fed agriculture throughout the TEB (Kitoh *et al.*, 2008). Further analysis of potential climate change in the Middle East will be critical for future studies on dust emission mitigation; however, it is beyond the scope of this thesis and not explored further here.
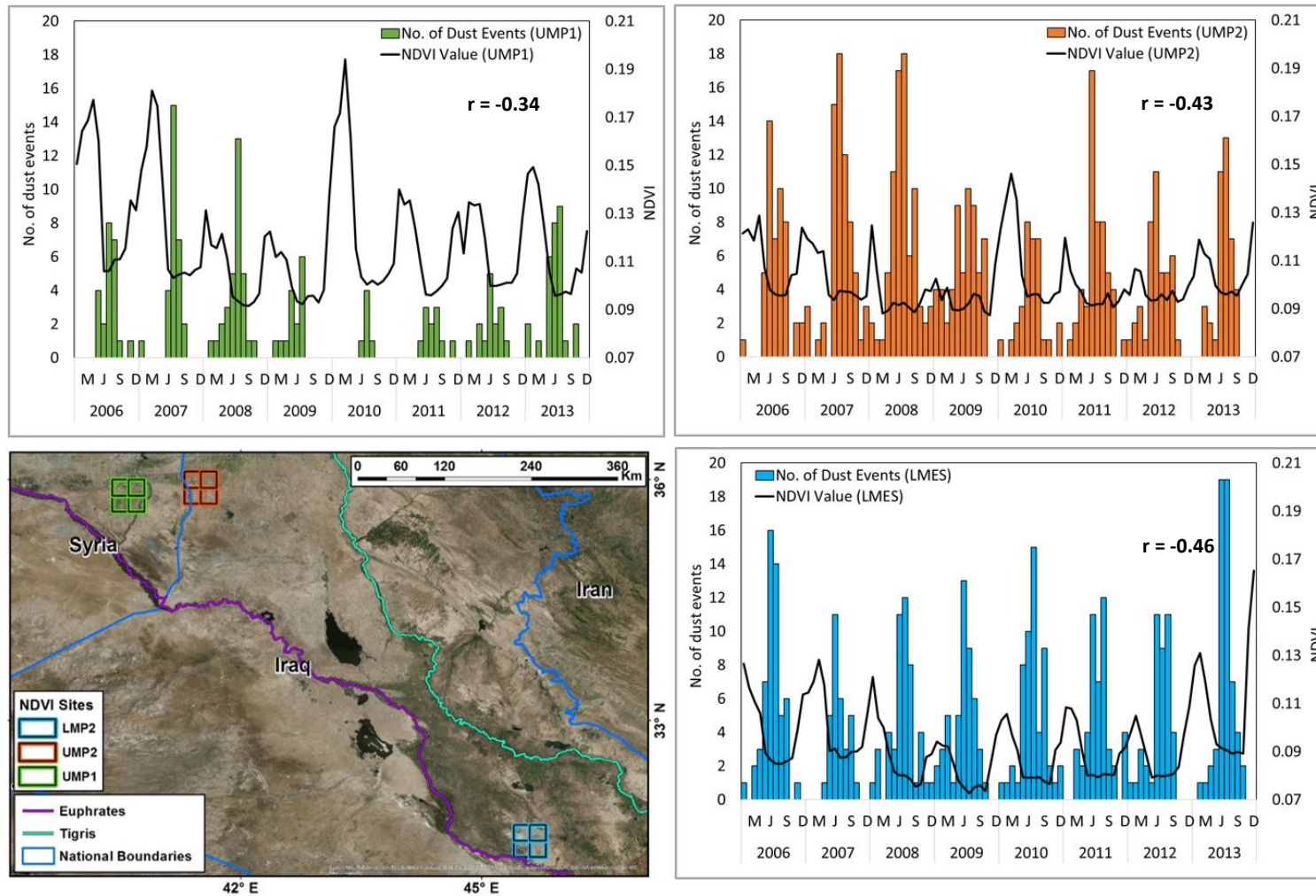
Figure 6.9: Variability of vegetation cover, as described by monthly NDVI values from MODIS (MOD13A3, collection 5) data (black line) at three dust emission hotspots in the Tigris Euphrates Basin, UMP1 (top left), UMP2 (top right) and LMP2 (bottom right). Dust emission frequency described by coloured bars.

Drought conditions between 2007 and 2013 have been represented by NDVI values in several dust emission hotspots in the TEB. The different response in both vegetation growth and dust emission frequency can be explained by different land use patterns. Winter rain-fed cropland appeared more sensitive to changes in precipitation than the largely barren emission hot spot in the south, showing higher variability in both NDVI and dust emission frequency. These examples demonstrate the diverse environmental conditions found on different dust emission surfaces within TEB, and their response to droughts. With the TEB set to become drier throughout the 21st Century, these differences will prove important for dust emission sources and land management practices in the coming decades.

6.4.3   Tigris Euphrates Basin – Socio-political influences

The severity of the 2007 – 2010 drought has been seen by many authors as a potential contributor to the rising tensions and subsequent internal conflict in Syria (Kelley et al., 2015). The breakdown of the agricultural sector and the diminishing economic status of the country propelled a large-scale migration of the rural workforce into already crowded urban centres, raising social tensions prior to the start of the conflict in March 2011 (Gleick, 2014). A large proportion of agricultural regions have been at the centre of many conflict zones, causing increased migration and adversely affecting agricultural production, particularly in the upland-agricultural areas of Syria (Jaafar and Woertz, 2016). This may have enhanced the dust emission frequency in Upper Mesopotamia during the post 2011 period (see Section 4.5), where emission frequency compares with the extreme drought period (2007 – 2009) (Fig. 6.8). Since the rise of the so-called Islamic State (ISIS) in 2014, much of this agricultural cropland in Syria and Iraq, have fallen under their control (Gibson et al., 2015). Despite the on-going conflict, agriculture productivity has been sustained under ISIS, as the regime seek to exploit the economic benefit of cereal production (Jaafar and Woertz, 2016). It will be interesting to monitor how dust emission frequency compares during ISIS control, especially in future years, where stocks of quality seed, needed to sustain profitable agriculture are due to expire, as the current international embargo prevents the import of additional seeds into ISIS territory (Jaafar and Woertz, 2016).

In southern Iraq, the Mesopotamia Marshes provide a historical example of how political factors impact on the environment (Richardson, 2005). These wetlands lie at the confluence

of the Tigris and Euphrates rivers (Fig. 6.10), formed of three separate marshes (Al-Hawizeh, Al-Hammar and the Central Marsh), which once formed the largest wetland ecosystem in the Middle East (Gibson et al., 2015). Previously, the Saddam regime drained the marshes through multiple upstream channel management programs (Richardson, 2005). These included the construction of the 'Third River' in 1993, diverting much of the Tigris River towards the irrigation channels around Baghdad (Gibson et al., 2015), resulting in a 90% reduction in vegetation cover by 1994 (Munro and Touron, 1997). After the removal of the Saddam Regime in 2003, efforts were made to divert waters back into the wetlands, resulting in 39% (29,250 km^2) of the area being re-flooded by 2005, with vegetation cover expanding by 800 km^2 per year (Richardson and Hussain, 2006). A substantial proportion of vegetation recovery is driven by irrigated agriculture on the banks of the Euphrates River in both the Al-Hammar and Central Marshes (Gibson et al., 2015). Importantly, vegetation stress continues in the region as high soil salinity and environmental pollution left over from the period of drainage mean that regeneration is not possible over the entire area (Richardson, 2005). Recently, the construction of a dike on the Karkeh River (Iran) - the main supply of fresh water to the sole-surviving natural marsh (Al-Hawzieh), and the 2007 - 2009 drought conditions, progressively reduced the extent of the marshes back to pre-2003 proportions (Gibson et al., 2015). As shown by the Sistan Basin, Iran (see Section 5.3.5), semi-permanent wetlands are highly effective dust sources, so it is interesting to use the high-resolution SEVIRI dust emission inventory to examine how these semi-permanent wetlands have reacted to recent changes in their hydrological regime.
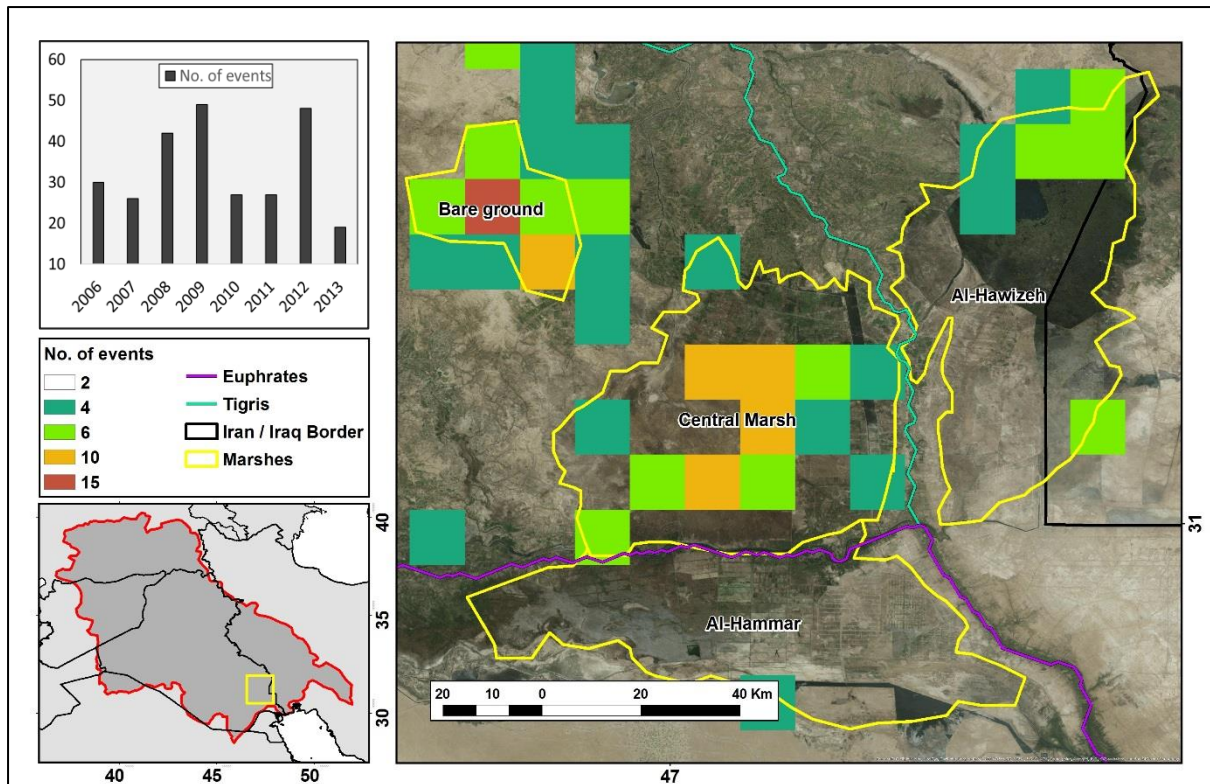
Figure 6.10: Dust emission climatology of the Mesopotamia Marshes (2006 – 2013).
Spatial distribution of emission surfaces described by number of dust events per 0.1° grid
square.

In total, 268 dust events were generated from the greater marshland area during the 2006 –
2013 period, with a concentration of events from the Central Marsh and an area of bare
ground to the north-west (Fig. 6.10). The Al Hammar Marsh appears the least active,
generating just 14 dust events. This marsh is most heavily cultivated, with evidence of
irrigation channels to the north and south sides of the marsh. Interestingly, dust emission
frequency is highest in the semi-natural Central Marsh (74 dust events), showing the greatest
sensitivity to drought conditions. Here, and throughout the Mesopotamia Marshes, dust
emission frequency increased during the extreme drought period 2007 – 2009 (Fig. 6.10),
while the emission frequency of the Central Marsh continued to rise, peaking during the dry
season of the following year (JJA 2010). While 2010 saw the TEB as a whole receive the first
prolonged period of positive SPI since the beginning of the drought (Fig. 6.8), this will have
increased river flow in the predominately drier south, rather than increased direct
precipitation (see Section 2.6.1). On cultivated surfaces, this increased flow will have
enhanced agriculture productivity, reducing emission potential; while on the un-cultivated,

saline-rich bare soils of the Central Marshes, the increased flow will have likely increased deflation potential by renewed sediment supply and surface crust breakdown. As demonstrated by the Tunisian and Algerian Chotts (Bryant et al., 1994) and the Etosha Pan (Bryant et al., 2003) examples (see Sections 2.4.3 and 2.5.1 respectively), desiccation of these ephemeral/seasonal pans during the following dry season (JJA) will provide concentrated areas of fine alluvial deposits, that are highly susceptible to erosion by surface winds. In the east, dust emissions from the Al-Hawizeh marsh are concentrated on the barren northern shoreline. Examination of historical Google Earth images show a continuous recession of this shoreline during the 2007-2009 drought, exposing a large area of marsh bed to surface deflation. Deflation here is therefore likely to be linked to the same desiccation process as seen in the Central Marsh.

Desiccation of these wetlands has exposed the environmental damage caused by upstream pollution, where large quantities of industrial waste, dumped into the area over decades, have developed dry marsh beds rich with heavy metals (Adriansen, 2006). During dust events in Kuwaiti City, atmospheric levels of copper (Cu), nickel (Ni), lead (Pb) and zinc (Zn) particles increase dramatically (Al Awadhi and Al Shuaibi, 2013) and it is possible that a proportion of these heavy metals are derived from the nearby Mesopotamia Marshes. Given the ecological and apparent environmental importance of the Marshes (Richardson et al., 2005), it will be important to observe how these wetlands develop in a drier 21st Century and how this affects their dust emission potential.

6.4.4   Tigris Euphrates Basin – Dusty days and climatic conditions

As shown throughout the period 2006 - 2013, TEB dust emission events peak during JJA. These months coincides with minimal soil moisture and vegetation cover on the regions extensive alluvial and rain-fed agricultural surfaces (see Section 6.4.2). However, for long-range dust emission to take place, sufficiently strong surface wind speed and vertical velocities are required to overcome emission thresholds and gravitational deposition (see Section 2.3.4). These summer months are synonymous with an intensification of the north-westerly Shamal winds, whereby a semi-permanent heat low over the Arabian Peninsula accelerates surface winds in response to a pressure gradient with high pressure areas in north Africa and the Mediterranean Sea (see Section 2.5.3). This is demonstrated here by the high proportion of

dust events travelling south-east from the Mesopotamia sub-regions (see Section 4.8). Consequently, recent studies suggest that TEB dust emissions during the period 2006 – 2013 have had a significant effect on horizontal visibility across the Arabian Peninsula. Meteorological station data show a dominance of north-westerly winds (Notaro et al., 2015), coinciding with the greatest atmospheric aerosol loads of the past four decades (Yu et al., 2015). Indeed, compared to a relatively low dust emission period (2001 – 2005), Notaro et al. (2015) detected no increase in local surface wind speeds, which they take to rule out local sources of the enhanced aerosol load.
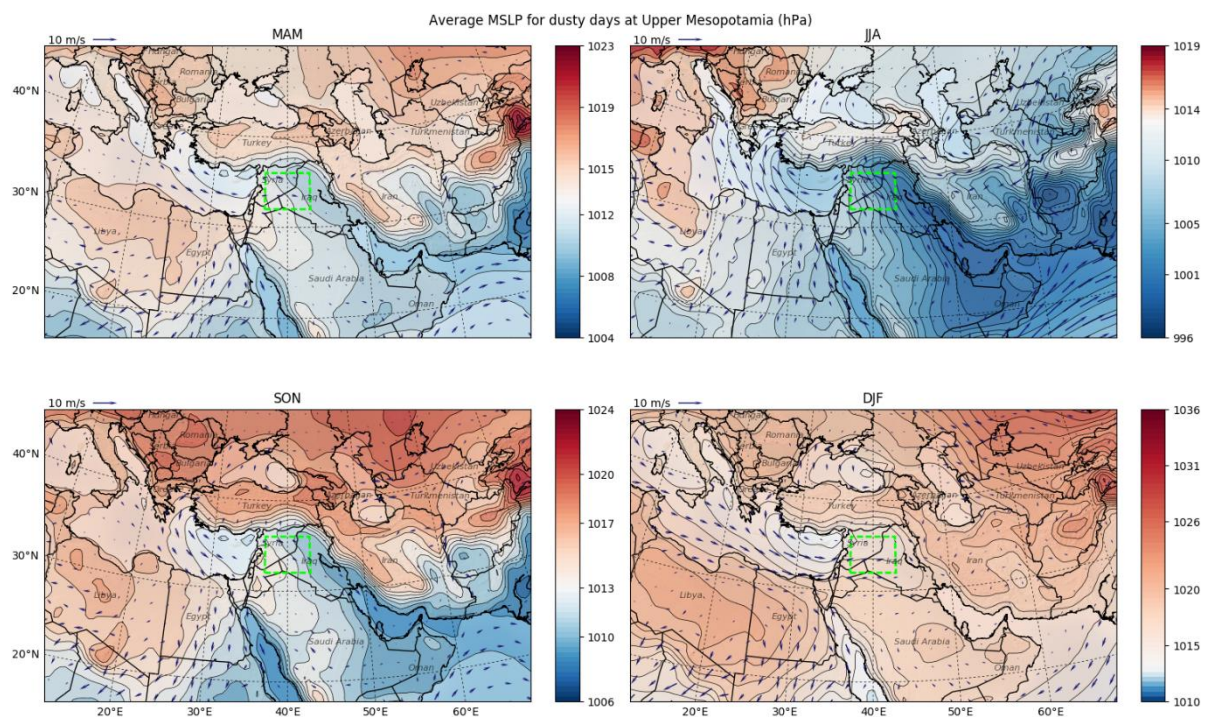
Figure 6.11: Seasonal (synoptic) SLP and 10 m vector wind averaged during days that exceed a threshold number of dust events (see Section 3.6).

To determine the synoptic patterns linked to peak dust activity, sea level atmospheric pressure (SLP) values from ERA-Interim reanalysis data (ECMWF) were averaged over the days on which the number of dust events exceeded a seasonal threshold (see Section 3.6). From these data, JJA dusty day show a clear prevailing synoptic pattern, whereby a trough of low pressure (below 1005 hPa) extends from the Arabian Sea through the Persian Gulf and across the TEB (Fig. 6.11). High pressure system develops over the western Mediterranean. The

resulting pressure gradient drives strong north-westerly surface (10 m) winds across the TEB with an average speed of about 10 m s^{-1}. This synoptic pattern is replicated, albeit with a weaker gradient, during dusty days in both MAM and SON, supporting previous studies (Bou Karam *et al.*, 2017; Hamidi *et al.*, 2013; Kaskaoutis *et al.*, 2015b), that have demonstrated link between dust emission and this circulation pattern at multiple geopotential heights (700 and 850 hPa).

Re-analysis simulations of typical summer Shamal conditions show a link to persistent nocturnal LLJs (Bou Karam et al., 2017). During a five day period (27 June – 2 July 2010), Bou Karam et al. (2017) consistently detected a low-level jet (LLJ) in the lower atmosphere (~500 m above the ground). Created by a nocturnal temperature inversion – typical over barren desert surface in stable conditions (Kaskaoutis et al, 2015), the jet thermally de-couples from the PBL (see Section 2.5.5). Removed from topographic frictional forces within the PBL, the Bou Karam et al. (2017) analysis sees the elevated jet accelerate to wind speeds in access of 20 m s^{-1} during the pre-sunrise morning hours (03:00 – 06:00 local time) – point of greatest inversion. Contrastingly, peak surface winds are out-of-phase with the LLJ, peaking instead towards the middle of the day. At this point, the LLJ's momentum is rapidly re-directed towards the surface in response to heating of the land surface and the subsequent breakdown of surface inversions, thermally recoupling the boundary layer with the elevated jet in the late morning (Knippertz and Todd, 2012). During re-analysis simulations, Bou Karam et al. (2017) observed sustained surface wind speeds above 7 m s^{-1} between 12:00 and 15:00 local time (09:00 and 12:00 UTC). Unlike the LLJ, high surface wind speeds are constrained by orthographic boundaries, limiting the highest Shamal winds to the alluvial channel across the TEB (areas below 500 m asl).

During this same period, 54 dust emission events were observed in the SEVIRI dust emission inventory, with a mean start time of 10:45 (local time), reacting directly to the out-of-phase response to LLJ momentum. Across the entire study period (2006 – 2013), 92% of JJA dust emissions in the TEB started between 06:00 and 15:00 (local time), indicating a persistent link between LLJs and summer-Shamal dust events.

6.5   Summary

In this chapter the spatial distribution of dust emission surfaces in the Middle East, derived from manual inspection of SEVIRI Dust RGB images, have been compared to previous studies that have used a range of remote sensing platforms and methods. When compared at a sub-regional scale, considerable variability exists between all of the previous studies, especially in the southern parts of the Arabian Peninsula. Here, the combination of low sampling frequency of polar orbiting satellites (TOMS/MODIS) and persistent southerly transport of dust emissions by Shamal winds, cause a transport bias in many of the previous analyses. Consequently, these studies falsely attributed these areas with the highest dust emission potential of the Middle East. Only now, with the high temporal resolution of the SEVIRI imagery, is it possible to account for this transport bias fully, tracking dust back to the point of first emission, and discounting source areas downwind as a result. These results instead describe the importance of upwind sources, especially the alluvial surfaces of the Tigris Euphrates Basin in the Mesopotamia sub regions.

The improvements in spatial accuracy provided by manual inspection of SEVIRI images are further demonstrated at the local scale, where comparisons with automated SEVIRI and MODIS Deep Blue retrievals continue to be offset by downwind transport. Furthermore, neither automated approaches were able to resolve the highly localised nature of dust emission surfaces, failing to replicate discrete areas of frequent emission (i.e. hotspots) described by the manual observations. Overall, the manually derived SEVIRI data outperformed the other products in this respect, making the high-resolution dust source inventory extremely adept at resolving landscape-scale dust sources.

Accordingly, these data were utilised in the sub-basin landform analysis of the Tigris Euphrates Basin, which unlike most previously investigated dust-emitting drainage basins, has a high population density and a significant proportion of cultivated surfaces on its alluvial landscapes. Agricultural and alluvial surfaces define many of the dust emission hotspots across the Middle East, making the results from the Tigris Euphrates Basin an ideal study area to formulate this discussion. This can be summarised by the following points.

- Low relief alluvial surfaces are the main landscape unit for dust emission, generating 35% of the 10,285 dust emission events during the period 2006 – 2013. This is closely followed

by low relief agricultural surfaces (32%), which show the greatest seasonality in emission frequency, producing nearly eight times as many dust events in the dry summer, compared to the more humid winter.

- Agricultural surfaces generate dust heterogeneously, with greatest dust activity in the north, where winter rain-fed wheat and barley dominate agricultural activity. Here, recent drought conditions have severely affected the winter growing season, reducing crop yields and exposing large areas to surface deflation. Consequently, dust emission peaked across the basin in 2009, at the peak of the worst drought in recorded history.

- Vegetation conditions, as described by monthly NDVI values in three most active emission hotspots, show the distinct seasonality of the basin. Dust emission frequency responds to low vegetation cover, with the dust emission notably reduced during 2010, in response to the highest NDVI values during the previous wet season (DJF, 2009/2010).

- Compared to the Lake Eyre Basin and the Chihuahua Desert analyses in Bullard et al. (2011), ephemeral lakes do not contribute a large proportion of dust events in the Tigris Euphrates Basin. However, the small scale nature of these landforms mean they are likely overlooked in the relatively coarse Parajuli et al. (2014) landscape unit map used here. Therefore, higher resolution landform data are required to match the spatial accuracy of the SEVIRI database, and resolve the emission potential of these small-scale landscape units.

- Social political influences on the environment have demonstrably had an impact on the dust emission potential of many land surfaces across the basin. These include the expansion and subsequent abandonment of agricultural lands in Iraq, over exploitation of ground water for irrigation in Syria and continued conflict and mass migration of rural communities; in each case, the dust emission potential has increased through removal of vegetation and decrease in soil moisture.

- The Mesopotamia Marshes provide an historical example whereby politically driven actions, have had a direct consequence on environmental conditions; with the redirecting of the Tigris River, reducing flow to what was the largest natural wetlands in the Middle East. The subsequent desiccation of these marshes is the likely cause for increased surface deflation during the study period (2006 – 2013). Recently re-flooded, the area is now partly cultivated, with these areas preferentially irrigated during recent drought

conditions, ameliorating the drying and increased emission frequency seen in the remaining semi-natural marsh areas.

- Analysis of synoptic patterns for dusty conditions, across the Tigris Euphrates Basin reveals a clear link to a low-pressure trough, extending from the southern extent of the Arabian Peninsula to the lower elevations of southern Iraq. Offset by high pressure to the NW, these conditions produce a powerful pressure gradient that induces average surface wind speeds close to 10 m s^{-1}. Consistent peaks in mid-morning dust emissions are linked with an out-of-phase relationship with nocturnal LLJs, accelerating surface winds in response to convective growth of the PBL, impinging on the fast moving elevated jet and shifting its momentum towards the surface.

Chapter 7: Conclusion

Mineral dust has been recognised as an important factor in many Earth systems (Shao et al., 2011), playing an important role in global radiative forcing (Ridley et al., 2016), land and sea nutrient cycles (Koren et al., 2006) and health and livelihoods of communities across dryland areas (Middleton, 2017). Accurate representation of dust emission sources and their respective emission frequencies are fundamental to correctly depict the potential impact of dust on each of these systems (Ashpole and Washington, 2013). Much of our current understanding of dust emission sources are based on coarse resolution plots of daily atmospheric dust loading (Prospero et al., 2002), or poorly constrained aerosol-climate models (Todd et al., 2008). This thesis set out to improve the accuracy by which dust sources in the Middle East – an important dust-emitting region, are resolved. Using sub-hourly images from SEVIRI Dust RGB product, dust plumes are manually observed in consecutive images to the time and location where they first appear, reproducing a map of precise dust sources and a climatology of dust activity during the period 2006 – 2013 (Chapter 4). This dust emission inventory provides the basis from which to investigate land surface characteristics of all dust sources (Chapter 5), helping to define which land surface and climatological processes dictate changes in dust emission frequency, and how these respond to changing environmental conditions, specifically periods of drought (Chapter 6).

The manually derived SEVIRI dust source inventory presented in this thesis is the first of its kind in the Middle East. This database provides the most detailed an up-to-date analysis of dust emission sources and their respective emission frequencies of all current dust emission data currently available. Overall, 27,680 individual dust emission events were manually tracked back to point of origin during the period 2006 – 2013, providing a high-resolution (0.1°) account of dust emission surfaces in the Middle East, and their respective dust emission climatology at a sub-hourly temporal resolution.

These data reveal a significant spatial variation in dust emission across the Middle East, with the gently sloping Arabian Peninsula producing more than double the number of dust events compared to the complex mountain topography of Iran. The number of dust events peak in Upper Mesopotamia, producing 29% of all dust events. Significantly, few dust events (less than 1%) emanate from the southern Arabian Peninsula. This contrasts with the results of

previous investigations, which recognised the Rub Al Khali sand sea and the foothills of the Al Hajar Mountains – Oman, as an effective dust source areas, with the latter described as the third dustiest region in the world (Prospero et al., 2002). Overall, dust emission surfaces appear highly concentrated, with 23% of all emissions emanating from an area, which covers only 1% of the total land surface area of the Middle East. This is indicative of highly localised dust emission processes, which could not be resolved by existing dust emission data.

Spatial variability in dust emission frequency emphasises the importance of preferential accumulation and availability of fine deflation material. Accordingly, analysis of land surface type shows dust activity increasing on low relief alluvial surfaces within drainage basins. The high spatial resolution of the SEVIRI dust emission inventory makes it possible to distinguish discrete areas of frequent dust emission (i.e. hotspots). These are typically found at lower elevations within the basin, where inspection of aerial imagery reveals multiple fluvial features, including rivers (Makran Coast, Jaz Moorian Basin) or ephemeral lakes (Sistan Basin) and ephemeral channels (Central Saudi Arabia). Here, seasonal peaks in emission frequency are linked to increased upstream precipitation, weathering and supply of fine material to the flat alluvial surfaces surrounding these fluvial features. In certain areas, the process of saltation bombardment is thought to act as a catalyst for dust emission, with migrating dunes identified on alluvial surfaces in central Saudi Arabia, Lower Mesopotamia and the Sistan Basin.

The most active hotspots are found in the upland areas of the Tigris Euphrates Basin – the largest drainage system in the Middle East. Here, and in many of the hotspots across the Middle East, croplands cover large parts of the alluvial surfaces. Dust emission frequency in these areas mimic the seasonal cropping cycle, being supressed in winter during the growing season of rain-fed wheat and barley, and peaking after springtime harvest, where fields are typically barren and exposed to surface winds.

The abundance of these anthropogenic surfaces distinguishes the Tigris Euphrates Basin from similar-scale dust sources around the world. The Tigris Euphrates basin produced 37% of all Middle East dust events during 2006 – 2013. Importantly, the basin, like a large proportion of the Middle East, has suffered prolonged drought conditions during this period. Different reactions in emission frequency have highlighted the greater sensitivity of rain fed agriculture

in the upland areas, experiencing increased frequency of dust emission during drought conditions. Analysis of monthly NDVI figures emphasised this, with non-drought years showing a large increase in vegetation cover and an immediate suppression in dust emission. In contrast, drought conditions in lowland irrigated croplands saw a smaller increase in dust emission frequency, with dust emission increasing during non-drought years, as increased winter channel flow replenished supply of fine sediment to the lowland alluvial plains.

In both the Tigris and Euphrates Basin and the wider Middle East, annual dust emission frequency increased in tandem with years of successive drought, culminating in peaks in both 2009 and 2012/2013. In the Tigris Euphrates Basin, these drought conditions have been linked to growing social tensions and sectarian violence leading to a mass migration of rural communities and agricultural field abandonment. It will be important to monitor how these and other socio-political influences on the environment effect dust emission variability in future years.

Dust emission across the Middle East is seasonal, with sources in Mesopotamia and Iranian sub-regions predominately peaking in JJA, while Arabian sources south of Mesopotamia peak in MAM. Relatively few dust events are produced in DJF in all sub-regions. This sub-regional seasonality resembles previous accounts of dust emission activity (e.g. Ginoux et al., 2012; Middleton, 1986), with peaks in dust emission linked to enhanced surface wind speeds, driven by seasonal synoptic patterns. Peak-JJA dust emission in the Tigris Euphrates Basin is widely associated in literature with north westerly Shamal winds. Analysis of days which produced the highest number of dust events in the Tigris Euphrates Basin show a distinctive low pressure trough (MSLP) from the Persian Gulf to the lower extents of the basin. Offset by high pressure to the NW, the steep pressure gradient creates an acceleration of north westerly surface winds, with average speeds reaching over 10 ms^{-1} in certain parts of the basin. With a peak in dust emissions during the mid to late-morning, JJA dust emissions in the Tigris Euphrates Basin appear to be enhanced by the convective re-coupling of the planetary boundary layer with fast moving LLJs above (approximately 500 m above the surface). This creates an out-of-phase increase in wind speeds, with surface winds peaking several hours behind the elevated jet. This process is frequently reported in other dryland environments, and is associated with dust emission in the Sistan Basin, where the frequency of dust emission peaks earlier than all other dust source areas.

Water or dust cloud obstruction, is a known limitation of satellite remote sensing of dust sources. During such conditions, the high temporal resolution of SEVIRI data provides greater accuracy than polar orbiting satellites; however, greater ambiguity persists where increased humidity – associated with cloud conditions, mask the dust signal in Dust RGB rendering. This effect is accounted for in the inventory, with a degree of confidence score attributed each dust event. These scores can be interpreted as a proxy for atmospheric conditions at time of emission, with the greater number of level 2 (cloudy dust events) occurring during the non-summer months, describing the increased frequency of sub-tropical cyclones tracking across the region from the Mediterranean Sea.

Determining dust sources from manual inspection of sub hourly images takes a considerable amount of time. Automating this process could conceivably produce results more efficiently. However, analysis of the Ashpole and Washington (2013) dust-tracking algorithm showed reduced spatial resolution and accuracy in the results, justifying the time required to perform the investigation manually. Data acquisition issues prevented the use of the highest temporal resolution (15 minute) in all years, with dust emissions during 2008 and 2009 observed at 30-minute resolution only. An investigation into potential uncertainty, created by reduced temporal resolution showed a 17% reduction in the number of dust events observed at the lower – 30 minute resolution, representing a potential underestimation of the emission frequency in these years. The number of dust events in 2008 / 2009, a period of extreme drought, could therefore, have potentially exceeded the 2013 peak.

For dust emission to be identifiable in the SEVIRI Dust RGB imagery, the plume must become cooler (i.e. thermally independent of the surface) (Brindley et al., 2012). This temperature difference may not develop instantaneously with the entrainment of the dust, allowing a time and subsequent transport bias in the positioning of where the plume first appears. With no field study available, it is not possible to determine potential errors caused by this effect, especially as it is likely to be extremely dynamic, dependent on air temperature and humidity, horizontal and vertical wind velocities, and thermal characteristics of the deflating material and the land surface. Accordingly, this effect is not represented in the spatial distribution of source locations. This is deemed acceptable, due to the likelihood of sufficient plume cooling taking place within a relatively short distance, which does not exceed more than a few kilometres, equivalent to 1-2 (4-5 km^2) pixels (Banks and Brindley, 2013).

The improvements in both spatial accuracy and resolution, compared to existing dust source data, gives the SEVIRI dust source inventory multiple practical applications. When combined with land surface information of a comparable resolution, these data could better constrain aerosol-climate models. These data will be extremely useful for policy makers and local communities alike, with improved future aerosol scenarios and accurately defined source areas helping to mitigate against significant dust-based hazards, in what is expected to be a drier and potentially dustier Middle East in the 21st Century (Kelley et al., 2015).

The land surface analysis presented here has demonstrated the high potential for agricultural surfaces to produce dust emission, and importantly their variable response to periods of drought. These data demonstrate that not all land surfaces of a certain type are equally sensitive to environmental conditions, helping to identifiy where land management strategies should be focussed. Further analyses, including comparisons with dryland agriculture throughout both the Middle East and globally, could provide valuable information required in the protection of nutrient-rich agricultural soils from wind erosion. Indeed, these data have already demonstrated how land and channel management practices have affected the dust emission potential and ecological impact of dust emission areas at varying scales – e.g. the Mesopotamian Mashes and Tigris Euphrates Basin. These data have the potential to be equally beneficial to investigations of the numerous dust emission hotspots in the Middle East.

Beyond these potential applications, the data produced in this investigation can be used to support several future research opportunities. These include a higher resolution inspection of land surface processes, specifically identifying the response in dust emission frequency on floodplains, as defined by a hydrological flood model. In this research, estimates from alluvial surfaces are simply defined by interpretation of aerial imagery or simplistic spatial relationships with river networks. With clearly defined areas of repeated inundation, these data could better describe dust emission response to specific flood events.

There still exists a need to improve our understanding of the total effect of dust in the atmosphere, from both a radiative forcing and public health perspective (Shao et al., 2011; Middleton, 2017). This thesis has focussed on the primary phase of dust emission (i.e. the source location); however, the dust emission point source data is ideal for trajectory

modelling. With the use of the National Oceanic and Atmospheric Administration (NOAA) HYSPLIT model, transport patterns and deposition areas from specific dust source locations can be analysed. Combined with AOD values, now readily inferred from SEVIRI data (Brindley and Russel, 2009; Klüser and Schepanski, 2009), these data will provide greater insights into the relative emission flux and the long-range impact of individual dust sources, which is not explored in the current inventory. Furthermore, these data will help to determine the importance of specific dust emission processes, providing valuable information for future climate simulations and policy makers.

References

Abdi Vishkaee, F., Flamant, C., Cuesta, J., Flamant, P., Khalesifard, H.R. (2011) Multiplatform observations of dust vertical distribution during transport over northwest Iran in the summertime. *Journal of Geophysical Research Atmospheres*. **116**(5), 1–13.

Abish, B., Mohanakumar, K. (2013) Absorbing aerosol variability over the Indian subcontinent and its increasing dependence on ENSO. *Global and Planetary Change*. **106**, 13–19.

Ackerman, S.A. (1997) Remote sensing aerosols using satellite infrared observations. *Journal of Geophysical Research: Atmospheres*. **102**(D14), 17069–17079.

Akbari, S. (2011) Dust Storms, Sources in the Middle East, and Economic Model for Survey its Impacts. *Australian Journal of Basic and Applied Sciences*. **5**(12), 227–233.

Al-Awadhi, J.M., AlShuaibi, A.A. (2013) Dust fallout in Kuwait city: Deposition and characterization. *Science of the Total Environment*. **461**–**462**, 139–148.

Alizadeh Choobari, O., Zawar-Reza, P., Sturman, A. (2013) Low level jet intensification by mineral dust aerosols. *Annales Geophysicae*. **31**(4), 625–632.

Alpert, P., Ganor, E. (2001) Comparison to surface observations over the Middle East for the extreme dust storm , March 14-17 , 1998 Abstract . A comparison of the TOMS aerosol index (AI) with both mea- surements of dust concentrations and synoptic data over the Middle East for and. *Journal of Geophysical Research*. **106**(D16), 18275–18286.

Ansmann, A., Tesche, M., Knippertz, P., Bierwirth, E., Althausen, D., Müller, D., Schulz, O. (2009) Vertical profiling of convective dust plumes in southern Morocco during SAMUM. *Tellus, Series B: Chemical and Physical Meteorology*. **61**(1), 340–353.

Ashpole, I., Washington, R. (2013) A new high-resolution central and western Saharan summertime dust source map from automated satellite dust plume tracking. *Journal of Geophysical Research Atmospheres*. **118**(13), 6981–6995.

Ashpole, I., Washington, R. (2012) An automated dust detection using SEVIRI: A multiyear climatology of summertime dustiness in the central and western Sahara. *Journal of Geophysical Research Atmospheres*. **117**(8).

Aubault, H., Webb, N.P., Strong, C.L., McTainsh, G.H., Leys, J.F., Scanlan, J.C. (2015) Grazing impacts on the susceptibility of rangelands to wind erosion: The effects of stocking rate, stocking strategy and land condition. *Aeolian Research*. **17**, 89–99.

Baddock, M.C., Bullard, J.E., Bryant, R.G. (2009) Dust source identification using MODIS: A comparison of techniques applied to the Lake Eyre Basin, Australia. *Remote Sensing of Environment*. **113**(7), 1511–1528.

Baddock, M.C., Gill, T.E., Bullard, J.E., Acosta, M.D., Rivera Rivera, N.I. (2011) Geomorphology of the Chihuahuan Desert based on potential dust emissions. *Journal of Maps*. **7**(1), 249–259.

Banks, J.R., Brindley, H.E. (2013) Evaluation of MSG-SEVIRI mineral dust retrieval products over North Africa and the Middle East. *Remote Sensing of Environment*. **128**, 58–73.

Banks, J.R., Brindley, H.E., Flamant, C., Garay, M.J., Hsu, N.C., Kalashnikova, O. V., Klüser, L., Sayer, A.M. (2013) Intercomparison of satellite dust retrieval products over the west African Sahara during the Fennec campaign in June 2011. *Remote Sensing of Environment*. **136**(June 2007), 99–116.

Barough, M.S., Kashani, S.S., Bidokhti, A.A., Ranjbar, A. (2010) The Numerical Study of Low Level Jets Formation in South Eastern of Iran.

Beaumont, P. (1996) Agricultural and environmental changes in the upper Euphrates catchment of Turkey and Syria and their political and economic implications. *Applied Geography*. **16**(2), 137–157.

Belnap, J; Warren, S.D. (2002) Patton's Tracks in the Mojave Desert, USA: An Ecological Legacy. *Arid Land Research and Management*. **16**(October 2013), 245–258.

Ben-Ami, Y., Koren, I., Rudich, Y., Artaxo, P., Martin, S.T., Andreae, M.O. (2010) Transport of North African dust from the Bodélé depression to the Amazon Basin: A case study. *Atmospheric Chemistry and Physics*. **10**(16), 7533–7544.

Benedetti, A., Mangold, A., Dethof, A., Dewitte, S., Chiapello, I., Huneeus, N., Flentje, H., Kinne, S., Morcrette, J.J., Boucher, O., Engelen, R.J., Fisher, M., Jones, L., Kaiser, J.W., Razinger, M., Simmons, A.J., Suttie, M. (2011) Aerosol analysis and forecast in the European Centre for Medium-Range Weather Forecasts Integrated Forecast System: 3. Evaluation by means of case studies. *Journal of Geophysical Research Atmospheres*. **116**(3), 1–18.

Bou Karam, D., Flamant, C., Chaboureau, J.P., Banks, J., Cuesta, J., Brindley, H., Oolman, L. (2017) Dust emission and transport over Iraq associated with the summer Shamal winds. *Aeolian Research*. **24**, 15–31.

Bou Karam, D., Flamant, C., Cuesta, J., Pelon, J., Williams, E. (2010) Dust emission and transport associated with a Saharan depression: February 2007 case. *Journal of Geophysical Research Atmospheres*. **115**(13).

Breeze, P.S., Drake, N.A., Groucutt, H.S., Parton, A., Jennings, R.P., White, T.S., Clark-Balzan, L., Shipton, C., Scerri, E.M.L., Stimpson, C.M., Crassard, R., Hilbert, Y., Alsharekh, A., Al-Omari, A., Petraglia, M.D. (2015) Remote sensing and GIS techniques for reconstructing Arabian palaeohydrology and identifying archaeological sites. *Quaternary International*. **382**, 98–119.

Brindley, H., Knippertz, P., Ryder, C., Ashpole, I. (2012) A critical evaluation of the ability of the Spinning Enhanced Visible and Infrared Imager (SEVIRI) thermal infrared red-green-blue rendering to identify dust events: Theoretical analysis. *Journal of Geophysical Research Atmospheres*. **117**(7), 1–20.

Broxton, P.D., Zeng, X., Sulla-Menashe, D., Troch, P.A. (2014) A global land cover climatology using MODIS data. *Journal of Applied Meteorology and Climatology*. **53**(6), 1593–1605.

Bryant, R.G. (1999) Application of AVHRR to monitoring a climatically sensitive playa. Case study: Chott el Djerid, southern Tunisia. *Earth Surface Processes and Landforms*. **24**(4), 283–302.

Bryant, R.G. (2003) Monitoring hydrological controls on dust emissions: preliminary observations from Etosha Pan, Namibia. *The Geographical Journal*. **169**(2), 131–141.

Bullard, J., Baddock, M., McTainsh, G., Leys, J. (2008) Sub-basin scale dust source geomorphology detected using MODIS. *Geophysical Research Letters*. **35**(15), 1–6.

Bullard, J.E., Baddock, M., Bradwell, T., Crusius, J., Darlington, E., Gaiero, D., Gasso, S., Gisladottir, G., Hodgkins, R., McCulloch, R., Mckenna-Neuman, C., Mockford, T., Stewart, H., Thorsteinsson, T. (2016) High latitude dust in the Earth system. *Reviews of Geophysics*. **54**(2), 1–39.

Bullard, J.E., Harrison, S.P., Baddock, M.C., Drake, N., Gill, T.E., McTainsh, G., Sun, Y. (2011) Preferential dust sources: A geomorphological classification designed for use in global dust-cycle models. *Journal of Geophysical Research: Earth Surface*. **116**(4).

Bullard, J.E., McTainsh, G.H. (2003) Aeolian-fluvial interactions in dryland environments: examples,

concepts and Australia case study. *Progress in Physical Geography*. **27**(4), 471–501.

Bullard, J.E., White, K. (2005) Dust production and the release of iron oxides resulting from the aeolian abrasion of natural dune sands. *Earth Surface Processes and Landforms*. **30**(1), 95–106.

Cao, H., Amiraslani, F., Liu, J., Zhou, N. (2015) Identification of dust storm source areas in West Asia using multiple environmental datasets. *Science of the Total Environment*. **502**, 224–235.

Chomette, O., Legrand, M., Marticorena, B. (1999) Determination of the wind speed threshold for the emission of desert dust using satellite remote sensing in the thermal infrared. *Journal of Geophysical Research*. **104**, 31207.

Choobari, O.A., Zawar-Reza, P., Sturman, A. (2014) The global distribution of mineral dust and its impacts on the climate system: A review. *Atmospheric Research*. **138**, 152–165.

Claquin, T., Schulz, M., Balkanski, Y., Boucher, O. (1998) Uncertainties in assessing radiative forcing by mineral dust. *Tellus, Series B: Chemical and Physical Meteorology*. **50**(5), 491–505.

Cooke, R., Brunsden, D., Doornkamp, J.C., Jones, D.K.C. (1985) *Cooke_1985.Pdf*. New York: Oxford University Press.

Cooke, R., Warren, A., Goudie, A. (1993) *Desert geomorphology:* London: UCL Press Limited.

Criado, C., Dorta, P. (2003) An unusual 'blood rain' over the Canary Islands (Spain). The storm of January 1999. *Journal of Arid Environments*. **55**(4), 765–783.

Cuesta, J., Marsham, J.H., Parker, D.J., Flamant, C. (2009) Dynamic mechanisms controlling the verticle redistribution of dust and the thermodynamic structure of theWest Saharan atmospheric boundary layer during summer. *Atmospheric Science Letters*. **10**, 34–42.

Currit, N. (2005) Development of a remotely sensed, historical land-cover change database for rural Chihuahua, Mexico. *International Journal of Applied Earth Observation and Geoinformation*. **7**(3), 232–247.

Didan, K. (2015) MOD13A3 MODIS/Terra vegetation Indices Monthly L3 Global 1km SIN Grid V006. NASA EOSDIS Land Processes DAAC.

Dubovik, O., Holben, B., Eck, T.F., Smirnov, A., Kaufman, Y.J., King, M.D., Tanré, D., Slutsker, I. (2002) Variability of Absorption and Optical Properties of Key Aerosol Types Observed in Worldwide Locations. *Journal of the Atmospheric Sciences*. **59**(3), 590–608.

Engelstaedter, S., Tegen, I., Washington, R. (2006) North African dust emissions and transport. *Earth-Science Reviews*. **79**(1–2), 73–100.

ESCWA, BGR (2013) Inventory of Shared Water Resources in Western Asia: 3-Tigris River Basin. *Inventory of Shared Water Resources in Western Asia*, 99–125.

Feng, S., Fu, Q. (2013) Expansion of global drylands under a warming climate. *Atmospheric Chemistry and Physics*. **13**(19), 10081–10094.

Formica, A.F., Burnside, R.J., Dolman, P.M. (2017) Rainfall validates MODIS-derived NDVI as an index of spatio-temporal variation in green biomass across non-montane semi-arid and arid Central Asia. *Journal of Arid Environments*. **142**, 11–21.

Gherboudj, I., Naseema Beegum, S., Ghedira, H. (2017) Identifying natural dust source regions over the Middle-East and North-Africa: Estimation of dust emission potential. *Earth-Science Reviews*. **165**, 342–355.

Gibson, G.R., Campbell, J.B., Zipper, C.E. (2015) Sociopolitical influences on cropland area change in

Iraq, 2001–2012. *Applied Geography*. **62**, 339–346.

Gill, T.E. (1996) Eolian sediments generated by anthropogenic disturbance of playas: human impacts on the geomorphic system and geomorphic impacts on the human system. . **17**, 207–228.

Gillette, D.A. (1999) A qualitative geophysical explanation for 'hot spot' dust emitting source regions. *Contributions to atmospheric physics*. **72**, 67–77.

Ginoux, P., Chin, M., Tegen, I., Prospero, J.M., Holben, B., Dubovik, O., Lin, S.-J. (2001) Sources and distributions of dust aerosols simulated with the GOCART model. *Journal of Geophysical Research*. **106**, 20255–20273.

Ginoux, P., Garbuzov, D., Hsu, N.C. (2010) Identification of anthropogenic and natural dust sources using moderate resolution imaging spectroradiometer (MODIS) deep blue level 2 data. *Journal of Geophysical Research Atmospheres*. **115**(5), 1–10.

Ginoux, P., Prospero, J.M., Gill, T.E., Hsu, N.C., Zhao, M. (2012) Global-scale attribution of anthropogenic and natural dust sources and their emission rates based on MODIS Deep Blue aerosol products. *Reviews of Geophysics*. **50**(3), 1–36.

Ginoux, P., Torres, O. (2003) Empirical TOMS index for dust aerosol: Applications to model validation and source characterization. *Journal of Geophysical Research*. **108**(D17), 4534.

Gleick, P.H. (2014) Water, Drought, Climate Change, and Conflict in Syria. *Weather, Climate, and Society*. **6**(3), 331–340.

Goudie, A.S. (2009) Dust storms: Recent developments. *Journal of Environmental Management*. **90**(1), 89–94.

Goudie, A.S., Middleton, N.J. (2001) Saharan dust storms: Nature and consequences. *Earth-Science Reviews*. **56**(1–4), 179–204.

Goudie, A.S., Middleton, N.J. (1992) The changing frequency of dust storms through time. *Climate Change*. **20**, 197–225.

Hamidi, M., Kavianpour, M.R., Shao, Y. (2017) A quantitative evaluation of the 3–8 July 2009 Shamal dust storm. *Aeolian Research*. **24**(July 2009), 133–143.

Hamidi, M., Kavianpour, M.R., Shao, Y. (2013) Synoptic analysis of dust storms in the Middle East. *Asia-Pacific Journal of Atmospheric Sciences*. **49**(3), 279–286.

Harrison, S.P., Kohfeld, K.E., Roelandt, C., Claquin, T. (2001) The role of dust in climate changes today, at the last glacial maximum and in the future. *Earth-Science Reviews*. **54**(1–3), 43–80.

Haywood, J.M., Allan, R.P., Culverwell, I., Slingo, T., Milton, S., Edwards, J., Clerbaux, N. (2005) Can desert dust explain the outgoing longwave radiation anomaly over the Sahara during July 2003? *Journal of Geophysical Research D: Atmospheres*. **110**(5), 1–14.

Heald, C.L., Ridley, D.A., Kroll, J.H., Barrett, S.R.H., Cady-Pereira, K.E., Alvarado, M.J., Holmes, C.D. (2014) Contrasting the direct radiative effect and direct radiative forcing of aerosols. *Atmospheric Chemistry and Physics*. **14**(11), 5513–5527.

Herman, J.R., Bhartia, P.K., Torres, O., Hsu, C., Seftor, C., Celarier, E. (1997) Global distribution of UV-absorbing aerosols from Nimbus 7/TOMS data. *Journal of Geophysical Research*. **102**(D14), 16911.

Holben, B.N., Eck, T.F., Slutsker, I., Tanré, D., Buis, J.P., Setzer, A., Vermote, E., Reagan, J.A., Kaufman, Y.J., Nakajima, T., Lavenu, F., Jankowiak, I., Smirnov, A. (1998) AERONET—A Federated Instrument Network and Data Archive for Aerosol Characterization. *Remote Sensing of Environment*. **66**(1), 1–

16.

Hsu, N.C., Herman, J.R., Torres, O., Holben, B.N., Tanre, D., Eck, T.F., Smirnov, A., Chatenet, B., Lavenu, F. (1999) Comparisons of the TOMS aerosol index with Sun-photometer aerosol optical thickness: Results and applications. *Journal of Geophysical Research: Atmospheres*. **104**(D6), 6269–6279.

Hsu, N.C., Jeong, M.J., Bettenhausen, C., Sayer, A.M., Hansell, R., Seftor, C.S., Huang, J., Tsay, S.C. (2013) Enhanced Deep Blue aerosol retrieval algorithm: The second generation. *Journal of Geophysical Research Atmospheres*. **118**(16), 9296–9315.

Hsu, N.C., Tsay, S., King, M.D., Herman, J.R. (2004) Aerosol Properties over Bright-Reflecting Source Regions. *IEEE Transactions on Geoscience and Remote Sensing*. **42**(3), 23.

Huete, A., Justice, C., Leeuwen, W. V. (1999) Modis Vegetation Index Algorithm Theoretical Basis. *Environmental Sciences*. (Mod 13), 129.

Husar, R.B., Tratt, D.M., Schichtel, B.A., Falke, S.R., Li, F., Jaffe, D., Gill, T., Laulainen, N.S., Lu, F., Reheis, M.C., Chun, Y., Westphal, D., Mckendry, I., Kuring, N., Feldman, G.C., Frouin, R.J., Merrill, J., Dubois, D., Vignola, F., Murayama, T., Nickovic, S., Wilson, W.E., Sassen, K., Sugimoto, N., Malm, W.C., Gasso, S., Holben, B.N., Gueymard, C., McClain, C. (2001) Asian dust events of April 1998 concentration over the valleys of the West Coast was about peaks mass mean diameter was 2-3 /• m , and the dust. . **106**(April 1998).

Jaafar, H.H., Woertz, E. (2016) Agriculture as a funding source of ISIS: A GIS and remote sensing analysis. *Food Policy*. **64**, 14–25.

Johnson, B.T., Brooks, M.E., Walters, D., Woodward, S., Christopher, S., Schepanski, K. (2011) Assessment of the Met Office dust forecast model using observations from the GERBILS campaign. *Quarterly Journal of the Royal Meteorological Society*. **137**(658), 1131–1148.

Kahn, R.A., Nelson, D.L., Garay, M.J., Levy, R.C., Bull, M.A., Diner, D.J., Martonchik, J. V., Paradise, S.R., Hansen, E.G., Remer, L.A. (2009) MISR aerosol product attributes and statistical comparisons with MODIS. *IEEE Transactions on Geoscience and Remote Sensing*. **47**(12), 4095–4114.

Kaskaoutis, D.G., Kosmopoulos, P.G., Nastos, P.T., Kambezidis, H.D., Sharma, M., Mehdi, W. (2012) Transport pathways of Sahara dust over Athens, Greece as detected by MODIS and TOMS. *Geomatics, Natural Hazards and Risk*. **3**(1), 35–54.

Kaskaoutis, D.G., Rashki, A., Francois, P., Dumka, U.C., Houssos, E.E., Legrand, M. (2015) Meteorological regimes modulating dust outbreaks in southwest Asia: The role of pressure anomaly and Inter-Tropical Convergence Zone on the 1-3 July 2014 case. *Aeolian Research*. **18**, 83–97.

Kaskaoutis, D.G., Rashki, A., Houssos, E.E., Mofidi, A., Goto, D., Bartzokas, A., Francois, P., Legrand, M. (2015) Meteorological aspects associated with dust storms in the Sistan region, southeastern Iran. *Climate Dynamics*. **45**(1–2), 407–424.

Kelley, C.P., Mohtadi, S., Cane, M.A., Seager, R., Kushnir, Y. (2015) Climate change in the Fertile Crescent and implications of the recent Syrian drought. *Proceedings of the National Academy of Sciences*. **112**(11), 3241–3246.

Kiamehr, R., Sjöberg, L.E. (2005) Effect of the SRTM global DEM on the determination of a high-resolution geoid model: A case study in Iran. *Journal of Geodesy*. **79**(9), 540–551.

Kim, D., Chin, M., Remer, L.A., Diehl, T., Bian, H., Yu, H., Brown, M.E., Stockwell, W.R. (2017) Role of surface wind and vegetation cover in multi-decadal variations of dust emission in the Sahara and Sahel. *Atmospheric Environment*. **148**, 282–296.

Kitoh, A., Yatagai, A., Alpert, P. (2008) First super-high-resolution model projection that the ancient 'Fertile Crescent' will disappear in this century'. *Hydrological Research Letters*. **2**(December 2007), 46–46.

Klüser, L., Kleiber, P., Holzer-Popp, T., Grassian, V.H. (2012) Desert dust observation from space - Application of measured mineral component infrared extinction spectra. *Atmospheric Environment*. **54**, 419–427.

Klüser, L., Martynenko, D., Holzer-Popp, T. (2011) Thermal infrared remote sensing of mineral dust over land and ocean: A spectral SVD based retrieval approach for IASI. *Atmospheric Measurement Techniques*. **4**(5), 757–773.

Knippertz, P. (2014) Mineral dust: A key player in the earth system. *Mineral Dust: A Key Player in the Earth System*. (May), 1–509.

Knippertz, P., Deutscher, C., Kandler, K., Müller, T., Schulz, O., Schütz, L. (2007) Dust mobilization due to density currents in the Atlas region: Observations from the Saharan Mineral Dust Experiment 2006 field campaign. *Journal of Geophysical Research Atmospheres*. **112**(21), 1–14.

Knippertz, P., Todd, M.C. (2012) Mineral dust aerosols over the Sahara: Meteorological controls on emission and transport and implications for modeling. *Reviews of Geophysics*. **50**(1).

Knippertz, P., Todd, M.C. (2010) The central west Saharan dust hot spot and its relation to African easterly waves and extratropical disturbances. *Journal of Geophysical Research Atmospheres*. **115**(12), 1–14.

Koch, J., Renno, N.O. (2005) The role of convective plumes and vortices on the global aerosol budget. *Geophysical Research Letters*. **32**(18), 1–5.

Kocurek, G. (1998) Aeolian system response to external forcing factors – A sequence stratigraphic view of the Saharan region, in Quaternary Deserts and Climatic Change, edited by A. S. Alsharhan et al., pp. 327 – 349, A. In *Quaternary Deserts and Climatic Change*. pp. 327–349.

Koren, I., Kaufman, Y.J. (2004) Direct wind measurements of Saharan dust events from Terra and Aqua satellites. *Geophysical Research Letters*. **31**(6), 10–13.

Koren, I., Kaufman, Y.J., Washington, R., Todd, M.C., Rudich, Y., Martins, J.V., Rosenfeld, D. (2006) The Bodélé depression: a single spot in the Sahara that provides most of the mineral dust to the Amazon forest. *Environmental Research Letters*. **1**(1), 14005.

Krah, M., McCarthy, T.S., Annegarn, H., Ramberg, L. (2004) Airborne dust deposition in the Okavango Delta, Botswana, and its impact on landforms. *Earth Surface Processes and Landforms*. **29**(5), 565–577.

Kutiel, H., Furman, H. (2003) Dust Storms in the Middle East: Sources of Origin and Their Temporal Characteristics. *Indoor and Built Environment*. **12**(6), 419–426.

Kutuzov, S., Shahgedanova, M., Mikhalenko, V., Ginot, P., Lavrentiev, I., Kemp, S. (2013) High-resolution provenance of desert dust deposited on Mt. Elbrus, Caucasus in 2009–2012 using snow pit and firn core records. *Cryosphere*. **7**(5), 1481–1498.

Lancaster, N., Baker, S., Bacon, S., Mccarley-holder, G. (2015) Catena Owens Lake dune fi elds : Composition , sources of sand , and transport pathways. *Catena*. **134**, 41–49.

Laurent, B., Marticorena, B., Bergametti, G., Mei, F. (2006) Modeling mineral dust emissions from Chinese and Mongolian deserts. *Global and Planetary Change*. **52**(1–4), 121–141.

Lawson, T.J. (1971) Haboob structure at Khartoum. *Weather,*. **26**, 105–112.

Lee, J.A., Allen, B.L., Petersons, R.E., Gregory, J.M., Moffett, K.E. (1994) Environmental Controls on Blowing Dust. . **19**.

Lee, J.A., Baddock, M.C., Mbuh, M.J., Gill, T.E. (2012) Geomorphic and land cover characteristics of aeolian dust sources in West Texas and eastern New Mexico, USA. *Aeolian Research*. **3**(4), 459–466.

Lee, J.J., Kim, C.H. (2012) Roles of surface wind, NDVI and snow cover in the recent changes in Asian dust storm occurrence frequency. *Atmospheric Environment*. **59**(June 2002), 366–375.

Legrand, M., Plana-Fattori, a., N'doumé, C. (2001) Satellite detection of dust using the IR imagery of Meteosat: 1. Infrared difference dust index. *Journal of Geophysical Research*. **106**(D16), 18251.

Lensky, I.M., Rosenfeld, D. (2008) Clouds-Aerosols-Precipitation Satellite Analysis Tool (CAPSAT). *Atmospheric Chemistry and Physics Discussions*. **8**(1998), 4765–4809.

Lev-Yadun, S., Gopher, A., Abbo, S. (2000) The cradle of agriculture. *Science*. **288**, 1602–1603.

Liu, M., Westphal, D.L., Walker, A.L., Holt, T.R., Richardson, K.A., Miller, S.D. (2007) COAMPS Real-Time Dust Storm Forecasting during Operation Iraqi Freedom. *Weather and Forecasting*. **22**(1), 192–206.

Mahowald, N.M., Bryant, R.G., Del Corral, J., Steinberger, L. (2003) Ephemeral lakes and desert dust sources. *Geophysical Research Letters*. **30**(2), 30–33.

Mahowald, N.M., Kloster, S., Engelstaedter, S., Moore, J.K., Mukhopadhyay, S., McConnell, J.R., Albani, S., Doney, S.C., Bhattacharya, A., Curran, M.A.J., Flanner, M.G., Hoffman, F.M., Lawrence, D.M., Lindsay, K., Mayewski, P.A., Neff, J., Rothenberg, D., Thomas, E., Thornton, P.E., Zender, C.S. (2010) Observed 20th century desert dust variability: Impact on climateand biogeochemistry. *Atmospheric Chemistry and Physics*. **10**(22), 10875–10893.

Mahowald, N.M., Luo, C. (2003) A less dusty future? *Geophysical Research Letters*. **30**(17), n/a-n/a.

Marsham, J.H., Parker, D.J., Grams, C.M., Johnson, B.T., Grey, W.M.F., Ross, A.N. (2008) Observations of mesoscale and boundary-layer scale circulations affecting dust transport and uplift over the Sahara. *Atmospheric Chemistry and Physics*. **8**(23), 6979–6993.

Marticorena, B., Bergametti, G. (1995) Modeling the atmospheric dust cycle: 1. Design of a soil-derived dust emission scheme. *Journal of Geophysical Research*. **100**(D8), 16415–16430.

Masutomi, Y., Inui, Y., Takahashi, K., Matsuoka, Y. (2009) Development of highly accurate global polygonal drainage basin data. *Hydrological Processes*. **23**(Decemberr 2008), 572–584.

Maurer, T., Herrmann, L., Stahr, K. (2009) The effect of surface variability factors on wind-erosion susceptibility: A field study in SW Niger. *Journal of Plant Nutrition and Soil Science*. **172**(6), 798–807.

McTainsh, G.H., Leys, J.F., Nickling, W.G. (1999) Wind erodibility of arid lands in the Channel Country of western Queensland, Australia,. *Annals of Geomorphology*. **116**, 113–130.

Meladze, M., Meladze, G. (2017) Climate change: A trend of increasingly frequent droughts in Kakheti Region (East Georgia). *Annals of Agrarian Science*. **15**(1), 96–102.

Micklin, P. (2007) The Aral Sea Disaster. *Annual Review of Earth and Planetary Sciences*. **35**(1), 47–72.

Middleton, N. (2016) Rangeland management and climate hazards in drylands: dust storms, desertification and the overgrazing debate. *Natural Hazards*, 1–14.

Middleton, N.J. (2017) Desert dust hazards: A global review. *Aeolian Research*. **24**, 53–63.

Middleton, N.J. (1986) Dust storms in the Middle East. *Journal of Arid Environments Arid Environ*. (10), 83–96.

Middleton, N.J., Goudie, A.S. (2001) Saharan dust: Sources and trajectories. *Transactions of the Institute of British Geographers*. **26**(2), 165–181.

Middleton, N.J., Sternberg, T. (2013) Climate hazards in drylands: A review. *Earth-Science Reviews*. **126**, 48–57.

Miliaresis, G.C. (2001) Geomorphometric mapping of Zagros Ranges at regional scale. *Computers and Geosciences*. **27**(7), 775–786.

Miller, S.D. (2003) A consolidated technique for enhancing desert dust storms with MODIS. *Geophysical Research Letters*. **30**(20), n/a-n/a.

Miller, S.D., Kuciauskas, A.P., Liu, M., Ji, Q., Reid, J.S., Breed, D.W., Walker, A.L., Mandoos, A. Al (2008) Haboob dust storms of the southern Arabian Peninsula. *Journal of Geophysical Research Atmospheres*. **113**(1), 1–26.

Morid, S., Smakhtin, V., Moghaddasi, M. (2006) Comparison of seven meteorological indices for drought monitoring in Iran. *International Journal of Climatology*. **26**(7), 971–985.

Moridnejad, A., Karimi, N., Ariya, P.A. (2015) Newly desertified regions in Iraq and its surrounding areas: Significant novel sources of global dust particles. *Journal of Arid Environments*. **116**, 1–10.

Myhre, G., Shindell, D., Bréon, F.-M., Collins, W., Fuglestvedt, J., Huang, J., Koch, D., Lamarque, J.-F., Lee, D., Mendoza, B., Nakajima, T., Robock, A., Stephens, G., Takemura, T., Zhang, H. (2013) Anthropogenic and Natural Radiative Forcing. *Climate Change 2013: The Physical Science Basis. Contribution of Working Group I to the Fifth Assessment Report of the Intergovernmental Panel on Climate Change*, 659–740.

Notaro, M., Yu, Y., Kalashnikova, O. V (2015) Regime shift in Arabian dust activity, triggered by persistent Fertile Crescent drought. *Journal of Geophysical Research Atmospheres*. **120**, 10229–10249.

Parajuli, S.P., Yang, Z.L., Kocurek, G. (2014) Mapping erodibility in dust source regions based on geomorphology, meteorology, and remote sensing. *Journal of Geophysical Research: Earth Surface*. **119**, 1977–1994.

Parajuli, S.P., Zender, C.S. (2017) Connecting geomorphology to dust emission through high-resolution mapping of global land cover and sediment supply. *Aeolian Research*. **27**, 47–65.

Pérez, C., Nickovic, S., Pejanovic, G., Baldasano, J.M., Özsoy, E. (2006) Interactive dust-radiation modeling: A step to improve weather forecasts. *Journal of Geophysical Research Atmospheres*. **111**(16).

Peters, M., Tetzlaff, G. (1988) The structure of West African Squall Lines and their environmental moisture budget. *Meteorology and Atmospheric Physics*. **39**(2), 74–84.

Prose, D. V., Metzger, S.K., Wilshire, H.G. (1987) Effects of substrate disturbance on secondary plant succession: Mojave Desert, California. *Journal of Applied Ecology*. **24**, 305–313.

Prospero, J.M., Ginoux, P., Torres, O., Nicholson, S.E., Gill, T.E. (2002) Environmental characterization of global sources of atmospheric soil dust identified with the NIMBUS 7 Total Ozone Mapping Spectrometer (TOMS) absorbing aerosol product. *Reviews of Geophysics*. **40**(1), 1002.

Rashki, A., Arjmand, M., Kaskaoutis, D.G. (2017) Assessment of dust activity and dust-plume pathways over Jazmurian Basin, southeast Iran. *Aeolian Research*. **24**, 145–160.

Reynolds, J.F., Smith, D.M.S., Lambin, E.F., Turner, B.L., Mortimore, M., Batterbury, S.P.J., Downing, T.E., Dowlatabadi, H., Fernandez, R.J., Herrick, J.E., Huber-Sannwald, E., Jiang, H., Leemans, R., Lynam, T., Maestre, F.T., Ayarza, M., Walker, B. (2007) Global Desertification: Building a Science for Dryland Development. *Science*. **316**(5826), 847–851.

Rezazadeh, M., Irannejad, P., Shao, Y. (2013) Climatology of the Middle East dust events. *Aeolian Research*. **10**, 103–109.

Richardson, C.J. (2005) The Restoration Potential of the Mesopotamian Marshes of Iraq. *Science*. **307**(5713), 1307–1311.

Richardson, C.J., Hussain, N. a. (2006) Restoring the Garden of Eden: An Ecological Assessment of the Marshes of Iraq. *BioScience*. **56**(6), 477.

Ridley, D.A., Heald, C.L., Kok, J.F., Zhao, C. (2016) An observationally constrained estimate of global dust aerosol optical depth. *Atmospheric Chemistry and Physics*. **16**(23), 15097–15117.

Roskovensky, J.K., Liou, K.N. (2003) Detection of thin cirrus from 1.38 µm/0.65 µm reflectance ratio combined with 8.6–11 µm brightness temperature difference. *Geophysical Research Letters*. **30**(19), 1985.

Schepanski, K., Tegen, I., Laurent, B., Heinold, B., Macke, A. (2007) A new Saharan dust source activation frequency map derived from MSG-SEVIRI IR-channels. *Geophysical Research Letters*. **34**(18), 1–5.

Schepanski, K., Tegen, I., Macke, A. (2012) Comparison of satellite based observations of Saharan dust source areas. *Remote Sensing of Environment*. **123**, 90–97.

Schepanski, K., Tegen, I., Todd, M.C., Heinold, B., Bönisch, G., Laurent, B., Macke, A. (2009) Meteorological processes forcing Saharan dust emission inferred from MSG-SEVIRI observations of subdaily dust source activation and numerical models. *Journal of Geophysical Research Atmospheres*. **114**(10), 1–18.

Seemann, S.W., Borbas, E.E., Knuteson, R.O., Stephenson, G.R., Huang, H.L. (2008) Development of a global infrared land surface emissivity database for application to clear sky sounding retrievals from multispectral satellite radiance measurements. *Journal of Applied Meteorology and Climatology*. **47**(1), 108–123.

Seidel, D., Fu, Q., Randel, W., Reichler, T. (2008) Widening of the tropical belt in a changing climate. *Nature Geoscience*. **1**(1), 21–24.

Shahgedanova, M., Kutuzov, S., White, K. (2012) of dust deposition events on Garabashi Glacier, Mt Elbrus, Caucasus, developed from snow pits using remote sensing, climate models and sedimentological analysis. *EGU General …*. **14**, 6147.

Shahriar Pervez, M., Budde, M., Rowland, J. (2014) Mapping irrigated areas in Afghanistan over the past decade using MODIS NDVI. *Remote Sensing of Environment*. **149**, 155–165.

Shao, Y. (2004) Simplification of a dust emission scheme and comparison with data. *Journal of Geophysical Research D: Atmospheres*. **109**(10), 1–6.

Shao, Y., Jung, E., Leslie, L.M. (2002) Numerical prediction of northeast Asian dust storms using an integrated wind erosion modeling system. *Journal of Geophysical Research Atmospheres*. **107**(24), 1–23.

Shao, Y., Lu, H. (2000) A simple expression for wind erosion threshold fiction velocity. *Journal of Geophysical Research*. **105**, 22437–22443.

Shao, Y., Wyrwoll, K.H., Chappell, A., Huang, J., Lin, Z., McTainsh, G.H., Mikami, M., Tanaka, T.Y., Wang, X., Yoon, S. (2011) Dust cycle: An emerging core theme in Earth system science. *Aeolian Research*. **2**(4), 181–204.

Sokolik, I.N. (2002) The spectral radiative signature of wind-blown mineral dust: Implications for remote sensing in the thermal IR region. *Geophysical Research Letters*. **29**(24), 2–5.

Sokolik, I.N., Toon, O.B. (1999) Incorporation of mineralogical composition into models of the radiative properties of mineral aerosol from UV to IR wavelengths. *Journal of Geophysical Research: Atmospheres*. **104**(D8), 9423–9444.

Sokolik, I.N., Winker, D.M., Bergametti, G., Gillette, D. a., Carmichael, G., Kaufman, Y.J., Gomes, L., Schuetz, L., Penner, J.E. (2001) Introduction to special section: Outstanding problems in quantifying the radiative impacts of mineral dust. *Journal of Geophysical Research*. **106**(D16), 18015.

Tanaka, T.Y., Kurosaki, Y., Chiba, M., Matsumura, T., Nagai, T., Yamazaki, A., Uchiyama, A., Tsunematsu, N., Kai, K. (2005) Possible transcontinental dust transport from North Africa and the Middle East to East Asia. *Atmospheric Environment*. **39**(21), 3901–3909.

Tegen, I. (2003) Modeling the mineral dust aerosol cycle in the climate system. *Quaternary Science Reviews*. **22**(18–19), 1821–1834.

Tegen, I., Fung, I. (1995) Contribution to the atmospheric mineral aerosol load from land surface modification. *Journal of Geophysical Research*. **100**, 18707–18726.

Tegen, I., Fung, I. (1994) Modelling mineral dust in the atmosphere: Sources, transport, and optical thickness. *Journal of Geophysical Research*. **99**, 22897–22914.

Tegen, I., Harrison, S.P., Kohfeld, K., Prentice, I.C., Coe, M., Heimann, M. (2002) Impact of vegetation and preferential source areas on global dust aerosol: Results from a model study. *Journal of Geophysical Research Atmospheres*. **107**(21).

Tegen, I., Werner, M., Harrison, S.P., Kohfeld, K.E. (2004) Relative importance of climate and land use in determining present and future global soil dust emission. *Geophysical Research Letters*. **31**(5), n/a-n/a.

Thieuleux, F., Moulin, C., Bréon, F.M., Maignan, F., Poitou, J., Tanré, D. (2005) Remote sensing of aerosols over the oceans using MSG/SEVIRI imagery. *Annales Geophysicae*. **23**(12), 3561–3568.

Thomas, D. (2011) *Arid zone geomorphology : process, form and change in drylands / edited by David S.G. Thomas Chichester Wiley-Blackwell*. 3rd ed. Chichester: Wiley-Blackwell.

Todd, M.C., Bou Karam, D., Cavazos, C., Bouet, C., Heinold, B., Baldasano, J.M., Cautenet, G., Koren, I., Perez, C., Solmon, F., Tegen, I., Tulet, P., Washington, R., Zakey, A. (2008) Quantifying uncertainty in estimates of mineral dust flux: An intercomparison of model performance over the Bodélé depression, northern Chad. *Journal of Geophysical Research Atmospheres*. **113**(24).

Torres, O., Bhartia, P.K., Herman, J.R., Ahmad, Z., Gleason, J. (1998) Derivation of aerosol properties from satellite measurements of backscattered ultraviolet radiation: Theoretical basis. *Journal of Geophysical Research: Atmospheres*. **103**(D14), 17099–17110.

Torres, O., Bhartia, P.K., Herman, J.R., Sinyuk, a., Ginoux, P., Holben, B. (2002) A Long-Term Record of Aerosol Optical Depth from TOMS Observations and Comparison to AERONET Measurements. *Journal of the Atmospheric Sciences*. **59**(3), 398–413.

Trigo, R.M., Gouveia, C.M., Barriopedro, D. (2010) The intense 2007-2009 drought in the Fertile Crescent: Impacts and associated atmospheric circulation. *Agricultural and Forest Meteorology*. **150**(9), 1245–1257.

Uno, I., Wang, Z., Chiba, M., Chun, Y.S., Gong, S.L., Hara, Y., Jung, E., Lee, S.S., Liu, M., Mikami, M., Music, S., Nickovic, S., Satake, S., Shao, Y., Song, Z., Sugimoto, N., Tanaka, T., Westphal, D.L. (2006) Dust model intercomparison (DMIP) study over Asia: Overview. *Journal of Geophysical Research Atmospheres*. **111**(12).

Vishkaee, F.A., Flamant, C., Cuesta, J., Oolman, L., Flamant, P., Khalesifard, H.R. (2012) Dust transport over Iraq and northwest Iran associated with winter Shamal: A case study. *Journal of Geophysical Research Atmospheres*. **117**(3), 1–14.

Volz, F.E. (1973) Infrared Optical Constants of Ammonium Sulfate, Sahara Dust, Volcanic Pumice, and Flyash. *Applied Optics*. **12**(3), 564.

Wald, a. E., Kaufman, Y.J., Tanré, D., Gao, B.-C. (1998) Daytime and nighttime detection of mineral dust over desert using infrared spectral contrast. *Journal of Geophysical Research*. **103**(D24), 32307.

Walker, A.L., Liu, M., Miller, S.D., Richardson, K.A., Westphal, D.L. (2009) Development of a dust source database for mesoscale forecasting in southwest Asia. *Journal of Geophysical Research Atmospheres*. **114**(18).

Wang, H., Jia, X., Li, K., Wang, H. (2014) External supply of dust in the Taklamakan sand sea, Northwest China, reveals the dust-forming processes of the modern sand sea surface. *Catena*. **119**, 104–115.

Wang, X., Zhou, Z., Dong, Z. (2006) Control of dust emissions by geomorphic conditions, wind environments and land use in northern China: An examination based on dust storm frequency from 1960 to 2003. *Geomorphology*. **81**(3–4), 292–308.

Washington, R., Todd, M., Middleton, N.J., Goudie, A.S. (2003) Dust-storm source areas determined by the total ozone monitoring spectrometer and surface observations. *Annals of the Association of American Geographers*. **93**(2), 297–313.

Washington, R., Todd, M.C. (2005) Atmospheric controls on mineral dust emission from the Bodélé Depression, Chad: The role of the low level jet. *Geophysical Research Letters*. **32**(17), 1–5.

Washington, R., Todd, M.C., Engelstaedter, S., Mbainayel, S., Mitchell, F. (2006) Dust and the low-level circulation over the Bodélé Depression, Chad: Observations from BoDEx 2005. *Journal of Geophysical Research Atmospheres*. **111**(3), 1–15.

Washington, R., Todd, M.C., Lizcano, G., Tegen, I., Flamant, C., Koren, I., Ginoux, P., Engelstaedter, S., Bristow, C.S., Zender, C.S., Goudie, A.S., Warren, A., Prospero, J.M. (2006) Links between topography, wind, deflation, lakes and dust: The case of the Bodélé Depression, Chad. *Geophysical Research Letters*. **33**(9), 1–4.

Webb, R., W, C., Rosenzweig, E., Levine, E.R. (1992) A global data set of soil particle size properties. *NASA Technical Memorandum*. (4286).

Wiggs, G.F.S., Van Der Meers, J., Small, I.., Hubbard, R., O'Hara, S.L., Wegerdt, J. (2003) The dynamics and characteristics of aeolian dust in dryland Central Asia: possible impacts on human exposure and respiratory health in the Aral Sea basin. *The Geographical Journal*. **169**(2), 142–157.

Yu, Y., Notaro, M., Liu, Z., Wang, F., Alkolibi, F., Fadda, E., Bakhrjy, F. (2015) Journal of Geophysical Research : Atmospheres. *Journal of Geophysical Research Atmospheres*. **120**, 1739–1758.

Yürekli, K. (2015) Impact of climate variability on precipitation in the Upper Euphrates-Tigris Rivers Basin of Southeast Turkey. *Atmospheric Research*. **154**, 25–38.

Zender, C.S. (2003) Spatial heterogeneity in aeolian erodibility: Uniform, topographic, geomorphic, and hydrologic hypotheses. *Journal of Geophysical Research*. **108**(D17), 4543.

Zender, C.S., Newman, D., Torres, O. (2003) Spatial heterogeneity in aeolian erodibility: Uniform, topographic, geomorphic, and hydrologic hypotheses. *Journal of Geophysical Research*. **108**(D17), 4543.

Zhang, J., Christopher, A. (2003) Longwave radiative forcing of Saharan dust aerosols estimated from MODIS, MISR, and CERES observations on Terra. *Geophysical Research Letters*. **30**(23), 1–4.

Zhu, A., Ramanathan, V., Li, F., Kim, D. (2007) Dust plumes over the Pacific, Indian, and Atlantic oceans: Climatology and radiative impact. *Journal of Geophysical Research Atmospheres*. **112**(16), 1–20.

Appendix